

Coherent Raman Spectroscopy Enabled by Photonic Integrated Circuits

Coherente ramanspectroscopie met behulp van geïntegreerde optische circuits

Haolan Zhao

Promotoren: prof. dr. ir. R. Baets, prof. dr. S. Clemmen
Proefschrift ingediend tot het behalen van de graad van
Doctor in de ingenieurwetenschappen: fotonica



Vakgroep Informatietechnologie
Voorzitter: prof. dr. ir. B. Dhoedt
Faculteit Ingenieurwetenschappen en Architectuur
Academiejaar 2017 - 2018

ISBN 978-94-6355-150-2
NUR 950
Wettelijk depot: D/2018/10.500/68

Promotoren:

Prof. dr. ir. Roel Baets Ghent University
Prof. dr. Stéphane Clemmen Ghent University

Examination Board:

Prof. dr. ir. Filip De Turck (Chair) Ghent University
Prof. dr. ir. Roel Baets (Promotor) Ghent University
Prof. dr. Stéphane Clemmen (Promotor) Ghent University
Prof. dr. ir. Bart Kuyken (Secretary) Ghent University
Prof. dr. Nicolas Le Thomas Ghent University
Prof. dr. Iwan Moreels Ghent University
Prof. dr. Goëry Genty Tampere University
of Technology
Prof. dr. Simon-Pierre Gorza Université libre de Bruxelles

Universiteit Gent
Faculteit Ingenieurswetenschappen en Architectuur

Vakgroep Informatietechnologie
Technologiepark-Zwijnaarde 15 iGent, B-9052 Gent, België

Acknowledgements

Ph.D. life is full of wonders. I still remember the cloudy and windy day that I had observed visible light generated from a chip for the first time. At that day, I had been staying in the measurement room for more than 12 hours. The room light was off, and I was wearing a protection goggle, which means I could barely see anything. The generated visible red, albeit weak, pale and flickering, was really charming. I was immediately impressed by its beauty. It was not only the beauty of its pestle color that is engaging. The fruits of success from weeks of hard work are also palatable.

However, beautiful things are ephemeral, and challenges constitute the staple in the diet of a Ph.D. student. Orchestrating a measurement, cracking a theory or Gantt-charting a fabrication process are by no means simple tasks. In retrospect, the Ph.D. life is an interesting journey to new findings. Yet the journey itself is not without pressure and frustrations. Fortunately, I have received so much help from many people. I am earnestly grateful to everyone who has directly or indirectly helped me in the past four point seventy-five years.

First of all, I would like to express my appreciation to my promotor Roel Baets. I owe my gratitude for his continuing guidance in research. Without his steering of the research direction, it is almost sure that I will go astray in the sea of photonics. His enthusiasm and confidence in research are also invigorating. His attitude always inspires me in the darkest days. It is reassuring to discuss with him, where seemingly formidable problems are reduced to elemental questions.

I am also very grateful to my co-promotor Stéphane Clemmen. His expertise in nonlinear optics and Raman scattering helped me a lot in resolving all the difficulties. His never-failing chase for perfection in research always leads me to revisit the result I have obtained. Unless substantial or even waterproof evidence is presented, he was always ready to raise a question that begins with what if. I would also like to express my gratitude to Bart Kuykens for his guidance in the first two years of my Ph.D. Without his help, it could have taken a much longer time for me to dive into the field of photonics.

I would like to thank the rest of the members of my examination board: prof. Filip De Turck, prof. Nicolas Le Thomas, prof. Iwan Moreels, prof. Goery Genty and prof. Simon-Pierre Gorza for their effort in reviewing my thesis. Their incisive comments and questions are highly valuable in achieving the final shape of the

thesis.

During my research, I have had many enlightening discussions with my colleagues. I would like to express my gratitude to Ashim Dhakal, Pieter Wuytens, Koen Alexander, Francois Leo, Ananth Subramanian, Ali Raza, Raphael Van Laer, Thijs Spuesens, Andreas De Groote, Artur Hermans, Thomas Van Vaerenbergh, Eva Ryckeboer, Ashwyn Srinivasan, Sulakshna Kumari, Antonio Ribeiro, Kasper Van Gasse, Alfonso Ruocco, Gunay Yurtsever and Amin Abbasi.

It is a luxury to work in the photonics group. A lot of the problems that I encountered during the Ph.D. cannot be solved without the help of our excellent support staff. I would like to express my thanks to the technical supports in measurement labs our group, Michael Vanslembrouck, Jasper Jans, Jelle Van de Walle and Jeroen Allaert. I would like to thank the administrative personnel in our group, Ilse Van Royen, Kristien De Meulder, Ilse Meersman, Mike Van Puyenbroeck and Bert Coryn. I would also like to thank the technical support in the cleanroom, Liesbet Van Landschoot, Steven Verstuyft, Muhammad Muneeb.

It is also great to be accompanied by my Chinese friends here to drive away nostalgia. My gratitude goes to Yufei, Yunpeng, Weiqiang, Chen, Ruijun, Bin, Yanlu, Zhechao, Ang, Lianyan, Yuxin, Xiaomin, Yuting, Xiaomin, Jing, Xin, Jie, Ye, Guanyun, Keqi, Qiangsheng, Yingchen, Jinghao, Haifeng, Qiang, Chonghuai, Zhenzhou, Mi, Yang, Naidi, Xiangfeng, Hong, and Zheng.

Finally, I would like to thank my family for their permanent support. There is an old saying in China that the child should not go far abroad when the parents are still living. Since Europe is some ten thousand kilometers away from home, I am grateful for their understanding. Special thanks to my wife, Huihui. It is difficult to imagine how my life would be without you.

August 2018, Gent

Haolan

Table of Contents

Acknowledgements	i
Nederlandse samenvatting	xxi
1 Resultaten	xxii
2 Conclusies en perspectieven	xxiv
English Summary	xxvii
3 Results	xxviii
4 Conclusions and Perspectives	xxx1
1 Introduction	1-1
1.1 Background and Challenges	1-1
1.2 Outline of the Thesis	1-4
1.3 Publications	1-6
1.3.1 Publications in International Journals	1-6
1.3.2 Publications in International Conferences	1-6
1.3.3 Publications in National Conferences	1-7
References	1-8
2 Introduction to Spontaneous and Coherent Raman Scattering	2-1
2.1 Introduction to Spontaneous Raman Scattering	2-1
2.2 Nuclear Motions as Harmonic Oscillators	2-4
2.3 Coherent Raman Scattering from the Perspective of Third-Order Nonlinear Processes	2-6
2.3.1 Nonlinear Polarizations	2-6
2.3.2 Kerr Nonlinearity	2-7
2.3.3 Coherent Raman Effects	2-8
2.4 Energy Flow of Coherent Raman Processes	2-11
2.4.1 Wave Equation with Nonlinear Polarization	2-12
2.4.2 Stimulated Raman Gain and Stimulated Raman Loss	2-14
2.4.3 Coherent Anti-Stokes Raman Scattering	2-15
2.5 Detection of CARS and SRS Signal	2-15
2.5.1 Detection of CARS Signal	2-16
2.5.2 Detection of SRS Signal	2-18
2.6 Conclusion	2-20

References	2-21
3 Stimulated and Spontaneous Raman Scattering in Waveguides: From a Quantum Mechanical Perspective	3-1
3.1 Raman Scattering from a Bulk Medium in Free Space	3-2
3.1.1 Spontaneous Raman Scattering	3-3
3.1.2 Stimulated Raman Scattering	3-5
3.2 Spontaneous and Stimulated Raman Scattering in Wave-Guiding Structures	3-7
3.3 Introduction to Silicon Nitride Waveguides	3-9
3.4 Raman Gain Coefficients of Silicon Nitride Waveguides	3-11
3.4.1 Raman Response Function and Scattering Cross-Section	3-11
3.4.2 Effective Index and Confinement Factor	3-14
3.4.2.1 TE polarization	3-15
3.4.2.2 TM polarization	3-16
3.4.3 Numerical Value of the Raman Gain Coefficients on Silicon Nitride Waveguides	3-17
3.4.3.1 Spontaneous Raman Gain Coefficient	3-17
3.4.3.2 Stimulated Raman Gain Coefficient	3-18
3.4.3.3 Relation Between the Spontaneous and Stimulated Raman Gain Coefficients	3-19
3.5 Propagation of Raman Signal in Waveguides	3-20
3.5.1 Spontaneous Raman Scattering in Waveguide	3-21
3.5.1.1 Forward Collection	3-21
3.5.1.2 Backward Collection	3-22
3.5.2 Stimulated Raman Scattering in Waveguides	3-23
3.5.2.1 Co-Propagating Stimulated Raman Scattering	3-23
3.5.2.2 Counter-Propagating Stimulated Raman Scattering	3-24
3.6 Conclusion	3-25
References	3-26
4 From Coherent Anti-stokes Raman Spectroscopy to Supercontinuum Generation	4-1
4.1 Phase-Matching Condition for CARS in Silicon Nitride Waveguides	4-2
4.2 Group Velocity Dispersion of Silicon Nitride Waveguides	4-4
4.2.1 Material Dispersion of Silicon Nitride	4-5
4.2.2 Waveguide Dispersion of Silicon Nitride Waveguides	4-5
4.2.3 Impact of Higher-Order Dispersion	4-11
4.2.4 Possible Paths Towards On-Chip CARS	4-13
4.3 Supercontinuum as a Broadband Light Source	4-16
4.4 Mechanisms for Supercontinuum Generation	4-18
4.4.1 Solitons and Soliton Fission	4-19
4.4.2 Modulation Instability and Soliton Dynamics	4-24
4.5 Waveguide Fabrication and Dispersion Engineering	4-25

4.6	Setup for Supercontinuum Generation	4-27
4.7	Demonstration of the First Visible-to-near-infrared Supercontinuum in a Silicon Nitride Waveguide	4-29
4.8	Conclusion	4-34
	References	4-36
5	Experimental Demonstration of Stimulated Raman Scattering on the Silicon Nitride Platform	5-1
5.1	Sample Fabrication	5-2
5.2	Experimental Setup for SRS	5-2
5.2.1	Modulation Transfer Detection Scheme	5-3
5.2.2	Electronics Instrumentations	5-6
5.2.3	Determination of the Modulation Frequency	5-7
5.2.3.1	Electromagnetic Interference Induced Offset	5-7
5.2.3.2	Noise Associated with the Setup	5-8
5.3	Parasitic Effects in SRS	5-10
5.3.1	Fabry-Perot Cavity Induced Fringes	5-11
5.3.2	Mach-Zehnder Interference Induced Fringes	5-15
5.4	SRS Spectrum on Silicon Nitride Waveguides	5-19
5.5	Comparison Between SRS and Spontaneous Raman Scattering	5-25
5.5.1	Estimation of the Spontaneous Raman Gain Coefficient	5-26
5.5.2	Estimation of the Stimulated Raman Gain Coefficient	5-27
5.5.3	Enhancement of SRS over Spontaneous Raman Scattering	5-28
5.5.4	Discrepancy Between Simulations and Experiments	5-29
5.5.5	Estimation of the Ultimate SRS Performance	5-30
5.5.6	Practical Improvements on SNR of SRS	5-34
5.6	Conclusions and Perspectives	5-35
	References	5-37
6	Conclusions and Perspectives	6-1
6.1	Conclusions from the Presented Work	6-1
6.2	Outlooks of Future Perspectives	6-3
	References	6-6
A	A Quantum Mechanical treatment of stimulated and spontaneous Raman scattering	A-1
A.1	Quantization of Electromagnetic Wave	A-1
A.1.1	Mode Function for Bulk Medium	A-2
A.1.2	Mode Function for Waveguides	A-3
A.1.3	Density of State	A-4
A.2	Quantization of Molecules	A-4
A.2.1	Nuclear Motion	A-5
A.3	Light-Matter Interaction	A-7
A.3.1	Perturbation Approximation of Light-Matter Interaction	A-8
A.4	Raman Scattering from An Ensemble of Molecules	A-9

A.5	Material Raman Function	A-11
A.6	Experimental Raman Scattering	A-11
A.6.1	Intensity of Light	A-12
A.6.2	Spontaneous Raman Scattering	A-12
A.6.2.1	Spontaneous Scattering in Bulk Medium	A-13
A.6.2.2	Spontaneous Raman Scattering in Waveguides	A-14
A.6.3	Stimulated Raman Scattering	A-14
A.6.3.1	Scattering from Signal to Pump	A-14
A.6.3.2	Stimulated Raman Scattering in Bulk Medium	A-15
A.6.3.3	Stimulated Raman Scattering in Waveguides	A-15
	References	A-16
B	Process Flow of Facet Polishing	B-1
	References	B-5
C	Estimation of Raman Susceptibility from Scattering Cross-Section	C-1
C.1	From Spontaneous to Stimulated Raman Gain	C-1
C.2	From Stimulated Raman Gain to Raman Susceptibility	C-2
C.3	Lorentzian Assumption of Raman Susceptibility	C-2
C.4	Estimation of the Strength of Raman Susceptibility for Pure Iso- propyl Alcohol	C-4
	References	C-5

List of Figures

- 1 De opbouw van een supercontinuum door het pompen van een dispersie-gemanipuleerde siliciumnitride golfgeleider met een Ti:saffier gepulste femtosecondelaser. Het piekvermogen (links) en gemiddeld vermogen (rechts) zijn tevens aangeduid op de figuur. xxiii
- 2 De opgemeten SRS spectra met een golfgeleider voor (rode stippellijn) en na (doorlopende rode lijn) het aanbrengen van DMSO. De spontane Ramanspectra voor DMSO zijn also referentie opgemeten met een confocale Ramanmicroscop (zwarte stippellijn) en met dezelfde golfgeleider (doorlopende blauwe lijn). xxiv
- 3 The buildup of the supercontinuum. It is initiated by pumping a dispersion-engineered silicon nitride waveguide with a Ti:Sapphire femtosecond pulsed laser. The peak powers (left) and the average powers (right) of the pulses are also indicated in the figure. xxix
- 4 The recorded SRS spectra from a silicon nitride waveguide before (dotted red line) and after (solid red line) the application of dimethyl sulfoxide (DMSO). Spontaneous Raman scattering taken from the same waveguide is shown in figure (dashed blue line). As a reference, the Raman spectrum of DMSO measured with a confocal microscope is also given in the figure (black dotted line). xxx
- 2.1 The molecular potential of a diatomic molecule (solid curve) and the potential of a harmonic oscillator (dashed curve). In the vicinity of the equilibrium R_0 , the harmonic oscillator model provides an excellent approximation of the real molecular potential. 2-4
- 2.2 The real part and imaginary part of the Raman susceptibility $\chi_R(\Omega)$. Note that $\Omega = \omega_p - \omega_s$. The real component exhibits an asymmetric pattern while the imaginary component has a symmetric Lorentzian shape. At zero detuning $\Omega = \omega_p$, the Raman susceptibility $\chi_R(\omega_p)$ is an imaginary number. 2-11
- 2.3 A typical CARS signal from dilute analytes. The majority of the CARS signal arises from the Kerr contribution $|\chi_K|^2$. In addition, although $|\chi_R(\Omega)|^2$ has a Lorentzian lineshape, its contribution is swamped by the anti-symmetric cross-term $2\chi_K \text{Re}\{\chi_R(\Omega)\}$ 2-17

3.1	The geometry of spontaneous Raman scattering in a bulk medium. An infinite plane wave (represented by the green square) is incident on a Raman medium over a volume of $dV = dA dz$. Part of the pump light experiences a Stokes shift and deflects from its original propagation direction. The total scattered power propagating within a solid angle of $d\Phi$ within the frequency range of $[\omega_s, \omega_s + d\omega_s]$ is denoted as P . The polarizations of the pump beam and the Stokes beam are denoted as \hat{e}_p and \hat{e}_s respectively.	3-4
3.2	The geometry of stimulated Raman scattering in a bulk medium. Both pump beam and signal beam are assumed to be infinite plane waves. The signal beam (red) is propagating along z direction polarized at \hat{e}_s . The pump beam (green) is propagating along a certain direction and it is polarized at \hat{e}_p . The polarization of the signal beam is decomposed to a component perpendicular \hat{e}_\perp and a component parallel \hat{e}_\parallel to the pump beam.	3-6
3.3	The structure of an air-clad strip waveguide and an air-clad slot waveguide. The top- and side-cladding of the silicon nitride is totally removed. The waveguide core sits on a thick layer of buried silicon dioxide (BOX) on the bottom. For strip waveguides, their dimensions are determined by the height h and the width w . The dimension of slot waveguides are determined by the height h , the width w , and gap size g	3-10
3.4	The scheme of evanescent Raman detection on silicon nitride waveguides. The structures of the waveguide (a) before and (b) after the application of analyte.	3-11
3.5	The spectral density of the differential cross-section of Raman scattering $\partial^2\sigma/\partial\omega\partial\Phi$ is shown as the solid red line in the figure. The differential cross-section of Raman scattering $d\sigma/d\omega$ is obtained by integrating $\partial^2\sigma/\partial\omega\partial\Phi$ over the whole spectrum, which is the actually the area of blue zone.	3-13
3.6	The geometrical coefficient of the fundamental TE mode of strip waveguides at various heights and widths available in BioPIX.	3-16
3.7	The comparison of the geometrical coefficient of the fundamental TE mode of a slot waveguide with a 150 nm slot and a strip waveguide.	3-17
3.8	The geometrical coefficient of the fundamental TM mode of strip waveguides with different width and heights.	3-18
3.9	Comparison of the geometrical coefficient of the fundamental TM mode of a slot waveguide with a 150 nm gap and a strip waveguide.	3-19
3.10	Two configurations of waveguide-based spontaneous Raman experiments. (a) Forward collection. We collect the scattered light propagates along $+z$ direction. (b) Backward collection. We collect the scattered light propagates along $-z$ direction.	3-21
3.11	The evolution of the Stokes power in the backward-collection and forward-collection configurations.	3-23

-
- 3.12 Two configurations of waveguide-enabled SRS experiments. (a) In the co-propagating SRS, both pump and signal beams are propagating along the $+z$ direction. (b) In the counter-propagating configuration, the signal beam is propagating along the $+z$ direction while the pump is along the $-z$ direction. 3-24
- 4.1 The material dispersion $\beta_{2,M}$ for silicon nitride deposited by PECVD and LPCVD techniques. We can see for this specific batch of silicon nitride (BioSiN2), the one deposited by LPCVD has much weaker normal dispersion. 4-6
- 4.2 The group velocity dispersion of both TE (left) and TM (right) modes of silicon nitride strip waveguides of different heights. The height of the waveguide h varies from 200 nm to 500 nm by steps of 50 nm. The width of the waveguide is fixed to 800 nm. A thinner waveguide has a darker color in the figure. 4-7
- 4.3 The group velocity dispersion of both TE (left) and TM (right) modes in silicon nitride strip waveguides of different widths. The width of the waveguide w varies from 400 nm to 1000 nm by a step of 100 nm. The height of the waveguide is fixed to 300 nm. A narrower waveguide has a darker color in the figure. 4-7
- 4.4 The group velocity dispersion of the TE mode in three different waveguide designs. (a) A conventional silicon nitride strip waveguides that is side- and top-clad with air and under-clad with silicon dioxide. (b) Two strip waveguides with 120 nm (blue solid) and 180 nm (red solid) of their BOX layer etched away. (c) A fully suspended strip waveguides with all of its BOX layer removed. . . 4-9
- 4.5 The group velocity dispersion of the TE mode of water-clad waveguides with (blue curve) and without (red curve) the BOX layer. . . 4-9
- 4.6 The group velocity dispersion of the TE mode of slot waveguides with different widths and heights. (Left) The waveguide width w varies from 600 nm to 1.3 μm with a resolution of 100 nm. The height is fixed to 300 nm and the slot gap is 150 nm. A darker color implies a narrower waveguide. (Right) The height h sweeps from 200 nm to 800 nm with a resolution of 100 nm. The width is fixed to 800 nm and the slot gap is 150 nm. A darker color implies a thinner waveguide. 4-10
- 4.7 (Left) The group velocity dispersion of both TE and TM modes of a slot waveguide and a strip waveguide. (Right) The structure of the slot and the strip waveguide. 4-11
- 4.8 The group velocity dispersion of the TE mode of a silicon nitride strip waveguide. The dimension of the silicon nitride core is $h \times w = 300 \text{ nm} \times 550 \text{ nm}$ and 120 nm of the silicon dioxide under-cladding is removed. 4-12

-
- 4.9 The CARS bandwidth of the TE mode of a 1-cm-long strip waveguide with an underetching of 120 nm. The CARS bandwidth is obtained by calculating $\text{sinc}^2(\Delta kL/2)$ for various pump wavelength. Only the group velocity dispersion β_2 is taken into account. . . . 4-13
- 4.10 The CARS bandwidth of the TE mode of a 1-cm-long strip waveguide with an underetching of 120 nm. The CARS bandwidth is obtained by calculating $\text{sinc}^2(\Delta kL/2)$ for various pump wavelength. Chromatic dispersion up to the 6th order is taken into account. . . 4-14
- 4.11 The CARS bandwidth of the TE mode of a 1-cm-long strip waveguide without underetching. The cross-section of the silicon nitride core is also $h \times w = 300 \text{ nm} \times 550 \text{ nm}$. The CARS bandwidth is obtained by calculating $\text{sinc}^2(\Delta kL/2)$ for various pump wavelengths. Chromatic dispersion up to the 6th order is taken into account. 4-15
- 4.12 The evolution of solitons with $N = 1, 2, 3, 4$ over a distance of three soliton periods. It is evident that although the fundamental soliton retains its temporal and spectral profile over distance, higher-order solitons experience periodic variation over propagation. The period of the variation is the same for all solitons. . . . 4-21
- 4.13 The propagation of solitons with $N = 4$ over a distance of three soliton period. β_3 is also included in the simulation. It is evident from the time domain that this soliton cannot retain its periodic variation. It breaks into three separate solitons. In the frequency domain, the output spectrum is much wider than the input spectrum. 4-21
- 4.14 The “Cherenkov condition” for dispersive wave generation. DW stands for dispersive wave. The “Cherenkov angle” θ is determined by the phases of the soliton ϕ_{sol} and dispersive wave ϕ_{DW} accumulated over an interval of t 4-23
- 4.15 (a) Schematic cross-section of the waveguide. (b) Scanning Electron Microscope (SEM) picture of the waveguide cross-section. The cross-section is preparing by sectioning the silicon nitride waveguide core with focused ion beam (FIB). The material around the silicon nitride core is deposited during FIB to enhance image contrast. 4-26
- 4.16 The spectrum of propagation loss of an underetched waveguide from 600 nm to 950 nm. 4-27
- 4.17 The measured group velocity dispersion of a waveguide with a nominal cross-section of $h \times w = 300 \text{ nm} \times 600 \text{ nm}$ (green curve). For comparison, the group velocity dispersion obtained in simulation are also shown for waveguides with a nominal cross-section of $h \times w = 300 \text{ nm} \times 600 \text{ nm}$ (blue solid curve) and a nominal cross-section of $h \times w = 315 \text{ nm} \times 600 \text{ nm}$ (red dashed curved). An underetching of 150 nm is taken into account in all these waveguides. 4-28

4.18	Group velocity dispersion of Si_3N_4 waveguides with various etching depths. The impact of an uncertainty in waveguide height of ± 10 nm is shown as the gray area.	4-28
4.19	Setup for SCG in an underetched silicon nitride waveguide. We can clearly observe that visible light is generated within the waveguide.	4-29
4.20	Output spectra from the waveguide at various pump levels. The peak power of the pump beam is shown on the left and the average input power is shown on the right to the output spectra. Each spectrum is shifted by 20 dB vertically for clarity.	4-30
4.21	(Top) Comparison between measured spectrum and simulation in the output and (below) evolution of the pulse inside waveguide with 874 W input peak power.	4-33
5.1	Setup for SRS experiment. A diode laser (LD785-SEV300, Thorlabs) and a CW tunable Ti: Sapphire laser (SOLSTIS, M2) are employed as the pump and the Stokes beam respectively. The diode laser is modulated at 38 MHz, and the induced gain in the Stokes beam is detected. Half-wave-plates and polarizing-beam-splitters are used to adjust the power and polarization of both beams. Two objectives couple the pump and the Stokes beams into opposite sides of the waveguide. The optical alignment is actively optimized by monitoring the transmission of both beams.	5-4
5.2	The workflow of the modulation transfer detection scheme for SRS. Initially, the pump beam is modulated while the Stokes beam remains CW. Raman interaction will transfer the modulation from the pump beam to the Stokes beam. In the detection side, a lock-in amplifier is used to reject the CW component (local oscillator) and record only the Raman component.	5-5
5.3	A schematic plot of the function of each electronic components in detecting the SRS signal.	5-6
5.4	(a) The setup for the dark offset and the dark noise measurement. The output of the Stokes beam is blocked by a beam blocker, and therefore the output registered by the lock-in arises only from the electronic instruments. (b) The setup for the system-wide offset and the system-wide noise measurement. The Stokes beam is unblocked, and the lock-in output is not only influenced by the electronic instruments, it is also influenced by the Stokes beam. Note that there is no waveguide in both scenarios.	5-9
5.5	The lock-in output with varying modulation frequencies. Both dark offset (solid blue) and system-wide offset (solid red) are presented. The inset shows the lock-in output from 30 MHz to 40 MHz. The time constant in both scenarios is set to 100 ms and the settling times is 1 s.	5-10

5.6	(a) The structure of a waveguide with vertical facets. (b) The structure of a waveguide with tilted facets. The process we used to introduce the tilted facets are discussed in detail in Appendix B. (c) The lock-in output for SRS measurements with these two types of waveguides. The sizeable oscillatory feature in the range of $100\ \mu\text{V}$ measured with vertical facets are significantly suppressed with tilted facets. A smooth signal around $2.3\ \mu\text{V}$ is obtained from waveguides with tilted facets, which constitutes substantial evidence that the parasitic signals induced by the FP cavity are suppressed.	5-12
5.7	The Fourier domain of the fringes. The 1st, 2nd and 3rd order peaks are readily observable.	5-14
5.8	The modal reflectivity of a θ -degree tilted facet is equivalent to the transmission between two waveguides rotated by 2θ	5-15
5.9	A typical spectral fringe that is observed after the application of DMSO.	5-16
5.10	The Fourier analysis of the fringes shown in Fig.5.9. It is clear there exists only one peak in the time domain, implying that the fringe is caused by a MZI-like cavity.	5-17
5.11	(a) The light incident on the waveguide is split into two arms. Most of the light couples into the waveguide mode while a small portion of the light couples into the cladding mode. (b) Collinear alignment of the objective allows the cladding mode to combine with the waveguide transmission, causing fringes in the lock-in. (3) The MZI effect can be circumvented by inserting a lateral displacement between these two objectives.	5-18
5.12	The response of the waveguide core below $1050\ \text{cm}^{-1}$ measured with spontaneous Raman scattering (blue dashed) and SRS scattering (red solid).	5-20
5.13	The response of the waveguide from $2250\ \text{cm}^{-1}$ to $2400\ \text{cm}^{-1}$. The spectra are measured with both spontaneous Raman scattering (blue solid) and SRS (red triangle).	5-21
5.14	Recorded SRS spectra from the waveguide before (dotted red) and after (solid red) the application of DMSO. Reference spontaneous Raman spectra for DMSO are taken separately with a confocal Raman microscope (black dotted) and with the same waveguide (dashed blue).	5-22
5.15	The SRS signal of different concentrations of DMSO in water. (a) SRS spectra of 50 %, 15 % and 2 % of DMSO measured with a time constant of 100 ms (blue) with a y-axis offset for clarity. The 15 % and 2 % data are shifted from the 50 % data by $-2\ \text{V}/\text{W}^2$ and $-4\ \text{V}/\text{W}^2$ respectively. (b) Mean-value-subtracted SRS spectra of 2 % of DMSO measured with both 100 ms (blue) and 600 ms (red). (c) The extracted peak height from the SRS spectra and its standard deviation.	5-23

-
- 5.16 Linear scaling of the lock-in output with incident pump and Stokes power. When the pump of one beam is tuned, the power of the other beam is set to 30 mW. The linear dependence of lock-in output on the input power is a piece of strong evidence that we are recording the SRS signal. 5-24
- 5.17 (a) Schematic representation of lock-in detection for one periodic signal. The lock-in amplifier records the amplitude of a periodic signal in the complex plane. It records the in-phase component X and quadrature component Y , and the amplitude R is calculated by $R = \sqrt{X^2 + Y^2}$. (b) Schematic representation of lock-in detection for two periodic signals. The total amplitude of the signal is influenced by the relative phase between individual signals. . . . 5-25
- 5.18 The setup for the spontaneous Raman measurement. We use the same sample for both SRS and spontaneous Raman scattering. The waveguide is pumped by a 785 nm laser to excite the fundamental TE mode. The spontaneous Raman signal in backward-propagation is captured and analyzed. 5-26
- 5.19 (a) Estimation of SNR for both spontaneous Raman scattering and SRS with different excitation powers in free space. At a low excitation power, the spontaneous technique outperforms SRS. However, the performance of SRS soon catches up with and surpasses its spontaneous counterpart at a higher excitation power. (b) The excitation power required for SRS to have the same performance as spontaneous Raman scattering is plotted with varying facet coupling efficiency T_{fo} . With a better coupling scheme, the SRS will outperform its spontaneous counterpart at a comparatively low power. 5-33
- 5.20 (a) The SNR of both SRS and spontaneous Raman scattering with different wavelength lengths. There exist an optimal length for both methods. (b) If the length of the waveguide is fixed at the optimal point, the best available performance is plotted for both methods. SRS shows a steeper dependency on propagation loss. . . 5-34
- B.1 Schematic of the process of facet polishing. (a) The structure of the sample we received from imec. (b) The structure of the sample after dicing. The dicing line is deliberately deviated by approximately 100 μm from the desired facet. (c) The structure of the sample after polishing. B-2
- B.2 Schematic of the sample holder. The sample holder is composed of two parts — a cover and a base. Two M3 screws are used to connect the cover and the base. B-3

- B.3 The process of mounting the samples. (a) The sample and sample holders are heated up to 100° . (b) Apply a few droplets of Crystalbond 509 solution. (c) After the application of Crystalbond 509 solution, wait for about 90 s and then stack the samples onto the base. The 3d plot in (c') shows the expected status of the sample block. (d) Rotate the sample-and-holder block by 90° and push the samples against a reference plane. Use a cotton swab to ensure the coplanar alignment of the sample facets. The 3d plot in (d') shows the final alignment of the sample block. B-4
- B.4 (a) The SEM picture and (b) microscope picture of the nanoparticles accumulated on the sample surface over the polishing process. The small spheres with have a diameter of 40 nm. These spheres do not easily come off with standard acetone-isopropyl alcohol cleaning. B-5
- B.5 The surface of the silicon nitride sample after SC1 cleaning. It is clear almost all the nanospheres are removed. B-6
- C.1 The real part (blue solid) and imaginary part (red solid) of the Raman susceptibility. The absolute variation of the these two components are most interested in estimating the strength of coherent Raman scattering. C-4

List of Tables

3.1	Properties of silicon nitride thin films deposited by PECVD and LPCVD techniques. This table is taken from Ref. [13].	3-11
3.2	Chemical properties of pure isopropyl alcohol (IPA) and the differential cross-section of Raman scattering for its 819 cm^{-1} Raman peak.	3-14
3.3	The parameters used for estimating the obtainable signal power of spontaneous Raman scattering. The upper half of the table are the raw parameters and the second half are the geometry-relevant parameters obtained with 2D FDTD simulations by FIMMWAVE.	3-20
4.1	The chromatic dispersion of waveguides with nominal cross-sections of $310\text{ nm} \times 500\text{ nm}$ and $290\text{ nm} \times 500\text{ nm}$. The chromatic dispersion used in the NLSE to obtain the blue curve in the top panel of Fig. 4.21 is shown in the last column.	4-31
4.2	The parameters used to simulate the SCG in an underetched silicon nitride waveguide. The result is presented in Fig. 4.21.	4-32
5.1	Parameters of a silicon nitride waveguide. It is used for estimating the strength of the FP-induced parasitic signal.	5-13
5.2	The theoretical and experimental values of the spontaneous Raman gain coefficient G_{\parallel} and the stimulated Raman gain coefficient g_{\parallel} . The theoretical values of G_{\parallel} and g_{\parallel} are 60 and 35 times larger than the experimental values, respectively.	5-29
5.3	The parameters used for comparing the performance of stimulated Raman scattering and spontaneous Raman scattering.	5-31
C.1	The properties of pure isopropyl alcohol (IPA).	C-4

List of Acronyms

C

CARS	Coherent anti-Stokes Raman Scattering
CCD	Charge-Coupled Device
CMOS	Complementary Metal-Oxide-Semiconductor
CRS	Coherent Raman Scattering
CW	Continuous Wave

D

DMSO	Dimethyl Sulfoxide
DW	Dispersive Wave

F

FP	Fabry-Perot
FWHM	Full Width Half Maximum

I

IPA	Isopropyl Alcohol
-----	-------------------

M

MZI	Mach-Zehnder Interferometer
-----	-----------------------------

P

PCF Photonic Crystal Fibers
PIC Photonics Integrated Circuits

S

SCG Supercontinuum Generation
SE-CARS Surface-Enhanced Coherent Anti-Stokes Raman Scattering
SOI Silicon-On-Insulator
SRS Stimulated Raman Scattering

T

TE Transverse Electric
TM Transverse Magnetic

Z

ZDW Zero-dispersion Wavelength

Nederlandse samenvatting –Summary in Dutch–

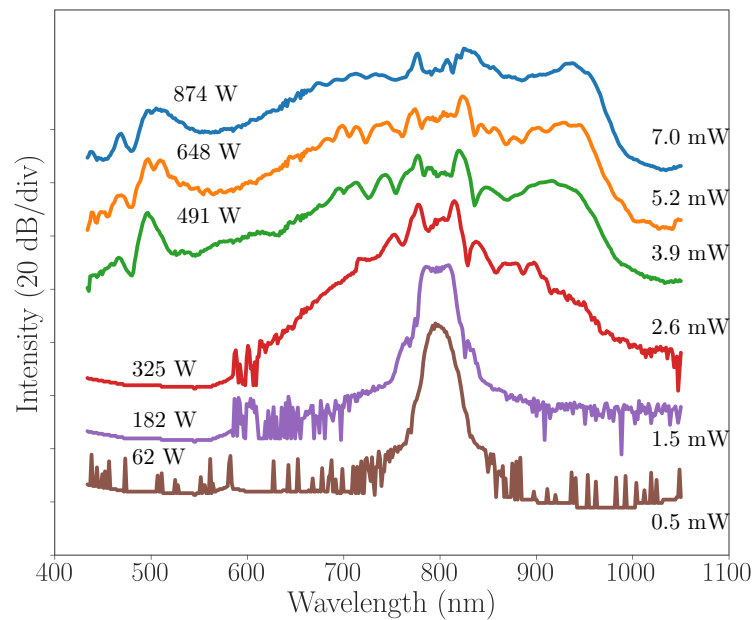
Ramanspectroscopie is erg in trek in de biomedische, fysische, chemische en omgevingswetenschappen vanwege zijn inzetbaarheid voor het kwalitatief en kwantitatief onderzoeken van de fundamentele trillingen van moleculen. Maar door de intrinsieke zwakte van het Ramanverstrooiingsproces is men typisch genoodzaakt om dure en omvangrijke instrumenten te gebruiken, zoals geavanceerde hoogvermogenlasers en gekoelde CCD-cameras. Dit verhindert het weidverspreid gebruik van Ramanspectroscopie buiten het laboratorium. In de context van de ERC Advanced Grant Inspectra stelt onze onderzoeksgroep de volgende oplossing voor: het gebruik van gintegreerde optische circuits (PICs) met een hoog-indexcontrast voor Ramandetectie, meer bepaald op een siliciumnitride platform. Het optische veld wordt geleid door de siliciumnitride enkelvoudige-modus-golfgeleiders en het Ramansignaal wordt geadresseerd door het uitdovende veld van de geleide mode. Het gebruik van siliciumnitride PICs biedt twee voordelen. Ten eerste vergroot het golfgeleidingseffect het volume van de Ramaninteractie aanzienlijk, hetgeen resulteert in een versterkt Ramansignaal. Ten tweede is de siliciumnitride nanofotonica nu een zeer ontwikkeld platform dat over een uitgebreid gamma gintegreerde lasers, spectrometers en hoogperformante spectrale functies (zoals filters, Arrayed Waveguide Gratings en Bragg-roosters) beschikt. Als een CMOS-compatibele technologie zijn siliciumnitride gintegreerde optische circuits veelbelovend om een volledig gintegreerde Ramansensor met een klein voetafdruk en lage kost te realiseren. Het potentieel van het siliciumnitride platform herkenkend, heeft onze groep de eerste experimentele demonstratie van on-chip spontane Ramanspectroscopie gerapporteerd voor de bulkvloeistof isopropylalcohol. De on-chip spontane Ramanmethode is daarna uitgebreid voor het adresseren van een monolaag van moleculen die gefunctionaliseerd waren bovenop de golfgeleider, en ook voor gasen in ppb-concentraties met behulp van een golfgeleider gefunctionaliseerd met een hypersorberend polymeer. Het voordeel van de golfgeleider-gebaseerde methode tegenover de microscoop-gebaseerde methode in het versterken van het Ramansignaal werd duidelijk aangetoond. Helaas bleek het Ramansignaal nog steeds te zwak om het gebruik van gekoelde detectoren te vermijden voor het spontane Ramanverstrooiingsproces. Dit verhinderde de demonstratie van een volledig gintegreerde Ramansensor. Gelukkig is coherente Ramanaverstrooiing (CRS) in staat om het Ramansignaal met vele grootteordes te versterken. In CRS worden de moleculen aangeslagen door twee laserstralen: een pomplaser en een Stokes-laser.

Het verschil in frequentie zorgt voor het exciteren van de moleculaire trillingen op een resonante manier. CRS is veelvuldig gecomplementeerd in twee vormen: coherente anti-Stokes Ramanverstrooiing (CARS) en gestimuleerde Ramanverstrooiing (SRS). CARS concentreert zich op de detectie van een nieuw voortgebracht licht bij de blauwverschoven frequentie, terwijl SRS zich richt op het detecteren van relatieve intensiteitsvariëaties van de geïncideerde stralen. De gigantische signaalversterking in CRS-technieken leidt tot een breed gamma van toepassingen in biomedische microscopie in de biologie en geneeskunde. Dit is ook zeer aantrekkelijk voor ons om het succes van CRS-microscopie na te bootsen op een siliciumnitride platform in spectroscopische toepassingen. Dit vormt de basis van de motivatie voor het werk verricht in dit doctoraat.

1 Resultaten

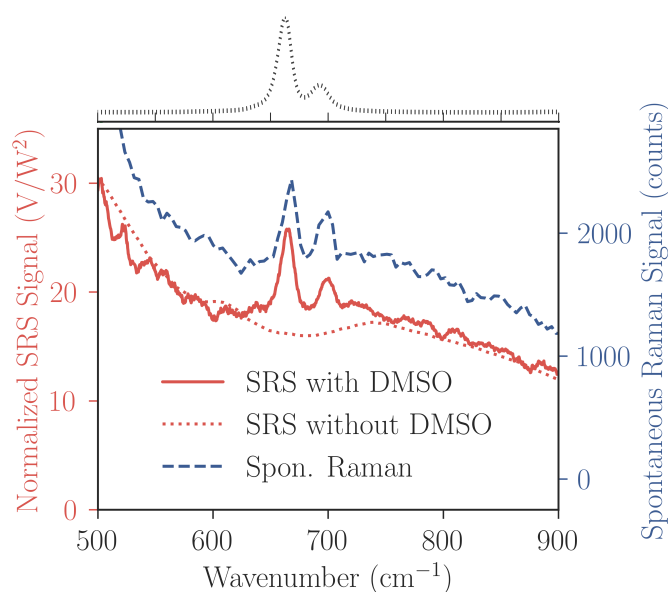
Deze thesis start met het onderzoeken van coherente anti-Stokes-Ramanverstrooiing (CARS) op een siliciumnitride platform. Aangezien CARS intrinsiek een viergolvenmengingsproces is, hebben we voor de efficiënte voortbrenging van de anti-Stokes-componenten uitdagende dispersiemanipulatietechnieken nodig om over een grote bandbreedte aan de fase-afstemmingsvoorwaarde te voldoen. Om de sterke materiaaldispersie van siliciumnitride uit te balanceren met de geometrische dispersie onderzochten we de siliciumdioxide ondermantel van de golfgeleider gedeeltelijk, hetgeen de anomale geometrische dispersie versterkt.

Om een goed begrip te verkrijgen van de dispersieve eigenschappen van het ontwikkelde siliciumnitride platform en om de weg te effenen voor de integratie van een breedbandige bron met hoge helderheid, demonstrenen we in hoofdstuk 3 supercontinuümgeneratie aangedreven door een femtosecondelaser via soliton-splitsing en dispersieve-golfgeneratie. Voor het eerst hebben wij gerapporteerd over een supercontinuüm dat het zichtbare tot infrarode spectrum omvat en gegenereerd wordt in een dispersie-gemanipuleerde siliciumnitride golfgeleider, zoals getoond in figuur 1. De resultaten worden in detail beschreven en vergeleken met theorie en simulaties. De demonstratie van supercontinuümgeneratie levert ons een waardevolle, breedbandige en integreerbare bron met hoge helderheid op voor biologisch significante toepassingen. Maar deze suggereert ook dat de materiaaldispersie moeilijk uit te balanceren is in een waterige omgeving. Hoewel CARS nog steeds gecomplementeerd kan worden in plasmonische structuren of met behulp van quasi-fase-afstemmingstechnieken, blijft zijn toepassing beperkt. SRS is te verkiezen over CARS voor golfgeleider-gebaseerde Ramansensoren omwille van de automatische fase-afstemming. In onze SRS-experimenten induceert de pompstraal een versterking van de Stokes-straal, die in de meeste gevallen vele grootteordes kleiner is dan het geïncideerde veld. Om de kleine versterking te detecteren bouwden we een opstelling gebaseerd op het modulatieoverbrengings-detectieschema. Het principe wordt in detail uitgelegd in hoofdstuk 5. Maar in dit schema is het gedetecteerde signaal onderhevig aan zowel de Kerr-niet-lineariteit als de Raman-niet-lineariteit. Door het nemen van maatregelen om te vermijden dat



Figuur 1: De opbouw van een supercontinuum door het pompen van een dispersie-gemanipuleerde siliciumnitride golfgeleider met een Ti:saffier gepulste femtosecondelaser. Het piekvermogen (links) en gemiddeld vermogen (rechts) zijn tevens aangeduid op de figuur.

het Raman-genduceerde signaal overstemd werd door het Kerr-genduceerde signaal, hebben we de eerste SRS-experimenten op een geventreerde siliciumnitride golfgeleider gedemonstreerd. In figuur 2 tonen we het vibrationele spectrum van



Figuur 2: De opgemeten SRS spectra met een golfgeleider voor (rode stippellijn) en na (doorlopende rode lijn) het aanbrengen van DMSO. De spontane Ramanspectra voor DMSO zijn also referentie opgemeten met een confocale Ramannmicroscop (zwarte stippellijn) en met dezelfde golfgeleider (doorlopende blauwe lijn).

DMSO met zowel SRS (doorlopende rode lijn) als spontane Ramanspectroscopie met een confocale microscoop (zwarte stippellijn) en spontane Ramanspectroscopie met diezelfde golfgeleider (doorlopende blauwe lijn). De resultaten zijn in goede overeenkomst met elkaar. In hoofdstuk 5 tonen we ook aan dat golfgeleider-gebaseerde SRS bijzonder geschikt is voor de kwantitatieve studie van moleculen omwille van de evenredigheid van de signaalsterkte met het vermogen van de optische excitaties en de concentratie van analyten. Daarnaast stelden we vast dat golfgeleider-gebaseerde SRS nog niet zijn ultieme prestatie heeft bereikt. Met verbetering van de modulatie, golfgeleiderontwerp, exciterend vermogen en lichtkoppeling, geloven wij dat golfgeleider-gebaseerde SRS ons in staat zal stellen om biologische significante moleculen in sub-millimolconcentraties te detecteren.

2 Conclusies en perspectieven

Het werk gepresenteerd in dit doctoraat vormt een stap in de richting van Raman-on-a-chip door het verkennen van twee fenomenen van coherente Ramanverstrooi-

ing coherente anti-Stokes Ramanverstrooiing (CARS) en gestimuleerde Ramanverstrooiing (SRS). De noemenswaardige verwezenlijkingen in dit werk zijn: Fase-afstemming op een siliciumnitride platform in het zichtbare golflengtebereik werd aangetoond door middel van dispersiemanipulatie. Met de fase-afstemmingstechniek en het wijde transparantiegebied van de siliciumnitride golfgeleider, toonden we octaafoverspannende supercontinuümgeneratie aan die het zichtbare tot infrarode golflengtebereik omvat. De beperkingen van de onze fase-afstemmingstechniek voor CARS in een waterige omgeving werd erkend en besproken. Speciale maatregelen om deze beperkingen te omzeilen werden theoretisch voorspeld. Gestimuleerde Ramanverstrooiing door middel van een siliciumnitride nanofotonische golfgeleider werd gedemonstreerd en we toonden aan dat de signaalsterkte vele grootteordes meer is dan in de spontane methode. Dit laat de verwezenlijking van Raman-on-a-chip met kamperatuurdetectoren en CW-lasers toe.

Het is belangrijk te benadrukken dat de instrumentatie voor de SRS experimenten nu geïntegreerd kan worden. Het SRS-systeem gebruikt in dit werk bestaat uit een lock-in versterker, een gebalanceerde detector en twee constante-golf lasers. Gentegreerde lock-in versterkers met een detectielimiet in de grootteorde van 100 nV zijn reeds aangetoond. Gentegreerde gebalanceerde detectors gebaseerd op silicium technologie, die geschikt zijn voor labo-op-een-chip toepassingen, bestaan eveneens. Monolithisch gentegreerde lasers met de nodige golflengte nog niet zijn aangetoond, maar de recente ontwikkelingen van technieken zoals transferprinten zijn veelbelovend, en zullen waarschijnlijk lasers met een golflengte van 785 nm op silicium nitride in de nabije toekomst mogelijk maken. In de toekomst beogen we de integratie van een raster van lasers op de chips, elk van deze lasers zal dan een specifieke Raman mode exciteren. Op deze manier kunnen we het Ramanspectrum op korte tijd vastleggen zonder gebruik te moeten maken van golflengteverstelbare lasers. Gezien de ontwikkeling van de afzonderlijke componenten die noodzakelijk zijn voor SRS, hebben we er goede hoop in dat volledig chipgebaseerde SRS systemen niet lang op zich zullen laten wachten.

Om in de richting van golfgeleider-gebaseerde CRS-technieken te gaan moet er meer werk verricht worden om de gevoeligheid van de SRS-techniek te verbeteren. Op dit moment is het beschikbare optische vermogen dat in de golfgeleider wordt gekoppeld gelimiteerd door de imperfectie van de randkoppelaars. Dit moet opgelost worden door nieuwe randkoppelaars met een lage modale reflectie en een laag koppelingsverlies te ontwerpen. Een andere verbetering van de gevoeligheid kan er komen door de combinatie van oppervlakteversterking met de CRS-processen. Aangezien de coherente Ramanverstrooiingsprocessen een hogere-ordeafhankelijkheid hebben ten aanzien van het invallende vermogen, kunnen we een veel grotere signaalsterkte bereiken door het gebruik van oppervlakteplasmonen gegenereerd op metalen nanostructuren om de coherente Ramanverstrooiingsprocessen te versterken.

English Summary

Over the past decades, Raman spectroscopy has become a powerful tool for chemical, pharmaceutical, and biomedical analysis. Since Raman spectroscopy probes the fundamental vibrations of a molecule, it requires no sample preparation, and its signal can be collected non-invasively. However, the intrinsic weakness of the Raman scattering process typically entails expensive and bulky instrumentations, including high-power lasers and deep-cooled CCD cameras. This demanding requirement in instrumentations hinders the broader application of Raman spectroscopy in non-laboratory environments.

To overcome these limitations on instrumentation, the photonics research group at Ghent University proposes to integrate the full Raman spectroscopic system onto a single photonic chip in the context of the ERC Advanced Grant InSpectra. This is made possible by high-index-contrast photonic integrated circuits (PICs) especially the silicon nitride platform. Firstly, silicon nitride nanophotonics is now a very mature platform providing not only integrated lasers and spectrometers. High-performance spectral functionalities such as filters, arrayed-waveguide gratings, and Bragg gratings have also been demonstrated. These high-performance on-chip components not only allow for the full integration of the Raman system with a small footprint at a low cost, but they also open up the possibility of multiplex Raman sensing that multiple analytes can be probed simultaneously. Secondly, on-chip Raman sensors are also capable of enhancing the Raman signal significantly. In conventional confocal Raman microscopy, the collected signal essentially originates from molecules within the confocal volume. Of all the Raman signal that is excited, only the Raman signal generated within a particular solid angle can be collected. Unfortunately, it has been previously shown that an expanded confocal volume always comes with a price of reduced collection angle. This trade-off poses a limitation on the maximal collectible Raman signal from a Raman microscope. In on-chip Raman scattering, the optical field is confined by the index contrast between the silicon nitride core and the analytes which function as the cladding. The Raman signal is probed by the evanescent tail of the guided modes. As the waveguide structure confines the optical field, one can significantly expand the Raman interaction volume by increasing the waveguide length without sacrificing the collection angle. As a result, this wave-guiding effect leads to a much-enhanced Raman signal.

In 2014, our group reported the first experimental demonstration of on-chip spontaneous Raman spectroscopy for isopropyl alcohol (IPA) with a silicon nitride waveguide. Later more useful analytes have been probed such as monolayers

of molecules functionalized on top of waveguides and gas in ppb-level with the help of hypersorbent polymer functionalized waveguides. These demonstrations showed clearly the advantages of integrated waveguides over traditional Raman microscopes. Nevertheless, the Raman signals in these demonstrations are still too low to avoid the use of deep-cooled detectors, which hurdles the demonstration a fully integrated Raman system.

Fortunately, coherent Raman scattering (CRS) provides us with a solution. In CRS, the molecules are excited simultaneously by two laser beams – a pump laser and a Stokes laser. If their frequency difference coincides with a Raman mode, these two lasers excite this vibration resonantly. The coherent excitation induces a strong light-matter interaction. As a result, the CRS signal can be orders of magnitude improved over spontaneous Raman scattering. Thanks to its superior signal strength, CRS has been widely used in optical microscopy as a highly sensitive and chemically selective tool for label-free biological analysis.

It is highly attractive to combine CRS with silicon nitride waveguides to leverage both wave-guiding and coherent excitation enhancement mechanisms. CRS is commonly implemented in two modalities: coherent anti-stokes Raman scattering (CARS) and stimulated Raman scattering (SRS). Although the underlying physics is the same for both CRS processes, they exhibit markedly different signal properties. CARS focus on detecting an induced field in a frequency blue-shifted from the input fields while SRS focus on detecting the intensity variation of the input fields. While both CRS modalities have been meticulously investigated from the perspective of Raman microscopy, waveguide-enabled CRS has remained largely unexplored. The investigation of CRS-on-chip forms the basis of the motivation for the work in this Ph.D. The goal is to develop and characterize silicon nitride waveguide-based CRS sensors that are suitable for on-chip Raman spectroscopic systems.

3 Results

The thesis can be roughly split into two parts. In the first part, we investigated if CARS can be combined with silicon nitride waveguides. We modeled CARS as a degenerate four-wave mixing process: a pump beam and a Stokes beam are injected into the Raman-active material, and we probe the newly generated anti-Stokes component. An efficient generation of this anti-Stokes component requires one to satisfy a challenging phase-matching condition. Molecular identification usually utilizes the “fingerprint” region of Raman modes, which typically spans from 500 cm^{-1} to 1500 cm^{-1} (15 THz - 45 THz). As a result, the silicon nitride waveguide should possess extremely low chromatic dispersion at the pump frequency to record CARS over the entire “fingerprint” region. A careful investigation of the dispersive property of silicon nitride waveguides revealed that this requirement could not be satisfied on centimeters-long waveguides. The phase-matching condition could only be met on waveguides with a much shorter length. However, a reduction in waveguide length would inevitably lead to a reduction in

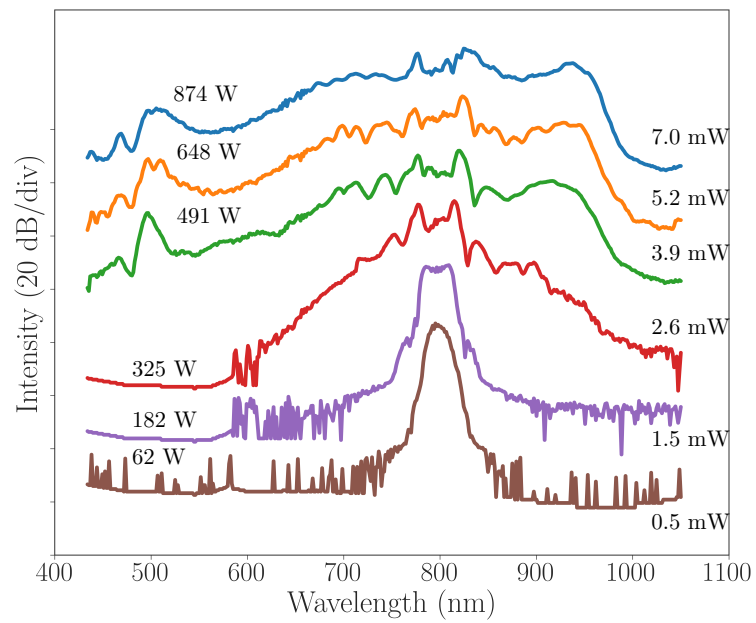


Figure 3: The buildup of the supercontinuum. It is initiated by pumping a dispersion-engineered silicon nitride waveguide with a Ti:Sapphire femtosecond pulsed laser. The peak powers (left) and the average powers (right) of the pulses are also indicated in the figure.

achievable signal intensity. This trade-off between CARS bandwidth and signal intensity significantly limited the applicability of CARS-on-chip.

Although our quest for CARS was unsuccessful, we identified a method to engineer silicon nitride waveguides to possess anomalous dispersion at 800 nm. This technique of under-etching provided us with a unique opportunity to study other third-order nonlinear optical processes below 1 μm in silicon nitride waveguides. One such example is supercontinuum generation (SCG) where a light source with a narrow linewidth is extended into a broadband light through nonlinear interactions. With our dispersion-engineering technique, we reported for the first time an octave-spanning supercontinuum covering the visible-to-near-IR regime generated in an integrated waveguide platform. The buildup of the supercontinuum with different pump powers is shown in Fig. 3. Both peak powers (left) and average powers (right) of the pulses are indicated in the figure. This result is discussed in detail in Chapter 4. Our work demonstrated for the first a supercontinuum that extended to sub-500 nm region. We believe our work on silicon nitride waveguide SCG paves the way towards an abundance of integrated applications in spectroscopy, optical coherence tomography, and precise frequency metrology.

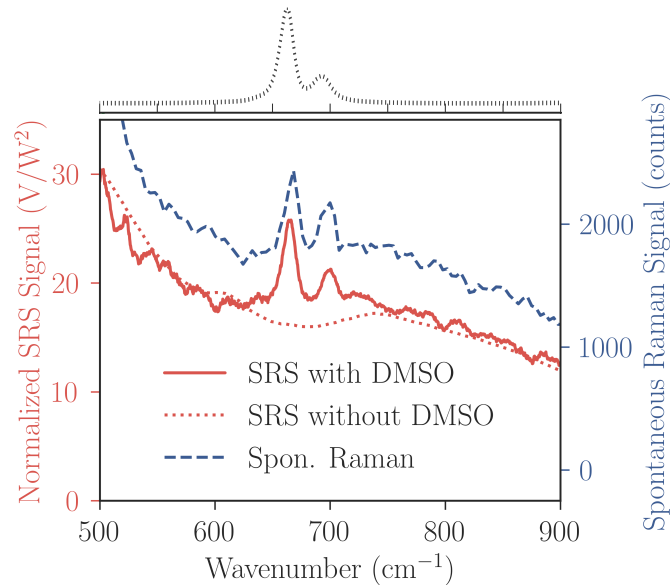


Figure 4: The recorded SRS spectra from a silicon nitride waveguide before (dotted red line) and after (solid red line) the application of dimethyl sulfoxide (DMSO). Spontaneous Raman scattering taken from the same waveguide is shown in figure (dashed blue line). As a reference, the Raman spectrum of DMSO measured with a confocal microscope is also given in the figure (black dotted line).

In the second part, we explored SRS on the silicon nitride platform. In SRS, instead of probing a newly generated anti-Stokes wave, we are detecting the inten-

sity variation of the Stokes beam induced by the pump beam. One primary benefit of SRS is that, unlike CARS, SRS is automatically phase-matched. However, it comes with a price that it is very demanding to resolve the small intensity variation induced by SRS in the presence of the intense original Stokes field. In this work, we used a modulation transfer detection scheme to resolve this small variation. With this approach, after successfully suppressing Kerr-induced parasitic signals, we demonstrated for the first time SRS on an integrated silicon nitride waveguide.

Figure 4 shows the Raman spectrum of dimethyl sulfoxide (DMSO) recorded with SRS (solid red line). Its intensity and shape are in good agreement with the spontaneous references obtained from the same waveguide (dashed blue line). The Raman spectrum of pure DMSO is also shown in this figure (dotted black line). It is clear both waveguide-based spontaneous Raman scattering and waveguide-based SRS are capable of reproducing the reference spectrum of DMSO. This result is discussed in detail in Chapter 5.

4 Conclusions and Perspectives

The work presented in this Ph.D. takes a step towards the all-on-a-chip Raman spectroscopy system by exploring coherent Raman scattering (CRS) in silicon nitride integrated waveguides. The first part of this thesis is devoted to coherent anti-stokes Raman scattering (CARS). We identified that the challenging phase-matching condition required by CARS makes this modality incompatible with the current silicon nitride platform without significant innovations in waveguide designs and experimental methods. In the second part of this thesis, we studied SRS with the silicon nitride platform. Thanks to its automatic phase-matching, we demonstrated the first SRS experiments on an integrated silicon nitride waveguide.

It is important to emphasize that the instrumentations used for SRS are now ready for integration. The SRS system we used in this work is composed mainly of a lock-in amplifier, a balanced detector, and two CW lasers. Current, high-performance integrated lock-in amplifiers have been realized where an input signal in the order of 100 nV can be detected. Integrated silicon-based balanced detectors suitable for lab-on-chip applications have also been demonstrated. Although monolithically integrated diode lasers at this wavelength have not been shown, the recent development of the transfer printing technique is promising to bring lasers emitting at 785 nm onto the silicon nitride platform. In the future, we envisage to integrate an array of lasers onto the chip, and each of the lasers is dedicated to one specific Raman mode. In this way, we can capture the Raman spectrum in a short time without widely-tunable lasers. With the development on discrete components required for SRS, we believe it is promising to demonstrate an all-on-a-chip SRS Raman system shortly.

To move the waveguide-enabled CRS techniques forward, we should first focus on improving the strength of the SRS signal. We believe the on-chip SRS technique has not achieved its ultimate performance yet. Many incremental improve-

ments can be implemented straightforwardly. With a combination of (a) reduction of coupling loss, (b) better modulation scheme and (c) use of slot waveguides, we believe it possible to enhance the SRS signal by another three orders of magnitude. Sub-millimole detection will be enabled with such a level of sensitivity, which is exciting to real applications.

1

Introduction

1.1 Background and Challenges

Raman scattering is a nonlinear process in which an incident photon is scattered inelastically by a molecule. The energy lost or gain between the incident photons and scattered photons corresponds to the energy of a vibrational mode. A Raman spectrum is obtained by measuring the intensity of the scattered photons as well as their frequency shifts. Because vibrational modes are inherent properties of the molecule, Raman spectrum allows for unambiguous molecular identification and quantification.

Raman scattering was first discovered by C. V. Raman and his student K. S. Krishnan in 1928 [1, 2] and independently by Grigory Landsberg and Leonid Mandelstam in the same year [3]. Although the potential of Raman scattering for spectroscopic sensing is already proposed soon after its discovery in 1928, Raman spectroscopy was mostly an esoteric technique confined to academic laboratories before the late-1980s. Most of the literature at that time were devoted to study the physical properties of Raman scattering itself [4].

The evolution of Raman spectroscopy has paralleled the maturation of its underlying enabling technologies. Over the past decades, lasers have become commodity items that are now available at a variety of wavelengths with high-power and high-brightness. High-sensitivity low-noise detectors have been increasingly available thanks to innovations in charge-coupled devices (CCD) and complementary metal-oxide-semiconductor (CMOS) imagers. These advances, in combina-

tion with improvements in laser line filters, microscopy and computer technology, have transformed Raman spectroscopy from a specialist technique to a powerful analytical tool [4, 5]. Nowadays, Raman spectroscopy has found wide popularity in biomedical, physical, chemical and environmental areas due to its capability of unambiguous molecular identification, its compatibility with aqueous samples and its ability to probe samples in a non-invasive manner [6–9].

In the recent years, there has been an increasing demand for miniaturized Raman device for in-situ detection. However, the intrinsic weakness of Raman scattering typically entails expensive and bulky instrumentations, including high-power lasers and deep-cooled CCD cameras. This requirement in instrumentations hinders the miniaturization of Raman systems and impedes broader applications of Raman spectroscopy in non-laboratory environments. At the moment, although hand-held Raman devices are already available on the market [10, 11], these devices usually come with a price tag of a few tens of thousands Euro. Besides, they are still relatively bulky for remote in-situ applications.

To overcome these limitations on instrumentation, the photonics research group at Ghent University proposes to integrate the full Raman spectroscopic system onto a single photonic chip in the context of the ERC Advanced Grant InSpectra. This is made possible by high-index-contrast photonic integrated circuits (PICs). One major advantage of on-chip Raman sensors is their capability of enhancing the Raman signal significantly. In conventional confocal Raman microscopy, the collected signal essentially originates from molecules within the confocal volume. Of all the Raman signal that is excited, only the Raman signal generated within a certain solid angle can be collected. Unfortunately, it has been previously shown in Section 2.7.1 of [12] that an expanded confocal volume always comes with a price of reduced collection angle. This trade-off poses a limitation on the maximal collectible Raman signal from a Raman microscope. In on-chip Raman scattering, the optical field is confined by the index contrast between the silicon nitride core and the analytes which function as the cladding. The Raman signal is probed by the evanescent tail of the guided modes. As the waveguide structure confines the optical field, one can significantly expand the Raman interaction volume by increasing the waveguide length without sacrificing the collection angle. As a result, this wave-guiding effect leads to a much-enhanced Raman signal.

On-chip Raman sensor can also enable the full integration of the Raman system with a small footprint at a low-cost thanks to its compatibility with the CMOS infrastructure. Currently, the most prominent PIC platform is probably the silicon-on-insulator (SOI) platform. Although SOI is a highly accurate and mature platform with a high level of yield, robustness, and reproducibility [13], it does not cover the essential bio-optical window spanning from 700 nm to 900 nm. This window is of particular importance for therapeutic applications, and it is also called *therapeutic window*. At this wavelength range, a laser does minimal photodam-

age to biological tissues and experiences negligible water absorptions. Among the therapeutic window, by far the most essential excitation wavelength used for Raman spectroscopy is 785 nm. The use of this wavelength is driven by multiple practical advantages. Firstly, auto-fluorescence of bio-samples is greatly suppressed at this wavelength. Fluorescence and Raman scattering are two competing processes while the former is usually orders of magnitude more efficient than its Raman counterpart. The presence of background fluorescence often renders the acquisition of Raman spectrum impossible. As most of the fluorescent modes can only be excited by visible light, the utilization of near-infrared (NIR) excitations, including 785 nm and 1064 nm lasers, is the most effective method to suppress the fluorescence background. Secondly, the use of 785 nm diode lasers allows one to access the majority of Raman modes of biochemical interest (from 500 cm^{-1} to 1500 cm^{-1}) with low-cost and high-performance silicon-based detectors. The silicon-based detectors have a high detection efficiency from 800 nm to 1000 nm, which covers the Raman modes from 238 cm^{-1} to 2738 cm^{-1} . Because of these advantages, we will also focus on the use of NIR diode lasers around 785 nm for on-chip Raman spectroscopy.

Silicon nitride (Si_3N_4) appears to be a promising candidate that is compatible with the NIR excitations while maintaining the compatibility with CMOS infrastructure. It has a broad transparency window from 500 nm to 5000 nm and a refractive of 1.94 at 785 nm. Currently, silicon nitride nanophotonics is already a very mature platform providing integrated lasers [14] and spectrometers [15]. High-performance spectral functionalities such as filters [16], arrayed-waveguide gratings [17], and Bragg gratings [18] have also been demonstrated. These high-performance on-chip components not only allow for the full integration of the Raman system with a small footprint at a low cost, but they also open up the possibility of multiplex Raman sensing that multiple analytes can be probed simultaneously. These benefit, coupled with the wave-guiding signal enhancement, make silicon nitride a very promising platform to demonstrate fully-integrated Raman spectroscopic systems.

In 2014, our group reported the first experimental demonstration of on-chip spontaneous Raman spectroscopy for isopropyl alcohol [19] with a silicon nitride waveguide. Later more useful analytes have been probed such as monolayers of molecules functionalized on top of waveguides [20] and gas at ppb-level with the help of hypersorbent polymer functionalized waveguides [21]. Nevertheless, the Raman signals in these demonstrations are still too low to avoid the use of deep-cooled detectors, which hurdles the demonstration a fully integrated Raman sensor.

Fortunately, coherent Raman scattering (CRS) provides us with a solution. In CRS, the molecules are excited simultaneous by two laser beams – a pump laser and a Stokes laser. If their frequency difference coincides with a Raman mode, these two lasers excite this vibration resonantly. The coherent excitation induces a

strong light-matter interaction. As a result, the CRS signal can be orders of magnitude improved over spontaneous Raman scattering. Thanks to its superior signal strength, CRS has been widely used in optical microscopy as a highly sensitive and chemically selective tool for label-free biological analysis.

It is highly attractive to combine CRS with silicon nitride waveguides to leverage both waveguiding and coherent excitation enhancement mechanisms. CRS is commonly implemented in two modalities: coherent anti-stokes Raman scattering (CARS) and stimulated Raman scattering (SRS). Although the underlying physics is the same for both CRS processes, they exhibit markedly different signal properties. CARS focuses on detecting an induced field in a frequency blue-shifted from the input fields while SRS focus on detecting the intensity variation of the input fields. While both CRS modalities have been meticulously investigated from the perspective of Raman microscopy [6], waveguide-enabled CRS has remained largely unexplored. The objective of this thesis is therefore to:

- Investigate whether coherent Raman spectroscopy is compatible with the silicon nitride platform.
- Develop a theoretical model for on-chip CRS with the aim to outline relevant design parameters and estimate signal strength.
- Fabricate and characterize on-chip CRS sensors based on optimized design parameters.
- Design and build an experimental setup that is capable of exciting and collecting the CRS signal from a waveguide-based CRS sensor.
- Identify and quantify the advantages of CRS sensor over spontaneous Raman sensors.
- Explore strategies to improve the performance of on-chip CRS sensors.

1.2 Outline of the Thesis

The structure of this thesis is as followed. We introduce the classical description of light-matter interaction and give a theoretical overview of CRS in **Chapter 2**. In this chapter, the optical fields are modeled as electromagnetic waves, and the molecules are treated as a collection of harmonic oscillators. Within this framework, we show that CRS can be modeled as third-order nonlinear processes. Both coherent anti-Stokes Raman scattering (CARS) and stimulated Raman scattering (SRS) will be discussed in this chapter.

In **Chapter 3**, we are concerned with the quantum mechanical description of spontaneous Raman scattering and SRS. In the classical treatment, SRS and spon-

taneous Raman scattering are treated as two different processes, which fails to recognize the inherent relationship between them. Since many works have been done on waveguide-based spontaneous Raman scattering [12, 22, 23], it is advisable to have a unified treatment that takes care of both waveguide-based spontaneous Raman scattering and waveguide-based SRS. The quantum mechanical description establishes the connection between them, especially their gain coefficients within a waveguide. The macroscopic equations governing the evolution of spontaneous signal and stimulated signal are also derived in this chapter.

In **Chapter 4**, we investigate the compatibility of the silicon nitride platform with CARS. This investigation reveals that waveguide-enabled CARS suffers from severe limitations. We will show that it is difficult to obtain the required phase-matching condition that is necessary for efficient CARS generation in a silicon nitride waveguide. However, our work demonstrates that silicon nitride waveguide can be engineered to exhibit anomalous dispersion at 800 nm. Recognizing this opportunity for silicon nitride nonlinear optics, we demonstrate the first visible-to-near-IR supercontinuum generation on an underetched silicon nitride integrated waveguide. This work was the first supercontinuum extending below 500 nm on an integrated platform, offering a novel compact visible broadband source for Raman spectroscopy, confocal microscopy, optical coherence tomography and precise frequency metrology.

Chapter 5 is devoted to the experimental demonstration of waveguide-enabled SRS. In this chapter, We identify a miscellaneous of noise sources and parasitic effects that prevent us from retrieving the SRS spectrum. The origin of these detrimental effects are examined in detail, and we have taken dedicated measures to suppress them. Eventually, we demonstrate the first SRS experiments enabled by an integrated waveguide. We show that the waveguide-based SRS sensors are capable of probing DMSO with a relatively low concentration. We also give a detailed analysis of the performance of SRS and spontaneous Raman scattering under various experimental conditions. The methods to improve the performance of SRS are also investigated.

In our demonstration, we employ a combination of CW lasers, a lock-in amplifier, and a balanced detector. Currently, all of these components have been demonstrated on an integrated platform with high performance. As a result, our work paves the path toward the chip-scale full integration of Raman sensors that are compatible with the CMOS infrastructure. Shortly, we envisage demonstrating an on-chip multiplexed SRS sensor with integrated multi-channel lock-in amplifiers each dedicated to a specific Raman wavelength. We believe this work will open new opportunities in real-time molecular identification and quantification, providing a versatile tool for drug development, health monitoring, and real-time environmental sensing.

Chapter 6, being the final chapter of this thesis, is dedicated to a short as-

assessment of the results presented in this work. We also discuss a few possible directions for future development.

1.3 Publications

1.3.1 Publications in International Journals

1. H. Zhao, S. Clemmen, A. Raza, R. Baets, Stimulated Raman spectroscopy of analytes evanescently probed by a silicon nitride photonic integrated waveguide, *Optics Letters*, 43(6), p.1403-1406 (2018)
2. A. Dhakal, F. Peyskens, S. Clemmen, A. Raza, P.C. Wuytens, H. Zhao, N. Le Thomas, R. Baets, Single mode waveguide platform for spontaneous and surface-enhanced on-chip Raman spectroscopy, *Interface Focus* (invited), 6(4), United Kingdom, p.article 20160015 (2016)
3. B. Kuyken, F. Leo, S. Clemmen, U.D. Dave, R. Van Laer, T. Ideguchi, H. Zhao, X. Liu, J. Safioui, S. Coen, S.P. Gorza, S. Selvaraja, S. Massar, R.M. Osgood Jr, P. Verheyen, J. Van Campenhout, R. Baets, W.M.J. Green, G. Roelkens, Nonlinear optical interactions in silicon waveguides, *Journal of nanophotonics* (invited), (2016)
4. A. Subramanian, E.M.P. Ryckeboer, A. Dhakal, F. Peyskens, A. Malik, B. Kuyken, H. Zhao, S. Pathak, A. Ruocco, A. De Groote, P.C. Wuytens, D. Martens, F. Leo, W. Xie, U.D. Dave, M. Muneeb, Pol Van Dorpe, Joris Van Campenhout, W. Bogaerts, P. Bienstman, N. Le Thomas, D. Van Thourhout, Zeger Hens, G. Roelkens, R. Baets, Silicon and silicon nitride photonic circuits for spectroscopic sensing on-a-chip , *Photonics Research* (invited), 5(3), p.B47 (2015)
5. H. Zhao, B. Kuyken, S. Clemmen, F. Leo, A. Subramanian, A. Dhakal, P. Helin, S. Simone, E. Brainis, G. Roelkens, R. Baets, Visible-to-near-infrared octave spanning supercontinuum generation in a silicon nitride waveguide, *Optics Letters*, 40(10), p.2177-2180 (2015)

1.3.2 Publications in International Conferences

1. H. Zhao, S. Clemmen, A. Raza, R. Baets, Demonstration of Stimulated Raman Scattering on a Silicon Nitride Photonic Integrated Waveguide, *Conference on Lasers and Electro-Optics*, United States, (2018).
2. S. Clemmen, A. Raza, A. Dhakal, F. Peyskens, A. Subramanian, P. Van Dorpe, P.C. Wuytens, H. Zhao, E.M.P. Ryckeboer, S. Severi, N. Le Thomas,

- R. Baets, Spectroscopic sensing with silicon nitride photonic integrated circuits, Photonics West 2017, Proc. SPIE 10106, Integrated Optics: Devices, Materials, and Technologies XXI (invited), United States, p.101060T (2017)
3. S. Clemmen, H. Zhao, F. Peyskens, A. Dhakal, P.C. Wuytens, A. Subramanian, N. Le Thomas, R. Baets, Coherent anti-Stokes Raman spectroscopy on chip, 28th IEEE Photonics Conference (IPC 2015) (invited), United States, p.623 (2015)
 4. S. Clemmen, H. Zhao, F. Peyskens, A. Dhakal, P.C. Wuytens, A. Subramanian, N. Le Thomas, R. Baets, Coherent anti-Stokes Raman spectroscopy on chip, 28th IEEE Photonics Conference (IPC 2015), United States, p.623-624 (2015)
 5. H. Zhao, B. Kuyken, F. Leo, S. Clemmen, E. Brainis, G. Roelkens, R. Baets, visible-to-near-infrared octave spanning supercontinuum generation in a partially under etched silicon nitride waveguide, CLEO, United States, (2015)
 6. C. Hu, A. Gassenq, Yolanda Justo, Kilian Devloo-Casier, H. Chen, H. Zhao, Christophe Detavernier, Zeger Hens, G. Roelkens, Short-wave Infrared PbS Colloidal Quantum Dot Photodetectors with AlOx Atomic Layer Deposition Passivation, 12th "Mid-Infrared Optoelectronics: Materials and Devices conference (MIOMD-XII), France, p.61 (2014)

1.3.3 Publications in National Conferences

1. P.C. Wuytens, A. Raza, H. Zhao, N. Turk, F. Peyskens, X. Nie, A. Dhakal, E.M.P. Ryckeboer, S. Clemmen, N. Le Thomas, R. Baets, On-chip Raman Spectroscopy, FEA Research Symposium 2017, Belgium, (2017)

References

- [1] C. V. Raman and K. S. Krishnan. *A New Type of Secondary Radiation*. *Nature*, 121(3):501–502, March 1928.
- [2] R. S. Krishnan and R. K. Shankar. *Raman effect: History of the discovery*. *Journal of Raman Spectroscopy*, 10(1):1–8, January 1981.
- [3] G. Landsberg and L. Mandelstam. *Eine neue Erscheinung bei der Lichtzerstreuung in Krystallen*. *Naturwissenschaften*, 16(28):557–558, July 1928.
- [4] J. D. Winefordner, editor. *Raman Spectroscopy for Chemical Analysis*. John Wiley & Sons, Inc, 2005.
- [5] Pavel Maousek and Michael D. Morris, editors. *Emerging Raman Applications and Techniques in Biomedical and Pharmaceutical Fields*. Springer-Verlag, 2010.
- [6] Ji-Xin Cheng and Xiaoliang Sunney Xie, editors. *Coherent Raman Scattering Microscopy*. Taylor & Francis, 2012.
- [7] Christoph Krafft, Gerald Steiner, Claudia Beleites, and Reiner Salzer. *Disease recognition by infrared and Raman spectroscopy*. *Journal of Biophotonics*, 2(1-2):13–28, February 2009.
- [8] Meng-Lei Xu, Yu Gao, Xiao Xia Han, and Bing Zhao. *Detection of Pesticide Residues in Food Using Surface-Enhanced Raman Spectroscopy: A Review*. *Journal of Agricultural and Food Chemistry*, 65(32):6719–6726, August 2017.
- [9] Bo Bao, Jason Riordon, Farshid Mostowfi, and David Sinton. *Microfluidic and nanofluidic phase behaviour characterization for industrial CO₂, oil and gas*. *Lab Chip*, 17(16):2740–2759, August 2017.
- [10] *TruScanTMRM Handheld Raman Analyzer*. <https://www.thermofisher.com/order/catalog/product/TRUSCANRM>.
- [11] *NanoRam[®]Handheld Raman Spectrometer*. <http://bwtek.com/products/nanoram/>.
- [12] Ashim Dhakal. *Nanophotonic Waveguide Enhanced Raman Spectroscopy*. PhD thesis, Ghent University, 2016.
- [13] David Thomson, Aaron Zilkie, John E Bowers, Tin Komljenovic, Graham T Reed, Laurent Vivien, Delphine Marris-Morini, Eric Cassan, Lopold Viot, Jean-Marc Fdli, Jean-Michel Hartmann, Jens H Schmid, Dan-Xia Xu, Frdric

- Boeuf, Peter OBrien, Goran Z Mashanovich, and M Nedeljkovic. *Roadmap on silicon photonics*. *Journal of Optics*, 18(7):073003, July 2016.
- [14] Weiqiang Xie, Thilo Stferle, Gabriele Rainò, Tangi Aubert, Suzanne Bisschop, Yunpeng Zhu, Rainer F. Mahrt, Pieter Geiregat, Edouard Brainis, Zeger Hens, and Dries Van Thourhout. *On-Chip Integrated Quantum-DotSilicon-Nitride Microdisk Lasers*. *Advanced Materials*, 29(16):1604866, February 2017.
- [15] Xiaomin Nie, Eva Ryckeboer, Gunther Roelkens, and Roel Baets. *CMOS-compatible broadband co-propagative stationary Fourier transform spectrometer integrated on a silicon nitride photonics platform*. *Optics Express*, 25(8):A409–A418, April 2017.
- [16] Alexander Gondarenko, Jacob S. Levy, and Michal Lipson. *High confinement micron-scale silicon nitride high Q ring resonator*. *Optics Express*, 17(14):11366–11370, July 2009.
- [17] Daoxin Dai, Zhi Wang, Jared F. Bauters, M.-C. Tien, Martijn J. R. Heck, Daniel J. Blumenthal, and John E Bowers. *Low-loss Si₃N₄ arrayed-waveguide grating (de)multiplexer using nano-core optical waveguides*. *Optics Express*, 19(15):14130–14136, July 2011.
- [18] Jie Sun, Purnawirman, Ehsan Shah Hosseini, Jonathan D. B. Bradley, Thomas N. Adam, Gerald Leake, Douglas Coolbaugh, and Michael R. Watts. *Uniformly spaced $\lambda/4$ -shifted Bragg grating array with wafer-scale CMOS-compatible process*. *Optics Letters*, 38(20):4002, October 2013.
- [19] Ashim Dhakal, Ananth Z. Subramanian, Pieter Wuytens, Frédéric Peyskens, Nicolas Le Thomas, and Roel Baets. *Evanescent excitation and collection of spontaneous Raman spectra using silicon nitride nanophotonic waveguides*. *Optics Letters*, 39(13):4025–4028, July 2014.
- [20] Ashim Dhakal, Pieter C. Wuytens, Frdric Peyskens, Karolien Jans, Nicolas Le Thomas, and Roel Baets. *Nanophotonic Waveguide Enhanced Raman Spectroscopy of Biological Submonolayers*. *ACS Photonics*, 3(11):2141–2149, November 2016.
- [21] Scott A. Holmstrom, Todd H. Stievater, Dmitry A. Kozak, Marcel W. Pruessner, Nathan Tyndall, William S. Rabinovich, R. Andrew McGill, and Jacob B. Khurgin. *Trace gas Raman spectroscopy using functionalized waveguides*. *Optica*, 3(8):891–896, August 2016.
- [22] Frédéric Peyskens. *Surface Enhanced Raman Spectroscopy Using a Single Mode Nanophotonic-Plasmonic Platform*. PhD thesis, Ghent University, 2016.

- [23] Pieter Wuytens. *Surface-Enhanced Raman Spectroscopy for Intracellular Sensing and Protease Activity Detection: From Chip Technology to Applications*. PhD thesis, Ghent University, 2017.

2

Introduction to Spontaneous and Coherent Raman Scattering

In this chapter, the classical description of both spontaneous Raman scattering and coherent Raman scattering will be introduced. The optical field is modeled as an electromagnetic wave, and the molecules are modeled as a collection of harmonic oscillators. Ref. [1] and Ref. [2] are influential in the preparation of this chapter.

We focus on the basics of coherent Raman scattering in this chapter. After a short introduction to spontaneous Raman scattering, we show that coherent Raman interactions can be modeled as third-order nonlinear processes. This recognition allows us to study coherent Raman processes with existing theories well developed for Kerr nonlinear interactions. Two coherent Raman processes — stimulated Raman scattering (SRS) and coherent anti-Stokes Raman scattering (CARS) — are studied within this framework.

2.1 Introduction to Spontaneous Raman Scattering

When one molecule is subjected to an electric field \mathbf{E} , this field can displace the electrons and the nuclei of the molecule in opposite directions and induces a dipole moment. In the first-order approximation, the strength of this induced dipole moment is proportional to the incident electric field as

$$\boldsymbol{\mu}(t) = \boldsymbol{\alpha}(t)\mathbf{E}(t), \quad (2.1)$$

where μ is the induced dipole moment, α is the polarizability of the molecules, and \mathbf{E} is the incoming electric field. For conceptual clarity, we make a linear and isotropic approximation and treat the polarizability as a scalar in the rest of this chapter. With this approximation, the incoming electric field and the induced dipole moment have the same polarization, therefore we can also drop their vector notation for simplicity.

The polarizability of a molecule is dependent on the distribution its nuclei and electrons. During vibrational motions, the distribution of nuclei changes periodically, which in turn results in a periodical change of the polarizability. Suppose the vibrations are described by a set of normal coordinates $\{Q\}$, we can express the polarizability α as a Taylor series of $\{Q\}$ as

$$\alpha = \alpha_0 + \sum_i \left(\frac{\partial \alpha}{\partial Q_n} \right)_0 Q_i(t) + \frac{1}{2} \sum_{i,j} \left(\frac{\partial^2 \alpha}{\partial Q_i \partial Q_j} \right) Q_i Q_j + \dots, \quad (2.2)$$

where Q_i and Q_j are the normal coordinates corresponding to the i -th and j -th molecular vibrational mode. In this equation, α_0 is classified as *static polarizability* which is independent of the vibrational motions.

In the first-order approximation, only the second term on the right-hand side of Eq. (2.2) that is proportional to $(\partial \alpha / \partial Q_n)_0$ is preserved. In this approximation, the impact of different vibrational modes are mutually independent, so it is sufficient to consider only one of them and we can omit the subscript. In a first approximation, the normal mode follows harmonic oscillation. Therefore, the normal coordinate Q varies as

$$Q(t) = Q_0(e^{-i\omega_v t} + c.c.), \quad (2.3)$$

where Q_0 is the amplitude of the harmonic oscillation, ω_v is the vibrational frequency and *c.c.* stands for “complex conjugate”. Maintaining only the first-order correction of Eq. (2.2), we have

$$\alpha = \alpha_0 + \left(\frac{\partial \alpha}{\partial Q} \right)_0 Q_0(e^{-i\omega_v t} + c.c.) = \alpha_0 + \alpha_1(e^{-i\omega_v t} + c.c.). \quad (2.4)$$

Here, the oscillating polarization induces dipole moments at a frequency other than the incident field, and it is the reason for Raman scattering. If we substitute Eq. (2.4) to Eq. (2.1) and write down explicitly the electric field of an optical wave as $E(t) = E_0 e^{i\omega_p t} + c.c.$, the induced dipole moment of this molecule becomes

$$\begin{aligned} \mu &= (\alpha_0 + \alpha_1(e^{-i\omega_v t} + c.c.)) \times (E_0 e^{-i\omega_p t} + c.c.) \\ &= \underbrace{\alpha_0 E_0 (e^{-i\omega_p t} + c.c.)}_{\text{Rayleigh scattering}} + \underbrace{\alpha_1 E_0 (e^{-i(\omega_p + \omega_v)t} + c.c.)}_{\text{anti-Stokes Raman scattering}} + \underbrace{\alpha_1 E_0 (e^{-i(\omega_p - \omega_v)t} + c.c.)}_{\text{Stokes Raman scattering}}. \end{aligned} \quad (2.5)$$

Evidently, there are three electric dipoles excited by the pump. They have a frequency of ω_p , $\omega_p + \omega_v$, and $\omega_p - \omega_v$ respectively. These excited dipoles will all re-emit light. The first term in Eq. (2.5) describes Rayleigh scattering in which the scattered field has the same frequency as the excitation field. The second and third terms account for Raman scattering. The higher-frequency term corresponds to anti-Stokes Raman scattering while the lower-frequency term corresponds to Stokes Raman scattering. If we measure the intensity of the scattered field with varying frequencies, we can obtain the frequency dependency of $\partial\alpha/\partial Q$, which contains the vibrational information of the molecule.

The total radiated power \mathcal{P}_s by a dipole μ is given by

$$\mathcal{P}_s(\omega_s) = \frac{\omega_s^4}{12\pi c^3 \epsilon_0} |\mu(\omega_s)|^2 = \frac{\omega_s^4 \alpha_1^2}{6\pi c^4 \epsilon_0^2} \underbrace{2c\epsilon_0 |E_0|^2}_{\text{intensity of light}}, \quad (2.6)$$

where E_0 is the incident electric field, α_1 is the vibration-dependent polarizability defined through Eq. (2.4), ω_s is the oscillation frequency of this dipole.

In Raman experiments, the vibration-dependent polarizability α_1 is rarely used. Instead, the strength of Raman interaction is commonly expressed by a quantity called *Raman scattering cross-section* σ [m^2]. A scattering cross-section is defined as followed: if an optical beam with intensity I_0 is incident on a molecule, the total scattered power P_s by this molecule is proportional to the input intensity with a proportionality factor. This proportionality factor is the scattering cross-section. Mathematically, this relationship is written as

$$\mathcal{P}_s = \sigma I_0, \quad (2.7)$$

where σ is the scattering cross-section.

The vibration-dependent polarizability α_1 can be connected to σ by comparing Eq. (2.7) and Eq. (2.6). Since the intensity of an optical beam is related to its electric field as $I_0 = 2\epsilon_0 c |E_0|^2$, the Raman scattering cross-section can be expressed with α_1 as

$$\sigma = \frac{\omega_s^4 \alpha_1^2}{6\pi c^4 \epsilon_0^2}. \quad (2.8)$$

The Raman scattered power given in Eq. (2.6) applies to one molecule. We can easily extend this result to a collection of molecules. Because the phase of vibrational motions $Q(t)$ at different molecules are not correlated, the phase of scattered photons from different molecules does not have a fixed relationship. The total scattered power from N molecules is simply N -times of the scattered power from one molecule $\mathcal{P}_s^{\text{total}} = N\sigma I_0$. This absence of phase relationship is one of the reasons why this scattering process is “spontaneous”.

This simplified model of Raman scattering predicts correctly the $\omega_s^4 = (\omega_p - \omega_v)^4$ dependence of the total power of the Raman scattered light. It also gives the

correct proportionality between the Raman scattered power and intensity of the pump beam $\mathcal{P}_s = \sigma I$. In addition, it outlines the selection rule of Raman scattering. A mode is “Raman-active” only when it induces a non-vanishing variation of the polarizability during vibrational motion.

However, we also point out that this treatment fails to predict some important features of spontaneous Raman scattering, including the Lorentzian lineshape of the Raman spectrum, and the ratio between anti-Stokes and Stokes signals. One expects from Eq. (2.5) that the anti-Stokes signal is of the same strength as its Stokes counterpart. However, the Stokes signal is actually stronger than the anti-Stokes signal by a factor [3]

$$\frac{\text{Intensity of Stokes scattering}}{\text{Intensity of anti-Stokes scattering}} = \left(\frac{\omega_p - \omega_v}{\omega_p + \omega_v} \right)^4 e^{\frac{\hbar\omega_v}{k_b T}}, \quad (2.9)$$

where k_b is the Boltzmann constant, T is the ambient temperature of the molecule and ω_v is the vibration frequency.

2.2 Nuclear Motions as Harmonic Oscillators

In this section, we will have a closer look at the vibrational motions of both diatomic and polyatomic molecules. The purpose of this section is to justify our assumption that vibrational motions can be modeled as harmonic oscillations. Readers are kindly referred to [4] for more information regarding the harmonic oscillator approximation for vibrational motions.

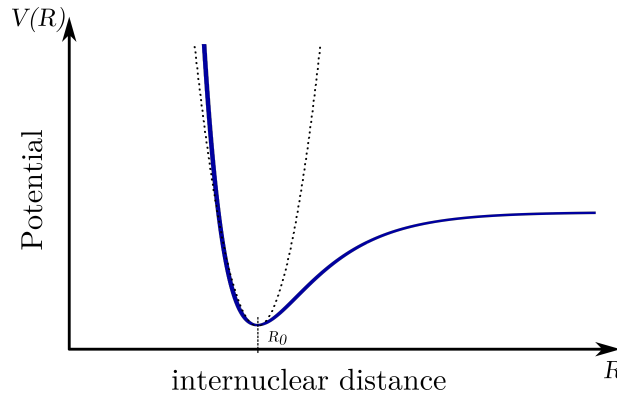


Figure 2.1: The molecular potential of a diatomic molecule (solid curve) and the potential of a harmonic oscillator (dashed curve). In the vicinity of the equilibrium R_0 , the harmonic oscillator model provides an excellent approximation of the real molecular potential.

The molecular potential of a diatomic molecule is shown in Fig. 2.1. The horizontal axis is the internuclear distance R between its two nuclei, and the vertical

axis is the molecular potential energy of the ground state $V(R)$. A molecule is balanced by a short-range repulsive force and a long-range attractive force. As a result, there exists an internuclear distance R_0 that the molecular potential energy reaches its minimum. This is the equilibrium position in terms of internuclear distance.

According to the principle of minimum energy, the configuration of a stable molecule should minimize its total potential energy. If the ambient temperature is not too high, the internuclear distance R will not deviate too much from R_0 . We can therefore expand the potential energy at the vicinity of R_0 as a Taylor series

$$V(R) = V(R_0) + \left(\frac{dV}{dR}\right)_{R_0} (R-R_0) + \left(\frac{d^2V}{dR^2}\right)_{R_0} (R-R_0)^2 + \text{higher order terms.} \quad (2.10)$$

At R_0 , the first order derivative of the potential energy vanishes $(dV/dR)_{R_0} = 0$ and $V(R)$ is dominated by the second-order term, which represents the potential of a harmonic oscillator

$$V(R) \approx V(R_0) + \underbrace{\left(\frac{d^2V}{dR^2}\right)_{R_0}}_{\text{Potential of a harmonic oscillator}} (R-R_0)^2. \quad (2.11)$$

This potential of a harmonic oscillator is shown as the dashed line in Fig. 2.1. It is clear that in the vicinity of R_0 , the potential of a harmonic oscillator is an excellent approximation to the real molecular potential.

The argument for diatomic molecules can be easily extended to polyatomic molecules. For a molecule with N nuclei, it requires $3N$ coordinates to fully specify its configuration. Of these $3N$ coordinates, three of them are used to specify the center of the molecule, and three extra coordinates are used to specify the orientation of the molecule (two for linear molecules). The rest $3N - 6$ (or $3N - 5$ for linear molecules) coordinates specify the vibrational degrees of freedom of the constituent nuclei. For example, for a diatomic molecule, it has only one vibrational degree of freedom — its internuclear distance R . If we denote the displacements of these $3N - 6$ (or $3N - 5$ for linear molecules) coordinates from their equilibriums as $\{q_i\}$, the potential energy of this polyatomic molecule is given by

$$V(q_1, q_2, \dots) = V(0, 0, \dots) + \sum_{i,j=1}^{N_{\text{vib}}} \frac{1}{2} \left(\frac{\partial^2 V}{\partial q_i \partial q_j} \right)_{q_{i,j}=0} q_i q_j + \text{higher order terms.} \quad (2.12)$$

where the number of vibrational modes N_{vib} is $3N - 6$ (or $3N - 5$ for linear molecules). Note that we have already utilized the fact that the first-order derivatives of the molecular potential $\partial V/\partial q_i$ vanish at equilibriums. Equation (2.12) is difficult to compute due to the cross-terms $q_i q_j$ for $i \neq j$. Fortunately, classical mechanics indicates that these cross-terms in Eq. (2.12) can be eliminated by

transforming $\{q_i\}$ to a set of new coordinates $\{Q_i\}$ [5]. In this new coordinate system, we have

$$V(Q_1, Q_2, \dots) = V(0, 0, \dots) + \sum_{i,j=1}^{N_{\text{vib}}} \frac{1}{2} \left(\frac{\partial^2 U}{\partial Q_i^2} \right)_{Q_i=0} Q_i^2 + \text{higher order terms.} \quad (2.13)$$

If we ignore the higher-order terms, we have

$$\Delta V = V(\dots, Q_i, \dots) - V(\dots, 0, \dots) = \frac{1}{2} \left(\frac{\partial^2 U}{\partial Q_i^2} \right)_{Q_i=0} Q_i^2. \quad (2.14)$$

This equation indicates that the vibrational motions can indeed be regarded as a collection of independent harmonic oscillators. Q_i is the normal coordinate of the i -th vibrational mode. It is worth mentioning that because Q_i is a linear combination of $\{q_i\}$, normal modes are actually synchronized oscillation patterns of all the nuclei.

2.3 Coherent Raman Scattering from the Perspective of Third-Order Nonlinear Processes

In spontaneous Raman scattering, one laser beam is used to excite the Raman signal. In coherent Raman scattering (CRS), two lasers are used — the one with a higher frequency is called *pump laser* and the one with a lower frequency is called *Stokes laser*. When the frequency difference between these two lasers coincides with a vibrational frequency, the optical fields actively drive the molecule and force them to oscillate coherently at the beat frequency between the field components. This coherent oscillation dramatically enhances the strength of light-matter interaction and result in a strong Raman signal. It is noteworthy that the coherent Raman processes shares many features with Kerr-induced nonlinear processes. In this section, we will show that both Kerr processes and coherent Raman processes can be understood from the perspective of third-order nonlinear interactions.

2.3.1 Nonlinear Polarizations

In nonlinear optics, the response of a material is usually modeled by expressing its polarization \mathbf{P} as a power series of the electric field of the incident radiation \mathbf{E} as [2]

$$\mathbf{P}(t) = \epsilon_0 [\chi^{(1)} \mathbf{E}(t) + \chi^{(2)} \mathbf{E}(t) \mathbf{E}(t) + \chi^{(3)} \mathbf{E}(t) \mathbf{E}(t) \mathbf{E}(t) + \dots], \quad (2.15)$$

where $\chi^{(1)}$, $\chi^{(2)}$, and $\chi^{(3)}$ are linear, second-order and third-order susceptibilities, respectively. The electric field \mathbf{E} and the polarization \mathbf{P} are vectors in three-dimensional space, and the susceptibilities are tensors.

The linear susceptibility $\chi^{(1)}$ is the dominant contribution to \mathbf{P} and it is related to the refractive index of materials. The second-order nonlinear susceptibility $\chi^{(2)}$ gives rise to second-order nonlinear processes such as optical rectification, second-harmonic generation, sum-frequency generation and the Pockels effect. However, the second-order nonlinear susceptibility $\chi^{(2)}$ vanishes for centrosymmetric materials. Most of the materials used in silicon photonics, including crystalline silicon, silicon nitride, and silicon dioxide are centrosymmetric. The lowest-order nonlinear processes that can occur in these materials must come from the third-order susceptibility $\chi^{(3)}$, which can be non-zero for both centrosymmetric and non-centrosymmetric materials. There exist many important third-order nonlinear processes, including self-focusing, third-harmonic generation, and four-wave mixing [2, 6, 7].

The origin of the third-order susceptibility $\chi^{(3)}$ can be roughly separated into two categories. The first one is the (almost) instantaneous nonlinear electronic response to external fields, which is classified as Kerr nonlinearity $\chi_K^{(3)}$. Third-order susceptibility $\chi^{(3)}$ can also be induced by the interplay between molecular vibrations to external fields, and it is called Raman nonlinearity $\chi_R^{(3)}$.

2.3.2 Kerr Nonlinearity

Kerr effect arises from the nonlinear electronic response to external fields. When an optical field is applied to a molecule, it displaces the nuclei and electrons to opposite direction. In dielectric materials, electrons are bounded by the nuclei. If the external field is not too strong, the electrons will be displaced linearly with the external field. This is the case we have described in Eq. (2.1). However, in the presence of a strong external field, the displacement is no longer proportional to the external field.

In Eq. (2.15), \mathbf{P} is the macroscopic polarization. To understand the origin of the Kerr effect, it is illustrative to write down explicitly the “microscopic polarization” of a molecule. This microscopic polarization is indeed the dipole moment of the molecule. In microscopic view, the dipole moment of a molecule under intense excitation is given by

$$\boldsymbol{\mu}(t) = \alpha \mathbf{E}(t) + \beta \mathbf{E}(t)\mathbf{E}(t) + \xi \mathbf{E}(t)\mathbf{E}(t)\mathbf{E}(t) + \dots, \quad (2.16)$$

where α is the polarizability. β and ξ are first-order and second-order hyperpolarizabilities respectively. We can clearly see that in a first-order approximation this equation is reduced to Eq. (2.1). The second-order hyperpolarizability can be connected to third-order susceptibility as [2]

$$\chi_K^{(3)} = \mathcal{L}^{(3)} N \xi, \quad (2.17)$$

where $\mathcal{L}^{(3)}$ is the local-field enhancement factor and N is the number of molecules. The local field enhancement $\mathcal{L}^{(3)}$ is often omitted in this equation. In this case, the

electric field given in Eq. (2.16) should be viewed as the local field on the molecule. This second-order hyperpolarizability ξ is the microscopic origin the Kerr effect.

In experiments, the Kerr effect is customarily viewed as a modification of the refractive index by the intensity of the incident field. Therefore the refractive index in the presence of the Kerr effect is usually described as [2]

$$n = n_0 + n_2 I, \quad (2.18)$$

where n_0 is the linear refractive index given by $n_0 = \sqrt{1 + \chi^{(1)}}$. n_2 is the nonlinear refractive index and I is the intensity of the optical field. The nonlinear refractive index is related to the third-order susceptibility $\chi_K^{(3)}$ as

$$n_2 = \frac{3\chi_K^{(3)}}{4n_0^2 \epsilon_0 c}. \quad (2.19)$$

2.3.3 Coherent Raman Effects

The response of vibrational motions to external fields can also induce a third-order susceptibility, and it is classified as Raman susceptibility. To understand the origin of this susceptibility, let us have a closer look at the coherent Raman processes.

The coherent Raman processes can be divided into two steps [1, 2]. In the first step, two optical beams— a pump beam and a Stokes beam— are incident on a molecule. Suppose the difference of their frequency corresponds to the intrinsic frequency of a normal mode. In this case, the optical fields exert a force on the vibrational degree of freedom of this molecule. This optical force drives the molecule to oscillate at the beat frequency between the field components. In the second step, this molecular oscillation modulates the refractive index of the medium at the beat frequency. When a third beam propagates through the material, it experiences this modulation and develops sidebands at shifted frequencies. In practice, coherent Raman experiments are carried out in degenerate configurations in the sense that the “third beam” is actually the pump or the Stokes beam. Below we will have a closer look at this process.

We start by examining the electromagnetic force exerted by the input fields. Suppose the vibrational frequency, the pump frequency, the Stokes frequency are ω_v , ω_p and ω_s , respectively. The frequency difference between the pump and the Stokes field is defined as $\Omega = \omega_p - \omega_s$, and we require this frequency difference is not far away from the molecular vibration frequency $\Omega \approx \omega_v$. The name of the optical fields also implicitly suggests that $\Omega > 0$.

The electromagnetic force $F(t)$ exerted on a dipole can be worked out from the principle of virtual work. In the first order correction (that is, no hyperpolarizabilities), the energy required to induced a dipole moment of $d\mu$ is given by

$$dW = \tilde{\mathbf{E}} \cdot d\tilde{\mu} = \tilde{\mathbf{E}} \cdot (\alpha d\tilde{\mathbf{E}}) = d\left(\frac{1}{2}\alpha\tilde{E}^2\right). \quad (2.20)$$

By the principle of virtual work, the force exerted by the optical field on the molecule along the vibrational degree of freedom Q is given by

$$\tilde{F}(t) = \frac{dW}{dQ} = \frac{1}{2} \left(\frac{d\alpha}{dQ} \right)_0 \tilde{E}^2. \quad (2.21)$$

Recall that the electric field of the incident optical excitations is given by

$$\tilde{E}(z, t) = E_p e^{i\mathbf{k}_p \cdot \mathbf{r} - i\omega_p t} + E_s e^{i\mathbf{k}_s \cdot \mathbf{r} - i\omega_s t} + c.c., \quad (2.22)$$

where the $E_{p(s)}$, $\mathbf{k}_{p(s)}$, $\omega_{p(s)}$ are the electric field, propagation constant and optical frequency of the pump (Stokes) beam.

Inserting Eq. (2.22) back to Eq. (2.21), we notice that the optical force is composed of the following frequency components: DC, $\omega_p + \omega_s$, $\omega_p - \omega_s$, $2\omega_p$, and $2\omega_s$. Among these components, only the one at $\omega_p - \omega_s$ is close to the molecular resonance frequency ω_v . As a result, only this component induces a non-negligible oscillatory motion of the molecule. The applied force at this frequency is given by

$$\tilde{F}(t) = \left(\frac{\partial \alpha}{\partial Q} \right)_0 E_p E_s^* e^{i(\mathbf{k}_p - \mathbf{k}_s) \cdot \mathbf{r} - i\Omega t} + c.c.. \quad (2.23)$$

As we have shown in the previous section, the molecular vibration can be modeled as a harmonic oscillation. The harmonic oscillation equation is given by

$$\frac{d^2 \tilde{Q}}{dt^2} + 2\zeta \frac{d\tilde{Q}}{dt} + \omega_v^2 \tilde{Q} = \frac{\tilde{F}(t)}{m}, \quad (2.24)$$

where ζ is the damping coefficient of the oscillator and m is the effective mass of this harmonic oscillator. To solve Eq. (2.24), we take an ansatz of $Q(\Omega, t)$ as

$$\tilde{Q}(\Omega, t) = Q_\Omega(\Omega) (e^{i(\mathbf{k}_p - \mathbf{k}_s) \cdot \mathbf{r} - i\Omega t} + c.c.). \quad (2.25)$$

Here $Q_\Omega(\Omega)$ can be viewed as the temporal independent part of $Q(\Omega, t)$. Inserting Eq. (2.25) and Eq. (2.23) into Eq. (2.24), we have

$$Q_\Omega(\Omega) = \frac{1}{m} \left(\frac{\partial \alpha}{\partial Q} \right)_0 \frac{E_p E_s^*}{-\Omega^2 - 2i\Omega\zeta + \omega_v^2}. \quad (2.26)$$

Similar to Eq. (2.5), the induced dipole moment is determined by the displacement of the harmonic oscillator as

$$\mu = \alpha \tilde{E}(z, t) = \left(\alpha_0 + \left(\frac{\partial \alpha}{\partial Q} \right)_0 Q(\Omega, t) \right) \tilde{E}(z, t). \quad (2.27)$$

The macroscopic polarization within a unit volume with N molecules due to

coherent excitation is then given by .

$$\begin{aligned}
\tilde{P} &= N\mu = \tilde{P}(\omega_{as}) + \tilde{P}(\omega_{cs}) + \tilde{P}(\omega_s) + \tilde{P}(\omega_p) \\
&= P(\omega_{as}) \exp\left(i(2\mathbf{k}_p - \mathbf{k}_s) \cdot \mathbf{r} - i\omega_{as}t\right) \\
&\quad + P(\omega_{cs}) \exp\left(i(2\mathbf{k}_s - \mathbf{k}_p) \cdot \mathbf{r} - i\omega_{cs}t\right) \\
&\quad + P(\omega_s) \exp\left(i\mathbf{k}_s \cdot \mathbf{r} - i\omega_s t\right) \\
&\quad + P(\omega_p) \exp\left(i\mathbf{k}_p \cdot \mathbf{r} - i\omega_p t\right) + c.c., \tag{2.28}
\end{aligned}$$

where ω_p and ω_s is the pump and Stokes frequency and

$$\omega_{cs} = 2\omega_s - \omega_p \text{ is the coherent Stokes frequency,}$$

$$\omega_{as} = 2\omega_p - \omega_s \text{ is the anti-Stokes frequency.}$$

The complex amplitude of the polarization at the anti-Stokes frequency is given by

$$P(\omega_{as}) = \frac{N}{m} \left(\frac{\partial \alpha}{\partial Q} \right)_0^2 \frac{1}{\omega_v^2 - \Omega^2 - 2i\Omega\zeta} E_p^2 E_s^* = 6\epsilon_0 \chi_R(\Omega) E_p^2 E_s^*, \tag{2.29}$$

where the Raman susceptibility is introduced as

$$\chi_R(\Omega) = \frac{N}{6\epsilon_0 m} \left(\frac{\partial \alpha}{\partial Q} \right)_0^2 \frac{1}{\omega_v^2 - \Omega^2 - 2i\Omega\zeta}. \tag{2.30}$$

The Raman susceptibility $\chi_R(\Omega)$ is a complex number. It is non-zero only in the vicinity of $\Omega = \omega_v$. Its imaginary component and real component are shown in Fig. 2.2.

With the newly defined Raman susceptibility, four major coherent Raman polarizations are given by

$$P(\omega_{as}) = 6\epsilon_0 \chi_R(\Omega) E_p^2 E_s^*, \tag{2.31a}$$

$$P(\omega_p) = 6\epsilon_0 \chi_R(\Omega) |E_s|^2 E_p, \tag{2.31b}$$

$$P(\omega_s) = 6\epsilon_0 \chi_R^*(\Omega) |E_p|^2 E_s, \tag{2.31c}$$

$$P(\omega_{cs}) = 6\epsilon_0 \chi_R^*(\Omega) E_s^2 E_p. \tag{2.31d}$$

These polarizations given in Eq. (2.28) are responsible for all first-order coherent Raman processes [1]. As we will show in the next section, $P(\omega_p)$ leads to the attenuation of the pump beam in stimulated Raman scattering (SRS) while $P(\omega_s)$ results in an exponential gain for the Stokes beam. These two effects are sometimes called *stimulated Raman loss (SRL)* and *stimulated Raman gain (SRG)*. $P(\omega_{as})$ is

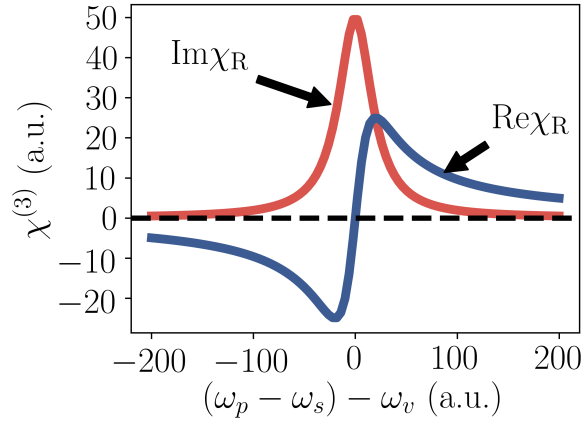


Figure 2.2: The real part and imaginary part of the Raman susceptibility $\chi_R(\Omega)$. Note that $\Omega = \omega_p - \omega_s$. The real component exhibits an asymmetric pattern while the imaginary component has a symmetric Lorentzian shape. At zero detuning $\Omega = \omega_v$, the Raman susceptibility $\chi_R(\omega_v)$ is an imaginary number.

the principal contribution to *coherent anti-Stokes Raman scattering (CARS)* and $P(\omega_{cs})$ is the primary contribution to *coherent Stokes Raman scattering (CSRS)*.

Comparing Eq. (2.31a-2.31d) to Eq. (2.15), it is clear that the Raman polarizations are proportional to the cube of electric field E^3 , highlighting that coherent Raman interactions can indeed be modeled as third-order nonlinear processes. The difference between the Kerr nonlinearity and the Raman nonlinearity is also evident by comparing Eq. (2.16) with Eq. (2.27). $\chi_K^{(3)}$ is induced by the second-order hyperpolarizability ξ while $\chi_R^{(3)}$ results from the modification of linear polarizability $\alpha(Q)$ by vibrational motions. It is also interesting to notice that the phase information of the pump beam is “washed away” in Eq. (2.31c) and Eq. (2.31b) in the sense that these polarizations contain only the square modulus of the pump field $|E_p|^2$.

2.4 Energy Flow of Coherent Raman Processes

In the previous section, we have obtained the nonlinear polarization for various coherent Raman processes. However, in Raman experiments, we are not probing directly the nonlinear polarizations. Therefore, it is interesting to investigate how these nonlinear polarizations are coupled with optical waves. To describe the connection between induced polarizations and optical fields, we explicitly evaluate Maxwell's wave equation in nonlinear media. With this wave equation, the energy flow of both SRS and CARS are investigated in this section.

2.4.1 Wave Equation with Nonlinear Polarization

The evolution of an optical field within a nonlinear optical medium can be described by the wave equation. The derivation of the wave equation can be found in many text books [2, 6, 7]. To begin with, we write down Maxwell's equations for a non-magnetic medium and charge-free medium as

$$\nabla \cdot \tilde{\mathbf{D}} = 0, \quad (2.32a)$$

$$\nabla \cdot \tilde{\mathbf{B}} = 0, \quad (2.32b)$$

$$\nabla \times \tilde{\mathbf{E}} = -\frac{\partial \tilde{\mathbf{B}}}{\partial t}, \quad (2.32c)$$

$$\nabla \times \tilde{\mathbf{B}} = \mu_0 \frac{\partial \tilde{\mathbf{D}}}{\partial t}. \quad (2.32d)$$

Taking the curl of Eq. (2.32c) and the time derivative of Eq. (2.32d), we can eliminate the magnetic field component $\tilde{\mathbf{B}}$. It leads to

$$\nabla^2 \tilde{\mathbf{E}} - \frac{1}{c^2} \frac{\partial^2 \tilde{\mathbf{E}}}{\partial t^2} = \frac{1}{\epsilon_0 c^2} \frac{\partial^2 \tilde{\mathbf{P}}}{\partial t^2}, \quad (2.33)$$

where we have split the displacement field $\tilde{\mathbf{D}}$ into two parts as $\tilde{\mathbf{D}} = \epsilon_0 \tilde{\mathbf{E}} + \tilde{\mathbf{P}}$. It is convenient to further decompose the polarization $\tilde{\mathbf{P}}$ into a linear and a nonlinear part as

$$\tilde{\mathbf{P}} = \tilde{\mathbf{P}}^{\text{NL}} + \tilde{\mathbf{P}}^{\text{L}}. \quad (2.34)$$

In order to derive the nonlinear propagation equation, it is instrumental to expand the electric field $\tilde{\mathbf{E}}$ and polarization $\tilde{\mathbf{P}}$ into the summation of a collection of discrete electromagnetic waves

$$\tilde{\mathbf{E}}(z, t) = \sum_n \mathbf{E}_n e^{-i(\omega_n t - k_n z)} + c.c., \quad (2.35)$$

$$\tilde{\mathbf{P}}(z, t) = \sum_n \mathbf{P}_n e^{-i(\omega_n t - k_n z)} + c.c.. \quad (2.36)$$

where we have assumed that the optical waves are traveling along the z axis. The linear polarization of an individual component is given by

$$\mathbf{P}_n^{\text{L}} = \epsilon_0 \chi^{(1)} \mathbf{E}_n, \quad (2.37)$$

where $\chi^{(1)}$ denotes the linear part of susceptibility which is related to the permittivity by $\epsilon^{(1)} = 1 + \chi^{(1)}$.

In this section, we limit to CW or quasi-CW excitations where both \mathbf{E}_n and \mathbf{P}_n are assumed to be time-independent. Although this assumption is not in general valid for pulse excitations, it is a good approximation when the laser linewidth is much narrower than the Raman linewidth. In the time domain, it means that this

treatment is valid when the duration of the optical field is much longer than the response time of Raman scattering. This steady-state solution provides us with an intuitive picture between nonlinear polarizations \mathbf{P}_n the electric fields \mathbf{E}_n .

Substituting Eq. (2.35) and Eq. (2.36) back into Eq. (2.33), with the slow-varying envelope approximation, we have

$$-2ik_n \frac{\partial \mathbf{E}_n}{\partial z} + \left(k_n^2 - \frac{\omega_n^2 (1 + \chi^{(1)})}{c^2} \right) \mathbf{E}_n = \frac{\omega_n^2 \mathbf{P}_n^{\text{NL}}}{c^2 \epsilon_0}. \quad (2.38)$$

Equation (2.38) can be simplified by noting that the electric field for each individual component \mathbf{E}_n is z -independent when the medium has no nonlinear response $\mathbf{P}_n^{\text{NL}} = 0$. In this case, a natural choice for the propagation constant of an individual component \mathbf{E}_n is

$$k_n = \frac{\omega_n}{c} \sqrt{1 + \chi^{(1)}} = \frac{\omega_n n_n}{c}, \quad (2.39)$$

where $n_n = \sqrt{1 + \chi^{(1)}}$ is the effective index for frequency ω_n . Substituting Eq. (2.39) into Eq. (2.38), we have

$$\frac{\partial \mathbf{E}_n}{\partial z} = i \frac{\omega_n}{2cn_n \epsilon_0} \mathbf{P}_n^{\text{NL}}. \quad (2.40)$$

This is the wave equation for nonlinear optical media with CW excitations. It connects the nonlinear polarization on the right-hand side of the equation to the optical field on the left-hand side. Eq. (2.40) indicates the optical field does not change with z without nonlinear polarizations. If the medium has a nonlinear response, the nonlinear polarization \mathbf{P}_n^{NL} induces variations on the electric field \mathbf{E}_n along z . Therefore, the nonlinear polarization acts as a ‘‘source’’ that modifies the electric field. It is important to mention that nonlinear polarizations \mathbf{P}_n^{NL} can be induced by both Kerr susceptibility and Raman susceptibility.

It is worth noticing that the phase relationship between the polarization \mathbf{P}_n^{NL} and the electric field \mathbf{E}_n is crucial. If the polarization is lagging or leading the electric field by $\pi/2$, the equation on the right is a real number. In this case, the medium induces a pure loss or gain on the optical field. In contrast, if the polarization has the same phase as the electric field, the nonlinear interaction only induces phase changes in the optical field.

Below we will apply Eq. (2.31a-2.31d) to Eq. (2.40) to study the influence of coherent Raman scattering of each of the optical fields. We assume a degenerate experiment configuration: the input is composed of a Stokes beam and a pump beam. Firstly, we will investigate the influence of CRS on these two input fields themselves. Next, we will investigate the influence of CRS on newly generated anti-Stokes frequency ω_{as} . The treatment of coherent-Stokes frequency ω_{cs} is identical to its anti-Stokes counterpart. However, due to its limited application for Raman sensing, the treatment of ω_{cs} is omitted in this thesis.

2.4.2 Stimulated Raman Gain and Stimulated Raman Loss

From Eq. (2.31c), we know the nonlinear polarization and the electric field at the Stokes frequency ω_s induced by CRS are

$$\tilde{P}(\omega_s, t) = P(\omega_s) \exp(i\vec{k}_s \cdot \vec{r} - i\omega_s t) + c.c., \quad (2.41)$$

$$\tilde{E}(\omega_s, t) = E(\omega_s) \exp(i\vec{k}_s \cdot \vec{r} - i\omega_s t) + c.c., \quad (2.42)$$

These equation is identical to our definition in Eq. (2.35) and (2.36). So we can substitute \tilde{P}_n^{NL} given in Eq. (2.40) with $\tilde{P}(\omega_s)$ given in Eq. (2.31c). It leads to

$$\frac{dE_s}{dz} = \frac{3i\omega_s}{n_s c} \chi_R^*(\Omega) |E_p|^2 E_s = -\alpha_s E_s, \quad (2.43)$$

where the gain coefficient for the Stokes beam α_s is defined as

$$\alpha_s = \frac{-3i\omega_s}{n_s c} \chi_R^*(\Omega) |E_p|^2. \quad (2.44)$$

In this equation, n_s is the refractive index of the material at ω_s , χ_R is the Raman susceptibility defined in Eq. (2.30), c is the speed of light in vacuum and $|E_p|$ is the amplitude modulus of the pump field. We know that when the frequency difference between the pump beam and the Stokes beam coincides with the vibrational frequency $\Omega = \omega_p - \omega_s = \omega_v$, $\chi_R^*(\Omega)$ is an imaginary number, and α_s turns out to be a negative real number. Therefore, the Stokes beam experiences a pure gain during Raman interaction, and this is the reason why this phenomenon is called *stimulated Raman gain (SRG)*.

Similar to SRG, we can write down the interplay between the nonlinear polarization $P(\omega_p)$ with the pump field $E(\omega_p)$. Similar to Eq. (2.43), the evolution of the pump beam is given by

$$\frac{dE_p}{dz} = \frac{3i\omega_p}{n_p c} \chi_R(\Omega) |E_s|^2 E_p = -\alpha_p E_p. \quad (2.45)$$

Here the gain coefficient given by

$$\alpha_p = \frac{-3i\omega_p}{n_p c} \chi_R(\Omega) |E_s|^2. \quad (2.46)$$

In this equation, n_p is the refractive index of the material at frequency ω_p and $|E_s|$ is the amplitude modulus of the Stokes field. Other parameters bear the same meaning as in Eq. (2.43). Since $\chi_R(\Omega)$ has an opposite sign to $\chi_R^*(\Omega)$, the pump beam experiences a pure attenuation during Raman interaction. Therefore, this phenomenon is called *stimulated Raman loss (SRL)*.

2.4.3 Coherent Anti-Stokes Raman Scattering

The nonlinear polarization corresponding to CARS is slightly different from that corresponding to SRS. The nonlinear polarization at the anti-Stokes frequency is given by

$$\tilde{P}(\omega_{as}, t) = P(\omega_{as}) \exp\left(i(2\vec{\mathbf{k}}_p - \vec{\mathbf{k}}_s) \cdot \hat{\mathbf{z}} - i\omega_{as}t\right) + c.c., \quad (2.47)$$

In order to implement Eq. (2.47) in Eq. (2.40), the nonlinear polarization should evolve as $\exp\left(i\vec{\mathbf{k}}_{as} \cdot \hat{\mathbf{z}} - i\omega_{as}t\right)$ instead of $\exp\left(i(2\vec{\mathbf{k}}_p - \vec{\mathbf{k}}_s) \cdot \hat{\mathbf{z}} - i\omega_{as}t\right)$. To solve this problem, we make the following transformation

$$\tilde{P}(\omega_{as}, t) = P(\omega_{as}) \exp\left(i(2\vec{\mathbf{k}}_p - \vec{\mathbf{k}}_s - \vec{\mathbf{k}}_{as}) \cdot \hat{\mathbf{z}}\right) \exp\left(i\vec{\mathbf{k}}_{as} \cdot \hat{\mathbf{z}} - i\omega_{as}t\right) + c.c., \quad (2.48)$$

and then Eq. (2.40) becomes

$$\frac{dE_{as}}{dz} = -i \frac{\omega_n}{2cn_n\epsilon_0} P(\omega_{as}) \exp\left(i(2\vec{\mathbf{k}}_p - \vec{\mathbf{k}}_s - \vec{\mathbf{k}}_{as}) \cdot \hat{\mathbf{z}}\right), \quad (2.49)$$

which can be written as

$$\frac{dE_{as}}{dz} = -\frac{3i\omega_{as}}{n_{as}c} \chi_R(\Omega) E_p^2 e^{i\Delta kz} E_s^* = -\kappa_{as} E_s^*. \quad (2.50)$$

The coupling coefficient κ_{as} is defined as

$$\kappa_{as} = \frac{3i\omega_{as}}{n_{as}c} \chi_R(\Omega) E_p^2 e^{i\Delta kz}. \quad (2.51)$$

where $\Delta k = \Delta \mathbf{k} \cdot \hat{\mathbf{z}} = (2\mathbf{k}_p - \mathbf{k}_s - \mathbf{k}_{as}) \cdot \hat{\mathbf{z}}$, n_{as} is the refractive index of the material at frequency ω_{as} and E_s is the Stokes field.

Equation (2.50) is different from both Eq. (2.43) and Eq. (2.45) in that it includes an extra phase-mismatch term. If the phase-mismatch vanishes, the anti-Stokes frequency experiences exponential gain. This situation is similar to the SRG experiment. However, if the phase mismatch Δk is non-zero, the anti-Stokes component would experience periodic gain and loss during propagation and produce a CARS signal much smaller than its SRS counterpart. Therefore, in practical CARS experiments, it is crucial to ensure the phase-matching condition $\Delta k = 0$.

2.5 Detection of CARS and SRS Signal

We have noticed the amplitudes of the nonlinear polarizations responsible for CARS ($P(\omega_{as})$) and SRS ($P(\omega_s)$ and $P(\omega_p)$) are comparable. However, this does not mean the detected signals in CARS and SRS have the same strength. To compare the strength of the detected signals, we have to take into account the difference in detection schemes.

2.5.1 Detection of CARS Signal

In the case CARS, we are probing a newly generated anti-Stokes component at frequency ω_{as} . If we assume the Stokes beam and the pump beam are not affected by CARS interaction, the electric field of the CARS signal over a distance of L is given by

$$E_{as}(L) = -\frac{3i\omega_{as}}{n_{as}c} \chi_R(\Omega) E_p^2 E_s^* L \operatorname{sinc}\left(\frac{\Delta k L}{2}\right) \exp\left(\frac{i\Delta k L}{2}\right). \quad (2.52)$$

The detectable CARS signal is the intensity of the anti-Stokes component ω_{as} . The connections between the intensity and the field amplitude of all the optical fields involved in CARS are given by

$$I(\omega_{as}) = 2n_{as}\epsilon_0 c |E_{as}|^2, \quad (2.53)$$

$$I(\omega_s) = 2n_s\epsilon_0 c |E_s|^2, \quad (2.54)$$

$$I(\omega_p) = 2n_p\epsilon_0 c |E_p|^2, \quad (2.55)$$

where $I(\omega_{as})$, $I(\omega_p)$, $I(\omega_s)$ are the intensities of the anti-Stokes beam, the pump beam and the Stokes beam respectively.

With Eq. (2.53-2.55), we can express the intensity of CARS signal $I(\omega_{as})$ with $I(\omega_s)$ and $I(\omega_p)$, which is given by

$$I(\omega_{as}) = \frac{9\omega_{as}^2}{4n_p^2 n_{as} n_s c^4 \epsilon_0^2} |\chi_R|^2 I_p^2 I_s L^2 \operatorname{sinc}^2\left(\frac{\Delta k L}{2}\right). \quad (2.56)$$

From this equation, we can clearly see that

$$I(\omega_{as}) \propto |\chi_R|^2 I_p^2 I_s L^2 \operatorname{sinc}^2\left(\frac{\Delta k L}{2}\right). \quad (2.57)$$

This equation indicates that the CARS signal is proportion to the square of the pump intensity I_p^2 and the square of interaction length L^2 while it scales linearly to the Stokes intensity I_s . Equation (2.57) also shows that the CARS signal scales with the square modulus of the Raman susceptibility $|\chi_R^{(3)}|^2$. A closer look at the CARS process reveals that the quadratic dependency on third-order susceptibility make the anti-Stokes component exhibit a parasitic signal called non-resonant background. Below we will have a closer look at this non-resonant background.

In deriving Eq. (2.56), only the Raman nonlinearity χ_R is explicitly taken into consideration. However, in practice, materials also exhibit the Kerr nonlinearity at the same time. The strength of the anti-Stokes signal is then a combination of both Kerr and Raman nonlinearity $|\chi_K + \chi_R(\Omega)|^2$. The Raman susceptibility $\chi_R(\Omega)$ is a complex number dependent on the frequency detuning Ω . In comparison, although the Kerr susceptibility χ_K is also a complex number that is relevant to

the frequency detuning Ω , the resonance frequency of the Kerr effect is much higher than its Raman counterpart. As a result, in the optical frequency range that is relevant to this work, the Kerr susceptibility χ_K is essentially a real constant independent of Ω [2]. As a result, the CARS intensity is given by

$$I_{\text{CARS}} \propto |\chi_K + \chi_R(\Omega)|^2 = |\chi_K|^2 + |\chi_R(\Omega)|^2 + 2\chi_K \text{Re}\{\chi_R(\Omega)\}. \quad (2.58)$$

The first term, $|\chi_K|^2$ is simply a constant contribution. Because it does not contain Raman information and it is independent of the Raman shift, it is called non-resonant background. The second term has a Lorentzian lineshape and the third term has an anti-symmetric lineshape.

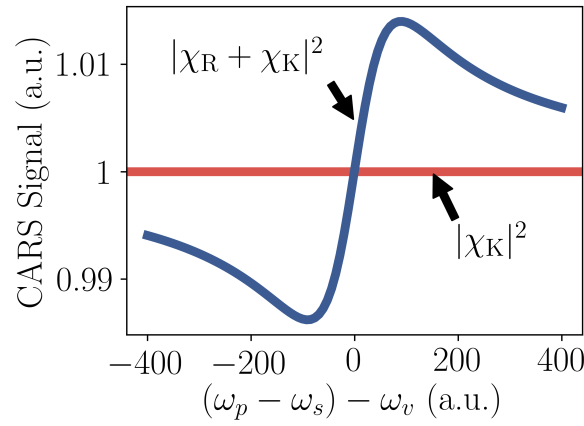


Figure 2.3: A typical CARS signal from dilute analytes. The majority of the CARS signal arises from the Kerr contribution $|\chi_K|^2$. In addition, although $|\chi_R(\Omega)|^2$ has a Lorentzian lineshape, its contribution is swamped by the anti-symmetric cross-term $2\chi_K \text{Re}\{\chi_R(\Omega)\}$.

If we are probing dilute analytes, the amplitude of the Kerr susceptibility χ_K is much larger than that of the Raman susceptibility $\chi_R(\Omega)$. In this case, the non-resonant background, which is proportional to $|\chi_K|^2$, can be orders of magnitude stronger than the second and the third term in Eq. (2.58). Of these two resonant terms, the anti-symmetric cross-term $2\chi_K \text{Re}\{\chi_R(\Omega)\}$ is much stronger over the last term $|\chi_R(\Omega)|^2$. As a result, the detected CARS signal is an anti-symmetric signal sitting on top of a large non-resonant background as shown in Fig. 2.3.

The sizeable non-resonant background makes it difficult to probe the small asymmetric CARS signal and reduces the signal-to-noise ratio of the CARS signal. Furthermore, most reference Raman spectra are measured with spontaneous Raman scattering, and they have the same lineshape as $\text{Im}\{\chi_R\}$ [1]. As a result, the distorted CARS spectrum cannot be compared with the references directly. One has to first reconstruct $\text{Im}\{\chi_R\}$ from the anti-symmetric signal $2\chi_K \text{Re}\{\chi_R\}$,

which is commonly performed with Kramers-Kronig transformation [8] and Hilbert transformation [9].

It is interesting to note the large Kerr nonlinearity χ_K in experiments also provides some advantages. Firstly, with a large Kerr nonlinearity, the CARS response, which is the cross-term, scales linearly with the concentration of analytes. Secondly, because $2\chi_K \text{Re}\{\chi_R\} \gg |\chi_R(\Omega)|^2$, The large Kerr nonlinearity also intensifies the absolute strength of Raman signal. However, in general, the large non-resonant background causes more problems than benefits [1]. Therefore, a collection of techniques have been devised to remove it. These new techniques include the implementation of polarization-sensitive CARS [10], times-resolved CARS [11], and interferometric CARS [12].

Kerr nonlinearity might also change the phase-matching condition. Within a Kerr media, an optical wave can modify its phase through the process of self-phase modulation (SPM) [6]. In this case, the phase-matching condition of CARS is modified to $\Delta k = 2k_p - k_s - k_{as} + k_{NL}$ where a nonlinear phase shift k_{NL} should be included. The nonlinear phase shift scales with the intensity of the optical pulse. However, we emphasize that CARS should always be operated on the condition that linear phase-mismatch $2k_p - k_s - k_{as}$ dominates over the nonlinear phase shift k_{NL} . It is only under this condition that the obtained CARS spectrum has a quadratic dependency on the Raman susceptibility as it is shown in Eq. (2.56). Otherwise, if the optical beams accumulate a large nonlinear phase over propagation, when the phase-matching condition is satisfied, the newly generated CARS signal will increase exponentially with the Raman susceptibility. In this case, the nonlinear waveguide can be viewed as a parametric amplifier [6, 13, 14] instead of a Raman sensor. We will have great difficulty in deciphering the Raman information. Therefore, we should always work in the configuration that the linear phase-mismatch $2k_p - k_s - k_{as}$ dominates over the nonlinear phase shift k_{NL} . To reflection this observation, in the rest of this thesis, we will not consider the nonlinear contribution to the phase-matching condition explicitly.

2.5.2 Detection of SRS Signal

SRS does not generate new frequencies. The detected signal in SRS is the variation of the initial incident beams. Under the non-depleted pump assumption, the electric field of the Stokes beam at position L can be estimated with Eq. (2.43). It is given by

$$E_s(L) = E_s(0) \exp\left(\frac{3i\omega_s}{n_s c} \chi_R^* |E_p|^2 L\right), \quad (2.59)$$

where $E_s(0)$ is the electric field of the input Stokes beam. Due to the intrinsic weakness of Raman interaction, Eq. (2.43) can be approximated as

$$E_s(L) = E_s(0) \left(1 + i \frac{3\omega_s}{n_s c} |E_p|^2 L \chi_R^* \right). \quad (2.60)$$

Photodetectors are only sensitive to the intensity of optical field. The intensity of transmitted Stokes beam is

$$\begin{aligned} I_s(L) &= 2n_s \epsilon_0 c E_s^* E_s \\ &= 2n_s \epsilon_0 c |E_s(0)|^2 \left(1 - i \frac{3\omega_s}{n_s c} |E_p|^2 L \chi_R \right) \left(1 + i \frac{3\omega_s}{n_s c} |E_p|^2 L \chi_R^* \right) \\ &= I_s(0) \left(1 + i \frac{3\omega_s}{n_s c} |E_p|^2 L (\chi_R^* - \chi_R) + \left(\frac{3\omega_s}{n_s c} |E_p|^2 L \right)^2 |\chi_R|^2 \right) \\ &= I_s(0) \left(1 + \frac{6\omega_s}{n_s c} |E_p|^2 L \text{Im}\{\chi_R\} + \left(\frac{3\omega_s}{n_s c} |E_p|^2 L \right)^2 |\chi_R|^2 \right). \end{aligned} \quad (2.61)$$

There are three-terms in the right-hand side of this equation. The first term is simply the intensity of the initial Stokes beam. The second and the third term are caused by SRS. The second term is proportional to $\text{Im}\{\chi_R\}$ while the last term is proportional to $|\chi_R|^2$. Since the strength of Raman interaction is very weak, the second term is much larger than the last term, and the last term can be ignored. Therefore, the intensity of the transmitted Stokes field containing the molecular information is given by

$$I_s(L) - I_s(0) = \Delta I_s = \frac{3\omega_s \text{Im}\{\chi_R\}}{n_p n_s c^2 \epsilon_0} I_s I_p L = g_R I_s I_p L, \quad (2.62)$$

where a new parameter, the *stimulated Raman gain* g_R is introduced. The stimulated Raman gain g_R is dependent only on material properties. We immediately notice this variation ΔI_s scales linearly with the imaginary part of the Raman susceptibility $\text{Im}\{\chi_R\}$. Compared to CARS, SRS has two advantages. Firstly, since the Kerr nonlinearity χ_K is a real number, SRS signals are free from non-resonant backgrounds. Secondly, it is found in experiments that the reference spontaneous spectra have the same lineshape as $\text{Im}\chi_R$. Therefore SRS is capable of producing the same spectral response as the spontaneous references [1]. It means that SRS results can be compared directly with existing references without pre-processing. Besides, the linear dependence of SRS signal on interaction length L and intensities of the pump I_p and the Stokes beam I_s also makes SRS results more natural to interpret, which are quite valuable for molecular quantification. However, it is worthwhile to point out that these benefits come at a price. In traditional SRS experiment, the SRS-induced variation ΔI_s is usually orders of magnitude weaker than the incident field $I_s(0)$. It is very challenging to detect such a small signal on

a vast background, and special techniques are required. Besides, the initial Stokes beam can also induce a large shot-noise, which deteriorates the SRS performance. Therefore, special care needs to be taken to implement SRS for spectroscopic sensing applications.

2.6 Conclusion

In this chapter, we examined the basics of coherent Raman scattering. We revealed that coherent Raman interactions could be modeled as third-order nonlinear processes. The nonlinear polarization induced by coherent Raman interaction are derived. Their interaction with the optical fields is carefully investigated with the wave equation for a nonlinear optical media. With this equation, we examined two coherent Raman interactions — stimulated Raman scattering (SRS) and coherent anti-Stokes Raman scattering (CARS). The properties of their spectra and the differences in detection schemes are discussed.

In short, we showed that CARS suffers from non-resonant backgrounds and it has an extra requirement of the phase-matching condition. However, it is straightforward to probe the CARS signal as the detected signal is the square modulus of a newly emitted field. SRS is automatically phase-matched, and it is also free from non-resonant backgrounds. However, the SRS signal radiates at frequencies that are identical to the incident beams, making it very challenging to resolve the SRS signal from the incident fields.

References

- [1] Ji-Xin Cheng and Xiaoliang Sunney Xie, editors. *Coherent Raman Scattering Microscopy*. CRC Press, 2013.
- [2] Robert W. Boyd. *Nonlinear Optics*. Academic Press, 2008.
- [3] Peter Vandenabeele. *Practical Raman Spectroscopy*. WILEY, 2013.
- [4] Donald A. McQuarrie. *Quantum Chemistry*. University Science Books, 2008.
- [5] Herbert Goldstein, Charles P. Poole Jr., and John L. Safko, editors. *Classical Mechanics*. Pearson Education, 2014.
- [6] Govind P. Agrawal. *Nonlinear Fiber Optics*. Academic Press, 2013.
- [7] Geoffrey New. *Introduction to Nonlinear Optics*. Cambridge University Press, 2011.
- [8] Yuexin Liu, Young Jong Lee, and Marcus T. Cicerone. *Broadband CARS spectral phase retrieval using a time-domain Kramers–Kronig transform*. *Opt. Lett.*, 34(9):1363–1365, May 2009.
- [9] Charles H. Camp, Young Jong Lee, and Marcus T. Cicerone. *Quantitative, comparable coherent anti-Stokes Raman scattering (CARS) spectroscopy: correcting errors in phase retrieval*. *Journal of Raman Spectroscopy*, 47(4):408–415.
- [10] Ji-Xin Cheng, Lewis D. Book, and X. Sunney Xie. *Polarization coherent anti-Stokes Raman scattering microscopy*. *Optics Letters*, 26(17):1341–1343, September 2001.
- [11] Francois M. Kamga and Mark G. Sceats. *Pulse-sequenced coherent anti-Stokes Raman scattering spectroscopy: a method for suppression of the non-resonant background*. *Optics Letters*, 5(3):126–128, March 1980.
- [12] Martin Jurna, Jennifer L. Herek, and Herman L. Offerhaus. *Implementation of vibrational phase contrast coherent anti-Stokes Raman scattering microscopy*. *Applied Optics*, 50(13):1839–1842, April 2011.
- [13] K. J. A. Ooi, D. K. T. Ng, T. Wang, A. K. L. Chee, S. K. Ng, Q. Wang, L. K. Ang, A. M. Agarwal, L. C. Kimerling, and D. T. H. Tan. *Pushing the limits of CMOS optical parametric amplifiers with USRN:Si7N3 above the two-photon absorption edge*. *Nature Communications*, 8:13878, January 2017.

- [14] J. S. Levy, A. Gondarenko, A. C. Turner-Foster, M. A. Foster, A. L. Gaeta, and M. Lipson. *Four-wave mixing in integrated silicon nitride waveguides*. In 2009 Conference on Lasers and Electro-Optics and 2009 Conference on Quantum electronics and Laser Science Conference, pages 1–2, June 2009.

3

Stimulated and Spontaneous Raman Scattering in Waveguides: From a Quantum Mechanical Perspective

In Chapter 2, we studied in detail two coherent Raman scattering (CRS) processes — coherent anti-Stokes Raman scattering (CARS) and stimulated Raman scattering (SRS). As we will show in Chapter 4, CARS requires a stringent phase-matching condition that can hardly be satisfied on the silicon nitride waveguide platform accessible to us. Therefore, most of the effort in the second part of this thesis is devoted to the development of waveguide-based SRS sensors. In Chapter 2, SRS is modeled as a third-order nonlinear process. This model treats spontaneous Raman scattering and CRS as entirely different processes. It fails to recognize the inherent similarity between spontaneous Raman scattering and CRS, especially SRS.

To illustrate this similarity, let us have a look at the stimulated and spontaneous emission of a two-level atom. It is experimentally observed that an atom in the excited state can decay into the ground state by emitting a photon. This emission can take place with or without the presence of an external electromagnetic field, where the former process is classified as *stimulated emission* and the latter process is classified as *spontaneous emission*. A scrutiny of these two processes reveals that spontaneous and stimulated emission are intimately related. It is now widely accepted [1] that the electromagnetic field is non-zero even in the vacuum state due to Heisenberg's uncertainty principle, i.e., there always exists

some electromagnetic radiation even in the vacuum. In spontaneous emission, this zero-point radiation serves to “stimulate” the atom to relax from the excited state to the ground state. In this sense, spontaneous emission is indeed a particular type of stimulated emission [1–3], where the vacuum fluctuation provides the stimulation.

This argument is also applicable to Raman scattering [2, 4]. Spontaneous Raman scattering can also be viewed as a particular type of stimulated Raman scattering process that is “stimulated” by the vacuum fluctuation. Since many works have been done on waveguide-based spontaneous Raman scattering [5–7], it is advisable to have a unified treatment that takes care of both waveguide-based spontaneous Raman scattering and waveguide-based SRS.

The theory of Raman scattering excited by the guided modes of optical fibers has been laid down in the Ph.D. thesis of David Alan Wardle [8]. His work focuses on the Raman response of glass fibers themselves. In his derivation, both optical fields and molecules are modeled quantum mechanically. This full quantum mechanical treatment is described in Appendix A of [8].

In this thesis, we will extend the treatment given by David Alan Wardle to silicon nitride waveguides. Both on-chip spontaneous Raman scattering and on-chip SRS will be discussed. The full quantum mechanical treatment of Raman scattering of analytes probed by the evanescent tail of guided modes is saved in Appendix A. The intention of this chapter is to present the macroscopic equations describing the process of Raman scattering both in bulk media and in waveguides. Two primary parameters, spontaneous Raman gain coefficient G_{\parallel} and stimulated Raman gain coefficient g_{\parallel} , are identified. Their relation with Raman scattering cross-section $d\sigma/d\Omega$ is also investigated. At the end of this chapter, the waveguide loss is taken into account and its influence on Raman scattering is explored for different experimental configurations.

3.1 Raman Scattering from a Bulk Medium in Free Space

Raman scattering is a complicated three-dimensional process. In principle, we need to keep track of the propagation directions and the polarization of the optical waves involved in Raman scattering. Fortunately, in this thesis we will only encounter substances without preferential orientations: silicon nitride waveguides are composed of two amorphous materials (silicon nitride, silicon dioxide), and the analytes we are probing are random liquids. For Raman scattering in these materials, the intensity of scattered field is independent of the propagation directions of the participating optical fields [9–11]. More precisely

- In spontaneous Raman scattering, suppose the pump beam is propagating along \mathbf{k}_p , and its electric field is pointing to $\hat{\mathbf{e}}_p$. Also, suppose we are prob-

ing the scattered field that is propagating along \mathbf{k}_s with its electric field polarized to $\hat{\mathbf{e}}$. In this case, the optical power of the scattered field is determined solely by the angle between $\hat{\mathbf{e}}_p$ and $\hat{\mathbf{e}}_s$. The optical power of the scattered field is independent of either \mathbf{k}_p or \mathbf{k}_s .

- In stimulated Raman scattering, suppose two excitations, a pump beam, and a signal beam are injected into a Raman material. In order to know the Raman-induced gain/loss on the signal/pump beam, all we need to know is the relation between their polarization $\hat{\mathbf{e}}_p$ and $\hat{\mathbf{e}}_s$. No information is needed regarding the propagation directions \mathbf{k}_p and \mathbf{k}_s .

This property greatly simplifies the problem of waveguide-based Raman scattering. In the rest of this chapter, the parallel sign (\parallel) and the perpendicular sign (\perp) refer only to the relation between polarizations.

3.1.1 Spontaneous Raman Scattering

We first investigate the spontaneous Raman scattering in a bulk medium. Assume the Raman signal is excited and collected in the free space. The configuration is shown in Fig. 3.1. Here the pump beam (green square) is an infinite plane wave with an optical frequency of ω_p . It is propagating along the $+z$ direction, and its electric field points to $\hat{\mathbf{e}}_p$. If a total power of P_p of the pump beam is incident on a unit volume $dV = dA dz$, during Raman scattering, a small portion of the pump photons will experience a frequency shift and deflect from their original propagation direction. The total power of the scattered photons that propagate within a solid angle of $d\Phi$ and a frequency range of $[\omega_s, \omega_s + d\omega_s]$ is given by

$$P_s = \frac{\omega_s}{\omega_p} P_p R d\Phi dz d\omega_s, \quad (3.1)$$

where R is a proportionality factor that is given by

$$R = \frac{1}{32\pi^2 \hbar \epsilon_0^2 c^4} \frac{n(\omega_s)}{n(\omega_p)} \omega_p \omega_s^3 [M_{\parallel}(|\Omega|) \cos^2 \theta + M_{\perp}(|\Omega|) \sin^2 \theta] h(\Omega, T), \quad (3.2)$$

in which

- ω_p and ω_s are the frequency of the pump and scattered light,
- Ω is the frequency shift between the pump photon and the scattered photon $\Omega = \omega_p - \omega_s$,
- $h(\Omega, T)$ is a function related to the frequency shift Ω and the ambient temperature T , and it is defined as

$$h(\Omega, T) = \begin{cases} \left(1 - e^{-\frac{\hbar\Omega}{kT}}\right)^{-1} & \text{if } \Omega > 0 \text{ (Stokes),} \\ \left(e^{-\frac{\hbar\Omega}{kT}} - 1\right)^{-1} & \text{if } \Omega < 0 \text{ (anti-Stokes),} \end{cases} \quad (3.3)$$

- $M_{\parallel}(|\Omega|)$ and $M_{\perp}(|\Omega|)$ are the material Raman response functions for different polarizations,
- \hbar is the reduced Planck constant,
- $n(\omega_p)$ and $n(\omega_s)$ are the refractive indices of the material at pump and signal frequencies,
- ϵ_0 is the vacuum permittivity,
- θ is the angle between the polarization of the pump beam \hat{e}_p and the scattered beam \hat{e}_s .

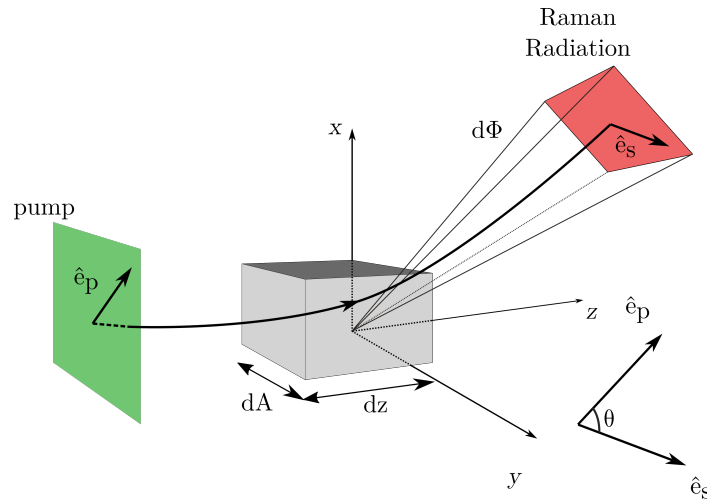


Figure 3.1: The geometry of spontaneous Raman scattering in a bulk medium. An infinite plane wave (represented by the green square) is incident on a Raman medium over a volume of $dV = dA dz$. Part of the pump light experiences a Stokes shift and deflects from its original propagation direction. The total scattered power propagating within a solid angle of $d\Phi$ within the frequency range of $[\omega_s, \omega_s + d\omega_s]$ is denoted as P . The polarizations of the pump beam and the Stokes beam are denoted as \hat{e}_p and \hat{e}_s respectively.

The material Raman response functions $M_{\parallel}(|\Omega|)$ and $M_{\perp}(|\Omega|)$ appeared in Eq. (3.2) describe the microscopic properties of the material itself. Although the exact value of $M_{\parallel}(|\Omega|)$ and $M_{\perp}(|\Omega|)$ can in principle be obtained through *ab initio* calculations, they are usually deduced from experimental results. In this thesis, it is sufficient to treat them as proportionality factors that are determined solely by $|\Omega|$. As we have stated at the beginning of this chapter, M_{\parallel} is the material response function for $\hat{e}_p \parallel \hat{e}_s$ and M_{\perp} describe the material response function for $\hat{e}_p \perp \hat{e}_s$. From Eq. (3.2) we can notice that

- The power of the scattered light is proportional approximately to ω_p^4 . This result is consistent with our treatment in chapter 2 where the Raman scattered power is also proportional to ω_p^4 .
- The Stokes scattered powers is stronger than the anti-Stokes scattered power by a factor of $\exp(\hbar\Omega/k_bT)$ which can be calculated from $h(\Omega, T)$.

3.1.2 Stimulated Raman Scattering

Figure 3.2 shows the configuration of SRS in a bulk medium. A signal beam and a pump beam are directed into a Raman medium. The signal beam is an infinite plane wave and it is represented by the red rectangle. It is propagating along the $+z$ direction and its electric field is polarized along \hat{e}_s .

The pump beam is also assumed to be an infinite plane wave and it is represented by the green rectangle in Fig. 3.2. Its optical intensity is I_p and its electric field is points to \hat{e}_p . The intensity of the pump beam I_p is measured as the optical power per unit area incident on a plane normal to the propagation direction of the pump beam itself. No assumption is made about the propagation direction of the pump beam.

We decompose the polarization of the signal beam \hat{e}_s into two components. One component is parallel to the pump $\hat{e}_\parallel \parallel \hat{e}_p$ and the other component is perpendicular to the pump $\hat{e}_\perp \perp \hat{e}_p$. We denote $\Lambda_\parallel(z)$ as the intensity of the part of the signal photons that has the following properties:

- it locates at z ,
- it lies within the frequency range of $[\omega_s, \omega_s + d\omega_s]$,
- it has the same polarization of the pump beam.

The evolution of $\Lambda_\parallel(z)$ due to SRS is given by

$$\frac{d\Lambda_\parallel}{dz} = \bar{g}_\parallel I_p \Lambda_\parallel(z), \quad (3.4)$$

where the stimulated Raman gain \bar{g}_\parallel is defined as

$$\bar{g}_\parallel = \frac{\Omega}{|\Omega|} \frac{\pi}{4\hbar\epsilon_0^2 c^2} \frac{\omega_s}{n(\omega_p)n(\omega_s)} M_\parallel(|\Omega|). \quad (3.5)$$

The parameters in Eq. (3.5) have the same meaning as in Eq. (3.2).

One can see from Eq. (3.4) that the gain of the signal beam is, again, not influenced by the propagation direction of the participating optical beams. Equation (3.5) predicts that the signal beam will experience the same amount of gain

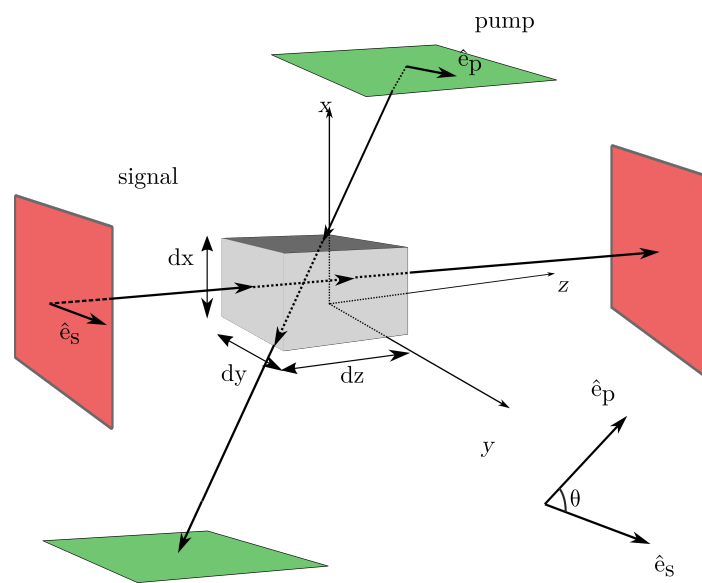


Figure 3.2: The geometry of stimulated Raman scattering in a bulk medium. Both pump beam and signal beam are assumed to be infinite plane waves. The signal beam (red) is propagating along z direction polarized at \hat{e}_s . The pump beam (green) is propagating along a certain direction and it is polarized at \hat{e}_p . The polarization of the signal beam is decomposed to a component perpendicular \hat{e}_\perp and a component parallel \hat{e}_\parallel to the pump beam.

\bar{g}_{\parallel} no matter which direction the pump beam is propagating to. We can easily extend the result to the case of $\hat{\mathbf{e}}_{\perp} \perp \hat{\mathbf{e}}_p$ by replacing the subscripts of \parallel with \perp in Eq. (3.4) and Eq. (3.5).

Equation (3.4) and Equation (3.5) do not pose limitation on the sign of Ω . If $\Omega > 0$, the signal is Stokes-shifted from the pump and it experiences a pure gain. If $\Omega < 0$ the signal is anti-Stokes-shifted and it experiences a pure loss. Similar to Chapter 2, the former phenomenon is sometimes called *stimulated Raman gain (SRG)* and the latter is classified as *stimulated Raman loss (SRL)*.

In most literature, SRS is described with the intensities of the optical fields instead of their spectral densities. In the CW and quasi-CW condition, the linewidth of the lasers is much narrower than the linewidth of the Raman modes [4]. In this case, the stimulated Raman gain \bar{g}_{\parallel} and the intensity of the pump beam I_p are roughly constant within the linewidth of the signal beam $\Delta\omega_s$. If we integrate both sides of Eq. (3.4) over the linewidth of the signal beam, $\bar{g}_{\parallel} I_p$ can be taken out of the integral, and we have

$$\frac{dI_s}{dz} = \int_{\Delta\omega_s} \bar{g}_{\parallel} I_p \Lambda_{\parallel}(z) = \bar{g}_{\parallel} I_p I_s. \quad (3.6)$$

where I_s is the intensity of the signal beam. In Chapter 2, we derived the evolution of the Stokes beam, and it is given by Eq. (2.62). If we take the limitation $L \rightarrow 0$ in Eq. (2.62), we can obtain the same equation as Eq. (3.6). It constitutes a piece of evidence that both derivations are correct.

An added value of the quantum mechanical treatment is that the spontaneous Raman scattering and stimulated Raman scattering are now connected. Both R and \bar{g} are now functions of $M_{\parallel}(|\Omega|)$ and $M_{\perp}(|\Omega|)$. In this way, once we know the spontaneous Raman response of a material, we can immediately estimate its stimulated response.

3.2 Spontaneous and Stimulated Raman Scattering in Wave-Guiding Structures

In the previous section, we investigated Raman scattering within a bulk medium where the optical excitations were taken as plane waves. In this section, we investigate both spontaneous Raman scattering and SRS in waveguides. The waveguide confines the optical fields, and the Raman signal is excited and collected by the guided modes. There exist a primary difference between waveguide-based and free-space Raman scattering. In a waveguide, only a portion of the optical field overlaps with the Raman medium. The Raman medium is the bio-cladding for integrated silicon nitride waveguide, and it is the liquid core for liquid-filled photonic crystal fibers.

We assume there are two beams propagating within the waveguide—a pump beam and a signal beam. Suppose the modes are confined in the xy plane and propagate along either $+z$ or $-z$.

We further assume the pump has an optical frequency of ω_p , a polarization of \hat{e}_p and a total optical power P_p . No assumption is made about the propagation direction of the pump beam. Now for the signal beam at frequency ω_s , we can decompose its polarization to a component parallel to the pump beam $\hat{e}_{\parallel} \parallel \hat{e}_p$ and a component perpendicular to the pump beam $\hat{e}_{\perp} \perp \hat{e}_p$. We use $\Gamma_{\parallel}(z)$ to denote the optical power of the part of the signal beam that

- (a) propagates along $+z$,
- (b) lies within the range of $[\omega_s, \omega_s + d\omega_s]$,
- (c) polarizes along the \hat{e}_{\parallel} .

The evolution of Γ_{\parallel} within the waveguide is given by

$$\frac{d}{dz}\Gamma_{\parallel}(z) = \underbrace{\frac{\omega_s}{\omega_p}R_{\parallel}P_p}_{\text{spontaneous}} + \underbrace{g_{\parallel}\Gamma_{\parallel}(z)P_p}_{\text{stimulated}}. \quad (3.7)$$

The first term on the right-hand side of Eq. (3.7) models spontaneous Raman scattering. In this term, R_{\parallel} represents the probability that a pump photon is scattered within a distance of dz into the signal beam. More precisely, the scattered photon preserves its original polarization, has an optical frequency within the range of $[\omega_s, \omega_s + d\omega_s]$, and propagates along the $+z$ direction. The second term on the right-hand side of Eq. (3.7) models SRS. The quantity $g_{\parallel}P_p$ describes the gain of the signal beam $\Gamma_{\parallel}(z)$ over dz .

The spontaneous Raman gain coefficient R_{\parallel} , and the stimulated Raman gain coefficient g_{\parallel} are given by

$$R_{\parallel} = \frac{1}{8\hbar\epsilon_0^2c^2} \frac{\omega_p\omega_s}{n(\omega_p)n(\omega_s)} h(\Omega, T) \iint_{\text{Raman Region}} M_{\parallel}(|\Omega|)|f_p|^2|f_s|^2 dx dy, \quad (3.8)$$

$$g_{\parallel} = \frac{\Omega}{|\Omega|} \frac{\pi}{4\hbar^2\epsilon_0^2c^2} \frac{\omega_s}{n(\omega_p)n(\omega_s)} \iint_{\text{Raman Region}} M_{\parallel}(|\Omega|)|f_p|^2|f_s|^2 dx dy, \quad (3.9)$$

where $n(\omega_p)$, and $n(\omega_s)$ are the effective indices of the pump beam and the signal beam, respectively. $f_p(x, y)$ and $f_s(x, y)$ are the normalized transverse mode profile of the pump and signal beam respectively. The other symbols bear the same meanings as in Eq. (3.2) and Eq. (3.5).

It is noteworthy that, unlike the results mentioned in the previous section, R_{\perp} and g_{\perp} cannot be obtained by simply replacing M_{\parallel} with M_{\perp} in Eq. (3.8) and

Eq. (3.9). The effective index of the guided modes $n(\omega_s), n(\omega_p)$ and their mode profiles $|f_p|^2, |f_s|^2$ should also be modified accordingly.

One can notice Eq. (3.8) and Eq. (3.9) differ from Eq. (3.5) and Eq. (3.2) mainly by the integral

$$\iint_{\text{Raman Region}} M_{\parallel}(|\Omega|) |f_p|^2 |f_s|^2 dx dy. \quad (3.10)$$

In this integral, the Raman response is weighted-averaged by the profile of the optical beam, which converts the material gain to the modal gain. This integral is determined by the exact geometry of the waveguides used for Raman sensing. In the following section, we will discuss in detail the procedure of calculating this integral for silicon nitride waveguides.

3.3 Introduction to Silicon Nitride Waveguides

Before embarking on the study of coherent Raman spectroscopy enabled by the silicon nitride platform, we shall briefly review the fundamental properties of the silicon nitride waveguides.

In this work, we will consider two types of silicon nitride waveguides for Raman sensors: (a) strip waveguides and (b) slot waveguides. The structures of these two types of waveguides are shown in Fig. 3.3. For both types of waveguides, a layer of silicon nitride is first deposited on top of a thick silicon dioxide layer. This silicon dioxide layer is also called the buried oxide (BOX) layer. The waveguides are then defined with deep-UV lithography and reactive ion-etching (RIE) [12]. In this work, the silicon nitride waveguides are fabricated through imec's silicon nitride photonics platform, BioPIX. In this platform, the thickness of the silicon nitride layer can either be 150 nm, 220 nm or 300 nm. The smallest feature size is 150 nm.

The overall width of the waveguide usually varies from 300 nm to 1500 nm. The silicon nitride core is under-clad by a thick layer of silicon dioxide (BOX) to suppress substrate leakage. Because the refractive index of the silicon nitride is lower than that of silicon, the guided modes tend to be less-confined within the silicon nitride core. As the silicon is highly absorbing below 1.1 μm , it is essential to use a thick BOX layer to prevent the guided-mode from leaking into the silicon substrate.

The structure of a strip waveguide is shown on the left-hand side of Fig. 3.3. There exist two degrees of freedom in strip waveguides: one can vary the height of the waveguide h and the width of the waveguide w . The structure of a slot waveguide is shown in the right-hand side of Fig. 3.3. Compared to strip waveguides, slot waveguides has three degrees of freedom: the height h , the width w , and the gap size g .

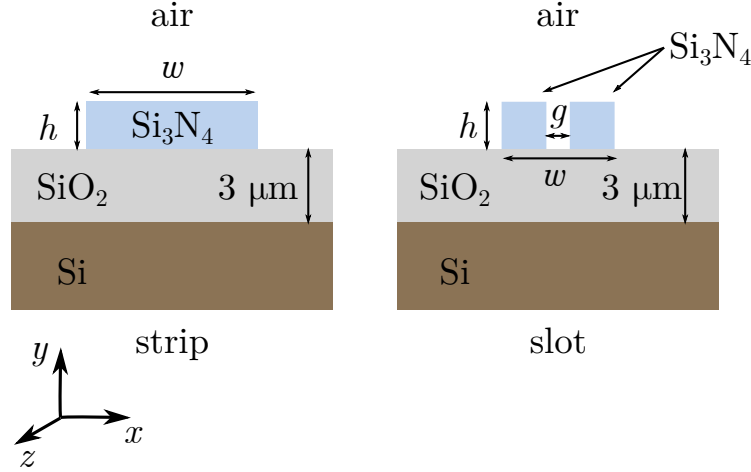


Figure 3.3: The structure of an air-clad strip waveguide and an air-clad slot waveguide. The top- and side-cladding of the silicon nitride is totally removed. The waveguide core sits on a thick layer of buried silicon dioxide (BOX) on the bottom. For strip waveguides, their dimensions are determined by the height h and the width w . The dimension of slot waveguides are determined by the height h , the width w , and gap size g .

Both strip and slot waveguides support a collection of modes. By convention, these supported modes are separated into two categories. If the electric field of a mode is mainly polarized along the x -direction, then this mode is called a *TE mode*. The modes with their electric fields mainly polarized along the y -direction are classified as *TM modes*. However, it is important to emphasize that these guided modes of strip waveguides are not strictly TE- or TM-polarized. They are indeed hybrid modes. However, the polarization of the guided modes is nearly linear in a strip waveguide. Therefore they are often referred to as quasi-TE or quasi-TM modes. For simplicity, we will refer them as TE/TM modes in this thesis.

In this work, we will encounter two different types of silicon nitride deposited by different processes: low-pressure chemical vapor deposition (LPCVD) and plasma-enhanced chemical vapor deposition (PECVD) [13]. The properties of LPCVD silicon nitride and PECVD silicon nitride are summarized in Table 3.1. In general, the LPCVD silicon nitride has a lower concentration of hydrogen, a subdued strain, a slightly higher refractive index and a much higher resistance to hydrofluoric acid (HF). However, LPCVD requires a very high deposition temperature ($> 700^\circ$) while PECVD can be carried out in a much milder condition. Besides, although the PECVD silicon nitride has a poorer homogeneity, its properties can be adjusted over a broad parameter space with different deposition conditions. It is noteworthy that the waveguides based on both deposition techniques can be optimized to have a propagation loss as low as 1 dB/cm [14].

	LPCVD	PECVD
Deposition Temperature (°C)	700-800	> 300
Typical deposition pressure (Pa)	20-70	60-700
Atomic percent of hydrogen	3-8	10-40
density (g/cm ³)	2.9-3.1	2.3-3.1
etch rate in 49% HF at 23 °C (nm/min)	8	150-300
etch rate in BHF (nm/min)	0.3-0.6	5-150
refractive index n	1.9-2.4	1.8-2.6
dielectric constant ϵ	6-7	6-9

Table 3.1: Properties of silicon nitride thin films deposited by PECVD and LPCVD techniques. This table is taken from Ref. [13].

3.4 Raman Gain Coefficients of Silicon Nitride Waveguides

In this section, we will calculate the Raman gain coefficients of analytes covering silicon nitride waveguides. The scheme of waveguides used for evanescent Raman sensing is shown in Fig. 3.4. During Raman sensing, the silicon nitride waveguide core is side- and top-clad by analytes. In the figure, the analytes are taken to be liquid, while gas samples can also be probed similarly. The evanescent tail of the guide mode overlaps with the analyte to excite and collect the Raman signal.

Because the TE modes of the strip waveguides tend to have a lower loss, in this chapter the pump beam and the signal beam are all taken to be TE-polarized. In this case, only the parallel gain coefficients R_{\parallel} and g_{\parallel} are relevant to us.

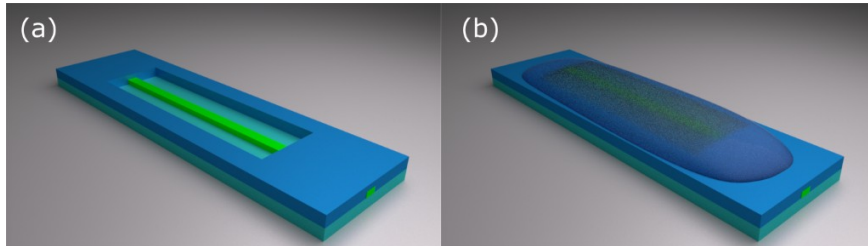


Figure 3.4: The scheme of evanescent Raman detection on silicon nitride waveguides. The structures of the waveguide (a) before and (b) after the application of analyte.

3.4.1 Raman Response Function and Scattering Cross-Section

To estimate the correct Raman gain coefficients R_{\parallel} and g_{\parallel} , we should first compute the value of the material response function $M_{\parallel}(|\Omega|)$. Since M_{\parallel} is difficult

to compute from first-principles, we will derive its value from spontaneous Raman scattering experiments. In those experiments, the Raman response is usually characterized by a quantity called scattering cross-section σ . Our purpose is to establish a connection between the scattering cross-section σ and the material response function $M_{\parallel}(|\Omega|)$ with the help of Eq. (3.1) and Eq. (3.2). We recall from Chapter 2 that the total Raman scattered power from N molecules is given by

$$P_s = NI_p\sigma, \quad (3.11)$$

where I_p is the intensity of the pump beam. For a liquid sample with a volume of $dV = dA dL$, the total number of molecules is given by

$$N = \frac{\rho dV N_A}{M_u}, \quad (3.12)$$

where M_u is the molar mass of the analytes, ρ is the density of the analyte, N_A is the Avogadro number. The intensity of the pump beam is given by

$$I_p = P_p \frac{1}{dA}. \quad (3.13)$$

With the help of Eq. (3.13) and Eq. (3.12), and taking into account the propagation direction of the scattered photon, we can rewrite Eq. (3.11) as

$$P_s = P_p \frac{1}{dA} \left(\frac{d\sigma}{d\Phi} \right) \frac{\rho dV N_A}{M_u} \Delta\Phi, \quad (3.14)$$

where P_s is the optical power of all the scattered photons that are propagating within a solid angle of $\Delta\Phi$, $\partial\sigma/\partial\Phi$ is the differential scattering cross-section of the analytes.

Comparing Eq. (3.14) to Eq. (3.1), we can see that the spontaneous Raman gain coefficient R can be obtained by multiplying the spectral density of the differential Raman scattering cross-section $\partial^2\sigma/\partial\omega\partial\Phi$ with the number of molecules within a unit volume

$$R_{\parallel} = \frac{\omega_p}{\omega_s} \left(\frac{\partial^2\sigma}{\partial\omega\partial\Phi} \right) \frac{\rho N_A}{M_u}. \quad (3.15)$$

It is important to notice that this relation holds only for the scattering cross-section $d\sigma/d\Phi$ measured with a parallel configuration. That is, the polarization of the scattered light and the pump should be the same. It can also be designated as $(d\sigma/d\Phi)_{\parallel}$. However, this notation is a bit too complicated, and we will drop the subscripts of \parallel wherever it does not cause confusions.

Most literature reports the differential Raman scattering cross-section $d\sigma/d\Phi$ (SI: $[\text{meter}^2(\text{sr})^{-1}]$) of a molecules. It can be converted to $\partial^2\sigma/\partial\Phi\partial\omega$ (SI: $[\text{meter}^2(\text{sr})^{-1}(\text{rad/s})^{-1}]$) by taking into account the lineshape of the Raman mode. The difference between these two quantities is shown in Fig. 3.5. $\partial^2\sigma/\partial\omega\partial\Phi$ is

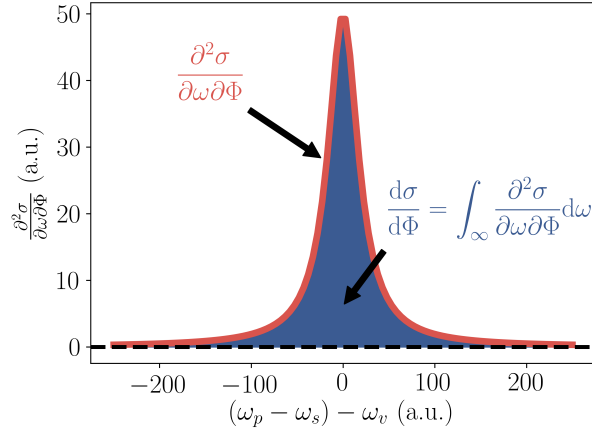


Figure 3.5: The spectral density of the differential cross-section of Raman scattering $\partial^2\sigma/\partial\omega\partial\Phi$ is shown as the solid red line in the figure. The differential cross-section of Raman scattering $d\sigma/d\omega$ is obtained by integrating $\partial^2\sigma/\partial\omega\partial\Phi$ over the whole spectrum, which is the actually the area of blue zone.

shown as the solid red line in the figure. We have assumed that $\partial^2\sigma/\partial\omega\partial\Phi$ has a Lorentzian lineshape. $d\sigma/d\Phi$ can be obtained by integrating the solid line over the whole frequency range. Its value is equal to the area of the blue zone shown in Fig. 3.5.

The response function M_{\parallel} can now be written as a function of $\partial^2\sigma/\partial\omega\partial\Phi$ as

$$M_{\parallel}(|\Omega|) = \left(\frac{\partial^2\sigma}{\partial\omega\partial\Phi} \right) \frac{\rho N_A}{M_u} \frac{32\pi^2 \hbar \epsilon_0^2 c^4}{\omega_s^4} \frac{n(\omega_p)}{n(\omega_s)}. \quad (3.16)$$

In most cases we are only interested in the maximal value of M_{\parallel} . If we assume the Raman mode has a Lorentzian lineshape, the maximal value of M_{\parallel} can be written as a function of $d\sigma/d\Phi$ as

$$\max(M_{\parallel}) = \frac{2}{\pi \Delta_R} \left(\frac{d\sigma}{d\Phi} \right) \frac{\rho N_A}{M_u} \frac{32\pi^2 \hbar \epsilon_0^2 c^4}{\omega_s^4} \frac{n(\omega_p)}{n(\omega_s)}, \quad (3.17)$$

where Δ_R is the full-width-half-maximum (FWHM) of the Raman peak whose unit is [rad/s].

In [8], the Raman response function of the glass core of a single mode fiber is estimated to be

$$\max(M_{\parallel, \text{glass}}) = 1.46 \times 10^{-101} \text{ C}^4 \text{ kg}^{-1} \text{ m}^{-1} (\text{rad/s})^{-4}. \quad (3.18)$$

It is interesting to do the same exercise for isopropyl alcohol (IPA). Based on its chemical properties listed in Table 3.2, the maximal value of M_{\parallel} for IPA is

found to be

$$\max(M_{\parallel, \text{IPA}}) = 1.15 \times 10^{-100} \text{ C}^4 \text{ kg}^{-1} \text{ m}^{-1} (\text{rad/s})^{-4}. \quad (3.19)$$

It suggests that the Raman response of IPA is around 10 times stronger than that of glasses. One might note that M_{\parallel} is proportional to the concentration of the analytes. The derivation of Eq. (3.16) involves only the number density of analytes ([molecules per meter³]) and we have utilized the fact that the number density of pure liquid is $\rho N_A / M_u$. If we are probing a substance from a mixture, we can replace $\rho N_A / M_u$ with the number density of that substance, which apparently is proportional to its concentration.

paramters	values
Molar mass M_u	60.1 g/M
Density ρ	786 kg/m ³
Refractive index	1.3776
Raman mode	819 cm ⁻¹
Differential cross-section $d\sigma/d\Phi$	5.8×10^{-31} cm ² /sr
FWHM of Raman mode	200 GHz
Angular frequency of the Stokes beam ω_s	2.25×10^{15} rad/s

Table 3.2: Chemical properties of pure isopropyl alcohol (IPA) and the differential cross-section of Raman scattering for its 819 cm⁻¹ Raman peak.

3.4.2 Effective Index and Confinement Factor

To obtain the Raman response of the analytes, we should average $M_{\parallel}(|\Omega|)$ over the profile of the pump and the signal beam. Fortunately, the calculation can be greatly simplified if we make the following observations: Firstly, it is valid to treat the analyte cladding of the silicon nitride as a homogeneous material. In this case, the Raman response function $M_{\parallel}(|\Omega|)$ is a constant over the Raman active area. Therefore, $M_{\parallel}(|\Omega|)$ can be taken out from the integral. Secondly, the signal beam usually has a similar mode profile as the pump beam. In practice, it is usually not a bad approximation to treat them as identical. As a result, the integration can be simplified to

$$\iint_{\text{Raman Region}} M_{\parallel}(|\Omega|) |f_p|^2 |f_s|^2 dx dy = M_{\parallel}(|\Omega|) \iint_{\text{analytecladding}} |f|^4 dx dy. \quad (3.20)$$

To gain an intuitive understanding of this integral, it proves to be useful to express it as

$$\iint_{\text{analytecladding}} |f|^4 dx dy = \frac{\eta}{A_{\text{eff}}}. \quad (3.21)$$

where the *effective mode area* A_{eff} and the *confinement factor* η are introduced as

$$\frac{1}{A_{\text{eff}}} = \iint_{-\infty}^{\infty} |f|^4 dx dy, \quad \eta = \frac{\iint_{\text{analytecladding}} |f|^4 dx dy}{\iint_{-\infty}^{\infty} |f|^4 dx dy}. \quad (3.22)$$

One can easily verify that A_{eff} has a dimensional area (SI: [meter²]) and it characterizes the size of the guided mode. The confinement factor η is dimensionless and it can be loosely regarded as the percentage of light propagating within the analyte. Therefore, Eq. (3.21) indicates that the Raman signal is maximized if the optical field is tightly-confined within a small area and has a large overlap with the analytes. If we also take into account the effective index of the mode, the influence of the waveguide geometry on R_{\parallel} and g_{\parallel} (see Eq. (3.8) and Eq. (3.9)) can be modeled as a new quantity the *geometrical coefficient*. It is defined as

$$\text{geometrical coefficient} = \frac{1}{n(\omega_p)n(\omega_s)} \frac{\eta}{A_{\text{eff}}}. \quad (3.23)$$

3.4.2.1 TE polarization

We first have a look at the geometrical coefficient when both pump beam and signal beam excite the fundamental TE mode of silicon nitride strip waveguides. Figure 3.6 show the geometrical coefficient of strip waveguides with various widths and heights. The waveguides are assumed to be covered with pure IPA ($n = 1.3776$). The refractive of silicon nitride is assumed to be 1.94 and the refractive index of the BOX is assumed to be 1.44. It is clear that for a given height, there exists an optimal width for which the geometrical coefficient is maximized. If the width is wider than the optimal value, the mode area A_{eff} increases and confinement factor η decreases. Therefore the overall geometrical coefficient decreases. If the width of the waveguide is narrower than the optimal value, the optical field is not adequately guided by the waveguide, which results in a rapid increase of the mode area A_{eff} . Although the field has a slightly larger overlap with the analytes, the overall geometrical coefficient also decreases.

It is proposed that the use of slot waveguides can greatly increase the geometrical coefficient. It is shown in [15] that slotted waveguides are capable of improving the confinement factor η significantly. In the meanwhile, the optical field is still tightly-confined within a small area A_{eff} . In Fig. 3.7 we plot the geometrical coefficient of a 300-nm-high slot waveguide with a 150 nm gap. The geometrical coefficient of a 300-nm-high strip waveguide is also shown in Fig. 3.7 for comparison. We observe that the geometrical coefficient is indeed significantly improved for slot waveguides. For a total width of 800 nm, the slot waveguide is performing 4-times as good as the strip waveguide. However, it is worth mentioning that slot waveguides tend to have a much higher propagation loss. As a result, the overall Raman signal recorded from a slot waveguide might be even lower

than that obtained from a strip waveguide. To obtain a strong Raman signal, one should consider carefully the trade-off between waveguide loss and geometrical coefficient.

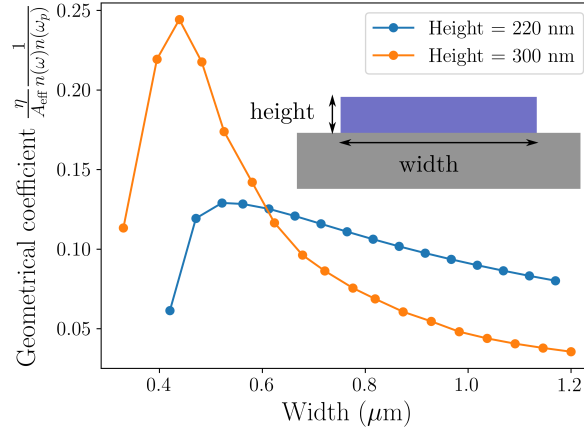


Figure 3.6: The geometrical coefficient of the fundamental TE mode of strip waveguides at various heights and widths available in BioPIX.

3.4.2.2 TM polarization

Now we assume both pump beam and signal beam couple to the fundamental TM mode of waveguides. Figure 3.8 shows the geometrical coefficient of strip waveguides at various widths and heights.

One can quickly notice that in the same geometry, the geometrical coefficient of the fundamental TM mode is about twice as large as the fundamental TE mode. A closer inspection of the mode profile suggests that although the effective area A_{eff} are comparable for both TM and TE modes, the TM mode has a more extensive overlap with the analytes. We can also learn from Fig. 3.8 that there exists an optimal width at which the geometrical coefficient is maximized. Similar to our previous discussion for TE modes, the optimized width is determined by the trade-off between the confinement factor η and the effective area A_{eff} .

Figure 3.9 compares the geometrical coefficient of a slot waveguide and a strip waveguide. The gap of the slot waveguide is 150 nm wide. We can see a slot waveguide can also significantly enhance the geometrical coefficient for TM modes. However, the improvement is not as significant as its TE counterpart. For a total width of 800 nm, the slot waveguide has a geometrical coefficient 2-times as large as the strip waveguide.

It is noteworthy that although the fundamental TM mode has a larger geomet-

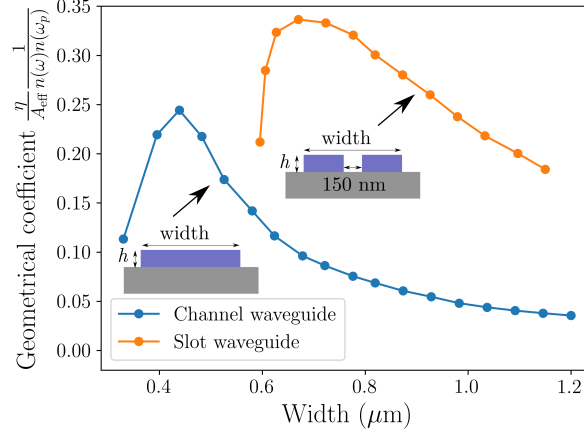


Figure 3.7: The comparison of the geometrical coefficient of the fundamental TE mode of a slot waveguide with a 150 nm slot and a strip waveguide.

rical coefficient, it typically has also a larger propagation loss [14]. As a result, the TM mode does not always manifest better performance than the TE mode.

3.4.3 Numerical Value of the Raman Gain Coefficients on Silicon Nitride Waveguides

The waveguide-based Raman gain coefficients can be now be rewritten with A_{eff} and η . They become

$$R_{\parallel} = \frac{1}{8\hbar\epsilon_0^2 c^2} \frac{\omega_p \omega_s}{n(\omega_p) n(\omega_s)} h(\Omega, T) M_{\parallel}(|\Omega|) \frac{\eta}{A_{\text{eff}}}, \quad (3.24)$$

$$g_{\parallel} = \frac{\Omega}{|\Omega|} \frac{\pi}{4\hbar^2 \epsilon_0^2 c^2} \frac{\omega_s}{n(\omega_p) n(\omega_s)} M_{\parallel}(|\Omega|) \frac{\eta}{A_{\text{eff}}}. \quad (3.25)$$

In the previous sections, we have already studied the material response function of the Raman analyte M_{\parallel} for liquid analyte. We have also studied the geometrical coefficient of the waveguide $\eta/(n(\omega_p)n(\omega_s)A_{\text{eff}})$. It is now a good time to give an numerical estimation of the gain coefficients R_{\parallel} and g_{\parallel} .

3.4.3.1 Spontaneous Raman Gain Coefficient

Suppose we are probing pure IPA with the evanescent field and suppose the properties of the waveguide and Raman interactions listed in Table 3.3, the maximal value of the spontaneous Raman gain coefficient R_{\parallel} is estimated to be

$$\max(R_{\parallel}) = 3.1 \times 10^{-20} \text{ m}^{-1} (\text{rad/s})^{-1}. \quad (3.26)$$

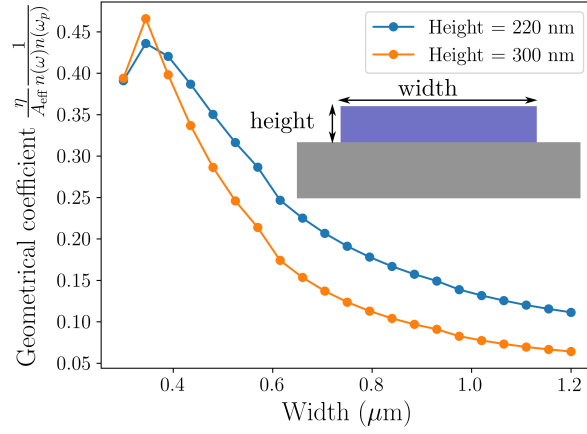


Figure 3.8: The geometrical coefficient of the fundamental TM mode of strip waveguides with different width and heights.

In practice we are more concerned with the Raman scattered power over one Raman mode instead of the spectral density of Raman scatter power. In this case, the evolution of the signal beam is usually rewritten as

$$\frac{\partial}{\partial z} P_s(z) = G_{\parallel} P_p, \quad (3.27)$$

where P_s is the Raman scattered power over the whole Raman mode. The spontaneous Raman gain coefficient G_{\parallel} for P_s is defined as

$$G_{\parallel} = \int_{-\infty}^{\infty} R d\Omega = \frac{\omega_s}{\omega_p} \frac{1}{8\hbar\epsilon_0^2 c^2} \frac{\omega_p \omega_s}{n(\omega_p)n(\omega_s)} h(\Omega, T) \frac{\eta}{A_{\text{eff}}} \int_{-\infty}^{\infty} M_{\parallel}(|\Omega|) d\Omega. \quad (3.28)$$

Suppose we are probing pure IPA with a guided mode whose properties are shown in Table 3.3, the gain coefficient G_{\parallel} is given by

$$G_{\parallel} = 6.2 \times 10^{-10} \text{ cm}^{-1}. \quad (3.29)$$

Here the properties of the analytes are also given in Table 3.3.

3.4.3.2 Stimulated Raman Gain Coefficient

Based on Eq. (3.25), we can also estimate the maximal stimulated Raman gain coefficient g_{\parallel} . With the parameters shown in Table 3.3, we have

$$\max(g_{\parallel}) = 0.37 \text{ m}^{-1} \text{ W}^{-1}. \quad (3.30)$$

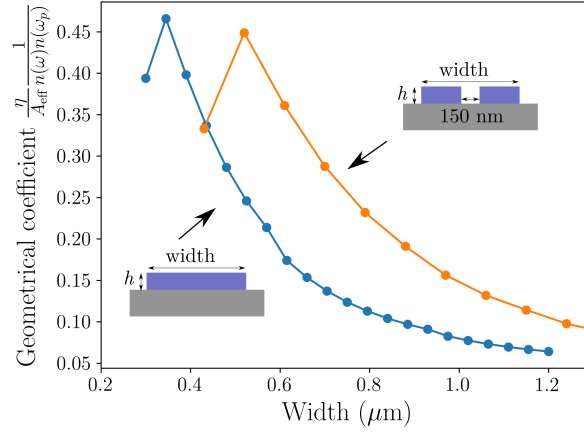


Figure 3.9: Comparison of the geometrical coefficient of the fundamental TM mode of a slot waveguide with a 150 nm gap and a strip waveguide.

Suppose we are using CW or quasi-CW lasers, the linewidth of signal beam Δ_ω will be much narrower than the Raman linewidth Δ_R . In this case, it is reasonable to assume the stimulated Raman gain g_{\parallel} is constant over the laser linewidth Δ_ω . If we integrate both sides of Eq. (3.7) over the laser linewidth Δ_ω , we have

$$\frac{dP_s}{dz} = g_{\parallel} P_p P_s. \quad (3.31)$$

Here P_s and P_p denotes the optical power of the injected signal beam and pump beam.

In some literatures [16], the pump and signal beams are also characterized by the optical intensity. The process of SRS is described accordingly as

$$\frac{dI_s}{dz} = g_I I_p I_s, \quad (3.32)$$

where I_p and I are the intensity of the pump and signal beams respectively.

These two definition of stimulated Raman gain coefficients can be connected with $g_I = g_{\parallel} A_{\text{eff}}$. For the IPA cladding, the maximal value of g_I is given by

$$\max(g_I) = \max(g_{\parallel}) A_{\text{eff}} = 10^{-13} \text{ m W}^{-1}. \quad (3.33)$$

3.4.3.3 Relation Between the Spontaneous and Stimulated Raman Gain Coefficients

Considerable work has been done for waveguide-enabled spontaneous Raman scattering by Ashim Dhakal [5]. He has studied the spontaneous Raman gain coeffi-

paramters	values
Waveguide height h	300 nm
Waveguide width w	700 nm
Refractive index of SiN	1.8987
Refractive index of IPA	1.3776
Pump wavelength	785 nm
Molar mass of IPA M_u	60.1 g/M
Density of IPA ρ	786 kg/m ³
Raman mode	819 cm ⁻¹
Differential cross-section $d\sigma/d\Phi$	5.8×10^{-31} cm ² /sr
lineshape	Lorentzian
FWHM of Raman mode	200 GHz
Effective area A_{eff}	$0.280 \mu\text{m}^2$
Confinement factor η	0.14

Table 3.3: The parameters used for estimating the obtainable signal power of spontaneous Raman scattering. The upper half of the table are the raw parameters and the second half are the geometry-relevant parameters obtained with 2D FDTD simulations by FIMMWAVE.

cient G_{\parallel} for various types of waveguides over a miscellaneous of material platforms. Therefore, it will be convenient to have an equation to convert the spontaneous gain coefficient G_{\parallel} to the stimulated gain coefficient ($\max(g_{\parallel})$). If we assume the Raman response has a Lorentzian lineshape, we can derive from Eq. (3.8) and Eq. (3.9) that

$$\frac{G_{\parallel}}{\max(g_{\parallel})} = h(\Omega, T) \frac{\hbar\omega_p}{2\pi \max(M_{\parallel})} \int_{-\infty}^{\infty} M_{\parallel} d\Omega = \frac{\hbar\omega_p}{4} h(\Omega, T) \Delta_R, \quad (3.34)$$

where Δ_R is the full-width-half-maximum of the Raman response. At room temperature, $h(\Omega, T)$ is close to unity. Suppose $\Delta_R = 2\pi \times 300$ GHz and $\hbar\omega_p = 1.55$ eV, the ratio between G_{\parallel} and $\max(g_{\parallel})$ is

$$\max(g_{\parallel}) \approx 10^7 \times G_{\parallel}. \quad (3.35)$$

Here the dimension of g_{\parallel} is [1/(m W)] and the dimension of G_{\parallel} is [1/m]. This relation is very handy in estimating the stimulated gain coefficient from spontaneous results.

3.5 Propagation of Raman Signal in Waveguides

In the previous section, we have obtained the spontaneous Raman gain coefficient R_{\parallel} , and the stimulated Raman gain coefficient g_{\parallel} . In this section, with the help of

R_{\parallel} and g_{\parallel} , we will derive the evolution of the signal beam under various experimental configurations. In principle, we should take into account the propagation loss, nonlinear loss, Kerr effect, free carrier effect and dispersive effects to give a complete description of the signal beam. Fortunately, in the CW or quasi-CW regime, only the propagation loss should be explicitly considered.

3.5.1 Spontaneous Raman Scattering in Waveguide

We begin with the spontaneous Raman scattering. We assume the waveguide extends along the z axis. The pump beam is coupled into the waveguide at $z = 0$, and it is propagating along the $+z$ direction. The pump beam will be scattered to both $+z$ and $-z$ direction as shown in Fig. 3.10. The scattered beam propagating along $+z$ is called the forward-collected signal and that along $-z$ is called the backward-collected signal. Although the forward-collected and the backward-collected signal enjoys the same Raman gain coefficient G_{\parallel} , the optical power collected at opposite end-facets might be different due to waveguide loss. We will consider (a) the forward-collected and the (b) backward-collected Raman signals separately.

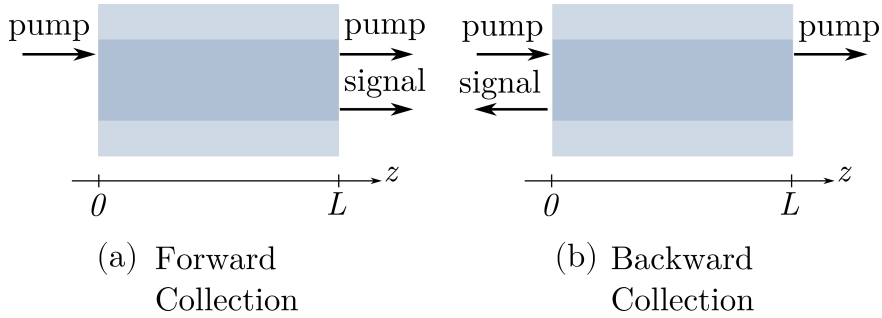


Figure 3.10: Two configurations of waveguide-based spontaneous Raman experiments. (a) Forward collection. We collect the scattered light propagates along $+z$ direction. (b) Backward collection. We collect the scattered light propagates along $-z$ direction.

3.5.1.1 Forward Collection

In the forward-collection configuration, the pump beam is propagating along $+z$. We are collecting the signal beam propagating along the same direction of the pump. In this case, the evolution of the signal beam is dictated by

$$\frac{dP_s}{dz} = G_{\parallel} P_p(z) - \alpha_s P_s(z), \quad (3.36)$$

where α_s is the linear propagation loss for the signal beam and G_{\parallel} is the spontaneous Raman gain. Due to the weakness of Raman interaction, we can safely

ignore the Raman-induced loss on the pump beam. Therefore the evolution of the pump beam is given by $P_p(z) = P_p(0)e^{-\alpha_p z}$ where α_p is the propagation loss for the pump beam. Taking into account the boundary condition that no signal beam is injected into the waveguide at $z = 0$, we obtain the evolution of the signal beam as

$$P_s(z) = G_{\parallel} \frac{1 - e^{-(\alpha_s - \alpha_p)z}}{\alpha_s - \alpha_p} P_p(0) e^{-\alpha_p z}. \quad (3.37)$$

If we further assume the signal beam and the pump beam are experiencing the same propagation loss $\alpha_p = \alpha_s = \alpha$, the optical power of the signal beam leaving the facet at $z = L$ is given by

$$P_s(L) = G_{\parallel} P_p(0) L e^{-\alpha L} \quad (3.38)$$

3.5.1.2 Backward Collection

In the configuration of backward-collection, the pump beam is propagating along the $+z$ direction while the signal beam is propagating along the $-z$ direction. The equation governing the evolution of the signal power is obtained by replacing z with $-z$ in Eq. (3.36) and it is given by

$$\frac{dP_s}{dz} = -G_{\parallel} P_p(z) + \alpha_s P_s(z). \quad (3.39)$$

Considering the boundary condition that no signal beam is injected into the waveguide at $z = L$, we have $P_s(L) = 0$. The optical power of the signal beam leaving the end-facet at $z = 0$ is given by

$$P_s(0) = G_{\parallel} P_p(0) \frac{1 - e^{-L(\alpha_p + \alpha_s)}}{\alpha_p + \alpha_s}. \quad (3.40)$$

This result can be simplified if $\alpha_p = \alpha_s = \alpha$, which is

$$P_s(0) = G_{\parallel} P_p(0) \frac{1 - e^{-2\alpha L}}{2\alpha}. \quad (3.41)$$

Comparing Eq. (3.41) with Eq. (3.38), we notice the optical power of the backward-collected signal and the forward-collected signal have different behavior. Suppose the waveguide loss is $\alpha = 2$ dB/cm, we plot the evolution of the backward-collected and the forward-collected signals in Fig. 3.11 with the length of waveguide L . We can immediately notice two features:

1. The optical power of the backward-collected signal increases monotonously with increasing waveguide length. However, there exists an optimal length for the forward-collected spontaneous Raman scattering experiments. The optical power of the forward-collected signal beam will first increase. After it reaches its peak value, it gradually decrease.

2. The maximal detectable optical power of the backward-collected signal is slightly higher than the maximal forward-collected signal.

We can see that it is almost always advantageous to collect the backward propagating signal if it is permitted by experimental conditions. However, if the length of the waveguide is shorter than the optimal length of the forward-collected configuration, the optical power for both configurations are almost identical and one can choose freely either of the configurations.

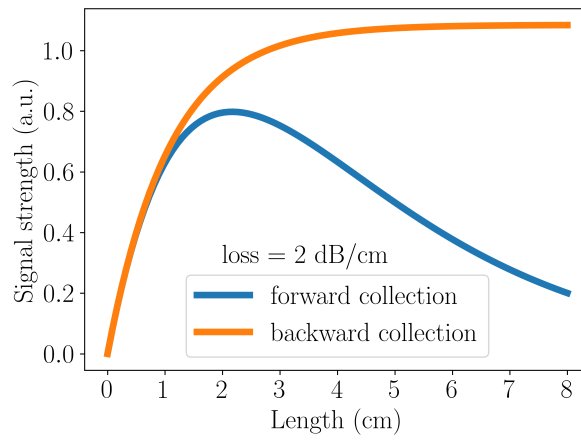


Figure 3.11: The evolution of the Stokes power in the backward-collection and forward-collection configurations.

3.5.2 Stimulated Raman Scattering in Waveguides

Now we have a look at the evolution of SRS in waveguides, where two lasers are coupled into the waveguides. Suppose the signal beam is coupled into the waveguide at $z = 0$ and it is propagating along $+z$. The SRS can take place with two different configurations as shown in Fig. 3.12. (a) In the first scenario, the pump beam is also coupled into the waveguide at $z = 0$, and it is propagating along $+z$. It is classified as the *co-propagating* configuration. (b) We can also couple the pump into the waveguide at $z = L$. It is referred to as the *counter-propagating* configuration.

3.5.2.1 Co-Propagating Stimulated Raman Scattering

In the co-propagating configuration, the evolution of the signal beam is governed by

$$\frac{dP_s}{dz} = g_{\parallel} P_s(z) P_p(z) - \alpha_s P_s(z), \quad (3.42)$$

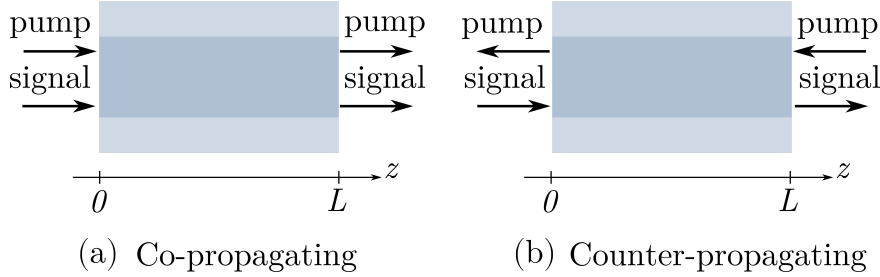


Figure 3.12: Two configurations of waveguide-enabled SRS experiments. (a) In the co-propagating SRS, both pump and signal beams are propagating along the $+z$ direction. (b) In the counter-propagating configuration, the signal beam is propagating along the $+z$ direction while the pump is along the $-z$ direction.

where α_s is the waveguide loss of the pump beam. In practical experimental conditions, it is valid to assume the Raman-induced loss on the pump is negligible. Therefore the evolution of the pump beam can also be written as $P_p(z) = P_p(0)e^{-\alpha_p z}$, where α_p is the waveguide loss of the pump beam. In this case, the evolution of the signal beam can be solved analytically as

$$P_s(z) = P_s(0) \exp\left(g_{\parallel} P_p(0) \frac{1 - e^{-\alpha_p z}}{\alpha_p} - \alpha_s z\right). \quad (3.43)$$

The optical power of the signal beam leaving the waveguide at $z = L$ is given by

$$P_s(L) = P_s(0) \exp(g_{\parallel} P_p(0) L_{\text{eff}} - \alpha_s L), \quad (3.44)$$

where *effective length* L_{eff} is introduced as

$$L_{\text{eff}} = \frac{1 - e^{-\alpha_p L}}{\alpha_p}. \quad (3.45)$$

3.5.2.2 Counter-Propagating Stimulated Raman Scattering

In the counter-propagating configuration, we assume that the signal beam is still injected into the waveguide at $z = 0$. The pump beam, however, is coupled into the waveguide at $z = L$. Ignoring the Raman-induced loss on the pump, we have

$$P_p(z) = P_p(L)e^{-\alpha_p(L-z)}, \quad \frac{dP_s}{dz} = g_{\parallel} P_s(z) P_p(z) - \alpha_s P_s(z). \quad (3.46)$$

The evolution of the optical power of the signal beam $P_s(z)$ can be solved analytically, and it is given by

$$P_s(z) = P_s(0) \exp\left(g_{\parallel} P_p(L) \frac{e^{-\alpha_p L}(e^{\alpha_p z} - 1)}{\alpha_p} - \alpha_s z\right). \quad (3.47)$$

At the output facet at $z = L$, the optical power of the signal beam is then

$$P_s(L) = P_s(0) \exp(g_{\parallel} P_p(L) L_{\text{eff}} - \alpha_s L), \quad (3.48)$$

where the definition of effective length is given in Eq. (3.45). Unlike spontaneous Raman scattering, we can immediately notice that the signal beam experiences the same amplification in both co-propagating and counter-propagating configurations. It suggests that we can choose the configuration that is easier to implement. Note that this conclusion might not be valid when Kerr nonlinearity, carrier effect, and nonlinear losses are taken into account. If we take into account these nonlinear effects, it has been shown in a silicon waveguide [17] that the signal beam in co-propagating configuration can have a slightly higher intensity.

Due to the weakness of the Raman effect, the power of the signal beam can be approximated as

$$\begin{aligned} P_s(L) &= P_s(0)(1 + g_{\parallel} P_p(L) L_{\text{eff}}) \exp(-\alpha_s L) \\ &= P_s(0) \exp(-\alpha_s L) + P_s(0) g_{\parallel} P_p(L) L_{\text{eff}} \exp(-\alpha_s L). \end{aligned} \quad (3.49)$$

Here we utilize the relation that $\exp(x) \approx 1 + x$ for $x \rightarrow 0$. Eq. (3.49) suggests that the signal beam leaving the waveguide can be viewed as a summation of two components. Only the second term on the right-hand side contains Raman information embedded in g_{\parallel} . This situation is different from spontaneous Raman scattering in Eq. (3.38) and Eq. (3.41). In spontaneous Raman scattering, all the photons at the shifted frequencies carry Raman information. As we will discuss in Chapter 5, the Raman-independent component in the SRS experiments proves to be quite detrimental. We have to take care to separate the Raman-independent component from the Raman-dependent one.

3.6 Conclusion

In this chapter, we re-introduced spontaneous Raman scattering and SRS from a quantum perspective. We first examined the Raman scattering in a bulk medium. Later the treatment is extended to waveguides. We studied theoretically and numerically the spontaneous and stimulated Raman gain coefficients G_{\parallel} , g_{\parallel} of IPA-clad silicon nitride waveguides. We also examined various experimental configurations. For waveguide-enabled spontaneous Raman scattering, we concluded it is always advantageous to collect the backward-propagating signal if it is allowed by experimental conditions. In the case of SRS, however, the signal beam experiences the same amplification in counter-propagating and co-propagating configurations. Therefore we can choose the either of the configuration based on experimental conditions.

References

- [1] David J. Griffiths. *Introduction to Quantum Mechanics*. Pearson Education International, second edition edition, 2005.
- [2] Marlan O. Scully and M. Suhail Zubairy. *Quantum Optics*. Cambridge University Press, 1997.
- [3] Marc Eichhorn and Markus Pollnau. *Spectroscopic Foundations of Lasers: Spontaneous Emission Into a Resonator Mode*. IEEE Journal of Selected Topics in Quantum Electronics, 21(1), January–February 2015.
- [4] Ji-Xin Cheng and Xiaoliang Sunney Xie, editors. *Coherent Raman Scattering Microscopy*. CRC Press, 2013.
- [5] Ashim Dhakal. *Nanophotonic Waveguide Enhanced Raman Spectroscopy*. PhD thesis, Ghent University, 2016.
- [6] Frédéric Peyskens. *Surface Enhanced Raman Spectroscopy Using a Single Mode Nanophotonic-Plasmonic Platform*. PhD thesis, Ghent University, 2016.
- [7] Pieter Wuytens. *Surface-Enhanced Raman Spectroscopy for Intracellular Sensing and Protease Activity Detection: From Chip Technology to Applications*. PhD thesis, Ghent University, 2017.
- [8] David Alan Wardle. *Raman scattering in optical fibres*. PhD thesis, The University of Auckland, 1999.
- [9] Isaac Freund. *Comment on Angular Dependence of Raman Scattering Intensity*. The Journal of Chemical Physics, 53(7):2989–2989, 1970.
- [10] T. C. Damen, R. C. C. Leite, and S. P. S. Porto. *Angular Dependence of the Raman Scattering from Benzene Excited by the He-Ne cw Laser*. Physical Review Letters, 14(1):9–11, Jan 1965.
- [11] S. P. S. Porto. *Angular Dependence and Depolarization Ratio of the Raman Effect*. Journal of the Optical Society of America, 56(11):1585–1589, November 1966.
- [12] Ashim Dhakal, Ananth Z. Subramanian, Pieter Wuytens, Frédéric Peyskens, Nicolas Le Thomas, and Roel Baets. *Evanescent excitation and collection of spontaneous Raman spectra using silicon nitride nanophotonic waveguides*. Optics Letters, 39(13):4025–4028, June 2014.

- [13] A Stoffel, A Kovács, W Kronast, and B Mller. *LPCVD against PECVD for micromechanical applications*. Journal of Micromechanics and Microengineering, 6(1):1–13, March 1996.
- [14] A. Z. Subramanian, P. Neutens, A. Dhakal, R. Jansen, T. Claes, X. Rottenberg, F. Peyskens, S. Selvaraja, P. Helin, B. Du Bois, K. Leyssens, S. Severi, P. Deshpande, R. Baets, and P. Van Dorpe. *Low-Loss Singlemode PECVD Silicon Nitride Photonic Wire Waveguides for 532-900 nm Wavelength Window Fabricated Within a CMOS Pilot Line*. IEEE Photonics Journal, 5(6):2202809, December 2013.
- [15] Ashim Dhakal, Ali Raza, Frédéric Peyskens, Ananth Z. Subramanian, Stéphane Clemmen, Nicolas Le Thomas, and Roel Baets. *Efficiency of evanescent excitation and collection of spontaneous Raman scattering near high index contrast channel waveguides*. Optics Express, 23(21):27391–27404, October 2015.
- [16] Govind P. Agrawal. *Nonlinear Fiber Optics*. Academic Press, 2013.
- [17] C. M. Dissanayake, I. D. Rukhlenko, M. Premaratne, and G. P. Agrawal. *Raman-Mediated Nonlinear Interactions in Silicon Waveguides: Copropagating and Counterpropagating Pulses*. IEEE Photonics Technology Letters, 21(19):1372–1374, October 2009.

4

From Coherent Anti-stokes Raman Spectroscopy to Supercontinuum Generation

In Chapter 1 we mentioned that waveguides could significantly increase the interaction volume between optical fields and analytes, which leads to an enhanced Raman signal. In Chapter 2, we suggested that the Raman signal can also be dramatically enhanced by exciting the molecules with two laser beams coherently. In Chapter 3 we had a closer inspection of stimulated Raman scattering (SRS) and drew a connection between waveguide-based SRS and waveguide-based spontaneous Raman scattering. Since waveguide-based spontaneous Raman spectroscopy has been investigated on dielectric waveguides and plasmonic structures [1, 2], Chapter 3 provides a solid theoretical foundation to study waveguide-based SRS.

Starting from this chapter, we will investigate if we can leverage both waveguiding enhancement and coherent excitation signal enhancement mechanisms simultaneously on an integrated silicon nitride platform. The first part of this chapter is devoted to coherent anti-Stokes Raman spectroscopy (CARS). We will show that silicon nitride waveguides possess strong chromatic dispersion over the therapeutic window (700 nm to 900 nm). This dispersion make it infeasible to produce the anti-Stokes component efficiently over a broad spectral range. In waveguide-based CARS, we can only choose strong CARS signals or broadband operation. This trade-off considerably limits the applicability of waveguide-based CARS technique. We believe new waveguide designs and experimental configurations are

needed before we can demonstrate CARS on a silicon nitride waveguide, which is unfortunately beyond the scope of this thesis.

Although the quest for on-chip CARS is not successful, our study on the chromatic dispersion of silicon nitride waveguides opens up new potential for silicon nitride nonlinear optics. Based on the Kerr nonlinearity of a silicon nitride waveguide itself, a wealth of nonlinear optical phenomena are enabled. Supercontinuum generation (SCG) pumped below $1\ \mu\text{m}$ is one of the examples. SCG on silicon nitride waveguides provides us with a unique opportunity to deliver an integrated, broadband, and high-brightness source for integrated biophotonic applications and precise metrology. In the second part of this chapter, we shift our focus from CARS to SCG. We first introduce the underlying mechanisms of SCG on a silicon nitride waveguide with the help of the nonlinear Schrödinger equation (NLSE). We show that dispersion-engineered silicon nitride waveguides that possess anomalous group velocity dispersion below $800\ \text{nm}$ are suitable for SCG extending to the blue range of the visible spectrum. Using a $100\ \text{fs}$ pulse laser, we then demonstrate for the first time an octave-spanning supercontinuum covering the visible-to-near-IR spectral range in a 1-cm -long dispersion-engineered waveguide.

4.1 Phase-Matching Condition for CARS in Silicon Nitride Waveguides

We showed at the end of Chapter 2 that the intensity of the newly generated anti-Stokes component $I(\omega_{as})$ is related to the wave-vector mismatch Δk as

$$I(\omega_{as}) \propto \text{sinc}^2\left(\frac{\Delta k L}{2}\right), \quad (4.1)$$

where $\Delta k = \Delta \mathbf{k} \cdot \hat{\mathbf{z}} = (2\mathbf{k}_p - \mathbf{k}_s - \mathbf{k}_{as}) \cdot \hat{\mathbf{z}}$. Ideally, we expect to operate at the situation the wave-vector mismatch vanishes $\Delta k = 0$. However, the perfect phase-matching is not always necessary, and the requirement of $\Delta k = 0$ can actually be relaxed. It is clear from Eq. (4.1) that the anti-Stokes component can be generated efficiently when the wave-vector mismatch is small enough $\Delta k \approx 0$.

To quantify the impact of wave-vector mismatch on phase-mismatch, it is convenient to introduce a new parameter called *coherence length* L_{col} . The coherence length is customarily defined as $L_{\text{col}} = 2\pi/\Delta\kappa$, where $\Delta\kappa$ is the maximal mismatch that can be tolerated. It is important to emphasize that the exact value of $\Delta\kappa$ varies for different applications. In CARS, it is desirable to have a certain level of flatness in the recorded anti-Stokes spectrum. Otherwise, it is troublesome to extract the Raman information. As a result, not without arbitrariness, we require the anti-Stokes component to stay within the full-width-half-maximum (FWHM)

of the sinc^2 function. In this case, we have

$$\begin{aligned} \text{sinc}^2 \frac{\Delta k L}{2} &> 0.5, \\ \Rightarrow L_{\text{col,CARS}} &= \frac{2.78}{\Delta \kappa}. \end{aligned} \quad (4.2)$$

In the study of the phase-matching condition, it proves to be rather cumbersome to keep track of Δk as a summation of three different wave-vectors. To handle the phase-mismatch more efficiently, we expand the wave-vectors of the anti-Stokes beam and the Stokes beam as Taylor series at the pump frequency $\omega = \omega_p$. They are given by

$$k(\omega_s) = k(\omega_p) + \beta_1(\omega_s - \omega_p) + \frac{\beta_2}{2}(\omega_s - \omega_p)^2 + \dots, \quad (4.3)$$

$$k(\omega_{as}) = k(\omega_p) + \beta_1(\omega_{as} - \omega_p) + \frac{\beta_2}{2}(\omega_{as} - \omega_p)^2 + \dots, \quad (4.4)$$

where β_i is the i -th order chromatic dispersion of k at the pump frequency and it is given by $\beta_i = \partial^i k / \partial \omega^i$. We soon notice that β_1 and β_2 are actually relevant to the group velocity and the group velocity dispersion at the pump frequency

$$\beta_1 = \left. \frac{\partial k}{\partial \omega} \right|_{\omega=\omega_p} = \frac{1}{v_g(\omega_p)}, \quad (4.5)$$

$$\beta_2 = \left. \frac{\partial^2 k}{\partial \omega^2} \right|_{\omega=\omega_p} = \frac{\partial}{\partial \omega} \frac{1}{v_g(\omega_p)}. \quad (4.6)$$

Inserting Eq. (4.3) and Eq. (4.4) into the definition of Δk , we can express the wave-vector mismatch as a function of chromatic dispersion as

$$-\Delta k = \beta_2 \Delta \omega^2 + \frac{\beta_4}{12} \Delta \omega^4 + \text{higher-order terms}, \quad (4.7)$$

where we have used the relation $\omega_{as} - \omega_p = \omega_p - \omega_s = \Delta \omega$. In a first approximation, we assume the dispersive property of a waveguide is mostly determined by $\beta_2 \Delta \omega^2$. In this case, the coherence length of CARS is given by

$$L_{\text{col,CARS}} = \frac{2.78}{|\beta_2| \Delta \omega^2}. \quad (4.8)$$

Apparently the coherence length is related to the group velocity dispersion β_2 and the frequency of the Raman mode $\Delta \omega$. In practice, most Raman modes with bio-significance fall within the range from 500 cm^{-1} to 1500 cm^{-1} (or 15 THz to 45 THz). In order to record the CARS signal over the entire range, Eq. (4.8) indicates that the group velocity dispersion of a 1-cm-long waveguide at the pump frequency ω_p should be smaller than

$$|\beta_2|_{\text{max}} = \frac{2.78}{L_{\text{WG}} \times \Delta \omega^2} = \frac{2.78}{1 \text{ cm} \times (2\pi \times 45 \text{ THz})^2} = 3.5 \text{ ps}^2/\text{km}. \quad (4.9)$$

4.2 Group Velocity Dispersion of Silicon Nitride Waveguides

We learned from the previous section that efficient CARS requires small group velocity dispersion at the pump frequency. The waveguide can have either normal dispersion or anomalous dispersion yet the absolute value of the group velocity dispersion β_2 should be smaller than $3.5 \text{ ps}^2/\text{km}$. In deriving this number, we assume the waveguide is 1 cm long, and the furthest Raman mode locates at 1500 cm^{-1} . In this section, we will investigate if this requirement can be fulfilled in silicon nitride waveguides.

To estimate the overall group velocity dispersion of a silicon nitride waveguide, we should take into account both material dispersion and geometry dispersion. (a) The refractive indices of dielectric materials vary with wavelengths $n(\omega)$, and this variation causes the group velocity to change. Therefore we expect dielectric materials themselves exhibit group velocity dispersion. This type of group velocity dispersion is an intrinsic property of materials and it is classified as *material dispersion*. (b) The wave-guiding effect can also induce group velocity dispersion. This effect can be easily understood for single-mode waveguides. In a single-mode waveguide, optical beams with different wavelengths usually have distinct mode profiles. As the waveguide cladding has a lower refractive index than the core, different mode profiles result in a varying effective indices. Since the effective index characterizes the phase velocity of a guided mode, this wavelength-dependent phase velocity will, in turn, induce a change in the group velocity. Because the geometry of the waveguide determines this type of group velocity dispersion, it is called *geometry dispersion*. Sometimes this dispersion is also called *waveguide dispersion*, highlighting that this dispersion is a result of the wave-guiding effect. It is imaginable that a small variation in the geometry of a high-index-contrast waveguide can significantly modify the mode profile of a guided mode and induce substantial geometry dispersion.

Apart from β_2 , another quantity, D , is also commonly used to characterize the group velocity dispersion in the literature. The definition of D is given by

$$D = -\frac{2\pi c}{\lambda^2} \frac{\partial^2 k}{\partial \omega^2} = -\frac{2\pi c}{\lambda^2} \beta_2. \quad (4.10)$$

Unfortunately, the numerical values of D and β_2 have opposite signs. In order to avoid confusion, the terminology of normal and anomalous dispersion are widely used. Normal dispersion means $D < 0$ (or $\beta_2 > 0$) while anomalous dispersion means $D > 0$ (or $\beta_2 < 0$). The requirement of $|\beta_2| < 3.5 \text{ ps}^2/\text{km}$ corresponds to $|D| < 10 \text{ ps}/(\text{nm km})$ at 800 nm . In this work, we will use β_2 , and it has a dimension of $[\text{s}^2/\text{m}]$.

4.2.1 Material Dispersion of Silicon Nitride

Let us first have a look at the material dispersion of silicon nitride. We knew in Chapter 3 that silicon nitride thin films can be deposited via either plasma-enhanced chemical vapor deposition (PECVD) or low-pressure chemical vapor deposition (LPCVD). Figure 4.1 shows the material dispersion $\beta_{2,M}$ of bulk silicon nitride deposited through LPCVD and PECVD processes. Both types of silicon nitride are taken from the batch of BioSiN2 of the BioPIX platform. To obtain the group velocity dispersion, we first measure the refractive index of a 300-nm-thick silicon nitride thin film with a commercial ellipsometer. The spectral variation of refractive index $n(\omega)$ is then fitted with a 6-order polynomial. The group velocity dispersion is derived from this polynomial. It is clear that both types of silicon nitride exhibit strong normal dispersion ($\beta_{2,M} > 100 \text{ ps}^2/\text{km}$) from 550 nm to 1200 nm. Since the material dispersion is much stronger than the desired overall dispersion ($|\beta_2| < 3.5 \text{ ps}^2/\text{km}$), the material dispersion should be balanced by the waveguide dispersion.

It is noteworthy that LPCVD silicon nitride has weaker group velocity dispersion over the range from 500 nm to 1200 nm. Besides, the LPCVD nitride has a slightly higher refractive index. This increased refractive index make it slightly easier for us to obtain anomalous dispersion in LPCVD silicon nitride waveguides. As a result, we will focus on this type of nitride for the rest of this chapter.

We should also point out that a silicon nitride thin film tends to crack when it gets thicker than 400 nm [3] due to strain. Although thicker silicon nitride layers are available with special treatments [3, 4], in this work the thickness of silicon nitride is limited below 300 nm. We are limited by the fabrication infrastructure accessible to us.

4.2.2 Waveguide Dispersion of Silicon Nitride Waveguides

In this section, we will investigate the waveguide dispersion for typical silicon nitride waveguides. It is important to emphasize that, unless explicitly mentioned, the material dispersion of silicon nitride and silicon dioxide have already been taken into account in all the results presented in the rest of this chapter.

We first investigate the waveguide dispersion of strip waveguides. The structure of a strip waveguide is shown in Fig. 3.3. In Fig. 4.2, we show the group velocity dispersion of strip waveguides at various heights h . We sweep h from 200 nm to 500 nm by steps of 50 nm. The width of the waveguide is fixed to 800 nm. In Fig. 4.2, a thinner waveguide has a darker color. The group velocity dispersion of both TE (left) and TM (right) modes is shown in this figure. We can see that a thicker (lighter color) silicon nitride core always contributes to anomalous dispersion for both modes. At small h , both modes possess strong normal dispersion, while the dispersion of the TM mode is much stronger. When the waveguide

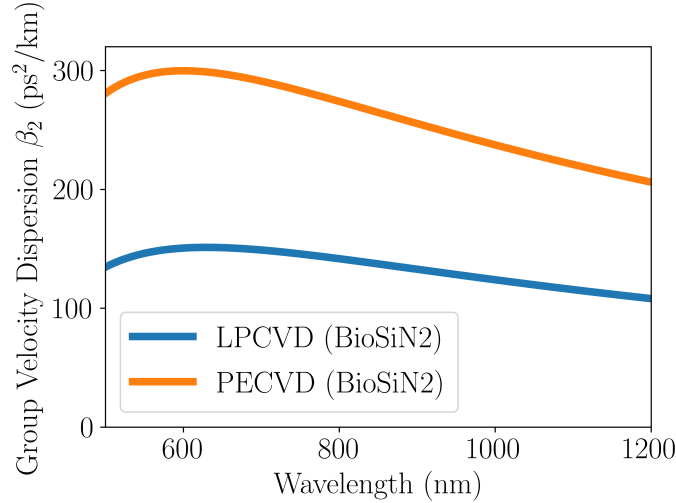


Figure 4.1: The material dispersion $\beta_{2,M}$ for silicon nitride deposited by PECVD and LPCVD techniques. We can see for this specific batch of silicon nitride (BioSiN2), the one deposited by LPCVD has much weaker normal dispersion.

uide core gets thicker, both modes exhibit anomalous group velocity dispersion for wavelengths above 850 nm, and the dispersion of both modes is comparable. Therefore, it is evident that we should go for thick silicon nitride to mitigate the problem of phase-mismatch. The thickest silicon nitride accessible in the BioPIX platform is 300 nm. With this thickness, we can reduce the absolute value of the group velocity dispersion.

We then investigate the impact of the waveguide width w . We fix the height of the waveguide to 300 nm and sweep the width of the waveguide w from 400 nm to 1000 nm with a step of 100 nm. The result is shown in Fig. 4.3. In this figure, we show the dispersion of the TE (left) and the TM modes (right). In this figure, a narrower waveguide has a darker color in the figure.

The first thing we notice is that the TM mode always possesses substantial normal dispersion and the value of this dispersion decreases monotonously with increasing waveguide widths w . The situation of the TE mode is a bit more complicated. Taking $\lambda = 785$ nm for example, the group velocity dispersion first decreases and then increases with increasing w . The minimal dispersion at $\lambda = 785$ nm is obtained when w is around 500 nm. However, it is also clear that we cannot engineer the waveguide to possess small dispersion that its absolute value is lower than $3.5 \text{ ps}^2/\text{km}$ for wavelength below 960 nm.

We have explained in Chapter 1 that most modern Raman spectroscopes utilize excitations at 785 nm, and we do not want to deviate too much from this wave-

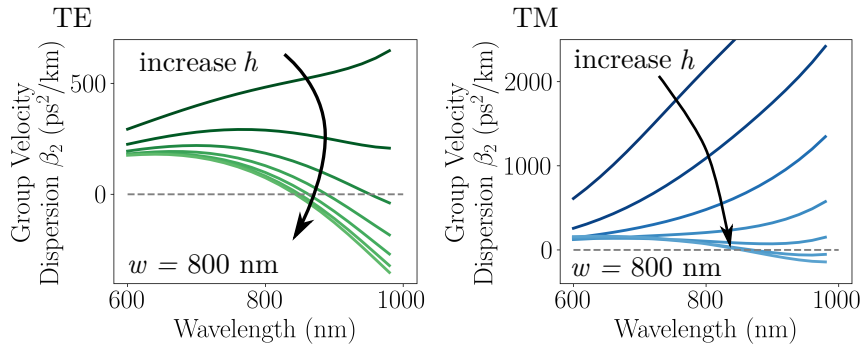


Figure 4.2: The group velocity dispersion of both TE (left) and TM (right) modes of silicon nitride strip waveguides of different heights. The height of the waveguide h varies from 200 nm to 500 nm by steps of 50 nm. The width of the waveguide is fixed to 800 nm. A thinner waveguide has a darker color in the figure.

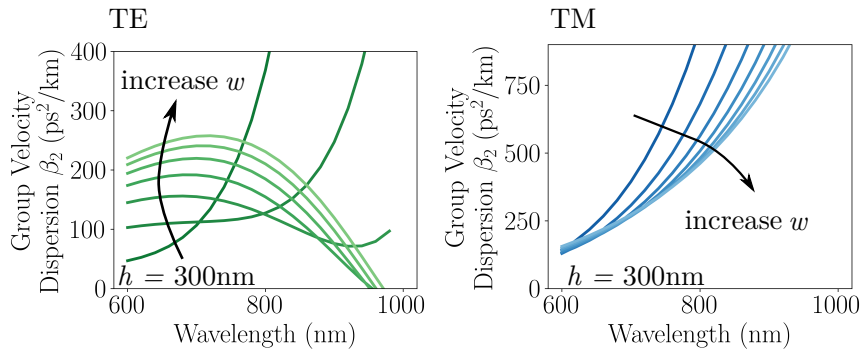


Figure 4.3: The group velocity dispersion of both TE (left) and TM (right) modes in silicon nitride strip waveguides of different widths. The width of the waveguide w varies from 400 nm to 1000 nm by a step of 100 nm. The height of the waveguide is fixed to 300 nm. A narrower waveguide has a darker color in the figure.

length. However, Figure 4.2 and Figure 4.3 indicate that we cannot engineer the waveguide to possess the desired small dispersion around this wavelength. Fortunately, it has been predicted and demonstrated in Ref. [5, 6] that suspended waveguides might help us to obtain small dispersion at short wavelengths. Inspired by these works, we investigate the impact of underetching on dispersion. The results are shown in Fig. 4.4. Here we consider only the TE mode. We show the dispersion of three different types of waveguides: (a) a normal strip waveguide that is underclad with a buried oxide (BOX) layer, (b) a strip waveguide with parts of its BOX layer removed and (c) a fully suspended strip waveguide with all of its BOX layer removed. We assume the width of the waveguide is 550 nm and the thickness is 300 nm. The first thing we notice in Fig. 4.4 is that a fully suspended strip waveguide (type (c)) has anomalous dispersion over the whole frequency range from 600 nm to 900 nm while a normal strip waveguide (type (a)) has normal dispersion over the same frequency range. Therefore, it is not surprising that gradual removal of the under-cladding pushes the group velocity dispersion from the normal regime to the anomalous regime. It is clear from Fig. 4.4 that if we remove 120 nm of the BOX layer on both sides of the waveguide, we can have relatively low dispersion around 785 nm. Indeed, it is possible to obtain arbitrarily small group velocity dispersion over the whole frequency range from 600 nm to 900 nm by removing its BOX layer gradually. Therefore we can indeed perform CARS with this types of underetched waveguides.

In the previous discussion, we have mostly focused on air-clad waveguides. It is noteworthy that Raman spectroscopy is commonly utilized to probe bio-relevant samples. Since a large number of bio-samples either exist in a liquid environment or are themselves liquids, it is essential for our Raman sensor to be compatible with liquids. Without loss of generality, we assume that the samples are dissolved in water. In this case, the silicon nitride waveguide is top- and side-covered with water, whose refractive index is 1.3.

The group velocity dispersion of the TE mode of water-clad samples is shown in Fig. 4.5. In this case, underetching is not able to bring the group velocity dispersion into the anomalous regime. Both waveguides possess strong normal dispersion over the whole therapeutic window from 700 nm to 900 nm. It suggests that we cannot obtain group velocity dispersion below $150 \text{ ps}^2/\text{km}$ waveguides accessible via BioPIX when they are covered with water.

The results shown in Fig. 4.4 and Fig. 4.5 indicate that we can indeed engineer β_2 to an arbitrarily small number around 785 nm if the waveguides are air-clad. As a result, if we consider only β_2 in the phase-matching condition, we can indeed perform CARS experiment in a 1-cm-long waveguide to probe Raman modes up to 45 THz for gas samples whose refractive indices are close to unity. However, for liquid-clad waveguides, a broadband CARS operation can only be achieved in much-shorter waveguides. This restriction on length will inevitably limit the

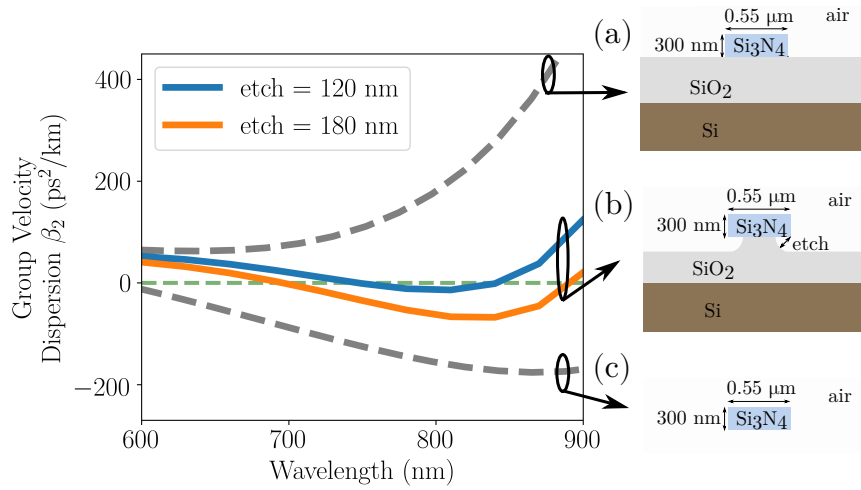


Figure 4.4: The group velocity dispersion of the TE mode in three different waveguide designs. (a) A conventional silicon nitride strip waveguides that is side- and top-clad with air and under-clad with silicon dioxide. (b) Two strip waveguides with 120 nm (blue solid) and 180 nm (red solid) of their BOX layer etched away. (c) A fully suspended strip waveguides with all of its BOX layer removed.

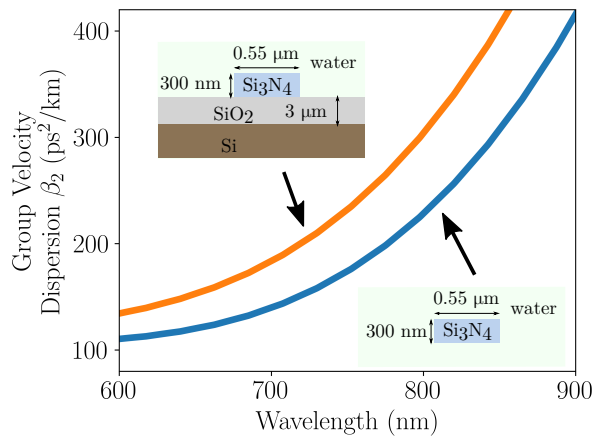


Figure 4.5: The group velocity dispersion of the TE mode of water-clad waveguides with (blue curve) and without (red curve) the BOX layer.

achievable signal intensity. Since an important motivation of waveguide-based Raman sensing is to enhance the signal by the wave-guiding effect, it is unwise to pose limitations on the waveguide length.

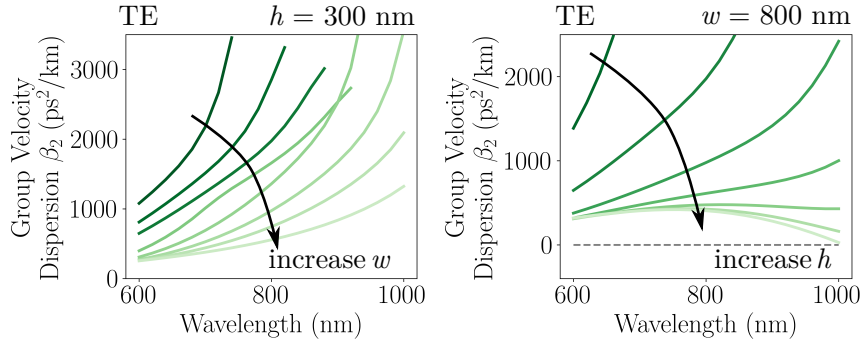


Figure 4.6: The group velocity dispersion of the TE mode of slot waveguides with different widths and heights. (Left) The waveguide width w varies from 600 nm to 1.3 μm with a resolution of 100 nm. The height is fixed to 300 nm and the slot gap is 150 nm. A darker color implies a narrower waveguide. (Right) The height h sweeps from 200 nm to 800 nm with a resolution of 100 nm. The width is fixed to 800 nm and the slot gap is 150 nm. A darker color implies a thinner waveguide.

To conclude this section, we would like to take a look at the group velocity dispersion of slot waveguides shown in Fig. 3.3. For the vertical slot waveguides we consider in this thesis, the electric field of the TE mode is highly confined within the slot region of the waveguide, which leads to an enhanced light-matter interaction and therefore a stronger Raman signal. To benefit from this E-field enhancement, we will consider only the TE mode in this section. Figure 4.6 shows the group velocity dispersion of slot waveguides with various widths and heights. It is important to note that the width of the slot g (see Fig. 3.3 and Fig. 4.7) of these waveguides is assumed to be 150 nm, which is limited by the fabrication processes accessible to us.

On the left-hand side of Fig. 4.6, the height of the slot waveguides is fixed to 300 nm. The width of the waveguide is scanned from 600 nm to 1.3 μm with a resolution of 100 nm. We can see that a wider waveguide tends to have weaker normal group velocity dispersion. However, for a fixed height of 300 nm the group velocity dispersion is always very strong ($> 250 \text{ ps}^2/\text{km}$) if we are pumping at 785 nm. On the right-hand side of Fig. 4.6, the width of the slot waveguides is fixed to 800 nm. We sweep the height of the waveguide from 200 nm to 800 nm with a resolution of 100 nm. It is clear that a thicker waveguide has weaker dispersion, yet it is also very strong ($> 250 \text{ ps}^2/\text{km}$) around 785 nm. Therefore, it is ill-advised to use slot waveguides for CARS. Although the optical field has more extensive overlap with analytes, the interaction length within slot waveguides is

seriously limited.

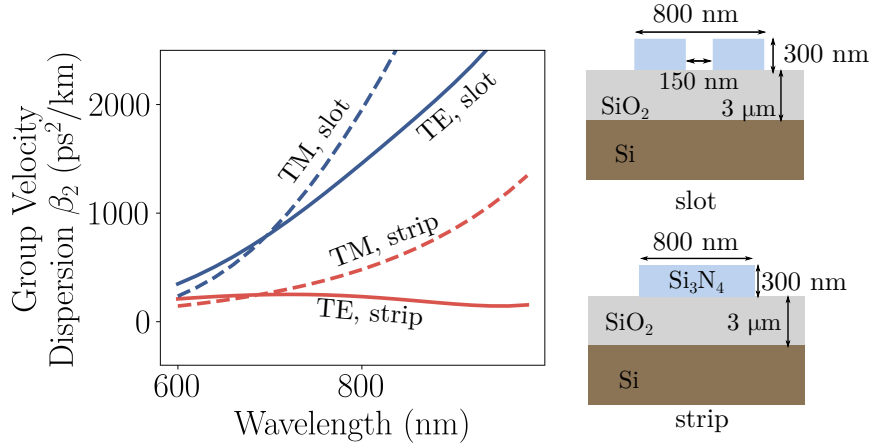


Figure 4.7: (Left) The group velocity dispersion of both TE and TM modes of a slot waveguide and a strip waveguide. (Right) The structure of the slot and the strip waveguide.

In Fig. 4.7, we compare the group velocity dispersion of a typical slot waveguide and a strip waveguide. We can quickly notice that both modes of the slot waveguide have a much stronger normal distribution than their strip counterparts. As a result, if the waveguide length is the fixed, slot waveguides have a much-reduced CARS bandwidth as compared to strip waveguides. It reaffirms that slot waveguides should not be considered for CARS applications.

4.2.3 Impact of Higher-Order Dispersion

In the previous discussion, we have only considered the group velocity dispersion β_2 explicitly. We show that the group velocity dispersion of underdetuned strip waveguides can be reduced to zero. It is then tempted to think that CARS can be performed over an infinite bandwidth. However, we should point out that the contribution of higher-order dispersion (β_4, β_6, \dots) cannot be ignored when β_2 vanishes. The higher-order dispersion will limit the CARS bandwidth when we are pumping close to the wavelengths where β_2 vanishes. In the literature of nonlinear optics [7], these wavelengths where β_2 vanishes are also called *zero-dispersion wavelengths (ZDWs)*. The higher-order dispersion might also help suppress β_2 if the waveguide is properly design [8, 9]. In this section, we will investigate the CARS bandwidth with the higher-order dispersion taken into account.

To illustrate the influence of higher-order dispersion, we take the waveguide shown in the inset of Fig. 4.8 for example. Suppose the geometry of the waveguide is $h \times w = 300 \text{ nm} \times 550 \text{ nm}$. Below the silicon nitride core, 120 nm of the BOX

layer. The overall dispersion of this waveguide is shown in Fig. 4.8. We can see this waveguide has two ZDWs at 775.5 nm and 861.4 nm respectively.

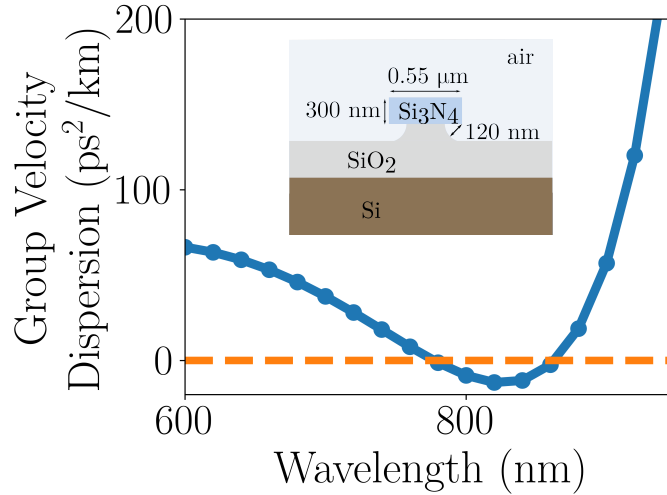


Figure 4.8: The group velocity dispersion of the TE mode of a silicon nitride strip waveguide. The dimension of the silicon nitride core is $h \times w = 300 \text{ nm} \times 550 \text{ nm}$ and 120 nm of the silicon dioxide under-cladding is removed.

If the pump is tuned to the vicinity of one of the ZDW, in the first order approximation that only β_2 is taken into account, we expect the CARS to have an infinite bandwidth. To illustrate this point, we assume two lasers — a pump beam at λ_p and a signal beam at λ_s are coupled into a 1-cm-long silicon nitride waveguide, and we calculate the normalized CARS signal at λ_{CARS} . The impact of phase-mismatch through $\text{sinc}^2(\Delta k L/2)$ is plotted in Fig. 4.9 for various pump wavelengths λ_p . The horizontal axis is the pump wavelength, and the vertical axis is the frequency shift of the CARS wavelength λ_{CARS} or the signal wavelength λ_s from the pump wavelength λ_p . The dimension of the frequency shift is $[\text{cm}^{-1}]$.

It is noteworthy that we do not explicitly require $\lambda_s > \lambda_p > \lambda_{\text{CARS}}$ in Fig. 4.9. The case of $\lambda_s < \lambda_p < \lambda_{\text{CARS}}$ corresponds to coherent Stokes Raman spectroscopy (CSRS) signal which is also dependent on $\text{sinc}^2(\Delta k L/2)$ [10]. We can see the FWHM of CARS indeed goes to infinity in the vicinity of the ZDWs.

If we consider the dispersion up to the 6th order in $\text{sinc}^2(\Delta k L/2)$, Fig. 4.9 becomes Fig. 4.10. It is clear the CARS bandwidth is greatly reduced to approximately 1700 cm^{-1} when the higher-order dispersion is taken into account. The CARS bandwidth at wavelengths where β_2 is non-vanishing is not significantly altered by the inclusion of higher-order dispersion.

To conclude this section, we take a look at the CARS bandwidth of a con-

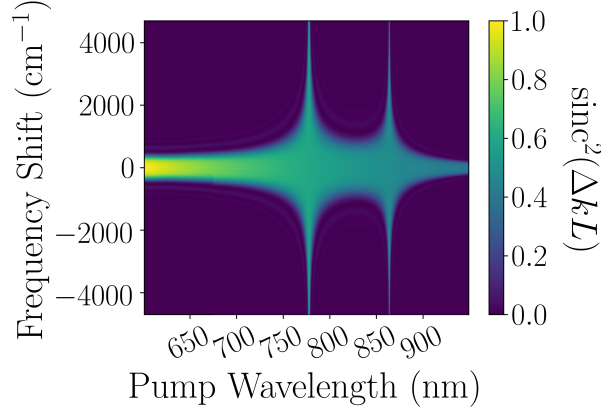


Figure 4.9: The CARS bandwidth of the TE mode of a 1-cm-long strip waveguide with an underetching of 120 nm. The CARS bandwidth is obtained by calculating $\text{sinc}^2(\Delta kL/2)$ for various pump wavelength. Only the group velocity dispersion β_2 is taken into account.

ventional silicon nitride strip waveguide without underetching. Its silicon nitride core has the same dimension as it is shown in Fig. 4.8 and it is also air-clad. The CARS bandwidth of a 1-cm-long non-dispersion-engineered waveguide at various pump wavelengths is given in Fig. 4.11. In this figure, chromatic dispersion up to the 6th order is taken into account. We can see the CARS bandwidth is limited to 180 cm^{-1} , which is too small for any Raman mode with bio-significance. It reaffirms that conventional strip waveguides cannot deliver the desired CARS bandwidth.

4.2.4 Possible Paths Towards On-Chip CARS

From the previous discussion, we can conclude that

1. An air-clad waveguide can be engineered to possess anomalous dispersion around 785 nm through underetching. Although this type of waveguides is still not suitable for bulk liquid CARS detection, it can nevertheless be used for gas sensing. Besides, we believe it is also capable of thin-film detection. It is imaginable that if we apply a thin film of analytes on top of the waveguide, its group velocity dispersion β_2 will not be significantly altered. Therefore, the phase-matching condition of CARS is still satisfied. The CARS bandwidth on an air-clad underetched waveguide can be engineered to above 1700 cm^{-1} , which is limited by the contribution of higher-order dispersion. This scenario for thin-film detection, however, might require delicate sample preparation to adhere the thin-film onto the waveguide.
2. If we would like to perform bulk liquid sensing with CARS in a 1-cm-

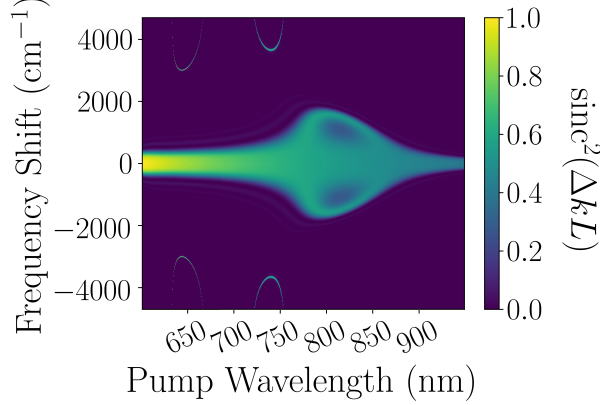


Figure 4.10: The CARS bandwidth of the TE mode of a 1-cm-long strip waveguide with an underetching of 120 nm. The CARS bandwidth is obtained by calculating $\text{sinc}^2(\Delta kL/2)$ for various pump wavelength. Chromatic dispersion up to the 6th order is taken into account.

long waveguide, one solution to the phase-mismatch is to balance β_2 with higher-order dispersion $\beta_4, \beta_6, \dots, \beta_{2m}$. This technique is widely used in broadband fiber optical parametric amplifiers [8, 9]. However, it is in practice very challenging to design a water-clad waveguide with a CARS bandwidth above 1500 cm^{-1} . Other methods, including the use of three lasers for non-degenerate CARS configuration [11, 12] and quasi-phase-matching CARS [13, 14] are also capable of extending the CARS bandwidth. However, it is also not trivial to enable CARS over a bandwidth of 1500 cm^{-1} on a water-clad silicon nitride waveguide.

3. The most straightforward method to extend the CARS bandwidth is probably to reduce the waveguide length. Note that the previous discussion is based on the assumption that the waveguide is 1 cm long. If the waveguide length is reduced to $1 \mu\text{m}$, the bandwidth can be enlarged by a factor of 100 if group velocity dispersion β_2 dominates the phase-mismatch. However, the reduction of waveguide length comes with a hefty price. Since the CARS intensity scale with L^2 , a decrease in waveguide length will quickly diminish the achievable CARS intensity. To extend the CARS bandwidth without sacrificing the CARS signal, we believe it is possible to perform surface-enhanced coherent anti-Stokes Raman scattering (SE-CARS). In SE-CARS, plasmonic structures are integrated with the dielectric waveguides. The electric field on the surface of these plasmonic structures is enhanced by orders of magnitude, which leads to a much stronger Raman signal. Therefore one can still expect to obtain a strong CARS signal with a much shorter plas-

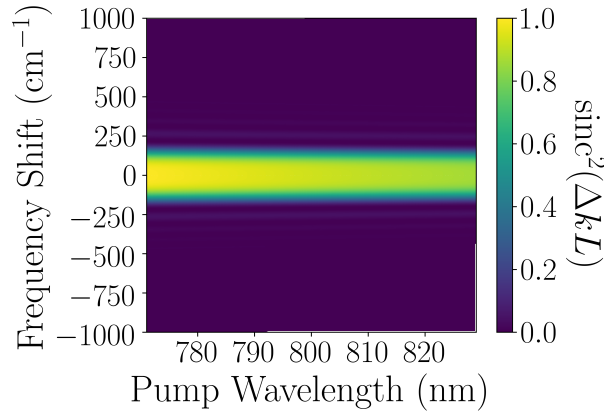


Figure 4.11: The CARS bandwidth of the TE mode of a 1-cm-long strip waveguide without underetching. The cross-section of the silicon nitride core is also $h \times w = 300 \text{ nm} \times 550 \text{ nm}$. The CARS bandwidth is obtained by calculating $\text{sinc}^2(\Delta kL/2)$ for various pump wavelengths. Chromatic dispersion up to the 6th order is taken into account.

monic structure. The plasmonic structures, however, can in general only be defined with challenging electron-beam lithography processes and it constitutes a research topic on its own.

In short, silicon nitride waveguides accessible to us always possess strong group velocity dispersion around 785 nm. Besides, the silicon nitride waveguide has a modest index contrast between the silicon nitride core and the cladding. As a result, it is difficult to satisfy the phase-matching condition for CARS around 785 nm. The problem of phase-matching is more troublesome when the analytes are dissolved in water. In this case, CARS-on-chip cannot be carried out by merely adjusting the dimensions of silicon nitride waveguides where the height is limited below 300 nm. The failure in satisfying the phase-matching limits the obtainable CARS intensity. This trade-off between bandwidth and signal intensity renders CARS ineffective, especially for aqueous samples. As Raman spectroscopy is widely used for biological applications, the limitation of CARS for aqueous samples severely limits the scope of its applications.

It is noteworthy that waveguide-based CARS suffers from another limitation that the CARS bandwidth becomes susceptible to the refractive index of analytes. As a result, we can have two distinct CARS spectra if we dissolve the same amount of solute in two solvents with different refractive indices. Or if we dissolve an analyte in the same solvent but with concentrations, we might also have distinct Raman spectra, unless the refractive indices of the solvent is the same as the analyte. Such artefacts make it challenging to interpret the CARS spectra. Therefore, we believe novel methods and techniques are required to combine CARS with silicon

nitride waveguides.

4.3 Supercontinuum as a Broadband Light Source

Although the quest for on-chip CARS proves to be unsuccessful, we find that a silicon nitride waveguide can possess anomalous dispersion below $1\ \mu\text{m}$. This anomalous dispersion proves to be quite valuable. It allows one to explore third-order nonlinear processes below $1\ \mu\text{m}$ in silicon nitride waveguides, which greatly extends the wavelength range of nonlinear silicon nitride photonics. Supercontinuum generation (SCG) is one of the examples enabled by this technique, and it provides us with an integrated, broadband and high-brightness source. This on-chip broadband source can enable a plenitude of applications including spectroscopy [15], optical coherence tomography [16] and precise frequency metrology [17]. For instance, this broadband source can be used for multiplex SE-CARS experiments that we have just discussed in the previous section. It is critical to emphasize that the SCG presented in the second part of this chapter is induced by the Kerr nonlinearity rather than the Raman nonlinearity. Besides, we are exploring the nonlinear response of the waveguide core rather than the response of the analytes.

SCG is a nonlinear process in which a laser beam is broadened to a "white-light" source covering a broad spectral range. The study of SCG is pioneered by the work of the Alfano group in 1970 [18] where a broadband light extending from 400 nm to 700 nm is obtained when a narrow band source is injected into a bulk borosilicate glass sample.

After the first demonstration, SCG have been extended to in a miscellaneous of materials, including liquids [19], gases [20] and a collection of fibers, ranging from single mode fibers [21], photonic crystal fibers (PCF) [22] to chalcogenide fibers [23]. A key advantage of fibers is the significant extension of nonlinear interaction length. In bulk medium, the nonlinear interaction only takes places near the focus of the laser beam. In the fiber platform, nonlinear interaction takes place along the whole fiber length. Among these fiber platforms, PCF provides an unprecedented degree of freedom in tailoring the dispersive properties. In combination with its low propagation loss, broadband single-modeness, and relatively high nonlinearity, PCF plays a central role in SCG out of both commercial and academic interest [24].

In the recent years, SCG on the silicon-on-insulator (SOI) platform is gaining momentum due to its compatibility with the CMOS infrastructure. The SOI-based SCG can potentially lead to integrated devices with compact footprints at very low costs. SOI platform has two prominent advantages for SCG: (1) Silicon has a large Kerr nonlinearity n_2 . (2) The SOI waveguide has a large index contrast. This index contrast allows one to engineer the waveguide dispersion to compensate for the material dispersion easily. As a result of these two advantages, a supercontinuum

can be generated with a few Watt of peak pump power within a few centimeters of a silicon waveguide [5, 6, 25–28].

Lately, the utilization of supercontinuum for bio-imaging and molecular detection is drawing research interest. In these applications, a supercontinuum covering the therapeutic window [29] is highly desirable where the tissues exhibit minimal scattering loss and absorption. This supercontinuum can also be used for frequency metrology and OCTs. The visible range, however, is not covered by the SOI-based supercontinuum due to the transparency of silicon.

To extend the supercontinuum down to short wavelengths, silicon nitride and doped silica have attracted significant research interest [30] due to their CMOS compatibility, wide transparency window and negligible two-photon absorption in the therapeutic window. Compared to doped silica, silicon nitride has a higher Kerr nonlinearity n_2 and a higher refractive index n [31]. Therefore, silicon nitride is an up-and-coming platform for SCG below 1 μm .

One problem associated with silicon nitride is its strong material dispersion in the normal regime. We will see in the next section that efficient SCG requires small anomalous dispersion. As a result, we have to introduce enough waveguide dispersion to balance the material dispersion. However, silicon nitride waveguides have only a modest index contrast, making it challenging to introduce the desired geometry dispersion. Besides, a silicon nitride thin film tends to crack when it gets thicker than 400 nm [3]. Based on the results in Fig. 4.2 and Fig. 4.3, it is improbable to engineer the ZDW below 900 nm with thin strip waveguides. As a result of these difficulties, the early attempts to extend supercontinuum to the visible range on the silicon nitride platform utilize pumps at either 1.3 μm [32] or 1.5 μm [33–35]. In these early works, novel waveguide designs [33, 35] and novel physical mechanisms, including cascaded $\chi(2)$ and $\chi(3)$ nonlinear processes [34] are explored. Despite these innovations, the shortest wavelength in these supercontinua cannot go below 665 nm.

It becomes increasingly clear that we should shift the ZDW below 1 μm to extend the supercontinuum beyond 665 nm. Fortunately, our simulation results in Fig. 4.4 suggest that anomalous dispersion can be obtained below 800 nm by removing part of the silicon dioxide under-cladding. Thanks to the underetching technique, we have successfully demonstrated the first visible-to-near-infrared supercontinuum in a 1-cm-long silicon nitride waveguide. We will introduce the details of this work in the rest of this chapter.

It should be mentioned that underetching the waveguide core is not the only method to shift the ZDW to shorter wavelengths. As it is shown in Fig. 4.2, thicker silicon nitride waveguides also have ZDWs at shorter wavelengths. However, advanced fabrication techniques, including crack barrier [3] and in-trench deposition [4], are necessary to prevent the silicon nitride layer from cracking. With these thick waveguides, almost at the same time of our demonstration of the visible-to-

near-infrared supercontinuum, J. Epping *et al* reported a supercontinuum generated in an LPCVD silicon nitride waveguide extending from 470 nm to 2130 nm with a pump lasing at 1064 nm [36]. In their work, a 1- μm -thick silicon nitride waveguide is used thanks to the in-trench deposition technique. In the following years, thick silicon nitride waveguides have also been implemented for coherent SCG with a span over 1.4 octave [37, 38] and a two-octave spanning SCG extending from 526 nm to 2.6 μm [39].

4.4 Mechanisms for Supercontinuum Generation

In this section we shall briefly introduce the mechanism of SCG in a waveguide. SCG can be performed over a broad parameter space. We sometimes group the mechanisms of SCG to two categories based on the group velocity dispersion (β_2) of the waveguide: (i) if we are pumping in the normal dispersion regime, the spectral broadening is mostly prompted by self-phase modulation (SPM) and Raman scattering. (ii) For SCG in the anomalous regime, the spectral broadening is induced mostly by modulation instability (MI) or soliton dynamics.

Although supercontinua generated in the normal dispersion regime tend to have smooth and featureless spectral shapes and a high degree of coherence, their spectral coverage is usually limited. Broad supercontinua are commonly generated by pumping ultra-short pulses in the anomalous dispersion regime. In this regime, two effects might initiate the SCG: soliton dynamics and modulation instability. Of these two mechanisms, soliton dynamics usually induce the broadest supercontinua, and we plan to implement it in our silicon nitride waveguide.

In this section, we will first introduce the concept of soliton, and we will point out that soliton fission and dispersive wave generation play critical roles in SCG. We will also review the differences between SCG initiated by soliton dynamics and MI. The SCG in the normal dispersion region, however, will not be discussed in this thesis. Readers are kindly referred to [7, 24, 40] for more information.

To study the soliton effects, we have to drop our previous assumption that the optical fields are CW or quasi-CW. The temporal shapes of the optical fields need to be considered explicitly. In this regime, an optical pulse is composed of multiple spectral components. Due to chromatic dispersion, each of these spectral components has a different propagation constant within the waveguide. When the pulse is propagating along the waveguide, one component might fall behind or catch up with another component, leading to changes in the temporal profile. This variation in the temporal shape induced by chromatic dispersion is classified as dispersive effect. The dispersive effect, along with Kerr nonlinear effect and self-steepening, can be modeled by a single equation: the Nonlinear Schrödinger

Equation (NLSE) [7, 24], which is given by

$$\frac{\partial E(z, t)}{\partial z} = \underbrace{\sum_{k \geq 2} i^k \frac{\beta_k}{k!} \frac{\partial^k E}{\partial t^k}}_{\text{Linear dispersion}} - \underbrace{\frac{\alpha_{\text{lin}}}{2} E}_{\text{Linear loss}} + \underbrace{i\gamma \left(1 + i\tau_{\text{shock}} \frac{\partial}{\partial t} \right) (|E|^2 E)}_{\text{Nonlinear effects}}.$$

Here $E(z, t)$ is the electric field of the optical pulse. The first term on the right-hand side describes the dispersive effects and β_k is the k -th order chromatic dispersion. The second term models the linear loss of the waveguide. The third term models the nonlinear effects. In this term, γ is the nonlinear coefficient introduced as

$$\gamma = \frac{\omega_0 n_2(\omega_0)}{c A_{\text{eff}}(\omega_0)}, \quad (4.11)$$

where n_2 is the nonlinear refractive index, and $A_{\text{eff}}(\omega_0)$ is the effective area defined as [7, 40]

$$A_{\text{eff}}(\omega_0) = \frac{\left(\iint_{-\infty}^{+\infty} |F(x, y, \omega_0)|^2 dx dy \right)^2}{\iint_{-\infty}^{+\infty} |F(x, y, \omega_0)|^4 dx dy}. \quad (4.12)$$

Here $F(x, y, \omega_0)$ is the transverse mode profile for the guided mode at frequency ω_0 . In Eq. (4.11), we have also taken into account the frequency dependency of the nonlinear coefficient γ through the inclusion of shock waves. The characteristic time scale associated with shock waves is given by $\tau_{\text{shock}} = 1/\omega_0$. However, we omit both free-carrier effect and nonlinear absorption due to their limited influence in large bandgap materials like silicon nitride. We also neglect the Raman contribution because its effect is also limited [41, 42].

4.4.1 Solitons and Soliton Fission

Suppose the higher-order dispersion and the frequency dependency of γ can be ignored in the NLSE, Eq. (4.11) is simplified to

$$\frac{\partial E}{\partial z} + \frac{i\beta_2}{2} \frac{\partial^2 E}{\partial \tau^2} = i\gamma |E|^2 E, \quad (4.13)$$

This equation predicts the existence of a special type of pulse in the anomalous regime. The spectral and temporal shapes of this type of pulse either do not change (fundamental soliton) or change periodically (higher-order soliton) during propagation. For these pulses, the dispersive effect and the nonlinear effect are delicately balanced and these pulses are referred to as *optical solitons*. In this work, we are especially interested in a family of solitons whose field amplitudes are given by

$$E(t) = N E_{\text{fs}} \operatorname{sech}(t/T_0) \exp(-i\omega_0 t), \quad (4.14)$$

where E_{fs} is the amplitude of the fundamental soliton, N is the soliton number and T_0 is the duration of the pulse. The amplitude of the fundamental soliton E_{fs} and soliton number N are also closely related to the nonlinear and the dispersive properties of the waveguide through

$$E_{\text{fs}} = \sqrt{\frac{1}{\gamma L_{\text{D}}}}, \quad N^2 = \frac{L_{\text{D}}}{L_{\text{NL}}}, \quad L_{\text{NL}} = \frac{1}{\gamma P_0}, \quad L_{\text{D}} = \frac{T_0^2}{|\beta_2|}. \quad (4.15)$$

Here L_{D} is dispersion length and L_{NL} is nonlinear length. They characterize the strength of the dispersive effect and the nonlinear effect within a waveguide. We can see the soliton requires a fix relationship between the nonlinearity and the dispersion of the waveguide.

The spectral and temporal evolution of solitons with $N = 1, 2, 3, 4$ are shown in Fig. 4.12. The solution with $N = 1$ in Eq. (4.14) corresponds to the fundamental soliton. Figure 4.12 shows that a fundamental soliton preserves its temporal and spectral shapes during propagation. If we fix the pulse duration T_0 and increase the peak power, we can obtain higher-order solitons with $N > 1$. In general, an N -th order soliton has a peak power N^2 times stronger than that of the fundamental soliton. Unlike the fundamental soliton, higher-order solitons do not preserve their profiles during propagation. Instead, their spectral and temporal shapes vary periodically, which is readily observed in Fig. 4.12. The evolution of higher-order solitons is initially dominated by self-phase modulation (SPM) [7] and it induces a spectral broadening of the pulse. Afterward, the dispersive effect soon catches up and induces a spectral narrowing. This alternation between SPM and the dispersive effect results in a periodic change of the spectral and temporal profiles of the higher-order solitons. This alternation is sometimes called *breathing effect*. The breathing period for all higher-order solitons is the same and it is given by $z = \pi L_{\text{D}}/2$ [7].

In the definition of soliton number N , there is no mechanism to restrict N to be an integer. It is then natural to ask what happens if we launch a pulse with a non-integer N into the waveguide. This is apparently the case for most experiments. Fortunately, it is shown [7] that if the launched pulse has a profile not significantly deviating from the shape of an N -th order soliton, the pulse can adjust its profile gradually and evolves into that N -th order soliton. More precisely, if a secant hyperbolic pulse with a soliton number of N' is launched into the waveguide, the pulse will gradually evolve into an N -th order soliton with $N' = N + \delta$ where $|\delta| < 0.5$.

In the previous discussion, we considered only the group velocity dispersion β_2 in NLSE. However, for ultrashort pulses (less than 5 ps), higher-order dispersion can no longer be ignored. Besides, for ultrashort pulses, we should also consider the frequency dependency of γ explicitly. In the presence of these effects, higher-order solitons turn out to be unstable.

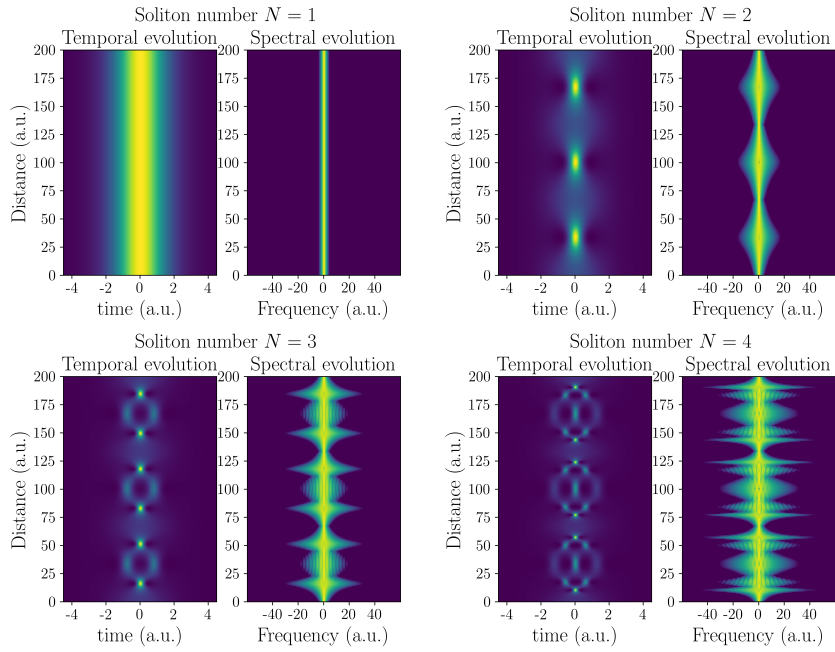


Figure 4.12: The evolution of solitons with $N = 1, 2, 3, 4$ over a distance of three soliton periods. It is evident that although the fundamental soliton retains its temporal and spectral profile over distance, higher-order solitons experience periodic variation over propagation. The period of the variation is the same for all solitons.

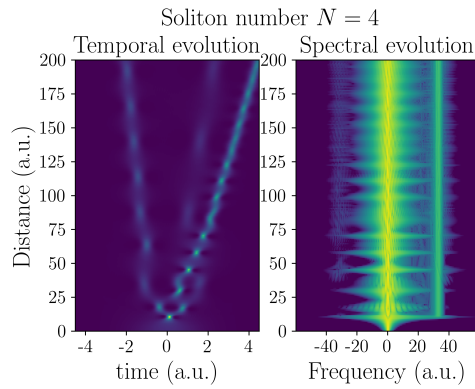


Figure 4.13: The propagation of solitons with $N = 4$ over a distance of three soliton period. β_3 is also included in the simulation. It is evident from the time domain that this soliton cannot retain its periodic variation. It breaks into three separate solitons. In the frequency domain, the output spectrum is much wider than the input spectrum.

A higher order soliton is composed of multiple fundamental solitons. It is the interference between the constituent fundamental solitons that forms a higher-order soliton. Under higher-order perturbations, including Raman effect, higher-order dispersion and higher-order nonlinear effects, a higher-order soliton will break into its constituent fundamental solitons. The break-up of higher-order solitons into multiple fundamental solitons is called *soliton fission*, and it is the primary mechanism for spectral broadening. To illustrate this point, we include the third-order dispersion in Eq. (4.13). In this case, the propagation of a soliton with $N = 4$ is shown in Fig. 4.13. It is evident from the time domain that this soliton cannot retain its periodic variation. It breaks into three separate solitons. In the frequency domain, the output spectrum is much wider than the input spectrum.

Another effect that contributes to SCG is the generation of dispersive waves. When a higher-order soliton breaks up into multiple fundamental solitons, part of the energy sheds away from the fundamental solitons into one or multiple new frequencies [7, 24, 43]. The appearance of the dispersive wave is also visible in Fig. 4.13. In the frequency, an optical wave appear at the frequency of 35 after a propagation distance of $z = 11$. Two theories are widely accepted to explain the emergence of these new optical waves.

In one theory [44], SCG is modeled as a cascaded four-wave mixing (FWM) process. In this theory, a soliton is decomposed into multiple spectral components, and the interaction between all these components through FWM results in the generation of dispersive waves.

In another theory, the dispersive wave generation is treated as Cherenkov radiation [45]. Cherenkov radiation denotes the generation of optical waves when a charged particle travels in a medium with a speed faster than the phase velocity of light within that medium. It is pointed out in [45, 46] that Cherenkov radiation is not limited to charged particles. Fast-moving electrical polarization can also give rise to Cherenkov radiation.

A closer inspection on Eq. (4.13) reveals that the propagation of solitons is given by [7, 45]

$$E(z, t) = N E_{\text{fs}} \operatorname{sech}(t/T_0) \exp(-i\omega_0 t + i(k_{\text{sol}} + \beta_0)z), \quad (4.16)$$

where k_{sol} is sometimes referred to as soliton wave-number and it is given by $k_{\text{sol}} = \gamma P_0/2$. The evolution of a wave at ω_0 is given by $\exp(-i\omega_0 t + i\beta_0 z)$. It is clear that the soliton is propagating “faster” than the guided mode by an extra wave-vector k_{sol} . Similarly, the polarization induced by the soliton is also traveling “faster” than the phase velocity of optical waves in the waveguide, and this polarization will give rise to new radiations. This radiation is the origin of dispersive waves.

In Cherenkov radiation, the propagation direction of the newly generated optical field is determined by the “Cherenkov condition”. The condition is shown in

Fig. 4.14. The radiation is emitted at the ‘‘Cherenkov angle’’ θ that satisfies the condition $\cos \theta = \phi_{\text{DW}}/\phi_{\text{sol}}$. Here ϕ_{DW} and ϕ_{sol} are the phase of the radiation and the soliton accumulated over the same interval t . In a waveguide, however, only the radiation with a vanishing θ can couple into a guided mode, which can be detected at the end of the waveguide. It implies that $\phi_{\text{sol}} = \phi_{\text{DW}}$. This waveguide-coupled radiation is called *dispersive wave* in the literature of SCG. In practice, the requirement of $\phi_{\text{sol}} = \phi_{\text{DW}}$ is widely used to predict the exact location of the dispersive wave.

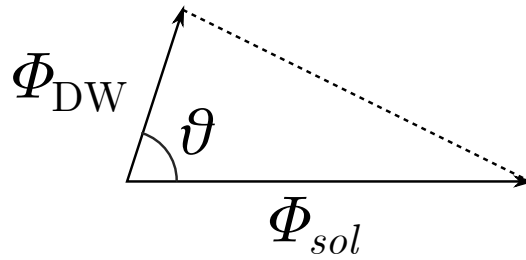


Figure 4.14: The ‘‘Cherenkov condition’’ for dispersive wave generation. DW stands for dispersive wave. The ‘‘Cherenkov angle’’ θ is determined by the phases of the soliton ϕ_{sol} and dispersive wave ϕ_{DW} accumulated over an interval of t .

The phases of the dispersive wave and the soliton at location z and time $t = z/v_g$ are given by [7]

$$\phi(\omega_{\text{DW}}) = \beta(\omega_{\text{DW}})z - \omega_{\text{DW}}(z/v_g), \quad (4.17)$$

$$\phi(\omega_{\text{sol}}) = \beta(\omega_{\text{sol}})z - \omega_{\text{sol}}(z/v_g) + \frac{1}{2}\gamma P_{\text{sol}}z, \quad (4.18)$$

where $v_g \equiv \beta_1$ is the group velocity of the soliton, ω_{DW} and ω_{sol} are the phases of the dispersive wave and the soliton respectively, P_{sol} is the peak power of the soliton and γ is the nonlinear coefficient. The dispersive wave emerges at the frequency such that $\phi(\omega_{\text{DW}}) = \phi(\omega_{\text{sol}})$. It means

$$\beta(\omega_{\text{DW}}) = \beta(\omega_{\text{sol}}) + \beta_1(\omega_{\text{DW}} - \omega_{\text{sol}}) + \frac{1}{2}\gamma P_{\text{sol}}. \quad (4.19)$$

To predict the location of the dispersive wave, we expand $\beta(\omega_{\text{DW}})$ at the soliton frequency ω_{sol} and define $\Omega = \omega_{\text{DW}} - \omega_{\text{sol}}$. If we take into account only the second and the third order chromatic dispersion β_2 and β_3 , we have

$$\beta_2\Omega^2 + \frac{\beta_3}{3}\Omega^3 - \gamma P_{\text{sol}} = 0, \quad (4.20)$$

The frequency shift of the dispersive wave is then given by

$$\Omega = -\frac{3\beta_2}{\beta_3} + \frac{\gamma P_{\text{sol}}\beta_3}{3\beta_2^2}. \quad (4.21)$$

We can see the location of the dispersive wave depends on the sign of β_2 and β_3 . For SCG in waveguides, we often encounter the situation that $\beta_2 < 0$ and $\beta_3 > 0$. In this case, Ω is also positive, implying that the dispersive wave is generated in the blue-shift region ($\Omega = \omega_{\text{DW}} - \omega_{\text{sol}} > 0$) compared to the pump frequency. It is also noteworthy that Ω is usually beyond the anomalous regime, and that is the reason why the dispersive wave constitutes an essential mechanism for extending the supercontinuum towards shorter wavelengths.

4.4.2 Modulation Instability and Soliton Dynamics

In the previous section, we have introduced the concept of soliton number N . The soliton number turns out to be useful to predict the dominating physical mechanism for spectral broadening. In general, for pulses with a soliton number much larger than one but still not too large ($N \gg 1$), spectral broadening is dominated by soliton dynamics. For pulses with a large soliton number ($N \gg 10$), the spectral broadening is caused by modulation instability, as the characteristic length of soliton fission $L_{\text{fiss}} = L_{\text{D}}/N \propto T_0$ increases quickly with the pulse duration T_0 . In the latter case, modulation instability (MI) is the dominant process for spectral broadening. MI is a process where an optical pulse spontaneously turns into a modulated beam or even a pulse train. MI is also explained in the context of degenerate four-wave mixing. In the frequency domain, MI can be seen as the spontaneous generation of sidebands on both sides of the pump and the central frequency of sidebands can be predicted via

$$2k_p = k_1 + k_2 + 2\gamma P, \quad (4.22)$$

$$2\omega_p = \omega_1 + \omega_2, \quad (4.23)$$

where ω_1 and ω_2 are the central frequencies of the sidebands, k_1 and k_2 are their propagation constants respectively. Once a long pulse turns into a modulated pulse or separate pulses, further broadening might follow. Especially, when picosecond pulses are launched into a waveguide, MI is capable of breaking the pulses into multiple sub-pulses with small soliton numbers. These short pulses might usher in again the soliton dynamics to further broaden the spectrum. However, in general, SCG initiated by MI is not as broad as the one initiated by soliton dynamics. It is also noteworthy that the sidebands are indeed amplified from background noise. As the background noise is chaotic, the spectral shape of the supercontinuum initiated by MI varies from pulse to pulse. As a result, the coherence of supercontinuum initiated by MI is usually lower. In view of these drawbacks, in this work, we will focus on SCG initiated by soliton dynamics [24].

4.5 Waveguide Fabrication and Dispersion Engineering

As we have shown in the previous section, the existence of solitons requires anomalous group velocity dispersion. However, on the silicon nitride platform, we conclude with extensive simulations that this anomalous dispersion is challenging to obtain by merely adjusting the width of the waveguides if the height of the waveguide is limited below 300 nm. Fortunately, Figure 4.4 suggests that we can remove the silicon oxide partly underneath the Si_3N_4 waveguide core to obtain anomalous dispersion with a 300-nm-thick waveguide.

Our silicon nitride waveguide is fabricated with deep UV lithography at imec. A 300-nm-thick silicon nitride film is grown via LPCVD on a 1.6 μm BOX layer. It is noteworthy that the BOX thickness is not fully optimized in this work and a thickness of 1.6 μm is barely enough [47] to avoid any significant substrate leakage. The waveguide is defined with reactive-ion etching (RIE). The waveguide has a nominal cross-section of $h \times w = 300 \text{ nm} \times 500 \text{ nm}$ and a length of 1 cm.

We remove part of the silica under-cladding with diluted hydrofluoric acid (HF) to engineer the dispersion. It is noteworthy that LPCVD silicon nitride is the natural choice for our SCG due to its high resistance to HF. In practice, the etching selectivity between SiO_2 and LPCVD Si_3N_4 is found to be 200 : 1.

The HF solution is prepared by mixing 1 part of HF (40 %) with 40 part of de-ionized water. The etching rate of the specific silicon dioxide under-cladding we are using is around 7 nm/min at room temperature. The whole chip is dipped into the diluted HF solution for around 20 min to remove 150 nm of the buried oxide. A schematic cross-section of the waveguide is shown in Fig. 4.15(a) and an Scanning Electron Microscope (SEM) picture is shown in Fig. 4.15(b). As the silicon nitride core is also attacked by HF, the process of underetching might increase the surface roughness of the silicon nitride waveguide. To investigate the impact on waveguide losses, we characterize the waveguide loss after underetching with a commercial supercontinuum source (NKT superK EXR-4) in a cutback measurement. The waveguide loss is shown in Fig. 4.16. The waveguide loss from 650 nm to 850 nm is about 11 dB/cm. As a reference, the waveguide loss before etching is 4 dB/cm

To confirm the validity of our simulation of β_2 , we first measure the waveguide group velocity dispersion with the interferometric method described in [5]. The waveguide has a nominal cross-section of $h \times w = 300 \text{ nm} \times 600 \text{ nm}$ and 150 nm of the oxide cladding is removed. The result is shown in Fig. 4.17 as the green curve. Each green dot corresponds to one measurement point. For comparison, we also plot the simulated β_2 of this waveguide as the blue curve in Fig. 4.17. We can see the experimental value slightly deviates from the simulation. This deviation might arise from inaccurate waveguide dimensions. Both silicon nitride and silicon dioxide have a strong charging effect when inspected under the SEM. As

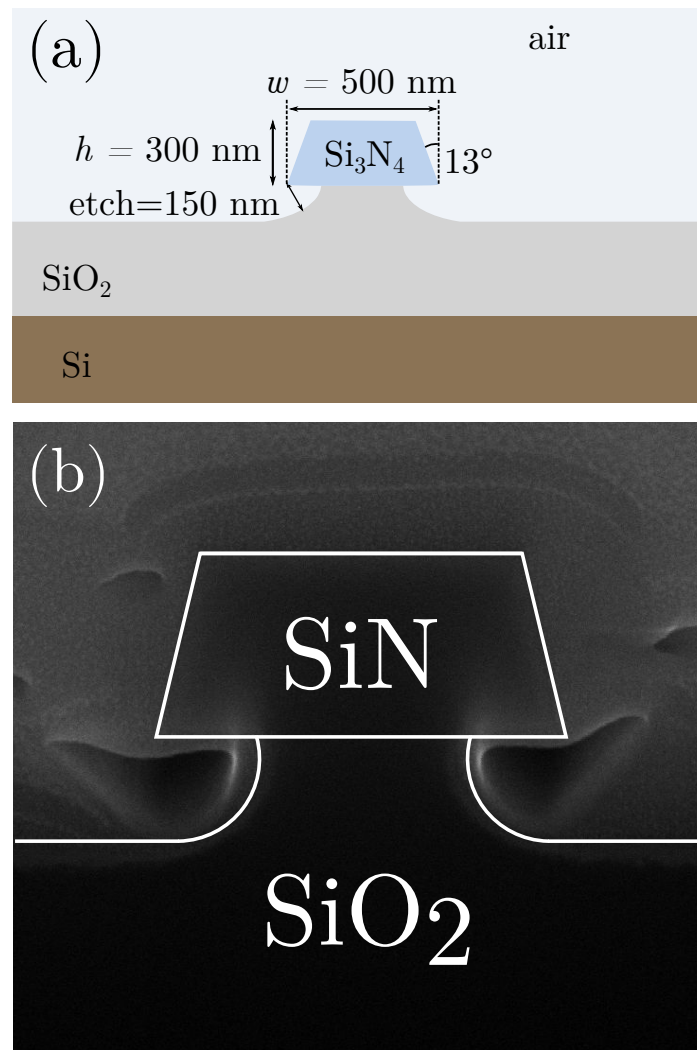


Figure 4.15: (a) Schematic cross-section of the waveguide. (b) Scanning Electron Microscope (SEM) picture of the waveguide cross-section. The cross-section is preparing by sectioning the silicon nitride waveguide core with focused ion beam (FIB). The material around the silicon nitride core is deposited during FIB to enhance image contrast.

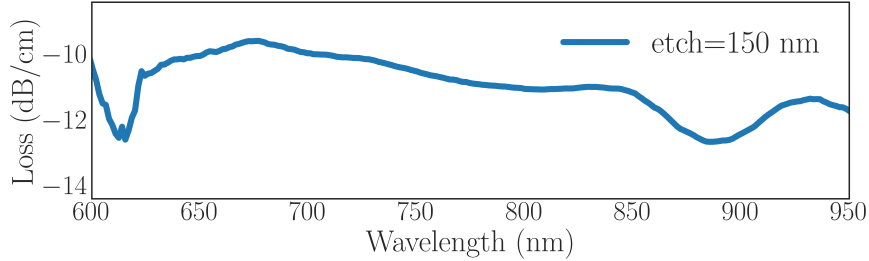


Figure 4.16: The spectrum of propagation loss of an underetched waveguide from 600 nm to 950 nm.

a result, the contrast between silicon nitride and silicon dioxide is blurry, making it difficult to determine precisely the height of the waveguide. Besides, the exact amount of silicon dioxide removed below the waveguide core is also difficult to quantify precisely. Therefore, it is highly possible that the fabricated waveguide is thicker than design. Indeed, if the height is $h = 315$ nm, the simulation result (red dashed curve) exhibits a good agreement with the experimental value as shown in Fig. 4.17.

Taken into this uncertainty in waveguide height, we simulate the group velocity dispersion of the fundamental quasi-TE mode of a dispersion-engineered waveguide. The simulation is performed via a full vectorial mode solver (FIMMWAVE), and the result is shown in Fig. 4.18. Note that the side-wall angle and the under-etching step are taken into account in this result. The waveguide we design for SCG has an etching depth of 150 nm, resulting in anomalous dispersion between 740 nm and 907 nm. The impact of the uncertainty in waveguide height (± 15 nm) is also included in the simulation, which is shown as the gray area in Fig. 4.18. We should emphasize that an uncertainty of 10 nm in height is within the fabrication tolerance of BioSiN2.

The increased confinement also enhances the nonlinearity of the waveguide by reducing the mode area. We estimate the effective nonlinearity to be $7/(W \text{ m})$ at 795 nm given a nonlinear index $n_2 = 24 \times 10^{-20} \text{ m}^2/\text{W}$ [31].

4.6 Setup for Supercontinuum Generation

Figure 4.19 shows the experimental setup for SC generation. We use a pulse train generated by a Ti:Sapphire laser (Mai Tai, Spectra-Physics) operating at 795 nm as pump. The pulses have a nominal squared hyperbolic secant shape in the temporal domain with an FWHM of 100 fs and a repetition rate of 80 MHz. To ensure the excitation of the fundamental TE mode of the waveguide, a combination of a half-wave plate and a polarizing-beam-splitter is used. The pump is coupled into

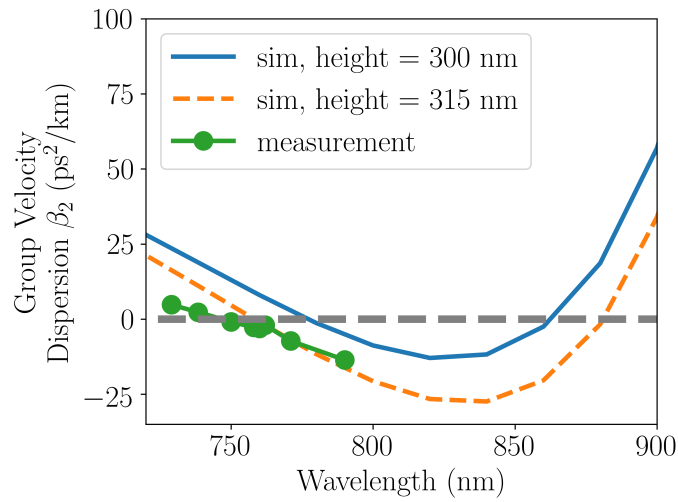


Figure 4.17: The measured group velocity dispersion of a waveguide with a nominal cross-section of $h \times w = 300 \text{ nm} \times 600 \text{ nm}$ (green curve). For comparison, the group velocity dispersion obtained in simulation are also shown for waveguides with a nominal cross-section of $h \times w = 300 \text{ nm} \times 600 \text{ nm}$ (blue solid curve) and a nominal cross-section of $h \times w = 315 \text{ nm} \times 600 \text{ nm}$ (red dashed curved). An underetching of 150 nm is taken into account in all these waveguides.

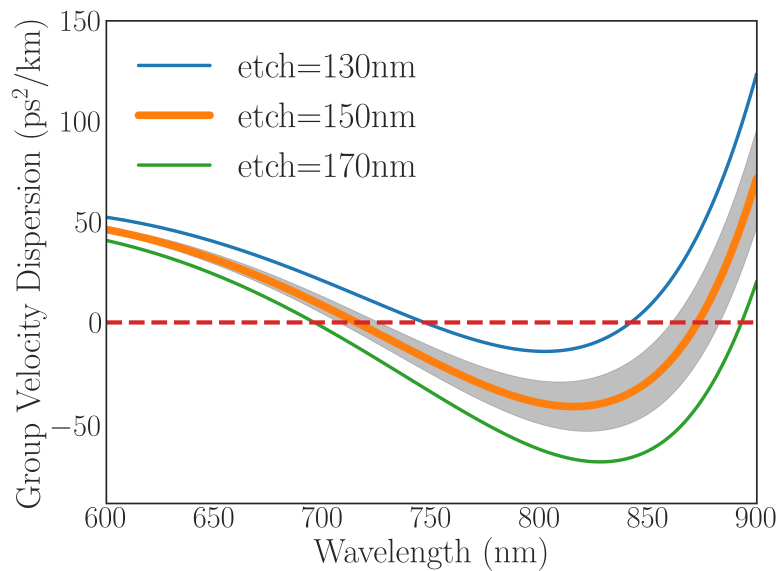


Figure 4.18: Group velocity dispersion of Si_3N_4 waveguides with various etching depths. The impact of an uncertainty in waveguide height of $\pm 10 \text{ nm}$ is shown as the gray area.

the waveguide using a microscope objective (40X, NA = 0.5) and the generated spectrum is coupled out with a lensed fiber (NA = 0.2). The coupling loss at the input is measured to be 8.5 dB. We use an optical spectrum analyzer (450 nm - 1050 nm , Advantest Q8381A) to record the generated spectrum.

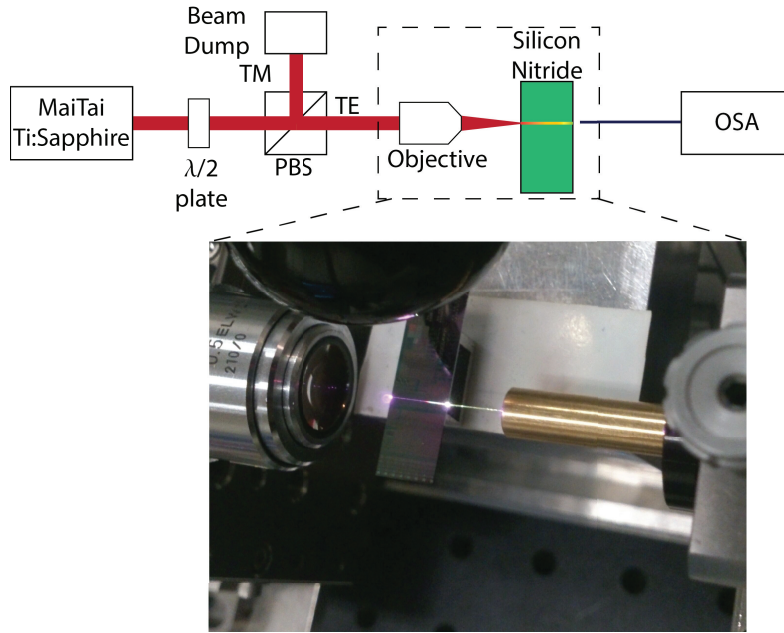


Figure 4.19: Setup for SCG in an underetched silicon nitride waveguide. We can clearly observe that visible light is generated within the waveguide.

4.7 Demonstration of the First Visible-to-near-infrared Supercontinuum in a Silicon Nitride Waveguide

Figure 4.20 shows the measured spectra at various input powers coupled into the waveguide. The peak powers are shown on the left of the spectra, and the average powers are shown on the right. At the lowest peak power of 62 W, the spectral width is the same as the input pulse. At 182 W, small ripples emerge in the center of the pulse, which is attributed to self-phase modulation (SPM) if we remember the breathing effect of higher-order solitons. At 491 W we see two peaks emerge at 917 nm and 495 nm. As we will show later, these peaks can be attributed to dispersive waves. When the power is further increased the dispersive wave centered at 917 nm red-shifts to 937 nm while the one at 495 nm virtually retains its spectral position. At the maximal available coupled power of 874 W, the -30 dB

bandwidth spans 492 nm from 488 nm to 978 nm, slightly more than an octave. From Fig. 4.19 one can see visible red light generated right after the input. The intensity of the red light increases along the propagation direction. Further increasing the power would help improve the spectral homogeneity yet we are limited by the damaging threshold of the input facet of the waveguide. To ensure no spectral broadening takes place in the collection fiber, we deliberately misaligned the lensed fiber both vertically and horizontally at the output facet to reduce the power of the spectra recorded in the OSA by 20 dB at the same coupling angle, and we observe no change in the shape of the spectrum. It implies that the spectrum experiences negligible broadening within the collection fiber.

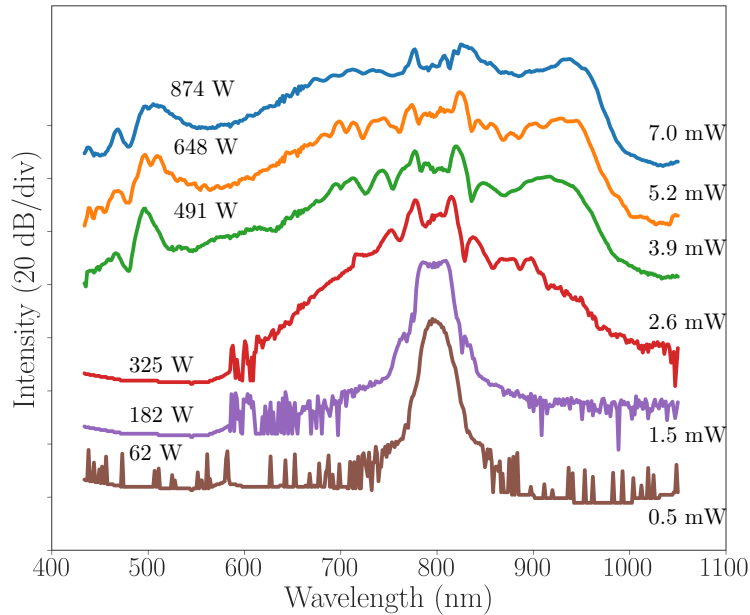


Figure 4.20: Output spectra from the waveguide at various pump levels. The peak power of the pump beam is shown on the left and the average input power is shown on the right to the output spectra. Each spectrum is shifted by 20 dB vertically for clarity.

To gain an insight into the physical mechanisms behind the spectral broadening, we model the SCG with the NLSE given in Eq. (4.11). The NLSE is numerically solved with the split-step Fourier algorithm.

To solve the NLSE, we need to know the dispersive and nonlinear parameters. We have pointed out that the dispersion of a waveguide is difficult to quantize precisely due to the uncertainty in waveguide height. As a result, an uncertainty of

10 nm in the waveguide height is included in Fig. 4.18. Besides, it is suggested [5] that we can obtain an excellent agreement between simulation and experiments for β_2 and β_3 by fine-tuning the waveguide height. However, the prediction for higher-order dispersion (β_4 - β_6) might deviate from the experimental results. The sign of the higher-order dispersion in simulation should nevertheless be the same as their experimental counterparts.

To reflect these observations, in solving the NLSE, we vary β_2 and β_3 simultaneously according to the thickness of the waveguide. For higher-order dispersion, we use the simulated data as a starting point and gradually vary their numbers to obtain a good agreement between simulation and experiments. The dispersion of a silicon nitride waveguide with nominal cross-section of $h \times w = 310 \text{ nm} \times 500 \text{ nm}$ and $h \times w = 290 \text{ nm} \times 500 \text{ nm}$ are given in Table. 4.1. The dispersion we used to obtain the spectrum in Fig. 4.21 is shown in the last column in Table. 4.1.

Dispersion	310 nm \times 500 nm	290 nm \times 500 nm	Final simulation
β_2 (ps ² /km)	-50	-26	-32
β_3 (ps ³ /km)	-12	-26	-23
β_4 (ps ⁴ /km)	-9×10^{-4}	-1.2×10^{-3}	-8×10^{-4}
β_5 (ps ⁵ /km)	-1.2×10^{-6}	-1.2×10^{-6}	-7×10^{-8}
β_6 (ps ⁶ /km)	1×10^{-7}	1×10^{-7}	7×10^{-9}

Table 4.1: The chromatic dispersion of waveguides with nominal cross-sections of 310 nm \times 500 nm and 290 nm \times 500 nm. The chromatic dispersion used in the NLSE to obtain the blue curve in the top panel of Fig. 4.21 is shown in the last column.

The peak power of the input P_{sol} , the waveguide loss α_{lin} and the FWHM of the pulse $T_{\text{FWHM}} = 1.763T_0$ are fixed parameters. The first two parameters are directly measured, and the last parameter is taken from the specifications of the laser. The nonlinearity γ , however, is not measured for this specific type of silicon nitride waveguide and it is treated as a flexible parameter. It is estimated to be $7 \text{ W}^{-1} \text{ m}^{-1}$. Due to the uncertainty in Kerr nonlinearity n_2 , we allow it to vary up to $\pm 30\%$. Finally, we also allow the pulses injected into the waveguide to be slightly chirped [48, 49]. The chirp is mainly included to explain the deviation of the measured laser linewidth from the specifications. We know from theory [7, 48, 49] that the time-bandwidth product of a sech^2 pulse is 0.44. However, the measured time-bandwidth product is slightly larger than that. To account for this difference, we allow the pulse to be slightly chirped with $C = 0.15$. This chirp parameter modifies the optical field of the sech^2 pulses by $\exp(-iCt^2/2T_0^2)$ where T_0 is the duration of the pulse. Note that the T_0 is different from the FWHM of a pulse T_{FWHM} by a factor of 1.763.

With the parameters shown in Table. 4.2 and Table. 4.1, the evolution of a pulse along the underetched waveguide is shown in Fig. 4.21. In the top panel of

parameters	Values
Peak power	874 W
Center wavelength	795 nm
Pulse duration (FWHM) Δt	100 fs
Nonlinearity γ	$5 \text{ W}^{-1} \text{ m}^{-1}$
Linear Chirp C	0.15

Table 4.2: The parameters used to simulate the SCG in an underetched silicon nitride waveguide. The result is presented in Fig. 4.21.

Fig. 4.21, we compare the output spectrum obtained in simulation and experiment. It reveals a reasonable agreement regarding the general shape.

It is noticeable that the predicted peak power at 495 nm is around 10 dB higher than the experimental result. We attribute this difference to a combination of higher scattering loss and stronger material absorption at the shorter wavelength. The increased loss is reflected in a measurement with a 445 nm laser (Wicked Laser, Spyder 3) where we found the waveguide becomes so lossy that no light could transmit through.

In Fig. 4.21, we can notice two peaks at 500 nm and 960 nm, which are beyond the anomalous dispersion regime extending from 740 nm to 907 nm approximately. We have previously attributed them to dispersive waves. Now it is a good time to have a closer look at them. If these two peaks are indeed dispersive waves, they should satisfy the ‘‘Cherenkov condition’’ given in Eq. (4.19). The ‘‘Cherenkov condition’’ can be re-written as

$$\sum_{n \geq 2}^6 \frac{\beta_n(\omega_{\text{sol}})}{n!} (\omega_{\text{DW}} - \omega_{\text{sol}}) = \frac{\gamma P_{\text{sol}}}{2}, \quad (4.24)$$

where $\beta_n(\omega_{\text{sol}})$ is the n -th order chromatic dispersion at soliton frequency, ω_{DW} is the frequency of the dispersive wave, ω_{sol} is the soliton frequency, and P_{sol} is the soliton power. With a peak soliton power of 874 W and the dispersion shown in Table 4.2, we do expect two dispersive waves around 500 nm and 940 nm respectively, which is in reasonable agreement with the experiment.

An important property of the supercontinuum that is not explored is the stability of the generated supercontinuum, which is usually characterized by the coherence for supercontinuum generated by pulsed sources. We learned from the previous discussion that supercontinuum initiated by soliton dynamics usually has a high degree of coherence while the supercontinuum commenced by MI usually has a poor coherence. Therefore we can estimate the coherence of the generated supercontinuum by the soliton number of the input pulses. The soliton number of the pulse is expected to be

$$N = \sqrt{L_D/L_{\text{NL}}} \approx 21, \quad (4.25)$$

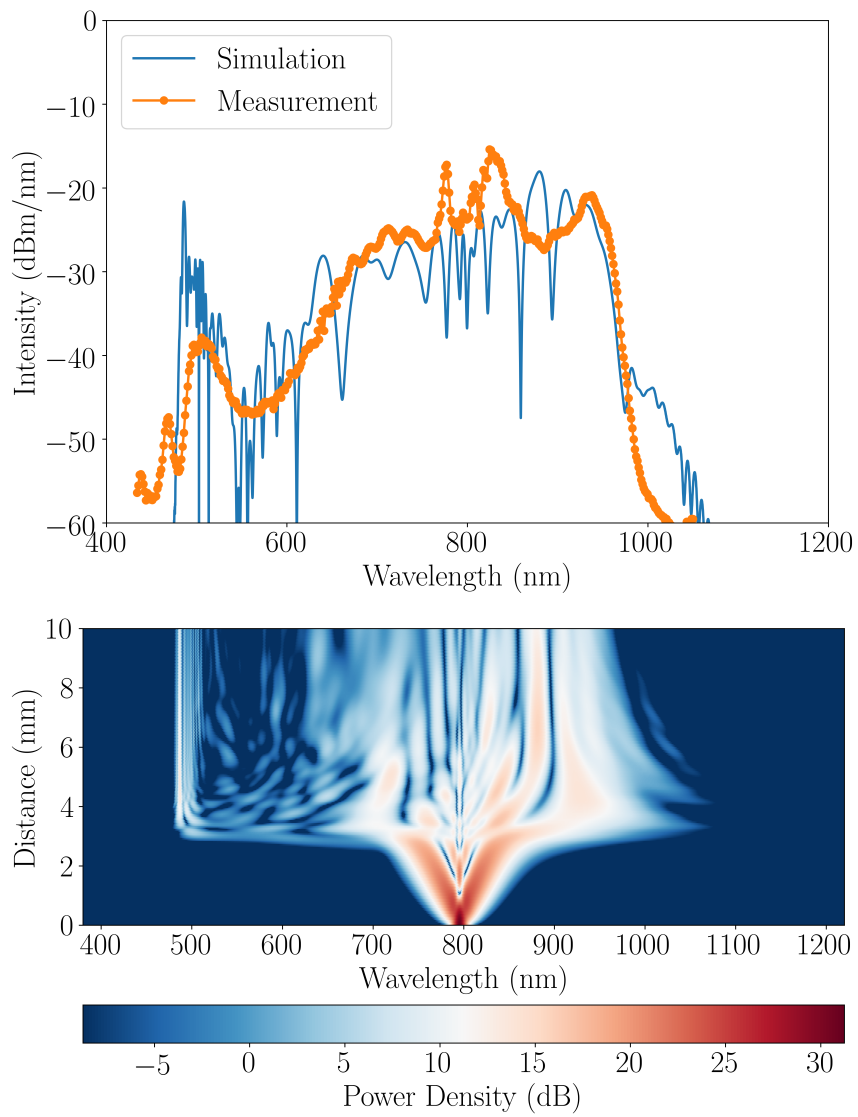


Figure 4.21: (Top) Comparison between measured spectrum and simulation in the output and (below) evolution of the pulse inside waveguide with 874 W input peak power.

where the dispersion length L_D and the nonlinear length L_{NL} are

$$L_D = \frac{T_0^2}{|\beta_2|} = 0.1 \text{ m}, \quad (4.26)$$

$$L_{NL} = \frac{1}{\gamma P_{\text{sol}}} = 2.3 \times 10^{-4} \text{ m}. \quad (4.27)$$

Although no universal condition is established to predict the coherence of the supercontinuum generated with arbitrary initial conditions, a soliton number of 21 implies [24, 40, 50] that the spectral broadening is partly initiated by MI, and it might limit the coherence of the supercontinuum. However, more works in the experiments are needed to determine the coherence of the supercontinuum.

4.8 Conclusion

In this chapter, we have investigated if silicon nitride waveguides can be used for CARS-based Raman sensors. We identified the challenges of phase-matching associated with waveguide-based CARS. If the thickness of the waveguide is limited below 300 nm, it is very challenging to generate an anti-Stokes component over a broad spectral range efficiently. Therefore, we believe the current silicon nitride waveguides accessible to us are not suitable for CARS-based Raman sensors without significant improvements in waveguide designs or experimental configurations.

During our study of waveguide dispersion, we realized anomalous dispersion could be achieved in a Si_3N_4 waveguide by removing partially its silicon dioxide under-cladding. Recognizing the potential of this technique for silicon nitride nonlinear optics, we demonstrated the first octave-spanning SCG covering a large part of the visible spectrum in an partially underetched silicon nitride waveguide. To the best of our knowledge, this work constituted the first visible SCG on an integrated platform, offering a novel compact visible broadband source for Raman spectroscopy, confocal microscopy, optical coherence tomography and precise frequency metrology.

The current demonstration with femtosecond lasers proves to be a bit too costly for many on-chip applications. Besides, an octave-spanning supercontinuum is not always necessary. In the future, we envision to replace the femtosecond lasers with low-cost fiber-based picosecond lasers. SCG can be demonstrated on either a straight waveguide or a resonator. In the first case, we believe a supercontinuum that covers a few tens of nanometer is obtainable in a 10-cm-long dispersion-engineered waveguide, which is sufficient for many Raman or OCT applications. In the second scenario, if we replace the straight waveguides with resonators, the field enhancement provided by the cavity can significantly enhance the nonlinear interaction. It may even allow one to use integrable on-chip lasers for frequency

comb generation. This all-on-a-chip frequency comb source, we believe, is useful for many metrological and sensing applications.

References

- [1] Ashim Dhakal. *Nanophotonic Waveguide Enhanced Raman Spectroscopy*. PhD thesis, Ghent University, 2016.
- [2] Frédéric Peyskens. *Surface Enhanced Raman Spectroscopy Using a Single Mode Nanophotonic-Plasmonic Platform*. PhD thesis, Ghent University, 2016.
- [3] Kevin Luke, Avik Dutt, Carl B. Poitras, and Michal Lipson. *Overcoming Si_3N_4 film stress limitations for high quality factor ring resonators*. *Optics Express*, 21(19):22829–22833, September 2013.
- [4] Jörn P. Epping, Marcel Hoekman, Richard Mateman, Arne Leinse, René G. Heideman, Albert van Rees, Peter J.M. van der Slot, Chris J. Lee, and Klaus J. Boller. *High confinement, high yield Si_3N_4 waveguides for nonlinear optical applications*. *Optics Express*, 23(2):642–648, January 2015.
- [5] François Leo, Utsav Dave, Shahram Keyvaninia, Bart Kuyken, and Gunther Roelkens. *Measurement and tuning of the chromatic dispersion of a silicon photonic wire around the half band gap spectral region*. *Optics Letters*, 39(3):711–714, January 2014.
- [6] Lianghong Yin, Qiang Lin, and Govind P. Agrawal. *Soliton fission and supercontinuum generation in silicon waveguides*. *Optics Letters*, 32(4):391–393, February 2007.
- [7] Govind P. Agrawal. *Nonlinear Fiber Optics*. Academic Press, 2013.
- [8] M. E. Marhic, N. Kagi, T.-K. Chiang, and L. G. Kazovsky. *Broadband fiber optical parametric amplifiers*. *Optics Letters*, 21(8):573–575, April 1996.
- [9] Qiang Lin, Jidong Zhang, Philippe M. Fauchet, and Govind P. Agrawal. *Ultrabroadband parametric generation and wavelength conversion in silicon waveguides*. *Optics Express*, 14(11):4786–4799, May 2006.
- [10] Robert W. Boyd. *Nonlinear Optics*. Academic Press, 2008.
- [11] Weilin Xie, Ihsan Fsaifes, Tarek Labidi, and Fabien Bretenaker. *Investigation of degenerate dual-pump phase sensitive amplifier using multi-wave model*. *Optics Express*, 23(25):31896–31907, December 2015.
- [12] J. Hansryd, P. A. Andrekson, M. Westlund, Jie Li, and P. O. Hedekvist. *Fiber-based optical parametric amplifiers and their applications*. *IEEE Journal of Selected Topics in Quantum Electronics*, 8(3):506–520, May 2002.

- [13] Boyuan Jin, Chongxiu Yu, Jinhui Yuan, Xinzhu Sang, Xingye Xiang, Zhanyong Liu, and Shuai Wei. *Efficient wavelength conversion based on quasi-phase-matched four-wave mixing in a silicon waveguide with a microring phase shifter*. *Journal of the Optical Society of America B*, 30(9):2491–2497, August 2013.
- [14] Jeffrey B. Driscoll, Noam Ophir, Richard R. Grote, Jerry I. Dadap, Nicolae C. Panoiu, Keren Bergman, and Richard M. Osgood. *Width-modulation of Si photonic wires for quasi-phase-matching of four-wave-mixing: experimental and theoretical demonstration*. *Optics Express*, 20(8):9227–9242, April 2012.
- [15] K. Lindfors, T. Kalkbrenner, P. Stoller, and V. Sandoghdar. *Detection and Spectroscopy of Gold Nanoparticles Using Supercontinuum White Light Confocal Microscopy*. *Physical Review Letters*, 93(3):037401, July 2004.
- [16] R. Leitgeb, W. Drexler, A. Unterhuber, B. Hermann, T. Bajraszewski, T. Le, A. Stingl, and A. Fercher. *Ultra-high resolution Fourier domain optical coherence tomography*. *Optics Express*, 12(10):2156–2165, May 2004.
- [17] Thomas Udem, Ronald Holzwarth, and Theodor W Hänsch. *Optical frequency metrology*. *Nature*, 416(3):233–237, March 2002.
- [18] R. R. Alfano and S. L. Shapiro. *Emission in the Region 4000 to 7000 Å Via Four-Photon Coupling in Glass*. *Physical Review Letters*, 24(11):584–587, March 1970.
- [19] Fujio Shimizu. *Frequency Broadening in Liquids by a Short Light Pulse*. *Physical Review Letters*, 19(19):1097–1100, November 1967.
- [20] P. B. Corkum, Claude Rolland, and T. Srinivasan-Rao. *Supercontinuum Generation in Gases*. *Physical Review Letters*, 57(18):2268–2271, November 1986.
- [21] P. Baldeck and R. Alfano. *Intensity effects on the stimulated four photon spectra generated by picosecond pulses in optical fibers*. *Journal of Light-wave Technology*, 5(12):1712–1715, December 1987.
- [22] Jinendra K. Ranka, Robert S. Windeler, and Andrew J. Stentz. *Visible continuum generation in air-silica microstructure optical fibers with anomalous dispersion at 800 nm*. *Optics Letters*, 25(1):25–27, January 2000.
- [23] Alireza Marandi, Charles W. Rudy, Victor G. Plotnichenko, Evgeny M. Dianov, Konstantin L. Vodopyanov, and Robert L. Byer. *Mid-infrared supercontinuum generation in tapered chalcogenide fiber for producing octave-spanning frequency comb around 3 μm*. *Optics Express*, 20(22):24218–24225, October 2012.

- [24] John M. Dudley and Roy Taylor, editors. *Supercontinuum Generation in Optical Fibers*. Cambridge University Press, 2010.
- [25] I-Wei Hsieh, Xiaogang Chen, Xiaoping Liu, Jerry I. Dadap, Nicolae C. Panoiu, Cheng-Yun Chou, Fengnian Xia, William M. Green, Yurii A. Vlasov, and Richard M. Osgood. *Supercontinuum generation in silicon photonic wires*. *Optics Express*, 15(23):15242–15249, November 2007.
- [26] Bart Kuyken, Xiaoping Liu, Richard M. Osgood Jr., Roel Baets, Günther Roelkens, and William M. J. Green. *Mid-infrared to telecom-band supercontinuum generation in highly nonlinear silicon-on-insulator wire waveguides*. *Optics Express*, 19(21):20172–20181, Oct 2011.
- [27] Jassem Safioui, François Leo, Bart Kuyken, Simon-Pierre Gorza, Shankar Kumar Selvaraja, Roel Baets, Philippe Emplit, Gunther Roelkens, and Serge Massar. *Supercontinuum generation in hydrogenated amorphous silicon waveguides at telecommunication wavelengths*. *Optics Express*, 22(3):3089–3097, February 2014.
- [28] François Leo, Simon-Pierre Gorza, Stéphane Coen, Bart Kuyken, and Gunther Roelkens. *Coherent supercontinuum generation in a silicon photonic wire in the telecommunication wavelength range*. *Optics Letters*, 40(1):123–126, January 2015.
- [29] Hiroyuki Yokoyama, Hiroshi Tsubokawa, Hengchang Guo, Jun-ichi Shikata, Ki-ichi Sato, Keiji Takashima, Kaori Kashiwagi, Naoaki Saito, Hirokazu Taniguchi, and Hiromasa Ito. *Two-photon bioimaging utilizing supercontinuum light generated by a high-peak-power picosecond semiconductor laser source*. *Journal of Biomedical Optics*, 12(5):054019, 2007.
- [30] David J. Moss, Roberto Morandotti, Alexander L. Gaeta, and Michal Lipson. *New CMOS-compatible platforms based on silicon nitride and Hydex for nonlinear optics*. *Nature Photonics*, 7(8):597–607, July 2013.
- [31] Kazuhiro Ikeda, Robert E. Saperstein, Nikola Alic, and Yeshaiah Fainman. *Thermal and Kerr nonlinear properties of plasma-deposited silicon nitride/silicon dioxide waveguides*. *Optics Express*, 16(17):12987, August 2008.
- [32] R. Halir, Y. Okawachi, J. S. Levy, M. A. Foster, M. Lipson, and A. L. Gaeta. *Ultrabroadband supercontinuum generation in a CMOS-compatible platform*. *Optics Letters*, 37(10):1685–1687, May 2012.
- [33] J. M. Chavez Boggio, D. Bodenmüller, T. Fremberg, R. Haynes, M. M. Roth, R. Eisermann, M. Lisker, L. Zimmermann, and M. Böhm. *Dispersion engineered silicon nitride waveguides by geometrical and refractive-index opti-*

- mization*. Journal of the Optical Society of America B, 31(11):2846–2857, November 2014.
- [34] Steven Miller, Kevin Luke, Yoshitomo Okawachi, Jaime Cardenas, Alexander L. Gaeta, and Michal Lipson. *On-chip frequency comb generation at visible wavelengths via simultaneous second- and third-order optical nonlinearities*. Optics Express, 22(22):26517–26525, November 2014.
- [35] Lin Zhang, Yan Yan, Yang Yue, Qiang Lin, Oskar Painter, Raymond G. Beausoleil, and Alan E. Willner. *On-chip two-octave supercontinuum generation by enhancing self-steepening of optical pulses*. Optics Express, 19(12):11584–11590, June 2011.
- [36] Jörn P. Epping, Tim Hellwig, Marcel Hoekman, Richard Mateman, Arne Leinse, René G. Heideman, Albert van Rees, Peter J.M. van der Slot, Chris J. Lee, Carsten Fallnich, and Klaus-J. Boller. *On-chip visible-to-infrared supercontinuum generation with more than 495 THz spectral bandwidth*. Optics Express, 23(15):19596–19604, July 2015.
- [37] Adrea R. Johnson, Aline S. Mayer, Alexander Klenner, Kevin Luke, Erin S. Lamb, Michael R. E. Lamont, Chaitanya Joshi, Yoshitomo Okawachi, Frank W. Wise, Michal Lipson, Ursula Keller, and Alexander L. Gaeta. *Octave-spanning coherent supercontinuum generation in a silicon nitride waveguide*. Optics Letters, 40(21):5117–5120, Nov 2015.
- [38] A. S. Mayer, A. Klenner, A. R. Johnson, K. Luke, M. R. E. Lamont, Y. Okawachi, M. Lipson, A. L. Gaeta, and U. Keller. *Frequency comb offset detection using supercontinuum generation in silicon nitride waveguides*. Optics Express, 23(12):15440–15451, Jun 2015.
- [39] Marco A. G. Porcel, Florian Schepers, Jörn P. Epping, Tim Hellwig, Marcel Hoekman, René G. Heideman, Peter J. M. van der Slot, Chris J. Lee, Robert Schmidt, Rudolf Bratschitsch, Carsten Fallnich, and Klaus-J. Boller. *Two-octave spanning supercontinuum generation in stoichiometric silicon nitride waveguides pumped at telecom wavelengths*. Optics Express, 25(2):1542–1554, January 2017.
- [40] John M. Dudley, Gory Genty, and Stéphane Coen. *Supercontinuum generation in photonic crystal fiber*. Reviews of Modern Physics, 78(4):1135–1184, October 2006.
- [41] Ashim Dhakal, Ali Raza, Frédéric Peyskens, Ananth Z. Subramanian, Stéphane Clemmen, Nicolas Le Thomas, and Roel Baets. *Efficiency of evanescent excitation and collection of spontaneous Raman scattering near*

- high index contrast channel waveguides*. Optics Express, 23(21):27391–27404, October 2015.
- [42] Ashim Dhakal, Ananth Z. Subramanian, Pieter Wuytens, Frédéric Peyskens, Nicolas Le Thomas, and Roel Baets. *Evanescent excitation and collection of spontaneous Raman spectra using silicon nitride nanophotonic waveguides*. Optics Letters, 39(13):4025–4028, July 2014.
- [43] P. Beaud, W. Hodel, B. Zysset, and H. Weber. *Ultrashort pulse propagation, pulse breakup, and fundamental soliton formation in a single-mode optical fiber*. IEEE Journal of Quantum Electronics, 23(11):1938–1946, November 1987.
- [44] M. Erkintalo, Y. Q. Xu, S. G. Murdoch, J. M. Dudley, and G. Genty. *Cascaded Phase Matching and Nonlinear Symmetry Breaking in Fiber Frequency Combs*. Physical Review Letters, 109(22):223904, November 2012.
- [45] Nail Akhmediev and Magnus Karlsson. *Cherenkov radiation emitted by solitons in optical fibers*. Physical Review A, 51(3):2602–2607, March 1995.
- [46] Gary Y. Wang and Elsa Garmire. *Generation of ultrashort second-harmonic pulses by compressing the Čerenkov output*. Optics Letters, 20(3):264–266, February 1995.
- [47] A. Z. Subramanian, P. Neutens, A. Dhakal, R. Jansen, T. Claes, X. Rottenberg, F. Peyskens, S. Selvaraja, P. Helin, B. Du Bois, K. Leyssens, S. Severi, P. Deshpande, R. Baets, and P. Van Dorpe. *Low-Loss Singlemode PECVD Silicon Nitride Photonic Wire Waveguides for 532-900 nm Wavelength Window Fabricated Within a CMOS Pilot Line*. IEEE Photonics Journal, 5(6):2202809, December 2013.
- [48] Rubens S. Miranda, Gloria R. Jacobovitz, Carlos H. Brito Cruz, and Marco A. F. Scarparo. *Positive and negative chirping of laser pulses shorter than 100 fsec in a saturable absorber*. Optics Letters, 11(4):224–226, April 1986.
- [49] P. Lazaridis, G. Debarge, and P. Gallion. *Time–bandwidth product of chirped sech² pulses: application to phase–amplitude-coupling factor measurement*. Optics Letters, 20(10):1160–1162, May 1995.
- [50] Goëry Genty, Stéphane Coen, and John M. Dudley. *Fiber supercontinuum sources (Invited)*. Journal of the Optical Society of America B, 24(8):1771–1785, August 2007.

5

Experimental Demonstration of Stimulated Raman Scattering on the Silicon Nitride Platform

In this chapter, we will investigate if stimulated Raman scattering (SRS) can be performed on a silicon nitride waveguide. One essential benefit of SRS is that the phase-matching condition is automatically satisfied. One major drawback of SRS is that the signal is embodied as a small intensity variation of the incident fields. To acquire small intensity variations of the signal beam, we build an experimental setup to detect the transfer of modulation from one optical field to another. The principle and implementation of the modulation transfer detection scheme are discussed in detail in this chapter.

With the setup for modulation transfer detection, we record the SRS spectra of dimethyl sulfoxide (DMSO) at various concentrations, and the results are compared with references from spontaneous Raman spectroscopy. We demonstrate that SRS is capable of reproducing the spontaneous spectrum with a much higher signal level. Although the stimulation by the Stokes beam dramatically intensifies the Raman signal, it also induces extra shot noise to the system. To understand the merits and drawbacks of SRS as compared to spontaneous Raman scattering, we also investigate the performance of both techniques regarding signal-to-noise ratio (SNR). Finally, future improvements in the performance of SRS are discussed.

5.1 Sample Fabrication

The samples used for SRS experiments are fabricated with deep UV lithography at imec. The silicon nitride waveguide core is deposited through Plasma-Enhanced Chemical Vapor Deposition (PECVD) and later patterned via deep-UV lithography and reactive-ion etching as depicted in [1]. We use PECVD silicon nitride instead of Low-Pressure Chemical Vapor Deposition (LPCVD) silicon nitrides because the waveguides fabricated with the former technique tend to have a lower propagation loss.

The scheme of the silicon nitride waveguides for SRS is shown in Fig. 3.4(a). The 1-cm-long waveguide has a cross-section of $w \times h = 700 \text{ nm} \times 300 \text{ nm}$. Its width is tapered up to $3 \mu\text{m}$ at both ends for better coupling efficiency. The bottom optical cladding is a $3.3 \mu\text{m}$ -thick layer of silica. Within the 8-mm-long sensing area, the top cladding is removed, allowing the evanescent tail of the guided mode to interact with analytes. In the remaining 2 mm of the waveguide, the silicon nitride core is covered by a layer of $1\text{-}\mu\text{m}$ -thick silica. The waveguide is terminated with two 15° angled facets to suppress modal reflection, with the aim of getting rid of spurious signals. This spurious signal will be discussed in detail in section 5.3. These tilted facets are created by dicing and polishing the whole silicon nitride chip, and the detail of facet polishing is given in Appendix B.

For liquid analyte detection, a few droplets of the analytes are applied to the chip. The situation is shown in Fig. 3.4(a). The top and side cladding of waveguides is constituted by the liquid analyte within the sensing area. The Raman interaction takes place in the evanescent field overlapped with this liquid-cladding, which is sometimes called bio-cladding to emphasize the scope of Raman spectroscopy.

5.2 Experimental Setup for SRS

In the previous chapter, we learned that the obtainable SRS signal in both co-propagating and counter-propagation configurations are the same. However, in the counter-propagating configuration, the phase-matched Kerr nonlinear effects are suppressed. As a result, we adopt this configuration for our on-chip SRS experiments. In this section, we first give an overview of the experimental setup. We will explain in detail the functions of the electronic instruments and introduce the principle of modulation transfer detection.

The complete setup for SRS experiment is shown in Fig. 5.1. A laser diode (LD785-SEV300, Thorlabs) emitting at 785 nm is used as the pump beam. It is modulated in intensity with a depth of 30 % at 38 MHz through direct modulation of the driving current. The modulation signal is provided externally by a lock-in amplifier to ensure frequency stability. A CW tunable Ti: Sapphire laser

(SOLSTIS, M2) is used as the Stokes beam. Two pairs of half-wave-plates and polarizing-beam-splitters are used to adjust the guided power for both beams. The polarizing-beam-splitters also guarantee the Stokes beam and the pump beam to excite the fundamental TE mode of the waveguide. Two objectives couple the pump and the Stokes beams into opposite sides of the waveguide. The transmission of both beams is monitored for optical alignment.

The input power is 30 mW before objectives for both beams and the time constant of the lock-in amplifier is set to 100 ms unless explicitly stated. A small part (4 %) of the Stokes beam is tapped before Raman interaction and serves to partially cancel the significant DC offset in the Raman signal measured by a balanced detector (PDB450A-AC, Thorlabs). The electrical signal from the photodiode is then amplified by 10^4 through a built-in transimpedance amplifier.

It is worth mentioning the time constant of lock-in amplifiers does not mean the time it takes to record one data point. A lock-in amplifier can be regarded as an RC filter, and the time constant determines the bandwidth of the filter. When a lock-in amplifier is exposed to a new signal, it takes a certain amount of time for the output of the lock-in amplifier to settle at the new value. The longer we wait, the closer the lock-in output gets to the real value of the input signal. The time we wait for the output to stabilize is called *settling time*. The settling time is proportional to the time constant, and it can be viewed as the time it takes to record one data point, which is roughly the SRS version of “integration time” for spontaneous Raman scattering experiments. In our research, we always set the settling time to 10τ where τ is the time-constant. With this settling time, the difference between the lock-in output and the signal is less than 0.1 % [2].

5.2.1 Modulation Transfer Detection Scheme

In the end of the previous chapter, the evolution of the Stokes field is given by

$$P_s(L) = \underbrace{P_s(0) \exp(-\alpha_s L)}_{\text{Local Oscillator, DC}} + \underbrace{P_s(0) g_{\parallel} P_p(L) L_{\text{eff}} \exp(-\alpha_s L)}_{\text{Raman or SRS Signal, RF}}. \quad (5.1)$$

The Stokes beam leaving the waveguide has two components. The first component is merely the original Stokes beam being attenuated by $\exp(-\alpha_s L)$. We will call this component *local oscillator*. The second part contains the molecular information which is encoded in g_{\parallel} . Therefore it is called *Raman signal* or *SRS signal*. Detecting the Raman signal in the presence of the local oscillator is not trivial due to two reasons: (1) the Raman signal and the local oscillator have the same optical frequency and (2) the intensity of the local oscillation is orders of magnitudes stronger than the Raman signal. A direct measurement of the Raman signal is challenging as it requires one to resolve a power variation of the optical field with a precision better than 10^{-6} . As a result, we cannot discriminate the Raman signal from the local oscillator in the optical domain.

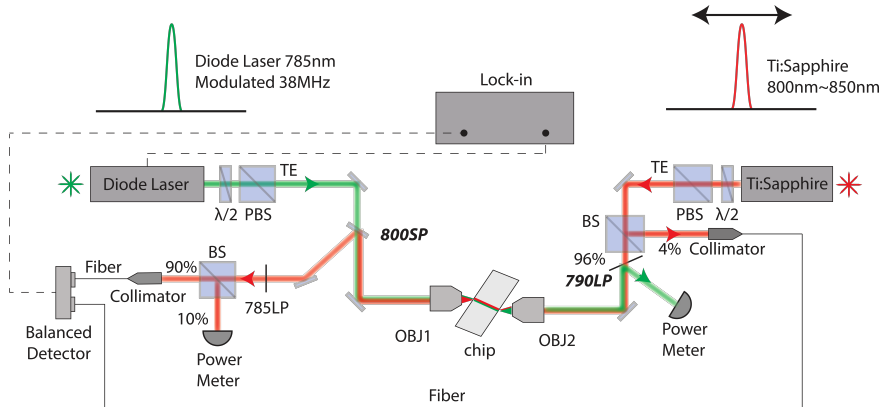


Figure 5.1: Setup for SRS experiment. A diode laser (LD785-SEV300, Thorlabs) and a CW tunable Ti: Sapphire laser (SOLSTIS, M2) are employed as the pump and the Stokes beam respectively. The diode laser is modulated at 38 MHz, and the induced gain in the Stokes beam is detected. Half-wave-plates and polarizing-beam-splitters are used to adjust the power and polarization of both beams. Two objectives couple the pump and the Stokes beams into opposite sides of the waveguide. The optical alignment is actively optimized by monitoring the transmission of both beams.

Fortunately, we can shift the frequency of the Raman signal relative to the local oscillator in the electronic domain. In this case, an electronic filter can separate these two components. This technique is called modulation transfer detection scheme, and it is well-established in electronic measurements [3]. The principle of modulation transfer detection is shown in Fig.5.2. One of the inputs - pump in this case - is first modulated in amplitude at a certain reference frequency while the Stokes remains CW. In the Fourier domain, the input pump is a component at frequency f_1 , and the Stokes is a component at DC.

When both beams are injected into the waveguide, the temporal profile of the pump beam is transferred onto the Stokes beam thanks to Raman interaction. At the output of the waveguide, we first remove the pump beam by an optical filter and direct only the Stokes beam to a photo-detector. Once we convert the Stokes beam from an optical signal to an electronic signal, we use a lock-in amplifier, which can be regarded as a tunable filter with an extremely narrow linewidth, to reject the local oscillator and record the Raman signal. The bandwidth of this filter is mainly controlled by the time constant of the lock-in amplifier. Since the local oscillator is DC while the Raman signal is in RF, the lock-in amplifier can reject the local oscillator with high efficiency and measure only the Raman signal.

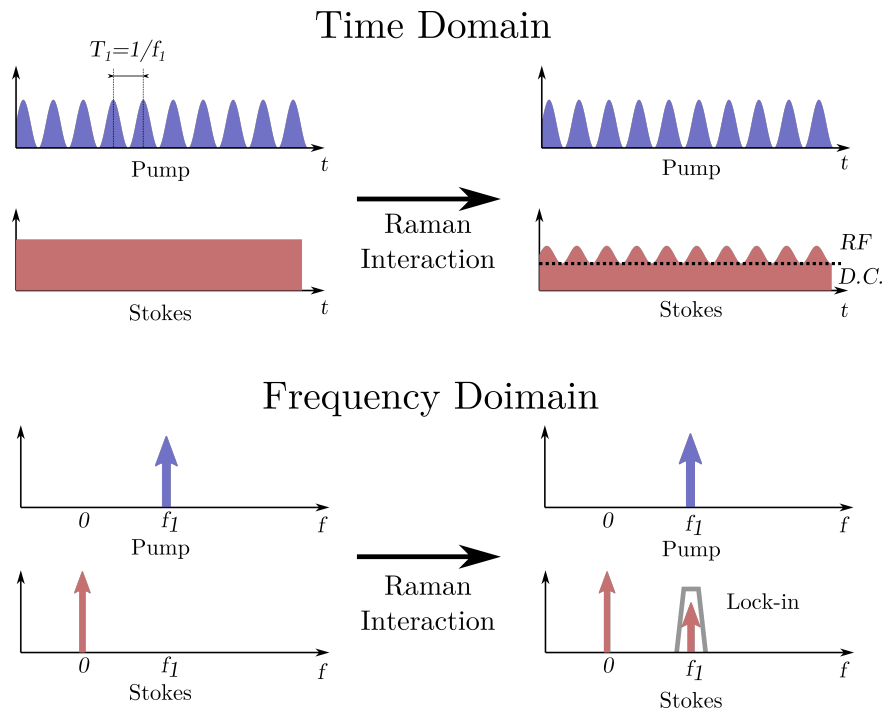


Figure 5.2: The workflow of the modulation transfer detection scheme for SRS. Initially, the pump beam is modulated while the Stokes beam remains CW. Raman interaction will transfer the modulation from the pump beam to the Stokes beam. In the detection side, a lock-in amplifier is used to reject the CW component (local oscillator) and record only the Raman component.

5.2.2 Electronics Instrumentations

The modulation transfer detection scheme for the Raman signal is summarized as a three-step process in Fig. 5.3. In the first step, the Raman signal is converted from photons to electrons. Although the Raman signal is weak, avalanche photodiodes (APD) or photomultiplier tubes (PMT) are not suitable for SRS as they will be quickly saturated by the intense local oscillator. Instead, a reversed biased PIN photodiode is best suited for SRS detection.

We use a balanced detector composed of two photodiodes to suppress the local oscillator by approximately 25 dB. A balanced detector takes two optical inputs, and the power difference of these two inputs is converted into a photocurrent output. If we have a reference beam possessing a similar optical power as the local oscillator, the local oscillator will be significantly suppressed by the balanced detector. In our SRS setup, we tap a small portion of the Stokes beam before Raman interaction and use it as reference. This pre-cancellation of the local oscillator is critical for our SRS experiment because it allows us to amplify the electrical signal with a transimpedance amplifier, as we will show later.

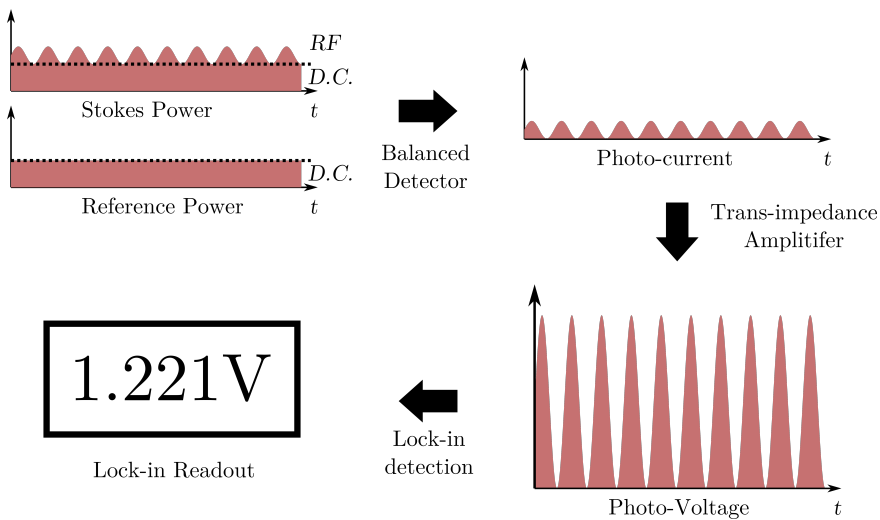


Figure 5.3: A schematic plot of the function of each electronic components in detecting the SRS signal.

In the second step, we convert the Raman signal from current to voltage. It is tempting to attach the balanced detector directly to the lock-in amplifier. However, this configuration proves to be inefficient. Most detectors are designed to work with circuits with an equivalent input impedance of $50\ \Omega$ to suppress the photovoltaic effect. The photovoltaic effect denotes the dependency of the output current on the output voltage, and it will distort the lineshape of Raman signal [4].

Therefore it is important keep the input impedance of the lock-in amplifier to $50\ \Omega$.

In our case, the photodiode is effectively a current source while the lock-in amplifier is sensitive to voltage. If we attach the balanced detector to the lock-in amplifier directly, the current-to-voltage conversion is performed by this humble impedance of $50\ \Omega$. For a given current the resulted voltage will be quite small. Instead, a transimpedance amplifier is capable of converting current to voltage with a ratio of $10^2\ \text{V/A}$ to $10^6\ \text{V/A}$. It has an impedance of $50\ \Omega$ to avoid the photovoltaic effect. In the experiment, we use a transimpedance amplifier with a conversion ratio of $10^4\ \text{V/A}$. The function of the balanced detector is now clear. If we do not partially cancel the local oscillator in the first step, it will easily saturate the transimpedance amplifier.

In the third step, a lock-in amplifier is used to separate the Raman signal from the local oscillator. A modulation frequency of 38 MHz is chosen for the (de-)modulation in our experiment. The lock-in amplifier serves dual purposes. It not only rejects the local oscillator at DC, its narrow bandwidth also reduces the noises and improves the signal-to-noise ratio.

5.2.3 Determination of the Modulation Frequency

The modulation frequency f_1 of the pump in Fig. 5.2 is critical for a successful SRS experiment. Ideally, we modulate the pump at a frequency high enough to suppress laser noise as well as thermal and mechanical fluctuations. In the meanwhile, the frequency should still stay within the bandwidth of our equipment. In our experiments, we are also influenced by the electromagnetic interference of the instruments. The lock-in amplifier is sending a powerful (a few volts) modulation signal to the pump laser. The connecting cable emits an electromagnetic interference and it can penetrate into other equipment. This interference might all show up in the output of the lock-in amplifier through different paths.

5.2.3.1 Electromagnetic Interference Induced Offset

In this subsection, we will record the offset of the lock-in output that is the average of the output from the lock-in amplifier. We first characterize this offset with the configuration shown in Fig. 5.4(a). In experiment, we connect all the optical and electronic components and turn on both lasers. Next, we place a beam blocker to stop the Stokes beam. Note that there is no waveguide in the beam path. We sweep the frequency of the modulation signal and record the average value of the lock-in output. This modulation signal is sent from the lock-in amplifier to the pump laser. Because the balanced detector registers no signal, it is a “dark” measurement. The lock-in amplifier output is a result of either electromagnetic interference or input offsets of the detectors.

The measurement result is shown in Fig. 5.5 as the solid blue curve. The inset of Fig. 5.5 shows the dark offset between 30 MHz to 40 MHz. The offset increases gradually from 100 nV at 1 kHz to 800 nV at 20 MHz. With a further increased modulation frequency, the dark offset rapidly decreases to sub-50 nV and stabilizes.

Next, we characterize the system-wide offset. The beam-blocker is removed in this configuration as shown in Fig. 5.4(b). There is also no waveguide in the beam path. The output of the Stokes laser is adjusted carefully to make sure 0.25 mW of the Stokes beam and 0.25 mW of the reference beam are coupled into the balanced detector. In this configuration, apart from the dark offset, we also notice a strong influence from the Stokes beam.

The result of system-wide offset is shown as the red line in Fig. 5.5. We can see the offset decreases almost monotonously with an increased modulation frequency. It drops from around 4000 nV at 1 kHz to below 50 nV at 36 MHz and stabilizes at this value for modulation frequency higher than 36 MHz. Comparing the dark offset and the system-wide offset in Fig. 5.5, we believe that the signal is limited by the dark offset for modulation frequencies above 36 MHz.

The origin of the offset in the dark measurement is not fully understood. It is suggested that this dark offset might arise from the WWV radio stations, which broadcast time signals on 2.5 MHz, 5 MHz, 10 MHz, 15 MHz and 20 MHz. Indeed, the agreement of the peaks at 5 MHz, 10 MHz and 15 MHz in the blue curve in Fig. 5.5 constitute a piece of evidence that we might be measuring the WWV signal. However, we do not have a good reason to explain the absence of peaks at 2.5 MHz and 20 MHz. We should emphasize that although the origin of the offset is not clarified, we can minimize its impact on SRS measurement by using a modulation frequency that is high enough.

5.2.3.2 Noise Associated with the Setup

Apart from the offset, it is also important to characterize the noise associated with the setup. Unlike offset, which is measured by taking the average of the lock-in output, the noise is characterized by recording its standard deviation. It is important to emphasize that the offset measured in the previous section is actually the “ambient noises”, while the noise we present in this section is the fluctuations of the “ambient noises”.

Although both noise and offset are sensitive to the modulation frequency, they have different impacts on measurement results. A practical difference between the offset and the noise is whether it can be suppressed by the lock-in amplifier. We mention that the lock-in amplifier can be regarded as a tunable electronic filter. If we adjust the time constant of the lock-in amplifier, we can reduce the influence of the noise. However, there is nothing we can do with the lock-in amplifier to suppress the offset. Therefore, in our experiment, the modulation frequency is set

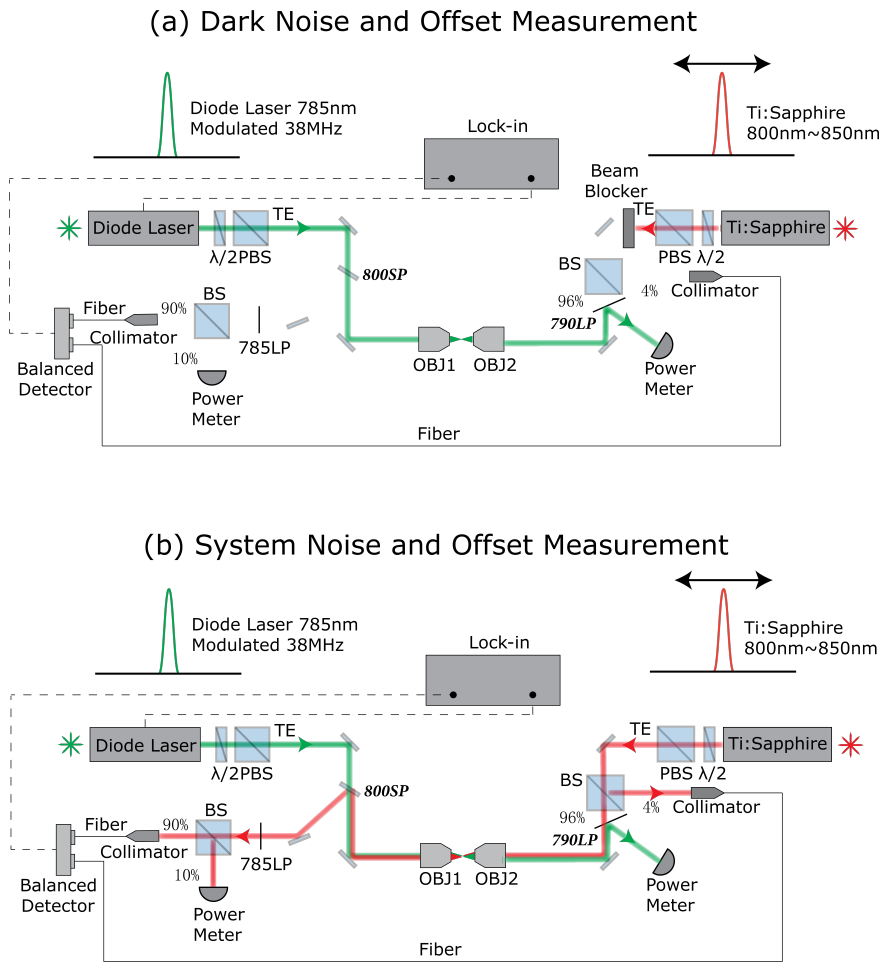


Figure 5.4: (a) The setup for the dark offset and the dark noise measurement. The output of the Stokes beam is blocked by a beam blocker, and therefore the output registered by the lock-in arises only from the electronic instruments. (b) The setup for the system-wide offset and the system-wide noise measurement. The Stokes beam is unblocked, and the lock-in output is not only influenced by the electronic instruments, it is also influenced by the Stokes beam. Note that there is no waveguide in both scenarios.

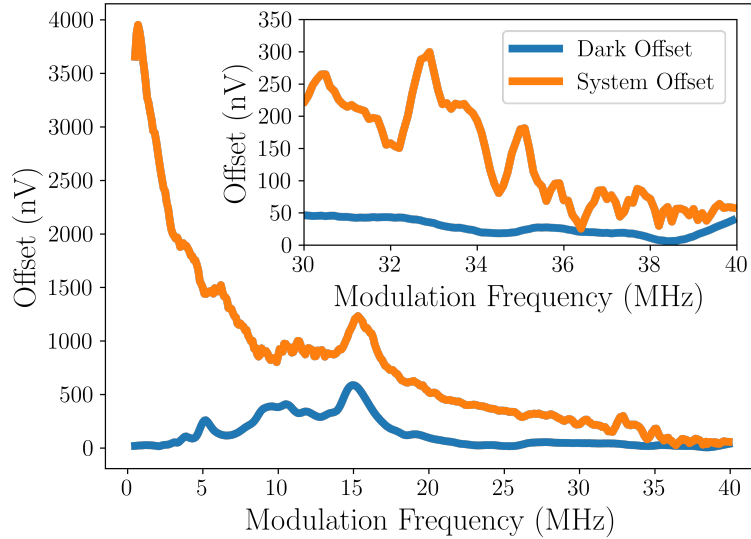


Figure 5.5: The lock-in output with varying modulation frequencies. Both dark offset (solid blue) and system-wide offset (solid red) are presented. The inset shows the lock-in output from 30 MHz to 40 MHz. The time constant in both scenarios is set to 100 ms and the settling times is 1 s.

to 38 MHz to minimize the offset. The noise is tackled with a longer time constant.

We measure the dark noise system-wide noise with the setups in Fig. 5.4(a) and Fig. 5.4(b), respectively. The dark noise is $\sigma_{\text{dark}} = 71 \text{ nV}/\sqrt{\text{Hz}}$. The system-wide noise is $\sigma_{\text{total}} = 82 \text{ nV}/\sqrt{\text{Hz}}$. The noise associated with the laser, including laser intensity noise and shot noise, is then

$$\sigma_{\text{laser}} = \sqrt{\sigma_{\text{total}}^2 - \sigma_{\text{dark}}^2} = 41 \text{ nV}/\sqrt{\text{Hz}}. \quad (5.2)$$

Here we assumed implicitly that these noise sources are mutually independent. Note that the measurement is performed with 0.25 mW of Stokes power incident on the balanced detector (corresponding to the maximum power injection in the measurements). In this case we also estimate the shot noise to be $40 \text{ nV}/\sqrt{\text{Hz}}$. Therefore we believe most of the noise associated with the laser arises from the shot noise.

5.3 Parasitic Effects in SRS

In our first attempts at recording SRS spectra, we realize SRS is accompanied by two types of parasitic nonlinear processes: two-photon absorption and nonlinear

phase change [3]. Two-photon absorption (TPA) refers to the simultaneous absorption of a pump photon and a Stokes photon, and it results in direct attenuation of the Stokes signal. In on-chip SRS, the large bandgap of silicon nitride and the low power level of the excitations ensure a negligible contribution from TPA. Nonlinear phase change, or cross-phase modulation (XPM), arises from the refractive index change induced by the pump beam and experienced by the probe beam. The refractive index change can arise either from thermal effects or the Kerr effect. Nonlinear phase change *per se* does not change the amplitude of the Stokes beam and is therefore not expected to induce any spurious signal. However, in practice the nonlinear phase change finds two interferometric paths converting itself into amplitude change, and the SRS signal can be swamped entirely by them: (i) The silicon nitride waveguide forms intrinsically a low-quality-factor Fabry-Perot (FP) cavity; (ii) A small portion of the Stokes beam can be coupled into cladding modes while most of the Stokes beam is coupled into a guided mode. The spurious transmission through cladding modes and the waveguide transmission constitute an unbalanced Mach-Zehnder interferometer. In this section, we shall discuss in detail the formation of these two interferometric paths and the spurious signal induced by them.

5.3.1 Fabry-Perot Cavity Induced Fringes

A waveguide can be viewed as a weak FP cavity. Suppose the intensity of the Stokes beam entering the waveguide is I_i and leaving the waveguide is I_o . In a lossless FP cavity, its transmission T is given by

$$T = \frac{(1 - R)^2}{(1 - R)^2 + 4R \sin^2 \phi_0}, \quad (5.3)$$

where ϕ is the half-pass optical length given by

$$\phi_0 = \frac{2\pi}{\lambda} n_{\text{eff}} L,$$

where n_{eff} is the effective index of the Stokes beam. We know that the pump beam is capable of modifying the effective index of the material through the Kerr effect or the thermo-optical effect. If we denote the index change as Δn , the half-pass optical length is modified to

$$\phi = \phi_0 + \Delta\phi = \frac{2\pi}{\lambda} (n + \Delta n) L. \quad (5.4)$$

Equation (5.3) can be expanded at the vicinity of $\Delta\phi = 0$ as

$$T = \frac{I_o}{I_i} = \frac{(1 - R)^2}{(1 - R)^2 + 4R \sin^2 \phi_0} + \underbrace{\frac{4R(1 - R^2) \sin 2\phi_0}{(1 + R^2 - 2R \cos 2\phi_0)^2} \Delta\phi}_{\Delta T} + \dots \quad (5.5)$$

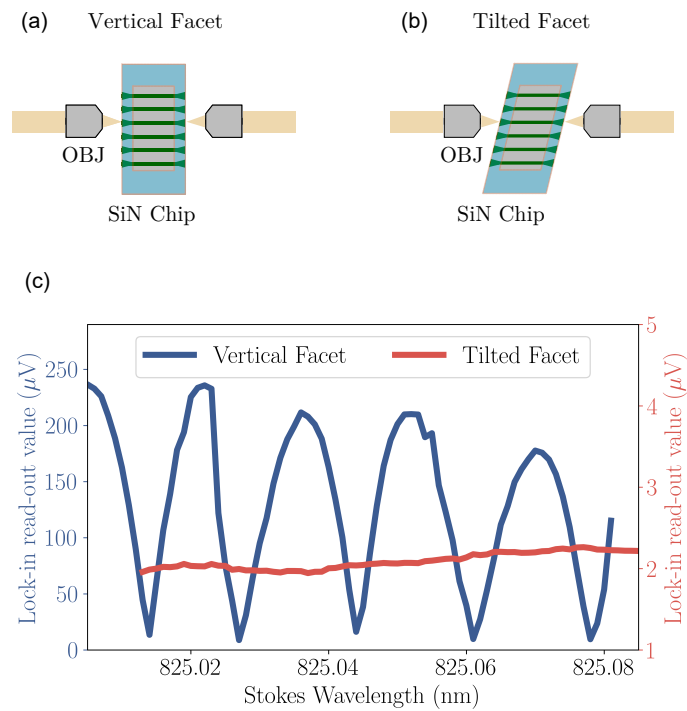


Figure 5.6: (a) The structure of a waveguide with vertical facets. (b) The structure of a waveguide with tilted facets. The process we used to introduce the tilted facets are discussed in detail in Appendix B. (c) The lock-in output for SRS measurements with these two types of waveguides. The sizeable oscillatory feature in the range of $100\ \mu\text{V}$ measured with vertical facets are significantly suppressed with tilted facets. A smooth signal around $2.3\ \mu\text{V}$ is obtained from waveguides with tilted facets, which constitutes substantial evidence that the parasitic signals induced by the FP cavity are suppressed.

Suppose the phase shift is caused by the instantaneous Kerr effect, we have

$$\Delta\phi = \frac{2\pi}{\lambda}\Delta nL = \frac{2\pi}{\lambda}n_2I_pL. \quad (5.6)$$

The nonlinear phase change $\Delta\phi$ can be converted to a variation in the transmittance of the Stokes beam through the FP cavity. A closer look at ΔT reveals that this parasitic effect has the same scaling as the SRS: it causes a variation in the intensity of the Stokes beam, and the amplitude of this variation is proportional to the intensity of both pump and Stokes beams. As a result, this parasitic signal cannot be discriminated from the Raman signal by the lock-in amplifier.

R_f	Reflection on the waveguide facet	6 %
L	Cavity length	1 cm
n	effective index of the cavity	1.65
λ	wavelength of the laser	0.8 μm
A_{eff}	Effective area	0.25 μm^2
n_2	Kerr coefficient	$2 \times 10^{-19} \text{ m W}^{-2}$

Table 5.1: Parameters of a silicon nitride waveguide. It is used for estimating the strength of the FP-induced parasitic signal.

An estimation of the intensity of this parasitic signal is useful. Based on the properties shown in Table. 5.1, the maximal modulation depth due to this parasitic effect for 10 mW of guided pump power amounts to

$$\frac{\Delta I_o}{I_o} = 1.7 \times 10^{-4}. \quad (5.7)$$

This modulation is much deeper than that induced by SRS. The modulation depth of the signal induced by SRS is in the range of 10^{-6} . As a result, this parasitic signal will overwhelm the Raman signal.

A typical spurious signal measured in the vicinity of 825 nm is shown as the solid blue curve in Fig. 5.6(c). We can see a fast oscillating feature with a period of approximately 37 pm. In theory, the FSR of the FP cavity formed by the facets of the waveguide is

$$\Delta\lambda_{\text{FSR}} = \frac{\lambda^2}{n_g L} = \frac{(825 \text{ nm})^2}{1.94 \times 1 \text{ cm}} = 35 \text{ pm}, \quad (5.8)$$

here the group index is taken to be $n_g = 1.94$. The consistency between the theoretical estimation and the experimental observation in terms of FSR constitutes the first piece of evidence that the fringes are indeed induced by the waveguide cavity. If the FP cavity indeed causes the fringes, we should be able to identify multiple peaks in the frequency domain as suggested by the higher order terms in

Eq. (5.5). As the second piece of evidence, we transform the fringes in Fig. 5.6(c) to the Fourier domain. Its Fourier spectrum is shown in Fig. 5.7 where we can immediately recognize the higher-order contributions to the fringes, highlighting the cavity origin of the fringes.

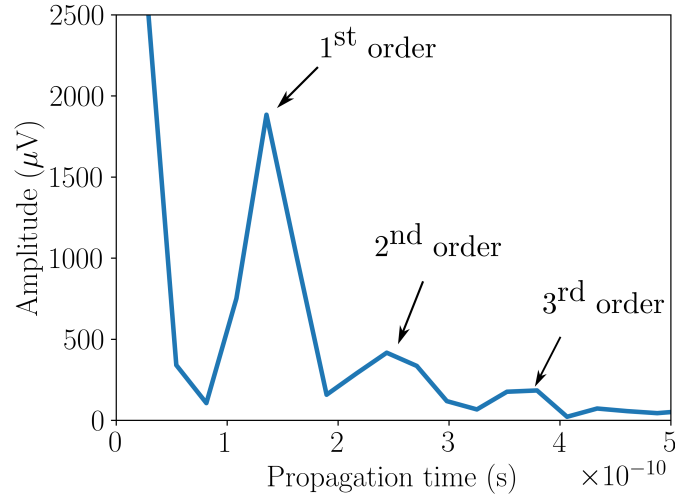


Figure 5.7: The Fourier domain of the fringes. The 1st, 2nd and 3rd order peaks are readily observable.

The spurious signal induced by the combination of FP cavity and nonlinear phase change constitutes a serious problem. It has the same modulation frequency as the SRS signal, so we cannot separate them with electronic filters, i.e. the lock-in amplifier. Its signal intensity is orders of magnitude stronger than the SRS signal, and it is oscillating quickly in the Raman spectrum. As a result, it overwhelms the SRS signal in practical experimental conditions.

To get rid of this spurious signal, we believe the only practical method is to suppress the modal reflection on the facet. The lock-in amplifier is sensitive to variations as small as 10^{-8} . The modulation depth obtained in SRS is in the range of 10^{-6} to 10^{-8} , while the parasitic effect has a modulation depth of 1.7×10^{-4} . Therefore, to utilize the full potential of the lock-in amplifiers, according to Eq. (5.5), we should suppress the modal reflection at the waveguide facets by at least four orders of magnitude.

While an anti-reflection coating can be deposited in our cleanroom, reaching such a level of reflection suppression is challenging. Instead of suppressing the reflection completely, a similar approach is to avoid the coupling of the reflected light back to the propagating mode of the silicon nitride waveguide. Tilted angle facet, a technique widely used in semiconductor lasers [5], has the potential to

do this. The back reflection from a tilted facet can be modeled as the transmission of the light to another waveguide tilted by 2θ . The equivalence is shown in Fig. 5.8 [5]. The tilted facet introduces a large wavefront mismatch in the connecting part of the two waveguide. This wavefront mismatch greatly reduces the modal overlap of the guided modes and significantly suppresses the transmission.

The performance of tilted facets is studied with 3D FDTD simulation in Lumerical. It is pointed out in [5] that we can have a better suppression of modal reflection when mode area in both sections of Fig. 5.8 are large. As a result, we introduce tilted facets to the taper section ($3\ \mu\text{m}$) rather than the detection section ($800\ \text{nm}$) to ensure a better performance. The angle θ is scanned from 0° to 20° and we find that the modal reflection is suppressed by at least 50 dB when θ is larger than 13° . Considering the fabrication tolerance, we terminate waveguides with 15° -angled facets. The effect of tilted angle facets is showcased in the solid red curve in Fig. 5.6(c). The process we used to introduce the tilted facets are discussed in detail in Appendix B. The introduction of tilted facets obliterates the fast oscillating parasitic signal, leaving us with only a smooth feature signal which is later identified as the Raman response from the silicon nitride waveguide core due to thermal fluctuations [6]. In short, we can now detect the Raman signal that is more than 50 times smaller than the FP-induced parasitic signal. This convincingly demonstrates the efficiency of the tilted facets.

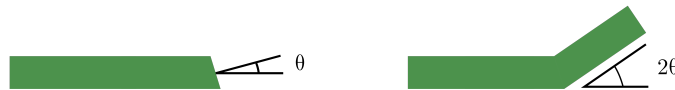


Figure 5.8: The modal reflectivity of a θ -degree tilted facet is equivalent to the transmission between two waveguides rotated by 2θ .

5.3.2 Mach-Zehnder Interference Induced Fringes

After suppressing the FP-induced parasitic signal, we soon realized the existence of another interferometric path when we were trying to probe the Raman response of DMSO. After applying a few droplets of DMSO, we recorded another set of fringes shown in Fig. 5.9. The Fourier transformation of Fig. 5.9 is shown in Fig. 5.10. We can see there exists only one peak in the frequency domain. It suggests that a Mach-Zehnder interferometer causes this parasitic signal. Similar to the FP-induced fringes, this MZI-induced spurious signal is also much stronger than the SRS signal. It has also a small period in the optical domain. As a result,

it should also be suppressed before we can extract the Raman peaks. To suppress it, we have to first identify the exact origin of it.

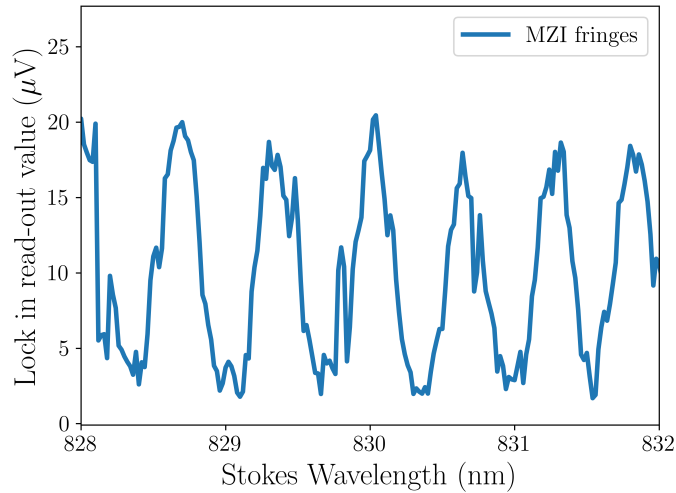


Figure 5.9: A typical spectral fringe that is observed after the application of DMSO.

We have considered multiples possible interferometric paths, including the interference between the TE and TM modes of the waveguide and the interference between the substrate propagation and waveguide mode. After some theoretical estimations, we believe the fringe in Fig. 5.9 is caused by the interference between the cladding mode and the waveguide mode. The situation is shown in Fig. 5.11. In a silicon nitride waveguide, most of the light is transmitted within the silicon nitride core. However, a small portion of light might propagate within the cladding. Note that the cladding transmission is not the evanescent tail of guided modes but rather stray light propagating in the cladding.

Assume we have a Stokes beam whose electric field is E_i . At the input facet of the waveguide, the Stokes beam can not only excite waveguide modes but also cladding modes. Without loss of generality, we assume one waveguide mode whose field is E_{wi} and one cladding mode whose field is E_{ci} are excited. We have

$$E_i = E_{wi} + E_{ci}. \quad (5.9)$$

These two modes will propagate with different propagation constants. When they recombine at the output facet of the waveguide, we have

$$E_{wo} = E_{wi}e^{-j\phi_w}, \quad (5.10)$$

$$E_{co} = E_{ci}e^{-j\phi_c}. \quad (5.11)$$

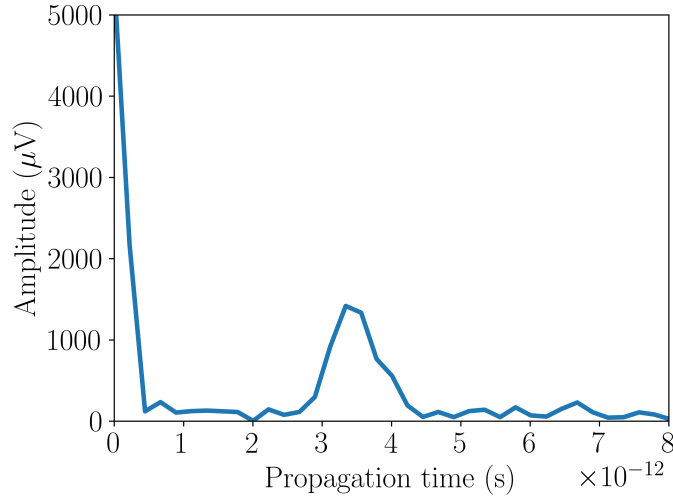


Figure 5.10: The Fourier analysis of the fringes shown in Fig.5.9. It is clear there exists only one peak in the time domain, implying that the fringe is caused by a MZI-like cavity.

Here the subscript w denotes the waveguide mode and the subscript c denotes cladding mode. ϕ is the phase accumulated during propagation. The intensity of the Stokes beam at the output is then

$$I_o \propto |E_{wo} + E_{co}|^2 = |E_{wi}|^2 + |E_{ci}|^2 + 2E_{ci}E_{wi} \cos(\phi), \quad (5.12)$$

in which $\phi = |\phi_w - \phi_c|$. Within the waveguide core, both Stokes and pump beams are highly confined. Therefore, the pump beam is capable of inducing an index change, which induces a nonlinear phase to the Stokes beam. In comparison, in the cladding, the Stokes beam experience a negligible Kerr-induced phase shift from the pump. Taking into account this nonlinear phase, we have

$$\phi = \phi_0 + \Delta\phi, \quad (5.13)$$

here ϕ_0 is the part of the phase difference between the waveguide mode and the cladding mode that is independent of the laser power and $\Delta\phi$ is dependent on the intensity of the pump beam. With the first-order approximation, we assume $\Delta\phi = \iota I_p$. If we expand I_o at the vicinity of $\Delta\phi = 0$, we have

$$I_o \propto |E_{wi}|^2 + |E_{ci}|^2 + 2E_{ci}E_{wi}(\cos(\phi_0) - \sin(\phi_0)\Delta\phi + \dots). \quad (5.14)$$

The intensity variation of the Stokes beam after the waveguide is given by

$$\frac{\Delta I_o}{I_p} = \propto 2E_{ci}E_{wi} \sin(\phi_0)\iota. \quad (5.15)$$

It is clear the MZI is also able to induce a response similar to SRS if we notice that $E_{ci}E_{wi}$ is proportional to the intensity of the Stokes beam. The FSR of an MZI is given by

$$\Delta\lambda_{\text{FSR}} = \frac{\lambda^2}{n_{gw}L_w - n_{gc}L_c}, \quad (5.16)$$

where n_{gw} is the group index of the guided TE mode at the Stokes frequency. L_w is the length of the waveguide. n_{gc} and L_c are the group index of the cladding transmission and its length, respectively. For the specific silicon nitride waveguide we used, the group index is n_{gw} is 1.94. The group index of the cladding is 1.48. Assuming $L_w = L_s = 0.2$ cm, the FSR of this MZI is estimated to be

$$\Delta\lambda_{\text{FSR}} = 0.8 \text{ nm}. \quad (5.17)$$

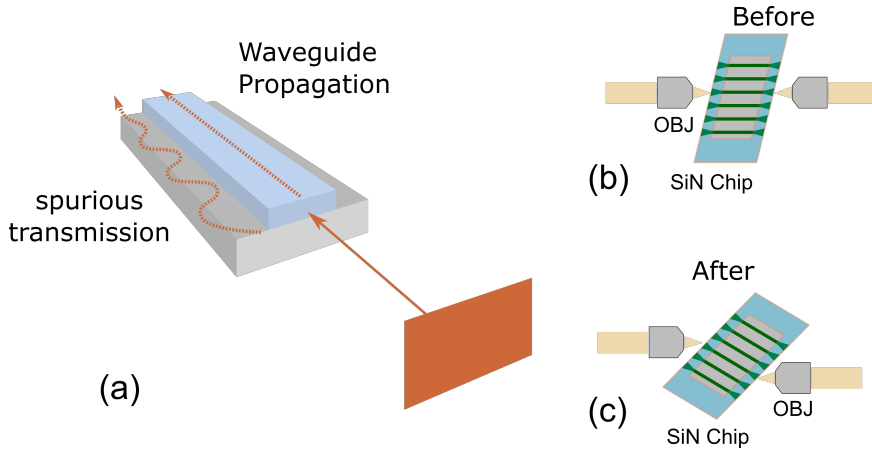


Figure 5.11: (a) The light incident on the waveguide is split into two arms. Most of the light couples into the waveguide mode while a small portion of the light couples into the cladding mode. (b) Collinear alignment of the objective allows the cladding mode to combine with the waveguide transmission, causing fringes in the lock-in. (3) The MZI effect can be circumvented by inserting a lateral displacement between these two objectives.

Since the measured FSR is 0.67 nm, we can see the theoretical estimation is in good agreement with the measurements. The length of 0.2 cm might need some further explanation. Remember that the waveguide is first fully covered with silicon dioxide. Later a 0.8-cm-long strip is removed to expose the silicon nitride core to the analyte. After the removal, there is still approximately 0.2 cm of silicon dioxide left on the entrance of the waveguide. This oxide-clad section is shown as the blue area in Fig. 5.11(b).

We realize that the MZI effect can be suppressed by preventing the cladding transmission from reaching the detector. As the oxide-cladding does not provide

lateral confinement, the cladding modes do not necessarily have the same propagation direction as the waveguide modes. We envision that if we insert a lateral displacement between the objectives, depicted in Fig. 5.11(c), the cladding transmission would not be collected by the out-coupling objective. As a result, the interference between cladding and waveguide modes should vanish. Indeed, rotating the sample by 30° and subsequently aligning the objective for maximum butt coupling efficiency allows us to successfully suppress the fringes in Fig. 5.9. In this case, we obtain the Raman spectra of DMSO covering the silicon nitride waveguide. The detail of this result will be discussed in the following section.

5.4 SRS Spectrum on Silicon Nitride Waveguides

We first test our setup by measuring the Raman spectrum of the silicon nitride waveguide itself. For the specific PECVD silicon nitride that makes the core of our waveguide, the Raman response exhibits a sharp peak at 2330 cm^{-1} and a broad feature below 1200 cm^{-1} [1, 6, 7]. We sweep the wavelength from 800 nm to 850 nm with a resolution of 0.05 nm to record the SRS spectrum. It corresponds to a Raman spectrum extending from 295 cm^{-1} to 1050 cm^{-1} with 0.74 cm^{-1} resolution (given the pump wavelength of 785 nm). In Fig. 5.12 we compare the response of the waveguide using spontaneous and stimulated excitation. We can readily see the excellent agreement of both spectra without any adjustment other than a proportionality factor.

It is essential to note the dimension of the SRS signal. The SRS results presented in this work are all normalized by the transmitted power of the pump beam and the Stokes beam. Since the unit of the lock-in signal is [Volt], and the dimension of laser power is [Watt]. The normalized SRS signal has a dimension of [Volt/Watt²].

We also record the sharp peak at 2330 cm^{-1} originating from the silicon nitride core. It is noteworthy that this peak is beyond the tuning range of the Ti:Sapphire laser if we use the diode laser as pump. To circumvent this problem, we use a pulsed laser at 775 nm (Katana-08, OneFive) as pump. We sweep the wavelength of the Ti:Sapphire laser (Stokes) from 944.5 nm to 946.5 nm with a resolution of 0.05 nm , and the SRS spectrum is shown in Fig. 5.13. The Raman peak at 2330 cm^{-1} can be readily observed. The result is noisier compared to Fig. 5.12 because the output power of the pulsed laser is much lower. The SRS result has a narrower linewidth than the spontaneous result, which showcases the advantage of SRS for high-resolution Raman measurements. The linewidth of the spontaneous result is limited by the resolution of the spectrometer in this case. Note that we always use the diode laser (LD785-SEV300, Thorlabs) apart from this measurement.

To record the SRS spectra of DMSO, we scan the wavelength of the Stokes

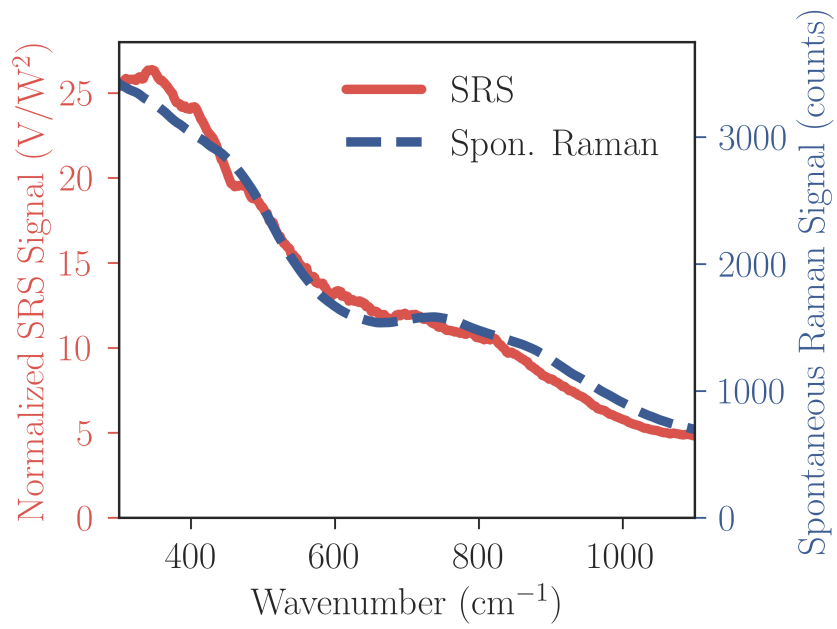


Figure 5.12: The response of the waveguide core below 1050 cm^{-1} measured with spontaneous Raman scattering (blue dashed) and SRS scattering (red solid).

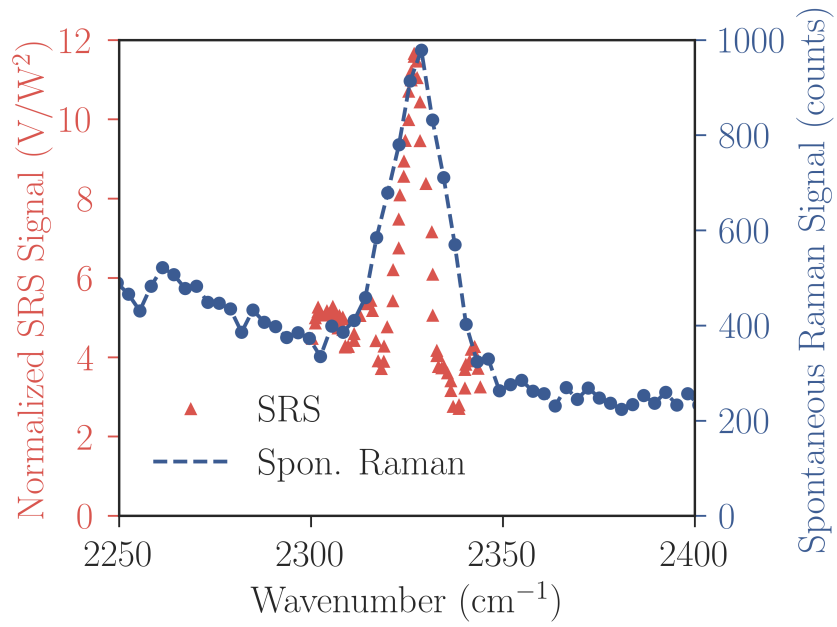


Figure 5.13: The response of the waveguide from 2250 cm⁻¹ to 2400 cm⁻¹. The spectra are measured with both spontaneous Raman scattering (blue solid) and SRS (red triangle).

beam from 817 nm to 845 nm with a resolution of 0.05 nm. In Fig. 5.14 we show the Raman spectra before (dotted red line) and after (solid red line) drop casting the DMSO. After the application of DMSO, we can readily notice the emergence of two peaks at 668.8 cm^{-1} and 699.3 cm^{-1} the position and relative intensity of which are in good agreement with the spontaneous Raman spectra obtained with a confocal Raman microscope (black dotted line) and with the same waveguide (dashed blue line).

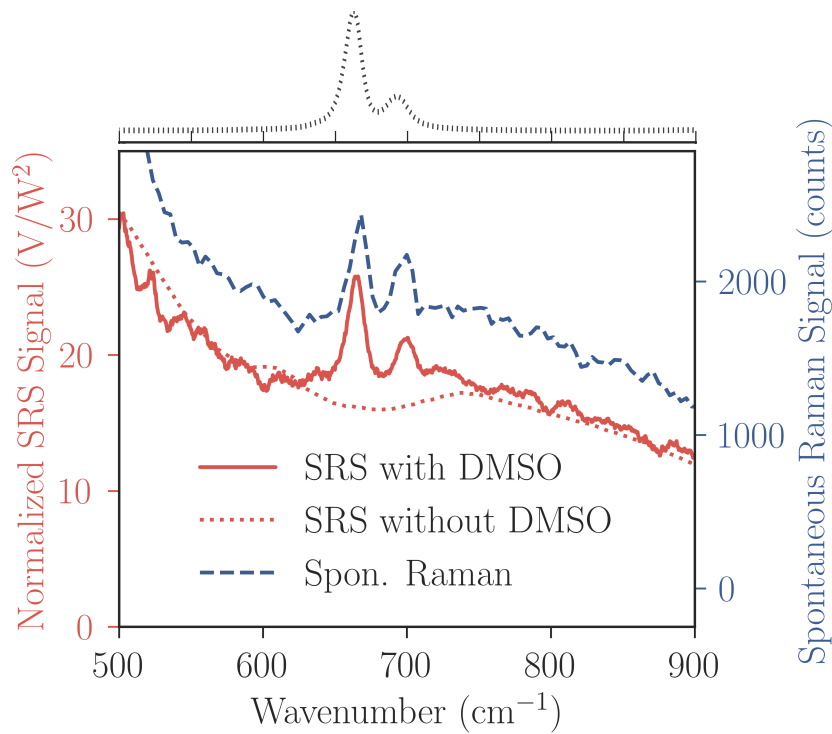


Figure 5.14: Recorded SRS spectra from the waveguide before (dotted red) and after (solid red) the application of DMSO. Reference spontaneous Raman spectra for DMSO are taken separately with a confocal Raman microscope (black dotted) and with the same waveguide (dashed blue).

In Fig. 5.15, the signal dependence on the concentration of DMSO in water is investigated using the 670 cm^{-1} Raman peak. Fig. 5.15(a) displays in blue lines the SRS spectra with 50%, 15% and 2% of DMSO dissolved in water recorded with a time constant of 100 ms. The spectra are vertically offset for clarity. The 15% and 2% data are shifted from the 50% data by -2 V/W^2 and -4 V/W^2 respectively. In the 2% measurement, the SRS spectrum is so noisy that the Raman peak is not identifiable. The Raman peak reappears after we extend the time con-

stant to 600 ms. The result is shown Fig. 5.15(b) as the red curve and the 100 ms result is repeated in blue, where both of the results are subtracted by their mean value respectively. The heights of the DMSO peak relative to the background are extracted, and the results are shown in Fig. 5.15(c). There is a gradual frequency shift of the Raman peak with reduced concentrations, which might arise from the dipole-dipole interaction of the DMSO-water complex [8]. This frequency shift is also observed in spontaneous Raman measurements. The height of the Raman peaks shows an excellent linearity concerning the DMSO concentration, which is crucial for quantitative analysis. For an input of 60 mW from both lasers, corresponding to 10 mW and 3 mW of effective Stokes and Pump power on the chip, the raw SNR of the 2% (280 mM) of DMSO is estimated to be 1.5. The signal level in the lock-in is 44 nV, and it corresponds to a modulation depth of 2×10^{-8} .

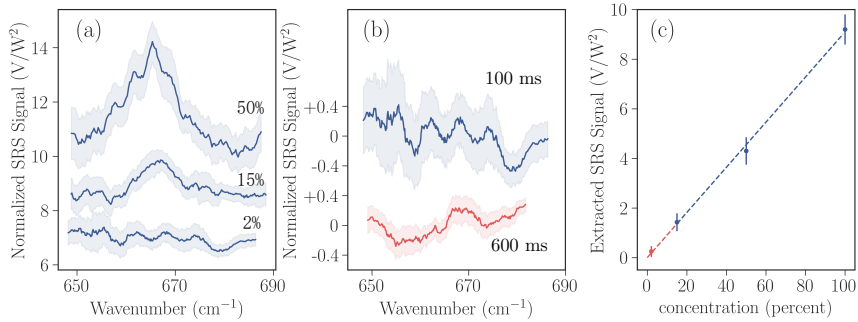


Figure 5.15: The SRS signal of different concentrations of DMSO in water. (a) SRS spectra of 50 %, 15 % and 2 % of DMSO measured with a time constant of 100 ms (blue) with a y -axis offset for clarity. The 15 % and 2 % data are shifted from the 50 % data by -2 V/W^2 and -4 V/W^2 respectively. (b) Mean-value-subtracted SRS spectra of 2 % of DMSO measured with both 100 ms (blue) and 600 ms (red). (c) The extracted peak height from the SRS spectra and its standard deviation.

It is worth mentioning that a correction has been implemented in all SRS results. This correction is related to the offset from the electronic equipment. Fig. 5.16 shows the signal registered by the lock-in at different incident pump and Stokes powers. The Stokes laser is tuned to 828.20 nm to record the 670 cm^{-1} Raman mode of DMSO. The time-constant of the lock-in amplifier is set to 100 ms. The electrical signal increases linearly with both pump power and Stokes power, which constitutes another piece of evidence that the signal is indeed induced by SRS.

However, one might also be surprised by the observation that the SRS signal has an unphysical negative intercept with the y -axis. This negative intercept can be explained by the operation principles of lock-in amplifiers. If a periodic signal $A_s \exp(i2\pi ft + i\theta_s)$ is injected into a lock-in amplifier, it measures the

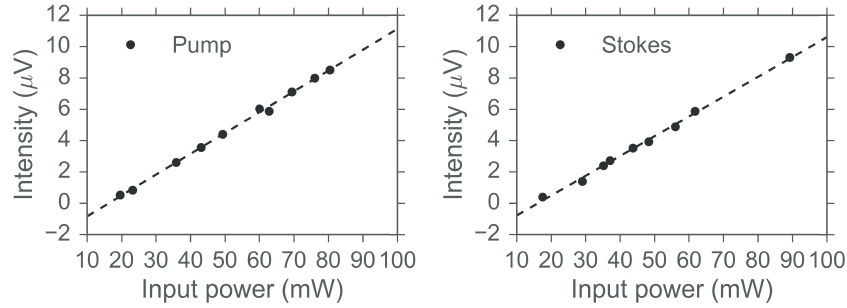


Figure 5.16: Linear scaling of the lock-in output with incident pump and Stokes power. When the pump of one beam is tuned, the power of the other beam is set to 30 mW. The linear dependence of lock-in output on the input power is a piece of strong evidence that we are recording the SRS signal.

root-mean-square value of the in-phase and quadrature component (X, Y) of the signal. These two components are given by

$$X + iY = \frac{A_s}{\sqrt{2}} e^{i\theta_s}. \quad (5.18)$$

The value of (X, Y) is customarily plotted in a complex plane shown in Fig. 5.17(a). As we are mostly interested in the amplitude of the signal, the quadrature is also represented with amplitude R and phase θ . The relationship between (X, Y) and (R, θ) is also shown in Fig. 5.17(a). The SRS results shown in this chapter are always the amplitude R .

When two periodic signals with the same frequency are injected, one with amplitude R and the other one R' , the combined amplitude in the lock-in is not necessarily $R + R'$. One has to take into account the phase relationship between these two signals. Fig. 5.17(b) gives a representation of the in-phase and quadrature components from two periodic signals

$$X'' + iY'' = \frac{A_s}{\sqrt{2}} e^{i\theta_s} + \frac{A'_s}{\sqrt{2}} e^{i\theta'_s}. \quad (5.19)$$

And the amplitude of the total signal is given by $R'' = \sqrt{X''^2 + Y''^2}$.

Recall that in determining the modulation frequency in Section 5.2.3, the measurement setup induces an offset in the lock-in amplifier. In that section, we plot only the amplitude of the offset R and the phase information is disregarded. In a closer examination, this offset has a fixed phase relationship with the SRS signals. In experiment, we find that the background is always lagging behind the Raman signal by approximately 140° . It suggests that the offset and the Raman signal adds destructively, and the outputs of the lock-in amplifier are always smaller than the

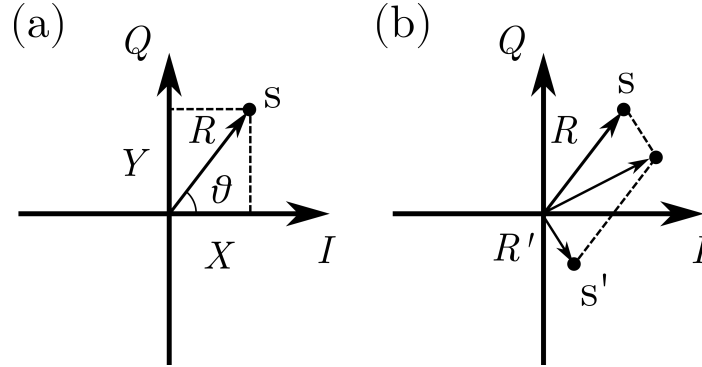


Figure 5.17: (a) Schematic representation of lock-in detection for one periodic signal. The lock-in amplifier records the amplitude of a periodic signal in the complex plane. It records the in-phase component X and quadrature component Y , and the amplitude R is calculated by $R = \sqrt{X^2 + Y^2}$. (b) Schematic representation of lock-in detection for two periodic signals. The total amplitude of the signal is influenced by the relative phase between individual signals.

real Raman signals. This phase difference is the reason why we have a negative intercept in Fig. 5.16. As the offset is comparable to the Raman signal when probing dilute samples, it is important to subtract it from the lock-in output. Throughout this chapter, all the SRS results have already been subtracted with this offset correctly.

5.5 Comparison Between SRS and Spontaneous Raman Scattering

Now we have recorded the SRS signal from DMSO, it is interesting to benchmark the performance of SRS against spontaneous Raman scattering in term of signal-to-noise ratio (SNR).

It is important to emphasize again that the SRS signal is the strength of the modulation of the Stokes beam, while the spontaneous Raman signal is the total optical power of the newly generated Stokes beam. As a result, while spontaneous signal can be detected with “simply” a spectrometer, SRS involves the comparatively sophisticated modulation transfer detection scheme. However, the amplitude of the signal is greatly enhanced in SRS, which allows the use of a room-temperature detector, while deep-cooled detectors are commonly used for spontaneous Raman scattering. Recognizing these merits and drawbacks in terms of instrumentation, we focus only on the SNR of both methods in this section.

5.5.1 Estimation of the Spontaneous Raman Gain Coefficient

To characterize the strength of the spontaneous Raman signal of a DMSO-clad waveguide, we use a confocal Raman microscope as shown in Fig. 5.18. A laser emitting at 785 nm is used as pump. The polarization of the pump beam is controlled by a half-wave plate to excite the fundamental TE mode of the waveguide. The pump is coupled into the waveguide by an objective, and the same objective is used to collect the backward-propagating spontaneous Raman signal. The pump beam is filtered out by a dichroic mirror and further suppressed by an edge filter. The spontaneous Raman signal is then directed into a 100 μm multi-mode fiber (MMF) which is connected to a spectrometer.

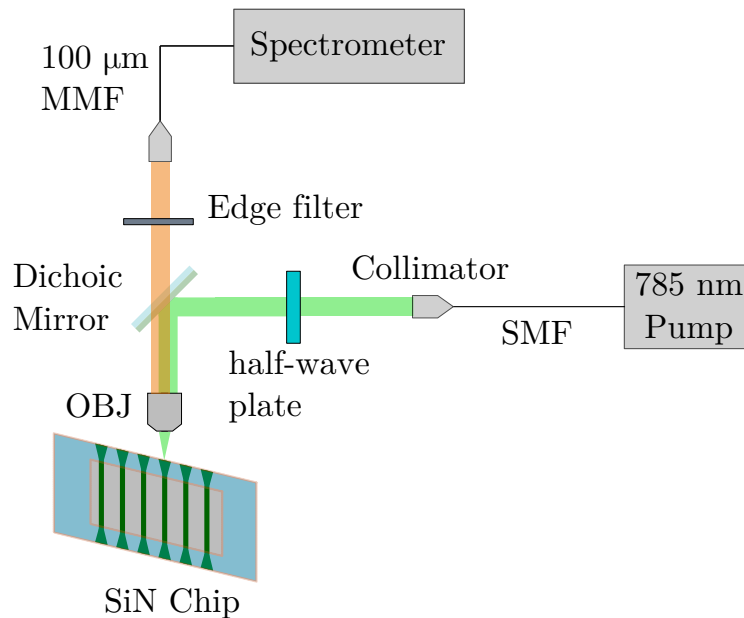


Figure 5.18: The setup for the spontaneous Raman measurement. We use the same sample for both SRS and spontaneous Raman scattering. The waveguide is pumped by a 785 nm laser to excite the fundamental TE mode. The spontaneous Raman signal in backward-propagation is captured and analyzed.

The Raman spectra of DMSO measured with the microscope is shown in Fig. 5.14. Note that we are using exactly the same waveguide for both spontaneous and stimulated measurements. The waveguide has a nominal cross-section of $w \times h = 700 \text{ nm} \times 300 \text{ nm}$ and the interaction length with DMSO is also 8 mm. The total counts registered by the spectrometer over the whole 670 cm^{-1} Raman mode amounts to $F = (5.8 \pm 0.2) \times 10^3$. To convert this counts recorded in spectrometer into photon numbers within the MMF, we should take into account

the optical transmission from the MMF to the camera within the spectrometer, the quantum efficiency of the camera, and the analog-to-digital conversion efficiency of the camera. In our setup, the conversion ratio from photon counts within the MMF to counts in camera is found to be $\zeta = 5.6 \pm 0.2$ photons per count [9].

The pump power measured before the objective is found to be $P_{pf} = 18.3$ mW. Given the transmission of the objective ($T_o = 0.76$) and the coupling loss from free-space to waveguide facet ($T_f = 0.4 \pm 0.1$), the pump power on chip is estimated to be

$$P_p = P_{p0}T_oT_f = (6 \pm 1) \text{ mW}. \quad (5.20)$$

Taking into account the integration time ($T = 0.233$ s), the transmission from the microscope to the MMF ($T_m = 0.8 \pm 0.1$), the transmission of the objective ($T_o = 0.76$), the coupling loss at facet ($T_f = 0.4 \pm 0.1$) and the energy of the Stokes photons $\hbar\omega = 1.5$ eV, we estimate the Stokes power right before leaving the waveguide is

$$P_s = \frac{\hbar\omega\zeta F}{TT_oT_mT_f} = (1.4 \pm 0.4) \times 10^{-13} \text{ W}. \quad (5.21)$$

Recall from the previous chapter that the collected spontaneous Raman power P_s is connected to the pump power P_p through the spontaneous gain coefficient G_{\parallel} as

$$P_s(0) = G_{\parallel}P_p(0)\frac{1 - e^{-2\alpha L}}{2\alpha}, \quad (5.22)$$

where we have assumed both pump and Stokes beams have the same loss. With this formula, we estimate the spontaneous Raman gain coefficient G_{\parallel} for the 670 cm^{-1} Raman mode of DMSO in waveguide to be

$$G_{\parallel} = \frac{P_s}{P_p} \frac{2\alpha}{1 - \exp(-2\alpha L)} = (5 \pm 2) \times 10^{-9} \text{ m}^{-1}, \quad (5.23)$$

where the propagation loss is taken to be $\alpha = 0.69/\text{cm} \equiv 3 \text{ dB/cm}$.

5.5.2 Estimation of the Stimulated Raman Gain Coefficient

The SRS result for pure DMSO is shown in Fig. 5.14. The maximal electrical signal at the lock-in amplifier is $I_{\text{det}} = 2.3 \mu\text{V}$ for the 670 cm^{-1} mode. Taking into account the sensitivity of the detector $R = 0.53 \text{ A/W}$, the amplification ratio of the transimpedance amplifier $A = 10^4 \text{ V/A}$, the transmission from the objective to the balanced detector $T_{\text{od}} = 0.35$, and coupling loss at facets $T_{\text{fo}} = 0.17$, the propagating SRS signal on-chip is

$$P_{s,RF}(L) = \frac{I_{\text{det}}}{ART_{\text{fo}}T_{\text{od}}} = (7.3 \pm 0.2) \times 10^{-9} \text{ W}. \quad (5.24)$$

The effective pump and Stokes power in free space are 20 mW and 60 mW respectively. Considering the coupling loss at facets $T_{\text{fo}} = 0.17$, the effective pump power on-chip is $P_p(L) = 3$ mW, and the effective Stokes power on-chip $P_s(0) = 10$ mW. Remember from Eq. (5.1) that the transmitted Stokes power is related to the pump and the Stokes power as

$$P_s(L) = \underbrace{P_s(0) \exp(-\alpha_s L)}_{\text{Local Oscillator, DC}} + \underbrace{P_s(0) g_{\parallel} P_p(L) L_{\text{eff}} \exp(-\alpha_s L)}_{\text{Raman Signal, RF}}. \quad (5.25)$$

where the effective length is defined as

$$L_{\text{eff}} = \frac{1 - e^{-\alpha_p L}}{\alpha_p}. \quad (5.26)$$

We can calculate the stimulated Raman gain as

$$g_{\parallel} = \frac{P_{s,RF}(L) \exp(\alpha_s L)}{P_s(0) P_p(L) L_{\text{eff}}} = (6 \pm 4) \times 10^{-2} \text{ W}^{-1} \text{ m}^{-1}. \quad (5.27)$$

5.5.3 Enhancement of SRS over Spontaneous Raman Scattering

As we have now obtained the gain coefficients of both SRS and spontaneous Raman scattering, we can compare the signal intensity of both modalities with the same excitation power. Assume that we have a pump beam of 20 mW in free space and we are probing pure DMSO with a waveguide whose nominal cross-section is $w \times h = 700 \text{ nm} \times 300 \text{ nm}$. Considering the coupling loss at the facet $T_{\text{fo}} = 0.17$, after an interaction length of 8 mm, the spontaneous Raman power in forward-collection is

$$\text{spontaneous power} = G_{\parallel} P_p e^{-\alpha L} L = (8.5 \pm 0.5) \times 10^{-14} \text{ W}. \quad (5.28)$$

Note that the length of the waveguide is assumed to be 1 cm, which is shorter than the optimal length for the forward-collection spontaneous Raman scattering experiments. Therefore the signal intensity for both forward-collection and backward-collection are almost identical.

In SRS, in addition to the pump of 20 mW, the Raman interaction is stimulated by a Stokes beam with a power of 60 mW in free-space. The SRS signal is given by

$$\text{SRS power} = g_{\parallel} P_p P_s L_{\text{eff}} e^{-\alpha L} = (6.9 \pm 0.2) \times 10^{-9} \text{ W}. \quad (5.29)$$

The enhancement of SRS signal over the spontaneous Raman one is determined to be

$$\text{enhancement} = \frac{\text{SRS power}}{\text{spontaneous power}} = (8 \pm 5) \times 10^4. \quad (5.30)$$

In theory, the enhancement ratio of SRS can also be estimated through [3]

$$\text{Rate}_{\text{SRS}}/\text{Rate}_{\text{Spon}} = n_s + 1, \quad (5.31)$$

where n_s is the number of Stokes photons within the analyte. The number of Stokes photon within the analytes can be estimated as

$$n_s = \frac{P_s}{\hbar\omega} T_{\text{fo}} \frac{L}{c/n_g} \exp(-\alpha L) \eta_0. \quad (5.32)$$

In our experiment $P_s = 60 \text{ mW}$ is the power of the Stokes beam in free-space, $T_{\text{fo}} = 0.17$ is the coupling efficiency from free-space to the waveguide, $\hbar\omega = 1.55 \text{ eV}$ is the energy of the photon, $L = 8 \text{ mm}$ is the length of the waveguide, c is the speed of light in vacuum, $n_g = 2$ is the group velocity of the Stokes beam, $-\alpha = 0.69/\text{cm}$ is the waveguide loss, $\eta_0 = 0.11$ is the ratio of the Stokes beam that is propagating within the waveguide. In this case, we estimate the enhancement ratio to be $(1.4 \pm 0.4) \times 10^5$. This estimation is in reasonable agreement with the other theoretical prediction and experiments, implying the consistency of our theoretical treatments.

5.5.4 Discrepancy Between Simulations and Experiments

In the previous chapter, we have estimated in theory the spontaneous gain coefficient G_{\parallel} and the SRS gain coefficient g_{\parallel} . We list the theoretical estimations along with experimental results in Table 5.2.

	Spon. Gain G_{\parallel}	Stim. Gain g_{\parallel}	Ratio between g_{\parallel} and G_{\parallel}
Theory	$3 \times 10^{-7}/\text{m}$	$2.1/(\text{W m})$	$7 \times 10^6/\text{W}$
Experiments	$5 \times 10^{-9}/\text{m}$	$6 \times 10^{-2}/(\text{W m})$	$1.2 \times 10^7/\text{W}$
Ratio between theory and experiments	60	35	0.6

Table 5.2: The theoretical and experimental values of the spontaneous Raman gain coefficient G_{\parallel} and the stimulated Raman gain coefficient g_{\parallel} . The theoretical values of G_{\parallel} and g_{\parallel} are 60 and 35 times larger than the experimental values, respectively.

Surprisingly, on the one hand, we notice that the experimental values of both SRS gain coefficient g_{\parallel} and spontaneous Raman gain coefficient G_{\parallel} are more than one order of magnitude smaller than the theoretical estimations. On the other hand, the theory gives a correct prediction of the ratio between g_{\parallel} and G_{\parallel} .

A similar discrepancy has also been observed in on-chip spontaneous Raman measurements for isopropyl alcohol (IPA) [1]. The experimental value of spontaneous Raman gain coefficient G_{\parallel} is also one order of magnitude smaller than

the theoretical prediction. Possibly, this discrepancy arises from an overestimation of the quantum enhancement. However, further investigations are necessary to pinpoint its origin.

5.5.5 Estimation of the Ultimate SRS Performance

Although the stimulation by the Stokes beam dramatically intensifies the Raman signal, it also induces extra shot noise to the system. The employment of room-temperature detectors further deteriorates the signal-to-noise ratio. When determining the modulation frequency, the shot noise associated with 0.25 mW of Stokes power incident on the balanced detector (corresponding to the maximum power injection in the measurements) is measured to be $41 \text{ nV}/\sqrt{\text{Hz}}$, while the dark noise is $71 \text{ nV}/\sqrt{\text{Hz}}$. It implies the dark noise still limits the performance in our demonstrations.

In recording the SRS signal from 2% DMSO, we used a time constant of 600 ms. It corresponds to a noise equivalent bandwidth of 114 mHz [2]. The total noise is then $71 \text{ nV}/\sqrt{\text{Hz}} \times \sqrt{114 \text{ mHz}} = 23.9 \text{ nV}$. The signal was measured to be 44 nV with 10 mW of guided Stokes power and 3 mW of guided pump power. Given this signal and noise, we expected to have an SNR of 1.8. The estimation is consistent with our experiments, where an SNR of 1.5 is obtained. If this electronic noise would be suppressed by a better detector, the shot-noise-limited SNR will increase to 3.5.

For a direct comparison, an SNR of 1.9 is measured in on-chip spontaneous Raman measurement with 3 mW of pump power on the chip in backward collection configuration. The integration time is 30 s. The integration time for the spontaneous Raman experiment is the same as that we used to record 2% DMSO with SRS in Fig. 5.15(b) with a 3 cm^{-1} resolution. The major noise source of the spontaneous measurements is the shot noise associated with the Raman background from the waveguide core.

On-chip spontaneous Raman scattering outperforms SRS with a small margin under the current excitation level. The detection limit for both methods is around 1% of DMSO. However, as we will show later, the SRS can gain more from improvements in both excitation powers and waveguide loss.

Before jumping into the discussion of improvements from the waveguide perspective, we emphasize that the current level of dark noise can be easily reduced by a better balanced-detector. The balanced detector used in our setup has a noise equivalent power (NEP) of $28.9 \text{ pW}/\sqrt{\text{Hz}}$, which accounts for the majority of the dark noise observed in the SRS experiments. However, balanced detectors with a much lower NEP ($5 \text{ pW}/\sqrt{\text{Hz}}$) are commercially available [10]. With these low noise balanced amplifiers, we believe it possible to work in the regime where the shot noise from the local oscillator dominates the dark noise. Therefore we assume

the fundamental noise source in SRS is the shot noise from the local oscillator. In this case, the signal and noise of SRS are given by

$$\text{Signal of SRS} = \underbrace{T_{\text{fo}}P_p}_{\text{input pump}} T_{\text{od}}T_{\text{fo}} \underbrace{T_{\text{fo}}P_s}_{\text{input Stokes}} g_{\parallel} L_{\text{eff}} e^{-\alpha L} \frac{T}{\hbar\omega}, \quad (5.33)$$

$$\text{Noise of SRS} = \sqrt{T_{\text{od}}T_{\text{fo}} \underbrace{T_{\text{fo}}P_s}_{\text{input Stokes}} e^{-\alpha L} \frac{T}{\hbar\omega}}, \quad (5.34)$$

where T is the integration time, and $\hbar\omega$ is the energy of the Stokes photon. The signal and the noise are all expressed as photon number. The meaning of the parameters and their experimental values are listed in Table. 5.3.

parameters	numerical value
facet-objective coupling T_{fo}	0.2
transmission after objective to detector T_{od}	0.35
waveguide loss α	0.26/cm
Stimulated Raman gain coefficient g_{\parallel}	$4.3 \times 10^{-2} \text{ W}^{-1} \text{ m}^{-1}$
Spontaneous Raman gain for pure DMSO G_{\parallel}	$5.9 \times 10^{-9} \text{ m}^{-1}$
Spontaneous Raman gain for background G'_{\parallel}	$2 \times 10^{-7} \text{ m}^{-1}$
Settling time T for SRS	1 s
Integration time T for SpRaman	30 s
Interaction Length L	1 cm

Table 5.3: The parameters used for comparing the performance of stimulated Raman scattering and spontaneous Raman scattering.

In the spontaneous measurement, the dominant noise source is the shot noise associated with the Raman response from the waveguide [11]. This is expected, because we have a sizeable overlap between the guided mode and the silicon nitride core. As a result, the Raman response of the waveguide core dominates the Raman signal, and its shot noise constitutes the primary noise term. The signal and noise of the spontaneous method become

$$\text{Signal of SpRaman} = T_{\text{od}}T_{\text{fo}} \underbrace{T_{\text{fo}}P_p}_{\text{input pump}} G_{\parallel} e^{-\alpha L} L \frac{T}{\hbar\omega}, \quad (5.35)$$

$$\text{Noise of SpRaman} = \sqrt{T_{\text{od}}T_{\text{fo}} \underbrace{T_{\text{fo}}P_p}_{\text{input pump}} G'_{\parallel} e^{-\alpha L} L \frac{T}{\hbar\omega}}, \quad (5.36)$$

where G'_{\parallel} is the spontaneous Raman gain of the waveguide core. For a 300-nm-thick strip waveguide, G'_{\parallel} is approximately $2 \times 10^{-7}/\text{m}$. We emphasize that G'_{\parallel} arise from the thermodynamic effects [6] of the silicon nitride waveguide and it

is immune to changes in the concentration of liquid analytes. To compare the performance of both spontaneous and stimulated methods, we assume the pump and the Stokes lasers in SRS are of equal power $P/2 = P_s = P_p$ where P is the pump power of the spontaneous method. In this case, we can ensure that the same amount of power is incident into the system for both methods for a fair comparison. The SNRs of these two configurations are given by

$$\text{SNR of SRS} = T_{\text{fo}}^2 \sqrt{e^{-\alpha L} T_{\text{od}}} \sqrt{\frac{T}{\hbar\omega}} \sqrt{\frac{P^3}{8} L_{\text{eff}} g_{\parallel}}, \quad (5.37)$$

$$\text{SNR of SpRaman} = T_{\text{fo}} \sqrt{\frac{T}{\hbar\omega}} \sqrt{e^{-\alpha L} T_{\text{od}}} \sqrt{PL} \frac{G_{\parallel}}{\sqrt{G'_{\parallel}}}. \quad (5.38)$$

There are a few important features to notice in these two equations:

1. The SNR of spontaneous Raman scattering is proportional to $P^{\frac{1}{2}}$ while the SNR of SRS is proportional to $P^{\frac{3}{2}}$. This suggests the performance of SRS ramps up more quickly than that of spontaneous Raman measurement with increasing excitation power within the waveguide.
2. The SNR of SRS is proportional to T_{fo}^2 , and it is proportional to T_{fo} for spontaneous measurements. It suggests the stimulated method gains more from better facet couplers.
3. The SNR of SRS scales linearly with the effective length of the waveguide. However, the SNR of spontaneous Raman scattering is proportional to $L^{\frac{1}{2}}$. Therefore improvements in fabrication that suppresses the waveguide loss will provide a more substantial benefit to SRS.
4. The SNR of both spontaneous Raman scattering and SRS scales linearly with the concentration of the analyte. So both techniques are suitable for quantitative chemical analysis.

It is helpful to explore the ultimate performance of both SRS and spontaneous Raman scattering in practical experimental conditions. Suppose we are probing pure DMSO with the evanescent field of a 1-cm-long stripe waveguide. The parameters of the experiments are listed in Table. 5.3.

We first compare the performance of both modalities with varying excitation powers. The estimated SNR for both techniques under varying excitations is shown in Fig. 5.19(a). It is clear that the spontaneous Raman technique outperforms SRS at lower excitation levels. However, at elevated excitation powers, the performance of SRS quickly catches up with and even surpasses its spontaneous counterpart. At $P = 700 \text{ mW}$, the SNR of SRS is about twice as good as that in spontaneous Raman scattering.

In Fig. 5.19(a), we notice there exists an excitation level that both spontaneous and stimulated methods have the same SNR. This tipping point is influenced by the coupling efficiency at the facet. In Fig. 5.19(b) we plot the relationship between the power of this tipping point and the facet coupling efficiency T_{fo} . It is clear that improvements in T_{fo} will enable SRS to outperform spontaneous Raman scattering at a relatively low excitation level.

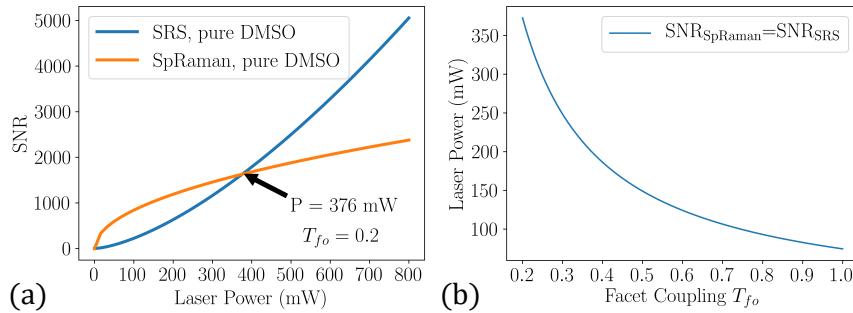


Figure 5.19: (a) Estimation of SNR for both spontaneous Raman scattering and SRS with different excitation powers in free space. At a low excitation power, the spontaneous technique outperforms SRS. However, the performance of SRS soon catches up with and surpasses its spontaneous counterpart at a higher excitation power. (b) The excitation power required for SRS to have the same performance as spontaneous Raman scattering is plotted with varying facet coupling efficiency T_{fo} . With a better coupling scheme, the SRS will outperform its spontaneous counterpart at a comparatively low power.

In Fig. 5.20(a) we investigate the impact of waveguide length on the performance. The excitation power is set to $P = 350$ mW in this case. Note that the pump and the Stokes power are $P_s = P_p = 175$ mW respectively. In both spontaneous and stimulated measurements, there exists an optimal length of the waveguide. For spontaneous scattering, the optimal length $L_{opt,sp}$ maximize $\sqrt{L}e^{-\alpha L}$. For a waveguide with a loss of 1 dB/cm, the optimal length for spontaneous Raman scattering is

$$L_{opt,sp} = 1/\alpha = 4.34 \text{ cm.} \quad (5.39)$$

For the stimulated Raman scattering, the optimal length should instead maximize $L_{eff}\sqrt{e^{-\alpha L}}$ and it is given by

$$L_{opt,SRS} = \ln(3)/\alpha = 4.77 \text{ cm.} \quad (5.40)$$

The optimal length of SRS is slightly longer than that for spontaneous Raman scattering, which is consistent with what we found in Fig. 5.20. Suppose the waveguide is always cut at its optimal length, we show the best available performance for both methods in Fig. 5.20(b). The performance of spontaneous Raman scattering is less influenced by waveguide loss. In comparison, SRS benefits more in a

low-loss waveguide and suffers more in a high-loss waveguide. It is worthwhile to point out the performance of SRS “blows up” with a vanishing propagation loss. Given that the current propagation loss (3 dB/cm) is already relatively low, improvements in waveguide loss might bring SRS a huge advantage. Note that we assume we are using the forward-collection configuration. However, because we are limited to the optimal length, the conclusion is also applicable to backward-collected spontaneous signals.

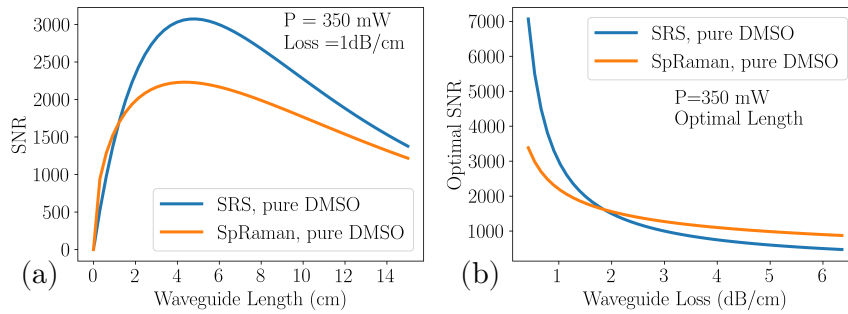


Figure 5.20: (a) The SNR of both SRS and spontaneous Raman scattering with different wavelength lengths. There exist an optimal length for both methods. (b) If the length of the waveguide is fixed at the optimal point, the best available performance is plotted for both methods. SRS shows a steeper dependency on propagation loss.

5.5.6 Practical Improvements on SNR of SRS

In the previous section, we learned that SRS can benefit from a better coupling, a higher excitation level and a lower waveguide loss. However, not all of these improvements are straightforward to implement. For example, we cannot increase the laser power indefinitely without damaging the waveguide facets. In practice, we identify three improvements that can be incorporated in future SRS experiments in a straightforward manner: (a) the reduction of coupling loss, (b) a better modulation scheme and (c) the use of slot waveguides.

- (a) It is demonstrated that mode size converters are capable of reducing the coupling loss substantially from 7.5 dB to below 1 dB. According to Fig. 5.19 and the discussion on SNR, such an improvement in T_{fo} is capable of boosting the signal level by more than 18 dB and the SNR by more than 12 dB. However, most designs of such mode size converters do not take into account the requirement of an extremely low back-reflection. In the present case, such a low back-reflection is required for waveguide-based SRS to get rid of the spurious signal. Currently, we do not have an optimized mode size

converter with a coupling loss lower than 1 dB in combination with a modal reflection lower than -40 dB yet.

- (b) Currently, our pump laser is direct-modulated with a 30 % modulation depth by the input current, and a deeper modulation is not achievable without introducing a significant distortion of the laser spectrum. Commercially available free-space resonant Pockel cells, acousto-optic modulators or broadband electro-optic modulators [3] can all achieve full-modulation of the pump beam. The improvement in modulation depth from 30 % to 100 % will improve the signal by 5.2 dB.
- (c) The last enhancement we talked about is the use of slotted waveguide rather than rib waveguides. It is shown in [12] that highly-confined slot waveguides are capable of improving the Raman conversion efficiency g_{\parallel} by 8-times. If the waveguide loss remains the same, the SRS will be improved by 9 dB by slot waveguides. However, this enhancement is not yet observed in the current SRS experiments because tested slot waveguides were excessively long and lossy. As it is discussed in the previous section, the optimal length of SRS scales with the inverse of the waveguide loss. Currently the propagation loss for the tested waveguide can be as high as 10 dB/cm, and the optimal length is only 0.45 cm. It is shown in Fig. 5.20(b) that the performance of SRS is sensitive to the propagation loss and waveguide length. Compared to spontaneous Raman experiment, the waveguide loss is more detrimental to SRS as it not only limits the strength of the Raman scattered light, it also lowers the enhancement gained from self-heterodyned detection by decreasing the transmittance of the original Stokes beam. As a result, the expected better performance of SRS in slotted waveguides has yet to be demonstrated. We believe an optimization of the waveguide loss which is closely related to the fabrication processes can reinstate the slot enhancement in SRS in the near future.

In the current setup, we reach a 5-order-of-magnitude enhancement in signal strength, and we believe there exist another 32.2 dB ($= 18$ dB + 5.2 dB + 9 dB) enhancement that is achievable by a combination of these improvements.

5.6 Conclusions and Perspectives

We demonstrated, for the first time, SRS on a CMOS-compatible silicon nitride waveguide with two CW excitations with room-temperature detectors. Apart from the waveguide enhancement, the SRS signal is intensified by five orders of magnitude as compared to the on-chip spontaneous result thanks to the stimulated excitation. The Raman spectra of 280 mM (2 %) of DMSO dissolved in water have been

successfully recorded from a 1-cm-long waveguide with sub-10-mW excitations on the chip and a time constant of 600 ms. Currently the ultimate performance of SRS has not been fully explored. Practically, we can only probe approximately 1 % of DMSO. However, based on the analysis given in Section 5.5.5 and Section 5.5.6, we believe on-chip SRS will allow for sub-millimole detection for molecules with bio-significance with improvements in modulation, waveguide design and light coupling.

In replacing the deep-cooled detectors in spectrometers, our work holds the potential to enable a full integration of the Raman sensor on a small foot-print chip that is compatible with CMOS infrastructure. We envisage an on-chip multiplexed SRS sensor with integrated multi-channel lock-in amplifiers each dedicated to a specific Raman wavelength. We believe this work will open new opportunities in real-time molecular identification and quantification, constituting a versatile tool for drug development, health monitoring, and real-time environmental sensing.

References

- [1] Ashim Dhakal, Ananth Z. Subramanian, Pieter Wuytens, Frédéric Peyskens, Nicolas Le Thomas, and Roel Baets. *Evanescent excitation and collection of spontaneous Raman spectra using silicon nitride nanophotonic waveguides*. Optics Letters, 39(13):4025–4028, June 2014.
- [2] Zurich Instruments AG. *HF2 User Manual - ziControl Edition*, 49900 edition.
- [3] Ji-Xin Cheng and Xiaoliang Sunney Xie, editors. *Coherent Raman Scattering Microscopy*. CRC Press, 2013.
- [4] *Silicon Photodiodes*. https://www.hamamatsu.com/resources/pdf/ssd/si_pd_kspd0001e.pdf.
- [5] Bozena Jaskorzynska, Johan Nilsson, and Lars Thylén. *Modal reflectivity of tapered, tilted-facet, and antireflection-coated diode-laser amplifiers*. Journal of the Optical Society of America B, 8(2):484–493, February 1991.
- [6] Nicolas Le Thomas, Ashim Dhakal, Ali Raza, Frédéric Peyskens, and Roel Baets. *Impact of fundamental thermodynamic fluctuations on light propagating in photonic waveguides made of amorphous materials*. Optica, 5(4):328–336, April 2018.
- [7] Scott A. Holmstrom, Todd H. Stievater, Dmitry A. Kozak, Marcel W. Pruessner, Nathan Tyndall, William S. Rabinovich, R. Andrew McGill, and Jacob B. Khurgin. *Trace gas Raman spectroscopy using functionalized waveguides*. Optica, 3(8):891–896, August 2016.
- [8] Victoria M. Wallace, Nilesh R. Dhumal, Florian M. Zehentbauer, Hyung J. Kim, and Johannes Kiefer. *Revisiting the Aqueous Solutions of Dimethyl Sulfoxide by Spectroscopy in the Mid- and Near-Infrared: Experiments and Car-Parrinello Simulations*. The Journal of Physical Chemistry B, 119(46):14780–14789, November 2015.
- [9] Pieter Wuytens. *Surface-Enhanced Raman Spectroscopy for Intracellular Sensing and Protease Activity Detection: From Chip Technology to Applications*. PhD thesis, Ghent University, 2017.
- [10] *EXALOS Balanced Transceiver*. <http://www.exalos.com/wp-content/plugins/csvproducts/lib/download.php?pdf=/productinfo/spec/EBR370002-02.pdf>.
- [11] Ashim Dhakal. *Nanophotonic Waveguide Enhanced Raman Spectroscopy*. PhD thesis, Ghent University, 2016.

-
- [12] Ashim Dhakal, Ali Raza, Frédéric Peyskens, Ananth Z. Subramanian, Stéphane Clemmen, Nicolas Le Thomas, and Roel Baets. *Efficiency of evanescent excitation and collection of spontaneous Raman scattering near high index contrast channel waveguides*. *Optics Express*, 23(21):27391–27404, October 2015.

6

Conclusions and Perspectives

6.1 Conclusions from the Presented Work

In this thesis, we explored if we can demonstrate coherent Raman scattering (CRS) on the silicon nitride platform. The target of this research was to demonstrate waveguide-based CRS sensors that combined both the wave-guiding enhancement and coherent excitation enhancement mechanisms. We expected to have a much-improved Raman signal that, combined with other photonic and electronic functionalities, allowed for an all-on-a-chip integrated Raman spectroscopic system. Two modalities of CRS were explored — coherent anti-stokes Raman scattering (CARS) and stimulated Raman scattering (SRS).

In the first modality, CARS was considered as the natural extension of spontaneous Raman scattering. In spontaneous Raman scattering, we probe the newly generated Stokes waves while the newly created anti-Stokes signals are detected in CARS. Due to this similarity in the detection scheme, CARS was demonstrated earlier than SRS in CRS microscopy, and it is more extensively used [1] nowadays. However, our work revealed that waveguide-enabled CARS suffered from severe limitations in detection bandwidth and wavelength length. CARS is usually modeled as a degenerate four-wave mixing process, and it requires the phase-matching condition between the pump beam, the Stokes beam and the newly created anti-Stokes beam. In CARS, the frequency difference between these optical fields is determined by the vibrational mode. Since the frequency shift of vibrational modes is typically quite significant (a few tens of THz), in the first-order approximation,

the phase-matching condition requires that the waveguide exhibits minimal group velocity dispersion β_2 at the pump wavelength.

This phase-matching condition was demanding for silicon nitride waveguides. Silicon nitride itself has substantial material dispersion over the therapeutic window from 700 nm to 900 nm. The modest index contrast between the silicon nitride core and the surround analytes, either gases or liquids, is usually insufficient to introduce enough geometry dispersion. In this work, we focused on conventional strip waveguides and slot waveguides available to us through the BioPIX project. The height of these waveguides might not exceed 300 nm. The impact of the waveguide geometry was carefully investigated for both TE and TM modes. In the end, we concluded that our CARS platform was only suitable for gas sensing and thin-film detection if part of the silicon dioxide undercladding is removed. The silicon nitride was not ideal for liquid sensing unless the waveguide length was significantly reduced due to the trade-off between wavelength length and CARS bandwidth. Since the CARS bandwidth was dictated by the frequency of the vibrational modes, one had to cut the waveguide length. This trade-off significantly limited the applicability of CARS-on-chip for liquid samples. However, most Raman analytes are themselves liquids or are dissolved in solvents. This inability to probe liquid samples rendered the method of CARS-on-chip less appealing.

Although our quest for on-chip CARS was not successful, the study on group velocity dispersion opened up the potential for silicon nitride nonlinear optics. We showed that the silicon nitride waveguide could be engineered to possess anomalous dispersion at 800 nm. This anomalous dispersion was made possible by removing the silicon dioxide undercladding of the silicon nitride core. This dispersion-engineering technique enabled a miscellaneous of silicon nitride nonlinear optical studies. Among them, supercontinuum generation (SCG) with a pump laser below 1 μm was particularly interesting to us as it provided us with a unique opportunity to deliver an integrated, broadband, and high-brightness source for integrated biophotonic applications, precise frequency metrology, and optical coherent tomography. With a dispersion-engineered waveguide, we obtained the first visible-to-near-IR supercontinuum extending below 500 nm with a femtosecond pump.

Subsequently, we shifted our focus to the modality of SRS. Compared to CARS, a key advantage of SRS was that it was automatically phase-matched. However, this advantage came at a price that unlike CARS and spontaneous Raman scattering where a new frequency component was probed, SRS detected a small intensity variation of the incident beams. This SRS-induced intensity variation was so small (10^{-6} to 10^{-8}) that conventional detectors could not resolve it.

To record the SRS signal, we introduced the modulation transfer detection scheme. Our on-chip demonstration of this detection scheme, however, was highly sensitive to parasitic signals induced by the Kerr nonlinearity associated with the

silicon nitride waveguide core. Although the nonlinear effects *per se* introduced only phase shifts, these phase shifts could be converted to SRS-like parasitic signals by two interferometric paths. The first path was the Fabry-Perot cavity formed by the waveguide facets. The second path was the Mach-Zehnder Interferometer (MZI) formed by the cladding mode and the waveguides mode of the silicon nitride waveguide.

With modification on the waveguide structure and the experimental setup, we eventually eliminated these two parasitic signals and recorded for the first time the Raman information of dimethyl sulfoxide (DMSO) with the on-chip SRS modality. Despite the complications in the experimental setup, the strength of the SRS signal was found to be five orders of magnitudes stronger than its spontaneous counterpart. A theoretical model was also developed in order to identify relevant parameters. We also estimated in theory the ultimate performance of SRS and spontaneous Raman scattering. At the moment, due to the extra shot noise inherent to the SRS technique, and due to imperfections in our current setup, on-chip SRS had not outperformed spontaneous Raman scattering yet. However, our theoretical model revealed that SRS would outperform spontaneous Raman scattering with a large margin if we can make improvements in facet coupling loss, waveguide loss and increase the laser power.

In short, on-chip CRS had many aspects yet unexplored, but we have already shown the potential of SRS in future all-on-a-chip Raman spectroscopic systems. This significant enhancement allowed for the use of CW lasers with milliwatt-level powers and uncooled detectors and, therefore, setting the basis of future all-on-a-chip Raman spectrometers suitable for both gas and liquid detection.

6.2 Outlooks of Future Perspectives

The SRS system we used in this work was composed of a lock-in amplifier, a balanced detector, and two CW lasers. Current, high-performance integrated lock-in amplifiers have been realized [2, 3] where an input signal in the order of 100 nV can be detected. Integrated silicon-based balanced detectors suitable for lab-on-chip applications have also been demonstrated [4, 5]. Although monolithically integrated diode lasers at this wavelength range have not been demonstrated, the recent development of the transfer printing technique is promising to bring lasers at 785 nm onto the waveguide [6–8]. We envisage to integrate an array of lasers onto the chip, and each of the lasers is dedicated to one specific Raman mode. In this way, we can capture the Raman spectrum without tuning the wavelength of the lasers. With the development on the components, we believe it is promising to demonstrate an all-on-a-chip SRS Raman system shortly.

A fully-integrated Raman system is expected to open up new applications. We have mentioned in Chapter 1 that an all-on-a-chip Raman system, in combination

with microfluidic systems [9, 10], can be used for biological detection, drug industry, and environmental sensing [11–14]. In addition to these applications, since the integrated Raman system is capable of greatly reducing the cost, SRS-on-chip might open up many new low-budget applications. For example, an integrated Raman sensor might be used to monitor the quality of the food. Raman spectroscopy has been utilized to determine the quality of single malt Whiskey [15], fresh milk [16, 17], the quality of olive oil [18] and powder adulterants in food [19]. Currently, Raman microscopes are employed in these demonstrations, which proves to be too expensive. Given the tremendous need for food authentication tools to prevent food fraud [20, 21], and given the chemical specificity provided by the Raman technique, the integrated Raman sensor will undoubtedly play a critical role in in-situ food quality screening.

Apart from integration, we can also move the waveguide-enabled CRS techniques forward by working on the following incremental improvements of the current Raman sensors:

Improve the signal strength of SRS In Chapter 5 we discussed the possibilities of enhancing the SRS signal by three orders of magnitudes through a combination of a better modulation scheme, a better balanced-detector, a low-loss and low-modal-reflection spot size converter, and low-loss slot waveguides. We believe these improvements are feasible to implement on the current setup. These improvements are expected to enhance the signal by at least three orders of magnitudes. With this three-order-of-magnitude enhancement, on-chip SRS is expected to find many exciting applications.

Another improvement that benefits us is the suppression of Raman background associated with the silicon nitride core. A primary advantage of SRS is that the shot noise associated with the Raman signal from the silicon nitride core is no longer the limiting factor in SRS experiments. However, this substantial background itself might be a few orders of magnitude stronger than the Raman signal from analytes in the cladding. In this case, it is very challenging to subtract the background from the overall signal to re-discover the Raman spectra of the analytes.

Resolving the discrepancy between theory and experiments To implement CRS in an integrated system, we need to have a better understanding of the theory of SRS. Currently, there exists a considerable discrepancy between the theoretical estimation and the experimental measurement for spontaneous Raman gain G_{\parallel} and stimulated Raman gain g_{\parallel} . We have briefly discussed this discrepancy in Section 5.5.4. As the quantum mechanical description employed in this work has estimated the strength of spontaneous Raman scattering and SRS in fibers with a high precision, this discrepancy suggests the theory we are using might have overlooked some crucial aspects on the

implementations. A better understanding of the theory is needed to identify the optimal design parameters for CRS sensors.

Exploiting plasmonic enhancement Plasmonic structure integrated on the top surface of a silicon nitride waveguide might significantly enhance CRS signals [22]. Both CARS and SRS can reap the benefits of plasmonic enhancement. We have already discussed one benefit of surface-enhanced CARS in Section 4.2.4 that the phase-matching condition is less a problem in a plasmonic waveguide. Because CARS has a much more straightforward detection scheme where no modulation transfer detection is required, CARS might constitute an excellent complementary CRS-sensor for future all-on-a-chip Raman. In the case of SRS, because the plasmonic structures enhance both excitations, surface-enhanced SRS signal can be enhanced by a billion-fold over surface-enhanced spontaneous Raman scattering (SERS) [23]. This dramatic enhancement is forecast to allow for single-molecule Raman spectroscopy.

References

- [1] Ji-Xin Cheng and Xiaoliang Sunney Xie, editors. *Coherent Raman Scattering Microscopy*. CRC Press, 2013.
- [2] A. Gnudi, L. Colalongo, and G. Baccarani. *Integrated lock-in amplifier for sensor applications*. In Proceedings of the 25th European Solid-State Circuits Conference, pages 58–61, Sept 1999.
- [3] P. M. Maya-Hernandez, L. C. Alvarez-Simon, M. T. Sanz-Pascual, and B. Calvo-Lopez. *An Integrated Low-Power Lock-In Amplifier and Its Application to Gas Detection*. *Sensors*, 14(9):15880–15899, September 2014.
- [4] G. de Cesare, A. Nascetti, R. Scipinotti, A. Zahra, and D. Caputo. *On-chip detection performed by amorphous silicon balanced photosensor for lab-on chip application*. *Sensing and Bio-Sensing Research*, 3(3):53–58, March 2015.
- [5] Mohammed Shafiqul Hai, Meer Nazmus Sakib, and Odile Liboiron-Ladouceur. *A 16 GHz silicon-based monolithic balanced photodetector with on-chip capacitors for 25 Gbaud front-end receivers*. *Optics Express*, 21(26):32680–32689, December 2013.
- [6] John Justice, Chris Bower, Matthew Meitl, Marcus B. Mooney, Mark A. Gubbins, and Brian Corbett. *Wafer-scale integration of group III-V lasers on silicon using transfer printing of epitaxial layers*. *Nature Photonics*, 6(9):610–614, August 2012.
- [7] Andreas De Groote, Paolo Cardile, Ananth Z. Subramanian, Alin M. Fecioru, Christopher Bower, Danae Delbeke, Roel Baets, and Günther Roelkens. *Transfer-printing-based integration of single-mode waveguide-coupled III-V-on-silicon broadband light emitters*. *Optics Express*, 24(13):13754–13762, June 2016.
- [8] Jing Zhang, Bahawal Haq, James O’Callaghan, Angieska Gocalinska, Emanuele Pelucchi, António José Trindade, Brian Corbett, Geert Morthier, and Gunther Roelkens. *Transfer-printing-based integration of a III-V-on-silicon distributed feedback laser*. *Optics Express*, 26(7):8821–8830, April 2018.
- [9] P. C. Ashok, G. P. Singh, K. M. Tan, and K. Dholakia. *Fiber probe based microfluidic raman spectroscopy*. *Optics Express*, 18(8):7642–7649, April 2010.
- [10] Xudong Fan and Ian M. White. *Optofluidic microsystems for chemical and biological analysis*. *Nature Photonics*, 5(10):591–597, October 2011.

- [11] Christoph Krafft, Gerald Steiner, Claudia Beleites, and Reiner Salzer. *Disease recognition by infrared and Raman spectroscopy*. *Journal of Biophotonics*, 2(1-2):13–28, February 2009.
- [12] Kenny Kong, Catherine Kendall, Nicholas Stone, and Ioan Notingher. *Raman spectroscopy for medical diagnostics From in-vitro biofluid assays to in-vivo cancer detection*. *Advanced Drug Delivery Reviews*, 89:121 – 134, July 2015.
- [13] Meng-Lei Xu, Yu Gao, Xiao Xia Han, and Bing Zhao. *Detection of Pesticide Residues in Food Using Surface-Enhanced Raman Spectroscopy: A Review*. *Journal of Agricultural and Food Chemistry*, 65(32):6719–6726, August 2017.
- [14] Bo Bao, Jason Riordon, Farshid Mostowfi, and David Sinton. *Microfluidic and nanofluidic phase behaviour characterization for industrial CO₂, oil and gas*. *Lab Chip*, 17(16):2740–2759, August 2017.
- [15] Praveen C. Ashok, Bavishna B. Praveen, and K. Dholakia. *Near infrared spectroscopic analysis of single malt Scotch whisky on an optofluidic chip*. *Optics Express*, 19(23):22982–22992, November 2011.
- [16] M.K. Nieuwoudt, S.E. Holroyd, C.M. McGoverin, M.C. Simpson, and D.E. Williams. *Raman spectroscopy as an effective screening method for detecting adulteration of milk with small nitrogen-rich molecules and sucrose*. *Journal of Dairy Science*, 99(4):2520 – 2536, April 2016.
- [17] Michél K. Nieuwoudt, Stephen E. Holroyd, Cushla M. McGoverin, M. Cather Simpson, and David E. Williams. *Screening for Adulterants in Liquid Milk Using a Portable Raman Miniature Spectrometer with Immersion Probe*. *Applied Spectroscopy*, 71(2):308–312, February 2017.
- [18] E. Consuelo Lpez-Dez, Giorgio Bianchi, and Royston Goodacre. *Rapid Quantitative Assessment of the Adulteration of Virgin Olive Oils with Hazelnut Oils Using Raman Spectroscopy and Chemometrics*. *Journal of Agricultural and Food Chemistry*, 51(21):6145–6150, October 2003.
- [19] Jianwei Qi, Kuanglin Chao, and Moon S. Kim. *Screening of adulterants in powdered foods and ingredients using line-scan Raman chemical imaging*. May 2015.
- [20] Romdhane Karoui and Josse De Baerdemaeker. *A review of the analytical methods coupled with chemometric tools for the determination of the quality and identity of dairy products*. *Food Chemistry*, 102(3):621 – 640, 2007.

- [21] Mark Woolfe and Sandy Primrose. *Food forensics: using DNA technology to combat misdescription and fraud*. Trends in Biotechnology, 22(5):222 – 226, May 2004.
- [22] Frédéric Peyskens. *Surface Enhanced Raman Spectroscopy Using a Single Mode Nanophotonic-Plasmonic Platform*. PhD thesis, Ghent University, 2016.
- [23] H. Kumar Wickramasinghe, Marc Chaigneau, Ryohei Yasukuni, Gennaro Picardi, and Razvigor Ossikovski. *Billion-Fold Increase in Tip-Enhanced Raman Signal*. ACS Nano, 8(4):3421–3426, April 2014.



A Quantum Mechanical treatment of stimulated and spontaneous Raman scattering

In this appendix, we will present the quantum mechanical treatment for both spontaneous Raman scattering and stimulated Raman scattering. This treatment has been laid down in the Ph.D. thesis of David Alan Wardle [1]. It is reproduced here mostly for completeness.

We start from the quantization of optical fields and the molecules. The light-matter interaction is then treated with the electric dipole approximation. This microscopic description of Raman scattering is then connected to macroscopic equations. With these macroscopic equations, we will investigate Raman scattering in bulk media and waveguides.

A.1 Quantization of Electromagnetic Wave

Electromagnetic radiation is usually treated as a wave-like object. The introduction of the particle-like properties is usually performed in the framework of second quantization. The comprehensive discussion of second quantization can be found in many textbooks, for example, [2, 3]. The quantization of optical fields starts from a finite volume. In a bounded system, the electric field can be written as a

summation of discrete modes:

$$\mathbf{E}(\mathbf{r}, t) = i \sum_k \sqrt{\frac{\hbar\omega_k}{2\epsilon_0}} [\alpha_k e^{-i\omega_k t} \mathbf{u}_k(\mathbf{r}) - c.c.], \quad (\text{A.1})$$

where α_k is the dimensionless amplitude of the k -th mode, ω_k is the angular frequency of the k -th mode, \mathbf{u}_k is one of the mode functions and *c.c.* is the shorthand for *complex conjugate*. The mode function \mathbf{u}_k satisfies the condition that

$$\left(\nabla^2 + \frac{\omega_k^2}{c^2} \right) \mathbf{u}_k = 0. \quad (\text{A.2})$$

It also satisfies the transversality condition

$$\nabla \cdot \mathbf{u}_k = 0. \quad (\text{A.3})$$

To quantize the field, we $\alpha_k e^{-i\omega_k t}$ by annihilation operator a_k . In this case, the electric field operator \mathbf{E} is given by

$$\mathbf{E}(\mathbf{r}, t) = i \sum_k \sqrt{\frac{\hbar\omega_k}{2\epsilon_0}} [a_k \mathbf{u}_k(\mathbf{r}) - h.c.], \quad (\text{A.4})$$

where a_k is the annihilation operator for the k -th mode. *h.c.* stands for Hermitian conjugate.

The Hamiltonian of this field is given by

$$H_F = \sum_k \hbar\omega_k a_k^\dagger a_k, \quad (\text{A.5})$$

where a_k^\dagger is the Hermitian conjugate of a_k which is also called creation operator. a_k^\dagger and a_k are also referred to as *ladder operators*.

A.1.1 Mode Function for Bulk Medium

It is convenient to write down explicitly the modes functions for some particular configurations. We first take a look at the mode functions of bulk media. Suppose we start from a finite cubic volume whose dimension is $L = V^{\frac{1}{3}}$ where V is its volume of the cube. Also, suppose we impose the periodic conditions on this cube, which are

$$\mathbf{u}_k(-L/2, y, z) = \mathbf{u}_k(L/2, y, z), \quad (\text{A.6})$$

$$\mathbf{u}_k(x, -L/2, z) = \mathbf{u}_k(x, L/2, z), \quad (\text{A.7})$$

$$\mathbf{u}_k(x, y, -L/2) = \mathbf{u}_k(x, y, L/2). \quad (\text{A.8})$$

The mode functions for this cube can be solved from Eq. (A.2) and Eq. (A.3). They are

$$\mathbf{u}_k(\mathbf{r}) = \hat{\mathbf{e}} \frac{1}{\sqrt{V}} e^{i\beta_k \cdot \mathbf{r}}, \quad (\text{A.9})$$

where $\hat{\mathbf{e}}$ is the polarization direction of the electromagnetic field. β_k is the wave number of the field and it is given by

$$\beta_k = \frac{2\pi \mathbf{k}}{L}. \quad (\text{A.10})$$

Here, \mathbf{k} is a three-dimensional vector that all of its components are integers. The dispersion between the angular frequency and the wave number for bulk media can be written as

$$\omega_k = c(\omega_k) |\beta_k|. \quad (\text{A.11})$$

where $c(\omega_k)$ is the phase velocity of the k -th mode.

A.1.2 Mode Function for Waveguides

In a wave-guiding structure, suppose the light is confined on the xy plane. The periodic condition then applies only to z , which is the propagation direction of the electromagnetic field. The boundary condition is

$$\mathbf{u}_k(x, y, -L/2) = \mathbf{u}_k(x, y, L/2). \quad (\text{A.12})$$

The mode functions within this waveguides can also be solved from Eq. (A.2) and Eq. (A.3). They are

$$\mathbf{u}_k(\mathbf{r}) = \hat{\mathbf{e}} f_k(x, y) \frac{1}{\sqrt{L}} e^{i\beta_k z} \quad (\text{A.13})$$

where f_k is the transverse mode profile, and β_k is the wave number of the k -th guided mode. The wavenumber is related to L as

$$\beta_k = \frac{2\pi k}{L}. \quad (\text{A.14})$$

In this equation, k is a positive integer. The dispersion relationship between ω_k and β_k is given by

$$\omega_k = c(\omega_k) \beta_k, \quad (\text{A.15})$$

where $c(\omega_k)$ is the phase velocity of the k -th mode.

A.1.3 Density of State

Later in this Appendix, we would need to estimate the number of photon and phonon mode. It is convenient to introduce the *density of state* (DOS), which is defined as the number of modes per unit angular frequency. Because each state occupies a unit volume in the \mathbf{k} space, in practice the DOS is usually computed by estimating the volumes.

In a bulk medium, the DOS at the vicinity of ω_k is given by

$$\rho_f(\omega_k) = 4\pi \left(\frac{L}{2\pi c(\omega_k)} \right)^3 \omega_k^2.$$

Similarly, the DOS of a waveguide at the vicinity of ω_k is

$$\rho_w(\omega_k) = \frac{L}{2\pi c(\omega_k)}.$$

A.2 Quantization of Molecules

Molecules are composed of nuclei and electrons. For a molecule with M particles (N electrons and $M - N$ nuclei), its wave function Ψ satisfied the non-relativistic Schrödinger equation

$$\left[\sum_{k=1}^M \frac{p_k^2}{2m_k} + V(\mathbf{r}_1, \mathbf{r}_2, \dots, \mathbf{r}_M) \right] \Psi(\mathbf{r}_1, \mathbf{r}_2, \dots, \mathbf{r}_M) = i\hbar \frac{\partial}{\partial t} \Psi(\mathbf{r}_1, \mathbf{r}_2, \dots, \mathbf{r}_M). \quad (\text{A.16})$$

Here p_k is the moment operator for the k -th particle. m_k is the mass of the particle and \mathbf{r}_k is its position. V is the total Coulomb interaction potential and Ψ is the wave function of the whole molecule.

Because the mass of a nucleus is much heavier than that of an electron, it is usually a good approximation to assume the nuclei are stationary. This approximation is called *Born-Oppenheimer approximation*. In this approximation, the Schrödinger equation becomes

$$\left[\sum_{k=1}^N \frac{p_k^2}{2m_e} + V(\mathbf{r}_1, \mathbf{r}_2, \dots, \mathbf{r}_N; R) \right] \Psi(\mathbf{r}_1, \mathbf{r}_2, \dots, \mathbf{r}_N; R) = i\hbar \frac{\partial}{\partial t} \Psi(\mathbf{r}_1, \mathbf{r}_2, \dots, \mathbf{r}_N; R). \quad (\text{A.17})$$

Here m_e is the mass of an electron, p_k is the momentum operator for the k -th electron and \mathbf{r}_k is the position of this electron. R is a parameter that takes into account the position of all the nuclei. Ψ is the wave function of the electron.

Eq. (A.17) contains information about two things: (1) the distribution of the electrons in space and (2) the temporal evolution of the system. In most cases, we

are only concerned with the temporal evolution of the wave function. In this case, we can rewrite the Schrödinger equation to

$$H |\chi(t)\rangle = i\hbar \frac{\partial}{\partial t} |\chi(t)\rangle, \quad (\text{A.18})$$

where H is the total Hamiltonian and $|\chi(t)\rangle$ is the state of the system.

The Hamiltonian arises from the electronic configuration is given by

$$H_E = \sum_q \hbar\omega_q |q\rangle \langle q|. \quad (\text{A.19})$$

where $|q\rangle$ is one of the electron eigenstate and ω_q is the angular frequency of this state.

Inserting Eq. (A.19) to Eq. (A.18), we obtain the general solution to $|\varphi_E(t)\rangle$ as

$$|\chi(t)\rangle_E = \sum_q c_q(t) e^{-i\omega_q t} |q\rangle, \quad (\text{A.20})$$

where c_q are time-independent at this moment. As no light-matter interaction is considered for the moment, the electron will not be excited or relax, and $c_q(t)$ will not vary in this case.

As we will show later, the molecule is interaction with optical fields is modeled with electric dipole interaction. It is useful to define dipole matrix elements $\mathbf{d}_{pq}(R)$ as

$$\mathbf{d}_{pq}(R) = e_0 \int d^3\mathbf{r}_1 \cdots \int d^3\mathbf{r}_N \Psi_p^* \left[\sum_{k=1}^N \mathbf{r}_k \right] \Psi_q. \quad (\text{A.21})$$

where e_0 is the electron charge and \mathbf{r}_k is the location of the k -th electron. The dipole moment operator for the electrons is defined as

$$\mathbf{D}(R) = \sum_{p,q} \mathbf{d}_{pq} |p\rangle \langle q|. \quad (\text{A.22})$$

In principle q and p and run through all the electronic states of a molecule. However, it is usually sufficient to consider only two electronic states — the ground state and the first excited state. The ground state is the state among $|g\rangle$ that has a lowest energy while the first excited state $|e\rangle$ has the second lowest energy. In this case, the dipole moment operator can be simplified to

$$\mathbf{D}(R) = \mathbf{d}_{eg}(R) (|e\rangle \langle g| + |g\rangle \langle e|). \quad (\text{A.23})$$

A.2.1 Nuclear Motion

In Chapter 2, we mentioned that the dipole moment of a molecule is influenced by the configuration of the nuclei from a classical perspective. From the definition of

$\mathbf{D}(R)$, we can see the dipole moment operator is explicitly dependent on R , which manifest the impact of the configuration of nuclei on the dipole moment operator.

Recall that the vibrational motions can be treated as a collection of independent oscillators. If we denote Q_l as the normal coordinate of the l -th mode, the dipole matrix element \mathbf{d}_{pq} can be expanded at R_0 as

$$\mathbf{d}_{pq}(R) = \mathbf{d}_{pq}(R_0) + \sum_l \left. \frac{\partial \mathbf{d}_{pq}(R)}{\partial Q_l} \right|_{R_0} Q_l + \dots, \quad (\text{A.24})$$

where the definition of R_0 is the same as Chapter 2. The summation should run through all the vibrational modes. However, as the vibrational modes are mutually independent, it is sufficient to focus on one particular vibrational mode for investigation. In this Appendix we will also not consider higher-order corrections of Q_l to $\mathbf{d}_{pq}(R)$. In this case, we can drop the subscript l and the dipole moment operator is simplified to

$$\begin{aligned} \mathbf{D}(R) &= \left(\mathbf{d}_{eg}(R_0) + \left. \frac{\partial \mathbf{d}_{pq}(R)}{\partial Q} \right|_{R_0} Q \right) (|e\rangle \langle g| + |g\rangle \langle e|) \\ &= (\mathbf{d}_{eg} + \mathbf{d}'_{eg} Q) (|e\rangle \langle g| + |g\rangle \langle e|). \end{aligned} \quad (\text{A.25})$$

Having established that the vibration modes can be regarded as independent harmonic oscillators, we can write down the Hamiltonian for a certain normal mode as

$$H_n = \hbar\Omega b^\dagger b, \quad (\text{A.26})$$

where b is the annihilation operator of the for this normal mode and Ω is the vibrational frequency. The eigenstate of this Hamiltonian is a number state that satisfies $H_n |n\rangle = n\hbar\Omega |n\rangle$. The quantization unit of energy associated with a vibrational mode $\hbar\Omega$ is also called *phonon*.

The general solutions of the vibrational mode are

$$|\chi(t)\rangle_N = \sum_{n=0}^{\infty} c_n(t) e^{-in\Omega t} |n\rangle, \quad (\text{A.27})$$

where $c_n(t)$ is independent of time at this stage as we have not considered explicitly the light-matter interaction. In this case, there are no phonons created or annihilated.

The normal coordinate of a normal mode can be given by the ladder operator b and b^\dagger as

$$\mathbf{Q} = \sqrt{\frac{\hbar}{2\mathcal{M}|\Omega|}} (b + b^\dagger). \quad (\text{A.28})$$

Here, \mathcal{M} is the effective mass of this vibrational mode.

A.3 Light-Matter Interaction

In the previous section, we have introduced the quantization of the fields and the vibrational modes of molecules. In this section, we will consider explicitly the process of Raman scattering. To begin with, we first write down explicitly the electric fields involved in Raman scattering. In both spontaneous Raman scattering and stimulated Raman scattering, a photon in pump mode is scattered to signal mode. Therefore, we need to consider two optical modes. Besides, since the pump mode is sufficiently intense, it can be treated as a classical electromagnetic wave. In contrast, the signal beam is usually weak (especially for spontaneous Raman scattering, which starts from vacuum fluctuations). It should be treated quantum mechanically. Therefore, the electric fields of these two modes are given by

$$\mathbf{E}(\mathbf{r}, t) = i\sqrt{\frac{\hbar\omega_p}{2\epsilon(\omega_p)}}[\alpha_p e^{-i\omega_s t} \mathbf{u}_p(\mathbf{r}) - h.c.] + i\sqrt{\frac{\hbar\omega_s}{2\epsilon(\omega_s)}}[a_s \mathbf{u}_s(\mathbf{r}) - c.c.], \quad (\text{A.29})$$

where ω_s and ω_p are the angular frequency for the pump mode and the signal mode respectively. \mathbf{u}_s and \mathbf{u}_p are their mode functions. α is related to the electric field of the pump mode and a_s is the annihilation operator of the signal mode.

The state of the whole system, including molecule and two optical fields, are described by

$$\sum_{\substack{q=g,e \\ m=0 \rightarrow \infty \\ n=0 \rightarrow \infty}} c_{qmn}(t) e^{-i\omega_q t} e^{-i\Omega t} e^{-in\omega t} |q\rangle |m\rangle |n\rangle. \quad (\text{A.30})$$

Here $|q\rangle$ is either the ground state $|g\rangle$ or the first excited state $|e\rangle$. $|m\rangle$ is the number state of the vibrational mode, and $|n\rangle$ is the number state of the signal mode.

The Hamiltonian of the system is

$$H = H_E + H_N + H_F + H', \quad (\text{A.31})$$

where H_E is the Hamiltonian associated with the electronic configuration given in Eq. (A.19). H_N is the Hamiltonian associated with the vibrational mode given in Eq. (A.26). H_F is the Hamiltonian of the optical fields given in Eq. (A.5). H' is the interaction energy between the molecule and the optical fields.

$$H'$$

is given by

$$H' = \mathbf{D} \cdot \mathbf{E}(\mathbf{r}), \quad (\text{A.32})$$

where we have implicitly assumed the light-matter interaction is mediated by the electric dipole.

Rewriting the light-matter interaction in the interaction picture is useful. The wave function in the interaction picture is defined as

$$\begin{aligned} |\Psi(t)\rangle_I &= e^{i(H_e+H_n+H_F)t/\hbar} |\Psi(t)\rangle \\ &= \sum_{\substack{q=g,e \\ m=0 \rightarrow \infty \\ n=0 \rightarrow \infty}} c_{qmn}(t) |q\rangle |m\rangle |n\rangle. \end{aligned} \quad (\text{A.33})$$

The Schrödinger equation in interaction picture becomes

$$H'_I(t) |\Psi(t)\rangle_I = i\hbar \frac{\partial}{\partial t} |\Psi(t)\rangle_I,$$

with the Hamiltonian in interaction picture H'_I is given by

$$H'_I(t) = e^{i(H_e+H_n+H_F)t/\hbar} H' e^{-i(H_e+H_n+H_F)t/\hbar}. \quad (\text{A.34})$$

A.3.1 Perturbation Approximation of Light-Matter Interaction

From here on, the investigation of light-matter interaction will always be carried out in the interaction picture. Therefore we will drop the subscript of I to avoid unnecessary complications. Suppose the system is in the state $|g\rangle |m\rangle |n\rangle$ at $t = 0$,

$$|\Psi(t=0)\rangle = |g\rangle |m\rangle |n\rangle. \quad (\text{A.35})$$

Physically this equation means the molecule is in ground state and it has m phonons in the vibrational mode. The incoming signal mode has n photons.

Based on the time-dependent perturbation theory, the evolution of $|\Psi(t=0)\rangle$ under the influence of H' can be expressed as a dyade series as

$$|\Psi(t)\rangle = |\Psi(0)\rangle + \sum_{n=1}^{\infty} \left(\frac{1}{i\hbar} \right)^n \int_0^t d\tau_n \int_0^{\tau_n} d\tau_{n-1} \cdots \int_0^{\tau_2} d\tau_1 \quad (\text{A.36})$$

$$H'(\tau_n) H'(\tau_{n-1}) \cdots H'(\tau_1) |\Psi(0)\rangle. \quad (\text{A.37})$$

In this equation, the n -th integral on the right-hand side is called the n -th order perturbation. If the time scale t we considered is short (that is $tH'/\hbar \ll 1$), the contribution from higher-order terms damps down rapidly. And we can approximate $|\Psi(t)\rangle$ with the first few terms.

In Raman scattering, one pump photon is annihilated to create one Stokes photon and one phonon, yielding a final state of

$$|\Psi_F\rangle = |g\rangle |m+1\rangle |n+1\rangle. \quad (\text{A.38})$$

The probability that the initial state of $|\Psi(t=0)\rangle$ evolves to $|g\rangle |m+1\rangle |n+1\rangle$ is given by

$$p = |\langle n+1 | \langle m+1 | \langle g | \Psi(t) \rangle|^2 \quad (\text{A.39})$$

Raman scattering is induced by the second-order perturbation [2, 3]. The probability that the initial state of $|\Psi(t=0)\rangle$ evolves to $|g\rangle|m+1\rangle|n+1\rangle$ through Raman scattering is given by

$$p = \left| \langle n+1 | \langle m+1 | \langle g | \left(\frac{1}{i\hbar} \right)^2 \int_0^t d\tau_2 \int_0^{\tau_2} d\tau_1 H'(\tau_2) H'(\tau_1) |g\rangle |m\rangle |n\rangle \right|^2. \quad (\text{A.40})$$

With the Hamiltonian given in Eq. (A.34). The Raman scattering probability can be evaluated explicitly to

$$p = \left| i \sqrt{\frac{\omega_p \omega_s (n+1)(m+1)}{8\hbar \epsilon_p \epsilon_s}} \sqrt{\frac{1}{\mathcal{M}|\Omega|}} \alpha f(\Omega + \omega_s - \omega_p, t) \mathbf{u}_p(\mathbf{r}) M_4 \mathbf{u}_s^*(\mathbf{r}) \right|^2, \quad (\text{A.41})$$

where M_4 is a matrix given by

$$M_4 = \sum_e \left[\left(\frac{1}{\omega_e - \omega_g - \omega_p} + \frac{1}{\Omega + \omega_e - \omega_g + \omega_s} \right) \mathbf{d}_{eg} \mathbf{d}_{eg}^t + \left(\frac{1}{\omega_e - \omega_g - \omega_p} + \frac{1}{\Omega + \omega_e - \omega_g + \omega_s} \right) \mathbf{d}'_{eg} \mathbf{d}_{eg}^t \right]. \quad (\text{A.42})$$

Here $f(\Omega, \omega_s, \omega_p, t)$ is defined as

$$f(\Omega + \omega_s - \omega_p, t) = \frac{1}{i(\Omega + \omega_s - \omega_p)} e^{i(\Omega + \omega_s - \omega_p)t - 1} \quad (\text{A.43})$$

It is noteworthy that Ω is the angular frequency of the vibration ($\hbar\Omega$ is the energy of the phonon), ω_s and ω_p are the angular frequency of the signal mode and the pump mode respectively. There is no requirement on the relation between $\omega_s - \omega_p$ and Ω .

A.4 Raman Scattering from An Ensemble of Molecules

In the previous section, we derived the microscopic probability p of Raman scattering. Precisely, this is the probability that, a photon in *one* particular pump mode is scattered into *one* particular signal mode mediated by *one* particular phonon mode after time t . This particular phonon mode has m phonons.

In this section, we will consider the Raman scattering from an ensemble of molecules modes within volume dV . We start from counting the number of photon states within the volume dV . In thermal equilibrium, the probability that a phonon mode has m phonons is given by $B(\Omega, m, T)$

$$B(\Omega, m, T) = \left(1 - e^{-\frac{\hbar|\Omega|}{kT}} \right) e^{-\frac{m\hbar|\Omega|}{kT}}, \quad (\text{A.44})$$

where k is the Boltzmann's constant and T is ambient temperature.

The number of phonon modes within the range of $[\Omega, \Omega + d\Omega]$ is given by

$$\rho(|\Omega|)dVd\Omega. \quad (\text{A.45})$$

Therefore, the number of phonon modes having m phonons in a small volume dV within the range of $[\Omega, \Omega + d\Omega]$ is given by

$$B(\Omega, m, T)\rho(|\Omega|)dVd\Omega. \quad (\text{A.46})$$

Assuming that the scattering are incoherent, the probability that a photon in *one* particular pump mode is scattered into *one* particular signal mode mediated by *all* phonon mode with m phonons within a volume of dV within frequency the range of $[\Omega, \Omega + d\Omega]$ and after time t is given by

$$\begin{aligned} P_m(t, \Omega) &= p \times N_{\text{phonon states}} \\ &= p \times B(\Omega, m, T)\rho(|\Omega|)dVd\Omega \end{aligned} \quad (\text{A.47})$$

Using the probability p given in Eq. (A.41), we have

$$\begin{aligned} P_m(t, \Omega) &= B(\Omega, m, T)\rho(|\Omega|)dVd\Omega \frac{\omega_p\omega_s(n+1)(m+1)}{8\hbar\epsilon_p\epsilon_s} \frac{1}{\mathcal{M}|\Omega|} |\alpha|^2 \\ &\quad \times |f(\Omega + \omega_s - \omega_p, t)|^2 |\mathbf{u}_p(\mathbf{r})|^2 |\mathbf{u}_s(\mathbf{r})|^2 \overline{(\mathbf{e}_p^t M_4 \mathbf{e}_s)^2} \end{aligned} \quad (\text{A.48})$$

where $\overline{(\mathbf{e}_p^t M_4 \mathbf{e}_s)^2}$ denotes an average over all orientations of the Raman scatters.

Taken into account the contribution of all frequencies Ω , we can derive the probability of scattering after time t mediated by *all* modes with m phonons $P_m(t)$

$$P_m(t) = \int_{-\infty}^{+\infty} P_m(t, \Omega) d\Omega \quad (\text{A.49})$$

Note that $f(\Omega + \omega_s - \omega_p, t)$ is a similar to a Dirac function. It has a peak at $\Omega = \omega_p - \omega_s$ and it is basically zero everywhere else. Therefore, all the terms except for $f(\Omega + \omega_s - \omega_p, t)$ can be taken out from the integral. The assumption is valid for CW excitations. Since we will be mostly concerned with CW Raman scattering, we can simplify Eq. (A.49) as

$$\begin{aligned} B(\Omega, m, T)dVd\Omega \frac{\omega_p\omega_s(n+1)(m+1)}{8\hbar\epsilon_p\epsilon_s} \frac{\rho(|\Omega|) \overline{(\mathbf{e}_p^t M_4 \mathbf{e}_s)^2}}{\mathcal{M}|\Omega|} |\alpha|^2 \\ \times |\mathbf{u}_p(\mathbf{r})|^2 |\mathbf{u}_s(\mathbf{r})|^2 \int_{-\infty}^{+\infty} |f(x, t)|^2 dx, \end{aligned} \quad (\text{A.50})$$

The integral can also be solved to

$$\int_{-\infty}^{+\infty} |f(x, t)|^2 dx = 2\pi t. \quad (\text{A.51})$$

The scattering rate is the time derivative of $P_m(t)$, which is given by

$$\begin{aligned} \text{rate}_m = B(\Omega, m, T) dV \frac{\omega_p \omega_s (n+1)(m+1)}{8\hbar \epsilon_p \epsilon_s} \frac{\overline{\rho(|\Omega|) (\mathbf{e}_p^t M_4 \mathbf{e}_s)^2}}{\mathcal{M}|\Omega|} |\alpha|^2 \\ \times |\mathbf{u}_p(\mathbf{r})|^2 |\mathbf{u}_s(\mathbf{r})|^2 2\pi \end{aligned} \quad (\text{A.52})$$

Physically, rate_m denotes the transition rate from *one* particular pump mode to *one* particular signal mode mediated by *all* phonon modes with m phonons. We have also implicitly required $\Omega = \omega_p - \omega_s$ in this equation due to the property of $f(\Omega + \omega_s - \omega_p, t)$.

A.5 Material Raman Function

In our derivation of rate_m , we notice the scattering rate is proportional to $\overline{(\mathbf{e}_p^t M_4 \mathbf{e}_s)^2}$. A closer inspection reveals that this term is only dependent on the angle formed by \mathbf{e}_p and \mathbf{e}_s . It is convenient to introduce material Raman response functions as

$$\begin{aligned} M_{\parallel} &= \frac{\overline{\rho(|\Omega|) (\mathbf{e}_p^t M_4 \mathbf{e}_s)^2}}{\mathcal{M}|\Omega|}, & \mathbf{e}_p \text{ is parallel to } \mathbf{e}_s. \\ M_{\perp} &= \frac{\overline{\rho(|\Omega|) (\mathbf{e}_p^t M_4 \mathbf{e}_s)^2}}{\mathcal{M}|\Omega|}, & \mathbf{e}_p \text{ is perpendicular to } \mathbf{e}_s. \end{aligned}$$

The material Raman response functions contain the microscopic features of Raman scattering. The electric dipole (\mathbf{d}_{eg}), and the effective mass of the vibrational mode \mathcal{M} are all included in $M(|\Omega|)$. It is noteworthy that although one can calculate $M(|\Omega|)$ from first principles, it is more practical to estimate their values from experiments. In Chapter 3 we have connected the strength of material response functions to Raman scattering cross-sections.

A.6 Experimental Raman Scattering

In this section, we will establish the relation between microscopic quantity rate_m and the macroscopic quantities — the intensity of the scattered light. The section is split into two parts, we first derive the macroscopic equations for spontaneous Raman scattering and then the treatment is extended to stimulated Raman scattering. In this section we will consider only parallel excitations. The extension to perpendicular excitations is discussed in Chapter 3

A.6.1 Intensity of Light

It is convenient to deal with the intensity of optical fields rather than its amplitude. According to Ref. [3], the intensity of an optical field can be written as

$$I_s(\mathbf{r}) = c(\omega)\hbar\omega_s n |\mathbf{u}_s(\mathbf{r})|^2, \quad (\text{A.53})$$

$$I_p(\mathbf{r}) = c(\omega_p)\hbar\omega_p |\alpha|^2 |\mathbf{u}_p(\mathbf{r})|^2. \quad (\text{A.54})$$

The total power of can then be calculated as

$$P_s = c(\omega)\hbar\omega_s n \int_{-\infty}^{\infty} |\mathbf{u}_s(\mathbf{r})|^2 dA \quad (\text{A.55})$$

$$P_p = c(\omega)\hbar\omega_p |\alpha|^2 \int_{-\infty}^{\infty} |\mathbf{u}_p(\mathbf{r})|^2 dA \quad (\text{A.56})$$

where the intensity of a beam is measured as the optical power per unit area incident on a plane (A) normal to the propagation direction of the beam itself and dA is the unit area of this plane (A). Specially, for waveguide modes, we have

$$P_s = c(\omega)\hbar\omega_s n \int_{-\infty}^{\infty} dy \int_{-\infty}^{\infty} dx |\mathbf{u}_s(\mathbf{r})|^2 = c(\omega_s)\hbar\omega_s n \frac{1}{L}, \quad (\text{A.57})$$

$$P_p = c(\omega)\hbar\omega_p |\alpha|^2 \int_{-\infty}^{\infty} dy \int_{-\infty}^{\infty} dx |\mathbf{u}_p(\mathbf{r})|^2 = c(\omega_p)\hbar\omega_p |\alpha|^2 \frac{1}{L}. \quad (\text{A.58})$$

Here, L is a arbitrary length that is defined in Eq. (A.13).

A.6.2 Spontaneous Raman Scattering

We know that rate_m describes the transition rate from *one* particular pump mode to *one* particular signal mode mediated by *all* phonon modes with m phonons. To obtain the number of photon scattered spontaneously, we have to first multiply rate_m by the number of signal modes within $[\omega_s, \omega_s + d\omega_s]$, and take the summation of over m , which is

$$\sum_{m=1}^{\infty} (\text{rate}_m \times N_{\text{signal modes}}). \quad (\text{A.59})$$

This equation gives the transition rate from *one* particular pump mode to $N_{\text{signal modes}}$ signal modes mediated by *all* phonon modes with *any number of* phonons. It is noteworthy that we assume the pump beam is CW. That is all the pump photons are within one optical state.

A.6.2.1 Spontaneous Scattering in Bulk Medium

In a bulk medium, the number of the signal modes is given by

$$\rho_f(\omega_k) = 4\pi \left(\frac{L}{2\pi c(\omega_k)} \right)^3 \omega_k^2. \quad (\text{A.60})$$

Therefore the total power of the spontaneously scattered photons within a frequency range of $d\omega_s$ is given by

$$\begin{aligned} dP_s &= \hbar\omega_s \sum_{m=1}^{\infty} N_{\text{photon states}} \times \text{rate}_m \\ &= \hbar\omega_s \sum_{m=1}^{\infty} 4\pi \left(\frac{L}{2\pi c(\omega_s)} \right)^3 \omega_s^2 \frac{dS}{4\pi} d\omega_s \times \text{rate}_m \\ &= \sum_{m=1}^{\infty} 4\pi \left(\frac{L}{2\pi c(\omega_s)} \right)^3 \omega_s^2 \frac{dS}{4\pi} d\omega_s B(\Omega, m, T) dV \frac{\omega_p \omega_s}{8\hbar\epsilon(\omega_p)\epsilon(\omega_s)} M_{\parallel} \\ &\quad \times (m+1) |\alpha|^2 |\mathbf{u}_p(\mathbf{r})|^2 |\mathbf{u}_s(\mathbf{r})|^2 2\pi \hbar \omega_s, \end{aligned} \quad (\text{A.61})$$

where we also take into account only a portion of photon is propagation within a solid angle of dS . Since both pump and signal modes supposed to be plane waves, the power of the pump beam incident on the volume of dV is given by

$$P_p = c(\omega_p) \hbar \omega_p |\alpha|^2 |\mathbf{u}_p(\mathbf{r})|^2 dA \quad (\text{A.62})$$

where we have assumed the volume is given by $dV = dA dz$. In this case, we have

$$|\alpha|^2 |\mathbf{u}_p(\mathbf{r})|^2 |\mathbf{u}_s(\mathbf{r})|^2 = \frac{P_p}{c(\omega_p) \hbar \omega_p dA} \frac{1}{V} = \frac{P_p}{c(\omega_p) \hbar \omega_p dA} \frac{1}{L^3}. \quad (\text{A.63})$$

If we place Eq. (A.63) into Eq. (A.61), we have

$$\begin{aligned} P_s &= P_p \frac{\omega_s}{\omega_p} \frac{\omega_p \omega_s^3}{32\pi^2 \hbar^2 \epsilon(\omega_p) \epsilon(\omega_s)} \frac{1}{c^3(\omega_s) c(\omega_p)} M_{\parallel} \left[\sum_{m=0}^{\infty} B(\Omega, m, T) (m+1) \right] dS dz d\omega_s \\ &= P_p \frac{\omega_s}{\omega_p} \frac{\omega_p \omega_s^3}{32\pi^2 \hbar^2 \epsilon(\omega_p) \epsilon(\omega_s)} \frac{1}{c^3(\omega_s) c(\omega_p)} M_{\parallel} h(\Omega, T) dS dz d\omega_s. \end{aligned} \quad (\text{A.64})$$

where P_s is the power of the scattered photon over a distance of dz , lies within a frequency interval of $[\omega_s, \omega_s + d\omega_s]$ and a solid angle of dS . We also define a new function $h(\Omega, T)$ which is dependent on the temperature and the phonon frequency as

$$h(\Omega, T) = \begin{cases} (1 - e^{-\frac{\hbar\Omega}{kT}}) & \text{if } \Omega > 0 \text{ (Stokes)} \\ (e^{-\frac{\hbar\Omega}{kT}} - 1) & \text{if } \Omega < 0 \text{ (anti-Stokes)} \end{cases}. \quad (\text{A.65})$$

It is worth mentioning there is a difference in terminology. In this Appendix, dS represents the solid angle over which we collect scattered photons while in Chapter 3 the solid angle is denoted by $d\Phi$.

A.6.2.2 Spontaneous Raman Scattering in Waveguides

Similarly, we can obtain the total power of photons scattered spontaneously within a waveguide. The density of the signal mode within a waveguide is given by

$$\rho_w(\omega_k) = \frac{L}{2\pi c(\omega_k)}. \quad (\text{A.66})$$

The mode function is defined in Eq. (A.13). Over a small volume of dV , the total power of the scattered photon is

$$\begin{aligned} dP_s &= \hbar\omega_s \sum_{m=1}^{\infty} \text{rate}_m \times N_{\text{photon states}} \\ &= \sum_{m=1}^{\infty} \frac{L}{2\pi c(\omega_k)} d\omega B(\Omega, m, T) dV \frac{\omega_p \omega_s}{8\hbar\epsilon(\omega_p)\epsilon(\omega_s)} M_{\parallel} \\ &\quad \times (m+1) |\alpha|^2 |\mathbf{u}_p(\mathbf{r})|^2 |\mathbf{u}_s(\mathbf{r})|^2 2\pi\hbar\omega_s. \end{aligned} \quad (\text{A.67})$$

With Eq. (A.57) and Eq. (A.58) we have

$$|\alpha|^2 |\mathbf{u}_p(\mathbf{r})|^2 |\mathbf{u}_s(\mathbf{r})|^2 = \frac{LP_p}{c(\omega_p)\hbar\omega_p} \frac{|f_p(\mathbf{r})|^2}{L} \frac{|f_s(\mathbf{r})|^2}{L} \quad (\text{A.68})$$

Recall that $dV = dzdA$. We can integrate dP_s over dA to derive the total scattered power that is coupled into the signal mode \mathbf{u}_s . It is given by

$$\begin{aligned} P_s &= \int_A dP_s \\ &= P_p \frac{\omega_s^2}{8\hbar\epsilon(\omega_p)\epsilon(\omega_s)} \frac{1}{c(\omega_s)c(\omega_p)} h(\Omega, T) dz d\omega_s \int_{-\infty}^{\infty} dy \int_{-\infty}^{\infty} dx |f_p(\mathbf{r})|^2 |f_s(\mathbf{r})|^2 M_{\parallel} \end{aligned} \quad (\text{A.69})$$

A.6.3 Stimulated Raman Scattering

A.6.3.1 Scattering from Signal to Pump

In stimulated Raman scattering, because the signal field are intense, we need to consider the reverse process the Raman scattering. In this case, a signal photon is also possible to be scattered into the pump field. This process is called *inverse Raman scattering*. Assume the system starts at a state

$$|\Psi_i\rangle = |g\rangle |m\rangle |n\rangle. \quad (\text{A.70})$$

In inverse Raman scattering, one pump phonon is created with one signal photon and one phonon are destroyed. Therefore, the final state is given by

$$|\Psi_f\rangle = |g\rangle |m-1\rangle |n-1\rangle. \quad (\text{A.71})$$

The calculation of the probability of inverse scattering is similar to Eq. (A.41). With some algebra, the probability of inverse Raman scattering is found to be

$$p' = \frac{\omega_p \omega_s n m}{8 \hbar \epsilon_p \epsilon_s} \frac{1}{\mathcal{M} |\Omega|} |\alpha|^2 f^2(\Omega, \omega_s, \omega_p, t) |\mathbf{u}_p(\mathbf{r})|^2 |\mathbf{u}_s(\mathbf{r})|^2 \overline{(\mathbf{e}_p^t M_4 \mathbf{e}_s)^2}. \quad (\text{A.72})$$

We notice that the probability of pump-to-signal scattering is similar to signal-to-pump scattering. One only has to replace $(m+1)(n+1)$ in the former situation with mn to obtain the latter situation.

A.6.3.2 Stimulated Raman Scattering in Bulk Medium

In stimulated Raman scattering, the total transition rate is the difference between the pump-to-signal transition rate and the signal-to-pump transition rate.

In stimulated Raman scattering, we are only concerned with *one* signal mode. Therefore, it is not necessary to multiply rate_m with the number of signal states. Besides, since $n \gg 1$, we can take the approximation that $(n+1) \approx n$. The total transition rate is then

$$B(\Omega, m, T) dV \frac{\omega_p \omega_s}{8 \hbar \epsilon(\omega_p) \epsilon(\omega_s)} M_{\parallel} n |\alpha|^2 |\mathbf{u}_p(\mathbf{r})|^2 |\mathbf{u}_s(\mathbf{r})|^2 2\pi \quad (\text{A.73})$$

Notice that the intensity is related to transition rate as

$$dI_s = \text{rate} \times \frac{\hbar \omega_s}{dA}, \quad (\text{A.74})$$

Taking into account the relation between intensity and mode functions, the change of the intensity of the signal mode over a distance of dz is given by

$$dI_s = \frac{\pi \omega}{4 \hbar^2 \epsilon(\omega_p) \epsilon(\omega_s)} \frac{M_{\parallel}}{c(\omega_p) c(\omega_s)} I_p(\mathbf{r}) I_s(\mathbf{r}) dz. \quad (\text{A.75})$$

A.6.3.3 Stimulated Raman Scattering in Waveguides

The stimulated Raman scattering in the waveguide is similar to Eq. (A.73). We only need to change the mode functions in free space to the mode functions in waveguides. Starting from

$$\frac{\pi \omega_p \omega_s}{4 \hbar \epsilon(\omega_p) \epsilon(\omega_s)} M_{\parallel} \frac{LP_s}{c(\omega_s) \hbar \omega_s} \frac{LP_p}{c(\omega_p) \hbar \omega_p} |\mathbf{u}_p(\mathbf{r})|^2 |\mathbf{u}_s(\mathbf{r})|^2 dA dz \quad (\text{A.76})$$

Integrating the rate over the volume, we have the

$$\begin{aligned}
dP_s &= \hbar\omega_s \frac{\pi\omega_p\omega_s}{4\hbar\epsilon(\omega_p)\epsilon(\omega_s)} \frac{LP_s}{c(\omega_s)\hbar\omega_s} \frac{LP_p}{c(\omega_p)\hbar\omega_p} \left(\int_{-\infty}^{\infty} dy \int_{-\infty}^{\infty} dx |\mathbf{u}_p(\mathbf{r})|^2 |\mathbf{u}_s(\mathbf{r})|^2 M_{\parallel} \right) dz \\
&= \hbar\omega_s \frac{\pi\omega_p\omega_s}{4\hbar\epsilon(\omega_p)\epsilon(\omega_s)} \frac{LP_s}{c(\omega_s)\hbar\omega_s} \frac{LP_p}{c(\omega_p)\hbar\omega_p} \left(\int_{-\infty}^{\infty} dy \int_{-\infty}^{\infty} dx \frac{|f_p|^2}{L} \frac{|f_s|^2}{L} M_{\parallel} \right) dz \\
&= \hbar\omega_s \frac{\pi\omega_p\omega_s}{4\hbar\epsilon(\omega_p)\epsilon(\omega_s)} \frac{P_s}{c(\omega_s)\hbar\omega_s} \frac{P_p}{c(\omega_p)\hbar\omega_p} \left(\int_{-\infty}^{\infty} dy \int_{-\infty}^{\infty} dx |f_p|^2 |f_s|^2 M_{\parallel} \right) dz
\end{aligned} \tag{A.77}$$

where dP is the change of the power of the signal mode over a distance of dz within the waveguide.

References

- [1] David Alan Wardle. *Raman scattering in optical fibres*. PhD thesis, The University of Auckland, 1999.
- [2] Mark Fox. *Quantum Optics: An Introduction*. Oxford University Press, 2006.
- [3] Rodney Loudon. *The Quantum Theory of Light*. Oxford University Press, 2000.

B

Process flow of facet polishing

In Chapter 5, we mention that a facet polishing technique is employed to suppress the reflection of light back to the guided modes at the waveguide facet. In this appendix, we will describe in detail the procedure for polishing the facets.

Fig. B.1(a) shows the structure of the silicon nitride sample we received from imec. For facet polishing, the sample is first diced along an angle of 15° with regard to the propagating direction of the guided mode, and the resulted structure is shown in Fig. B.1(b). The surface roughness of diced facets is in the range of $10\ \mu\text{m}$ to $20\ \mu\text{m}$ depending on the composition and thickness of the diamond saw [1]. This roughness is unacceptable for high-efficiency butt coupling.

To increase the coupling efficiency, we should reduce the surface roughness to the nanometer range. A straightforward method to smooth the facet is to lap and polish the end-facet of the whole sample. In this process, a rotating polishing head, called jig, holds the sample and moves across the polishing pad. A slurry with suspended particles is applied onto a rotating polishing pad. The relative motion of the jig and the polishing pad "squeezes" the particles to smooth the waveguide facet.

The surface roughness is determined by the size of the suspended particles. A rule of thumb to choose the particle is that the surface roughness is equal to two times the size of the nanoparticle. We start from fused aluminum oxide abrasives with a diameter of $3\ \mu\text{m}$ to remove approximately $80\ \mu\text{m}$ of the material. Then we change to a much finer alkaline colloidal silica abrasive with a diameter of $40\ \text{nm}$ to remove another approximately $10\ \mu\text{m}$ of the sample. Both types of the abrasive are purchased from Logitech.

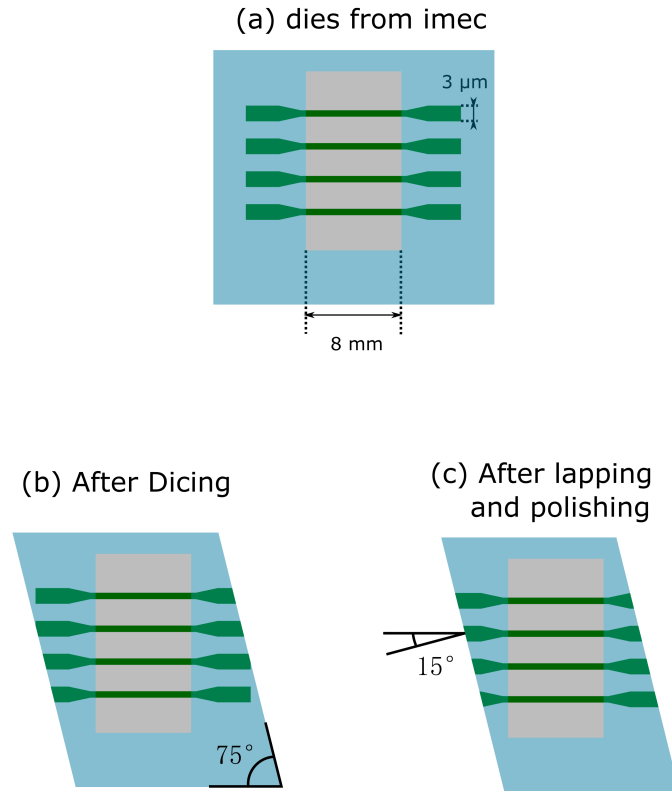


Figure B.1: Schematic of the process of facet polishing. (a) The structure of the sample we received from imec. (b) The structure of the sample after dicing. The dicing line is deliberately deviated by approximately $100\ \mu\text{m}$ from the desired facet. (c) The structure of the sample after polishing.

Although substrate and top surface polishing are widely used in microelectronics and silicon photonics for wafer planarization and sample thinning-down, the process of facet polishing is less established. In our case, we have to modify the PM5 polishing platform (Logitech) in our cleanroom for facet polishing. We also need to use a home-made sample holder to fasten the samples during polishing.

The sample holder is made of stainless steel as shown in Fig. B.2(a). The dimensions of the holder are shown in Fig. B.2(b). It is composed of two parts. The large piece is called the base and the small piece the cover. The samples are first adhered to the holders by glues and later reinforced by the clamping force provided by the sample holder. The glue we used is mostly composed of Crystalbond 509. It is prepared by crushing the Crystalbond 509 stick into smaller pieces and

dissolve 20 parts of Crystalbond 509 in 80 parts of acetone by weight.

The process of mounting the samples is shown in Fig. B.3. In the first step in Fig. B.3(a), we heat up both samples and sample holder with a hotplate (100 °C). Once the samples are heated up, we apply a few droplets of glue onto the top surfaces of samples and the sample holders. The acetone within the glue would quickly evaporate. In approximately 90 s, there will be no acetone left in the glue. The evaporation of acetone leaves a thin homogeneous layer of liquid Crystalbond 509 covering the surface. Next, we stack the samples one by one and place the sample stack on top of the base as shown in Fig. B.3(c). In this step, we try to align the samples parallel to the sides of the sample holder coarsely. In the last step in Fig. B.3(d), we turn the sample holder by 90° and push the facets against a hard surface to ensure the sample facet is parallel to the sides of the sample holder. Once the samples are aligned, we screw the cover to the base and apply a few droplets of glue to reinforce the connection between the samples and the sample holder.

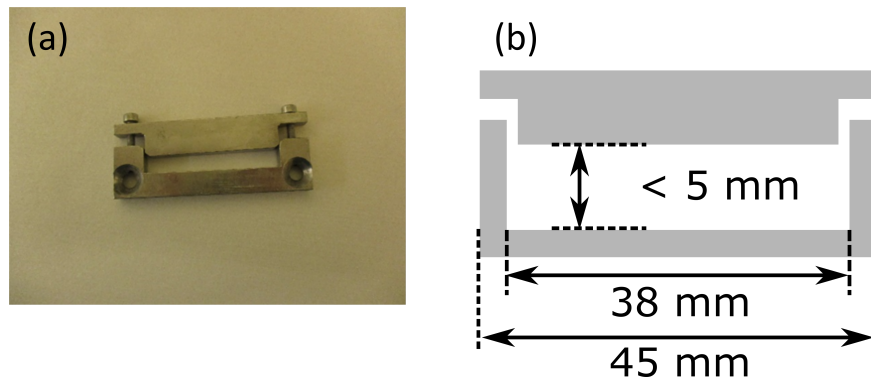


Figure B.2: Schematic of the sample holder. The sample holder is composed of two parts — a cover and a base. Two M3 screws are used to connect the cover and the base.

Next, we mount the sample stack to a jig for polishing. We configure the jig in such a way that a force equivalent to approximately 400 g of weight is applied to the facets of the sample stack. We use the same force for both polishing procedures.

A groove-less plate is used for initial coarse polishing. This coarse polishing is also called lapping. Before lapping, the metal plate is first pre-conditioned with 9 μm particles for 15 min at a speed of 40 rpm by a grooved metal conditioner. Both the polishing plate and the conditioner are made of cast iron. The process of conditioning is critical to prepare a highly-flat surface. During the conditioning, possible surface scratches caused during previous polishing or rusts developed on the surface during storage will be removed. Once the plate is conditioned, we place

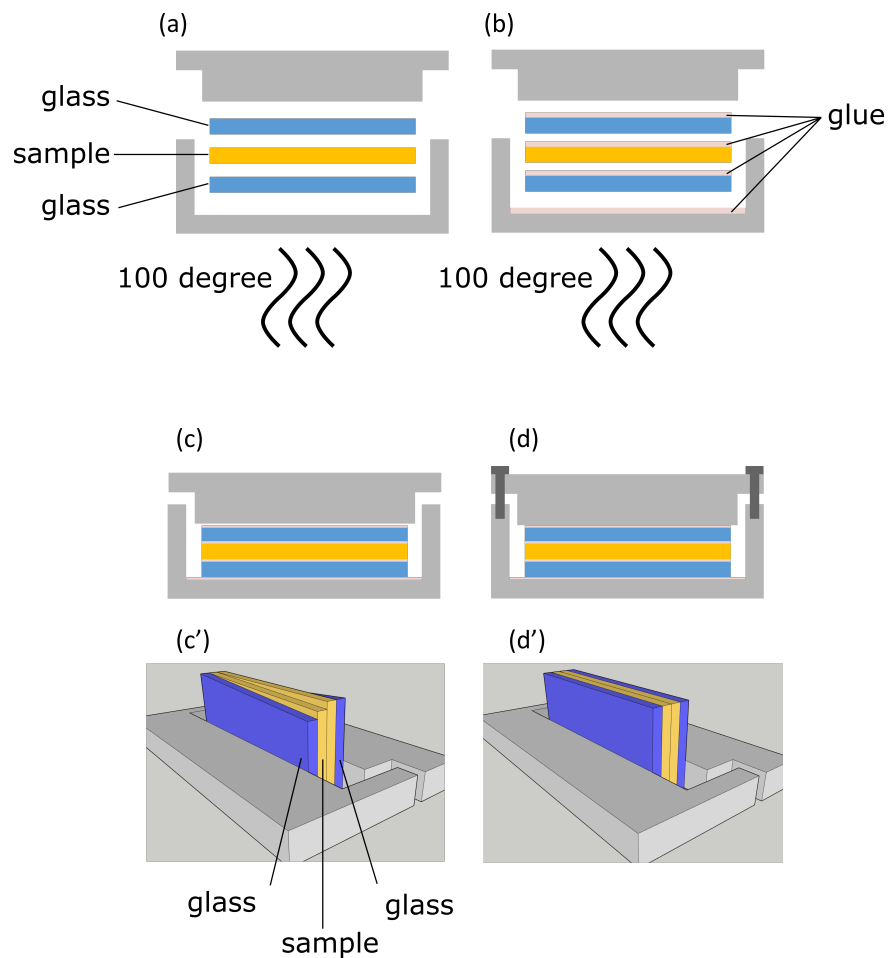


Figure B.3: The process of mounting the samples. (a) The sample and sample holders are heated up to 100° . (b) Apply a few droplets of Crystalbond 509 solution. (c) After the application of Crystalbond 509 solution, wait for about 90 s and then stack the samples onto the base. The 3d plot in (c') shows the expected status of the sample block. (d) Rotate the sample-and-holder block by 90° and push the samples against a reference plane. Use a cotton swab to ensure the coplanar alignment of the sample facets. The 3d plot in (d') shows the final alignment of the sample block.

the jig on the metal plate and apply a slurry with $3\ \mu\text{m}$ particles for lapping. The speed of the metal plate is set to 40 rpm. A gauge is attached to the jig to monitor the thickness. In this process, we will remove $80\ \mu\text{m}$ of the material.

Then we move to a groove-less polyurethane plate for the finer-grain polishing. The polyurethane pad is first conditioned with de-ionized (DI) water for 15 min by a diamond conditioner at a speed of 70 rpm. We use the SF1 slurry from Logitech for polishing. The rate of the polyurethane plate is set to 70 rpm during polishing. SF1 is made of alkaline colloidal silica particles with a diameter of 40 nm. We remove $10\ \mu\text{m}$ of the material in this process.

After polishing, we unmount the sample from the holder by heating up the whole block to 100° with a hotplate. When the Crystalbond 509 fully melts, we remove the sample carefully from the holder. Relative movement of samples along lateral directions should be minimized. The sample is then cleaned with Standard Clean 1 (SC1) solution for 30 min. The SC1 solution is prepared by first mixing 30 mL of NH_4OH (28%), 30 mL H_2O_2 (30%) and 150 mL of DI water. The solution is then heated up to 70° .

The SC1 cleaning is critical in removing all the remaining silicon dioxide nanoparticles on the edge of the chip. The surface of the sample right after polishing and is shown in Fig. B.4. We can see the waveguides are covered by many spheres with a diameter of 40 nm. Fig. B.5 shows the top surface of the sample after SC1 cleaning, and it is clear almost all the remaining particles are removed by SC1.

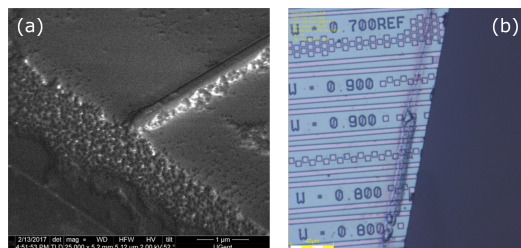


Figure B.4: (a) The SEM picture and (b) microscope picture of the nanoparticles accumulated on the sample surface over the polishing process. The small spheres with have a diameter of 40 nm. These spheres do not easily come off with standard acetone-isopropyl alcohol cleaning.

References

- [1] Hadi Baghsiahi, Kai Wang, Witold Kandulski, Richard C. A. Pitwon, and David R. Selviah. *Optical Waveguide End Facet Roughness and Optical Cou-*

C

Estimation of Raman susceptibility from Scattering Cross-section

In the vast body of the literature, the strength of the Raman response is given by the Raman scattering cross-section. However, in the treatment of coherent Raman scattering, the Raman susceptibility is frequently used. In this appendix, we try to connect these two parameters.

C.1 From Spontaneous to Stimulated Raman Gain

It is known that the spontaneous and stimulated Raman scattering are two closely related processes. The spontaneous Raman can also be regarded as a "stimulated" process, yet the "stimulation" is supplied by the vacuum fluctuation of the electromagnetic field rather than a laser. As these two processes share many common features, it is possible to convert the differential Raman scattering cross-section $d\sigma/d\Omega$ to the stimulated Raman gain parameter g_R . The formula is well established from [1] and it is given by

$$g_R = \frac{8\pi cM}{\hbar\omega_s^3 n^2 \Delta\nu} \frac{d\sigma}{d\Omega} \quad (\text{C.1})$$

where

- c is the speed of light in vacuum [m/s]
- M is the molecular density [cm^{-3}]

- \hbar is the reduced planck constant [J s]
- ω_s is the angular frequency of the Stokes Raman scattering component [rad/s]
- n is the ambient refractive index
- $\Delta\nu$ is the Raman Full-Width-Half-Maximum linewidth [cm^{-1}]
- $d\sigma/d\Omega$ is the Raman scattering cross-section [cm^2/sr]

From a dimensional analysis, we can see that the stimulated Raman gain coefficient has a dimension of [m/W], which is consistent with the definition in most textbooks.

C.2 From Stimulated Raman Gain to Raman Susceptibility

We have already established in chapter 2 the evolution of the Stokes beam in the process of stimulated Raman scattering. It is given by

$$\begin{aligned} I_s(L) &= \frac{3\omega_s}{n^2 c^2 \epsilon_0} (2\epsilon_0 n c |E_s|^2) (2\epsilon_0 n c |E_p|^2) L \text{Im}\{\chi_R\}, \\ &= \frac{3\omega_s}{n^2 c^2 \epsilon_0} I_s I_p L \text{Im}\{\chi_R\} \end{aligned} \quad (\text{C.2})$$

The evolution of the Stokes beam in stimulated Raman scattering can also be written as

$$\frac{dI_s}{dz} = g_R I_s I_p \quad (\text{C.3})$$

Comparing these two definitions of the stimulated Raman scattering, we can see that the stimulated Raman gain g_R and the imaginary of the susceptibility are strictly related as

$$\frac{3\omega_s \max \text{Im}\{\chi_R\}}{n^2 c^2 \epsilon_0} = g_R. \quad (\text{C.4})$$

We should note that in the estimation of stimulated Raman gain coefficient g_R , we are actually calculating its maximal value. This is taken care of by also taking the maximal value of the Raman susceptibility $\max \text{Im}\{\chi_R\}$.

C.3 Lorentzian Assumption of Raman Susceptibility

From Eq. (C.4) we can obtain the imaginary part of Raman susceptibility $\text{Im}\{\chi_R\}$. However, in the case of CARS we are often measuring the real part of $\text{Re}\{\chi_R\}$.

Although one can convert $\text{Im}\{\chi_{\text{R}}\}$ to $\text{Re}\{\chi_{\text{R}}\}$ with the help of Kramers-Kronig relations, it is also possible to utilize the fact $\text{Im}\{\chi_{\text{R}}\}$ has a Lorentzian lineshape. We first write down the Raman susceptibility at the vicinity of a vibrational mode

$$\begin{aligned}\chi_{\text{R}}(\Omega) &= \frac{1}{6\epsilon_0} \frac{N}{m} \left(\frac{\partial\alpha}{\partial Q} \right)_0^2 \frac{1}{\omega_v^2 - \Omega^2 - 2i\Omega\gamma} \\ &\approx \frac{1}{12\epsilon_0\omega_v} \frac{N}{m} \left(\frac{\partial\alpha}{\partial Q} \right)_0^2 \frac{1}{\omega_v - \Omega - i\zeta} \\ &= K \times \frac{1}{\omega_v - \Omega - i\zeta}.\end{aligned}\quad (\text{C.5})$$

Since we know the values of ω_v and Ω , $\chi_{\text{R}}(\Omega)$ can be fully determined if we know the values of ζ and K . Fortunately, both of them can be obtained from the references in spontaneous Raman experiments.

First, we notice the imaginary part of the susceptibility is given by

$$\text{Im}\{\chi_{\text{R}}\} = K \times \frac{\zeta}{(\omega_v - \Omega)^2 + \zeta^2}.\quad (\text{C.6})$$

And the real part is given by

$$\text{Re}\{\chi_{\text{R}}\} = K \times \frac{\omega_v - \Omega}{(\omega_v - \Omega)^2 + \zeta^2}.\quad (\text{C.7})$$

In the literature, the linewidth of Raman peaks are usually provided. Notice that $\text{Im}\{\chi_{\text{R}}\}$ has a Lorentzian lineshape, we can estimate ζ based on the data of Raman linewidth as

$$\zeta = \frac{\Delta\nu}{2}\quad (\text{C.8})$$

where $\Delta\nu$ is the full-width-half-maximum of a Raman mode. We also know that at zero detuning $\Omega = \omega_v$, the Raman susceptibility is a pure imaginary number given by

$$\max \text{Im}\{\chi_{\text{R}}\} = K \times \frac{1}{\zeta}.\quad (\text{C.9})$$

Therefore, we can easily calculate the constants in Eq. (C.6) as

$$K = \max \text{Im}\{\chi_{\text{R}}\} \times \frac{\Delta\nu}{2}\quad (\text{C.10})$$

In most situations, we are only concerned with the amplitude of Raman susceptibilities. In Fig. C.1 we can see the general shape of both imaginary and real component of a typical Raman susceptibility. To estimate the strength of coherent Raman response, we only need to know $\Delta \text{Re}\{\chi_{\text{R}}\}$ and $\Delta \text{Im}\{\chi_{\text{R}}\}$, which happen to be of the same value. If we denote them as $\Delta\chi_{\text{R}}$, we have

$$\Delta\chi_{\text{R}} = \max \text{Im}\{\chi_{\text{R}}\}\quad (\text{C.11})$$

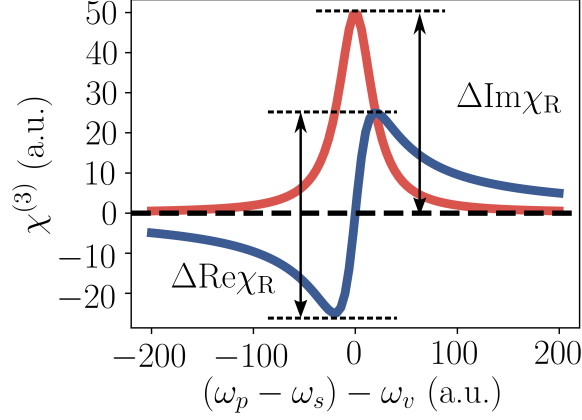


Figure C.1: The real part (blue solid) and imaginary part (red solid) of the Raman susceptibility. The absolute variation of these two components are most interested in estimating the strength of coherent Raman scattering.

C.4 Estimation of the Strength of Raman Susceptibility for Pure Isopropyl Alcohol

In this section we will estimate the Raman susceptibility of isopropyl alcohol (IPA). The parameter of this liquid is given in the following table

refractive index n	1.377
pump wavelength λ_p	785 nm
molecular density	$7.87 \times 10^{21} / \text{cm}^3$
Raman line ν_v	819 cm^{-1}
Raman linewidth $\Delta\nu$	10 cm^{-1}
Raman scattering cross-section $d\sigma/d\Omega$	$5.8 \times 10^{-31} \text{ cm}^2/\text{sr}$

Table C.1: The properties of pure isopropyl alcohol (IPA).

The stimulated Raman gain coefficient in bulk IPA is given by

$$g_R = \frac{8\pi c M}{\hbar \omega_s^3 n^2 \Delta\nu} \frac{d\sigma}{d\Omega} = 1.2 \times 10^{-12} \text{ m/W} = 0.12 \text{ cm/GW}. \quad (\text{C.12})$$

The peak Raman susceptibility can be obtained as

$$\max \text{Im}\{\chi_R\} = \frac{g_R n^2 c^2 \epsilon_0}{3\omega_s} = 2.5 \times 10^{-22} \text{ m}^2/\text{V}^2. \quad (\text{C.13})$$

We also have

$$\Delta \text{Re}\{\chi_R\} = \Delta \text{Im}\{\chi_R\} = 2.5 \times 10^{-22} \text{ m}^2/\text{V}^2. \quad (\text{C.14})$$

References

- [1] F. J. McClung and D. Weiner. *Measurement of Raman Scattering Cross Sections for Use in Calculating Stimulated Raman Scattering Effects*. Journal of the Optical Society of America, 54(5):641–643, May 1964.

